

**UCLA**

**UCLA Electronic Theses and Dissertations**

**Title**

Exploring Reaction Mechanisms of Short-Lived Carbocation and Radical Intermediates via Synergetic Modern Computational Methods and Collaborative Experiments

**Permalink**

<https://escholarship.org/uc/item/0jg5c2jp>

**Author**

Lee, Woojin

**Publication Date**

2023

Peer reviewed|Thesis/dissertation

UNIVERSITY OF CALIFORNIA

Los Angeles

Exploring Reaction Mechanisms of Short-Lived Carbocation and Radical Intermediates via  
Synergetic Modern Computational Methods and Collaborative Experiments

A dissertation submitted in partial satisfaction of the  
requirements for the degree Doctor of Philosophy  
in Chemistry

by

Woojin Lee

2023

© Copyright by

Woojin Lee

2023

## ABSTRACT OF THE DISSERTATION

Exploring Reaction Mechanisms of Short-Lived Carbocation and Radical Intermediates via  
Synergetic Modern Computational Methods and Collaborative Experiments

by

Woojin Lee

Doctor of Philosophy in Chemistry

University of California, Los Angeles, 2023

Professor Kendall N. Houk, Co-Chair

Professor Hosea M. Nelson, Co-Chair

This dissertation describes the investigation of reaction mechanisms involving short-lived carbocation and radical intermediates through the synergetic application of modern computational techniques and experimental validation. Density Functional Theory (DFT) and Molecular Dynamics (MD) simulations are employed as the primary computational methods to predict the behavior of those reactive intermediates and to gain insights into their various reaction pathways. Collaborative experiments with experimental groups are conducted to validate the computational results, enhancing the reliability and robustness of the computational findings. The dissertation is organized into two main sections. Chapters 1–6 mainly explore mechanistic investigations of nonclassical and vinyl carbocations, providing a comprehensive

understanding of their properties and reactions. Chapters 7–8 focus on research involving radicals, analyzing their roles in site- and stereo-selective reactions.

Chapter 1 delves into Winstein-Trifan solvolysis using modern molecular dynamics techniques under the guidance of Professor Kendall N. Houk. The studies found that the solvolysis of *exo*-norbornyl brosylate accompanied by  $\sigma$ -bridging occurs in a dynamically concerted process, while *endo*-solvolysis happens in a dynamically stepwise fashion.

Chapters 2–5 provide comprehensive studies of C–H insertion and Friedel-Crafts reactions of vinyl carbocations. The collaborative mentorship of Professor Kendall N. Houk and Professor Hosea M. Nelson shaped these chapters. Chapters 2 and 3 describe the development of  $\text{Li}^+$ -Ureide catalysis in the generation of vinyl carbocations from vinyl triflates and its impact on vinyl cation C–H insertion reactions. Chapter 4 discusses the formation of medium-sized rings through vinyl carbocation intermediates. Both computational and experimental studies revealed that canonical Friedel-Crafts reactions were involved in the process. Chapter 5 describes the electrochemical fluorination of vinyl boronates via donor-stabilized vinyl carbocation intermediates. DFT calculations were utilized to determine the oxidation potential of vinyl boronates, providing support for further experimental mechanistic studies.

Chapter 6 summarizes a collaborative work between the laboratories of Professor Kendall N. Houk and Professor Isaac J. Krauss. The Krauss lab observed an unusual mechanistic switch from homoallylation to cyclopropylcarbynylation of aldehydes. DFT calculations suggested that the origin of the mechanistic change was associated with carbocation stabilization by

substituents. Experimental mechanistic studies were subsequently employed to corroborate the predicted reaction pathway.

Chapter 7 presents a joint research project between the laboratories of Professor Kendall N. Houk and Professor Jiannan Zhao. The Zhao group discovered a diastereoselective radical aminoacylation of olefins facilitated by N-heterocyclic carbene catalysis. Computations were performed to elucidate the full reaction pathway, revealing that the radical coupling step is the diastereoselectivity- and rate-determining step. Additionally,  $\pi$ - $\pi$  interactions were found to be the origin of the selectivity. The computational findings were further validated by experimental studies.

Chapter 8 details a collaborative project between the laboratories of Professor Kendall N. Houk and Professor Massimo Bietti. The Bietti group carried out the site- and diastereo-selective oxygenation of unactivated C-H bonds in bicyclic and spirocyclic hydrocarbons containing cyclopropyl moieties using 3-ethyl-3-(trifluoromethyl)dioxiranes (ETFDO). DFT calculations were conducted to understand the underlying factors responsible for the selectivities. The calculations found that hyperconjugation effects originating from the Walsh orbital of the cyclopropane ring play a crucial role in the selective  $\alpha$ -C-H bond oxidations. Additionally, the computational studies provided evidence of divergent radical and cationic pathways in the ETFDO oxygenations.

The dissertation of Woojin Lee is approved.

Alexander M. Spokoyny

Neil K. Garg

Hosea M. Nelson, Committee Co-Chair

Kendall N. Houk, Committee Co-Chair

University of California, Los Angeles

2023

*This dissertation is dedicated to my parents, Kyoung Soon Lee and Taeyoung Lee,  
my wife, Minjeong Park, and my son, Eden Hyun Lee.*



## TABLE OF CONTENTS

ABSTRACT OF THE DISSERTATION .....	ii
COMMITTEE PAGE .....	v
DEDICATION PAGE .....	vi
TABLE OF CONTENTS.....	vii
LIST OF FIGURES .....	xi
LIST OF SCHEMES .....	xvii
LIST OF TABLES.....	xix
ACKNOWLEDGEMENTS.....	xx
BIOGRAPHICAL SKETCH .....	xxvi
CHAPTER ONE: Molecular Dynamics of the Norbornyl Cation and Its Generation in Winstein-Trifan Solvolysis: The Timing of $\sigma$ -Bridging Establishes Anchimeric Assistance .....	1
1.1 Contributions .....	1
1.2 Abstract.....	1
1.3 Introduction.....	1
1.4 Computational Methods.....	4
1.5 Results and Discussion .....	5
1.6 Conclusion .....	10
1.7 References.....	12
CHAPTER TWO: Computational Exploration of the Nature of $\text{Li}^+$ -Ureide Anion Catalysis on Formation of Highly Reactive Vinyl Carbocations and Subsequent C–C Bond Forming Reactions.....	16
2.1 Contributions .....	16

2.2 Abstract.....	16
2.3 Introduction .....	17
2.4 Computational Methods.....	18
2.5 Results and Discussion .....	19
2.6 Conclusion .....	25
2.7 References.....	26
CHAPTER THREE: Urea-Catalyzed Vinyl Carbocation Formation Enables Mild	
Functionalization of Unactivated C–H Bonds .....	30
3.1 Contributions .....	30
3.2 Abstract.....	30
3.3 Introduction .....	31
3.4 Results and Discussion .....	32
3.5 Conclusion .....	40
3.6 References.....	41
CHAPTER FOUR: Accessing Medium-sized Rings via Vinyl Carbocation Intermediates .....	
4.1 Contributions .....	44
4.2 Abstract.....	44
4.3 Introduction .....	44
4.4 Results and Discussion .....	46
4.5 Conclusion .....	53
4.6 References.....	55

CHAPTER FIVE: Electrochemical Fluorination of Vinyl Boronates Through Donor-Stabilized Vinyl Carbocation Intermediates .....	59
5.1 Contributions .....	59
5.2 Abstract.....	59
5.3 Introduction .....	59
5.4 Results and Discussion .....	61
5.5 Conclusion .....	70
5.6 References.....	72
CHAPTER SIX: A Mechanistic Switch from Homoallylation to Cyclopropylcarbinylation of Aldehydes .....	79
6.1 Contributions .....	79
6.2 Abstract.....	79
6.3 Introduction .....	79
6.4 Results and Discussion .....	81
6.5 Conclusion .....	87
6.6 References.....	88
6.7 Supplementary Information .....	90
CHAPTER SEVEN: Diastereoselective Radical Aminoacylation of Olefins through N-Heterocyclic Carbene Catalysis .....	92
7.1 Contributions .....	92
7.2 Abstract.....	92
7.3 Introduction .....	93
7.4 Results and Discussion .....	96

7.5 Conclusion .....	110
7.6 References.....	111
CHAPTER EIGHT: Divergent Radical and Cationic Pathways in C( <i>sp</i> <sup>3</sup> )–H Bond Oxygenation of Bicyclic and Spirocyclic Hydrocarbons Bearing Cyclopropane Moieties Promoted by Dioxiranes .....	
Dioxiranes .....	120
8.1 Contributions .....	120
8.2 Abstract.....	120
8.3 Introduction .....	121
8.4 Experimental and Computational Results.....	126
8.5 Discussion.....	135
8.6 Conclusion .....	148
8.7 Supplementary Information .....	150
8.8 References.....	158

## LIST OF FIGURES

### CHAPTER ONE

<b>Figure 1.1</b> a) Winstein-Trifan acetolysis. b) Nonclassical 2-norbornyl cation. c) Classical 2-norbornyl cation. d) Equilibria of 2-norbornyl cations. e) This work. ....	3
<b>Figure 1.2</b> Transition state ensembles of <i>exo</i> - and <i>endo</i> -solvolysis.....	4
<b>Figure 1.3</b> a) Energy profile of the <i>exo</i> - and <i>endo</i> -norbornyl brosylate solvolysis. b) Transition state structures of <i>exo</i> - and <i>endo</i> -solvolysis. ....	5
<b>Figure 1.4</b> a) Plot of C <sub>6</sub> –C <sub>2</sub> and C <sub>2</sub> –O bonds during <i>exo</i> -solvolysis simulations. b) Histogram of trajectory time-to-bridging ( <i>exo</i> ). c) Plot of C <sub>6</sub> –C <sub>2</sub> and C <sub>2</sub> –O bonds during <i>endo</i> -solvolysis simulations. d) Histogram of trajectory time-to-bridging ( <i>endo</i> ). ....	7
<b>Figure 1.5</b> a) Histogram graph of selected bond lengths during 2-norbornyl cation 500 fs simulations (29 trajectories). b) Histogram graph of selected bond lengths during norbornane 500 fs simulations (26 trajectories).....	9

### CHAPTER TWO

<b>Figure 2.1</b> a) Li <sup>+</sup> -ureide-catalyzed vinyl carbocation formation and its C–C bond forming reactions. b) Structure of the dimer of the lithium salt of the urea optimized by DFT computations. ....	18
<b>Figure 2.2</b> Proposed reaction mechanism. ....	20
<b>Figure 2.3</b> Computational investigation of the overall reaction process with ωB97X-D/6-311+G(d,p) // ωB97X-D/6-31G(d,p) in the gas phase at 298.15 K.....	21
<b>Figure 2.4</b> 3-D structures of complex <b>9</b> , <b>11</b> , <b>13</b> and C–H insertion transition state <b>10</b> .....	22
<b>Figure 2.5</b> Computational studies of the vinyl cation reactivity in the absence of counter anion with ωB97X-D/6-311+G(d,p) in the gas phase at 298.15K.....	23

## CHAPTER THREE

**Figure 3.1** Vinyl cation insertion reactions and hydrogen-bond donor catalysts. a) Lithium-promoted intramolecular C–H insertion reactions of vinyl cations. b) Chiral thiourea-catalyzed additions to oxocarbenium cations via chloride abstraction. c) Functionalization of unactivated C–H bonds catalyzed by ureas. ....31

**Figure 3.2** Urea catalyzed Friedel–Crafts reactions. Isolated yield after column chromatography a) Scope of vinyl triflates and arenes. b) C–H insertion, Friedel–Crafts cascade. <sup>a</sup>10 equiv arene. <sup>b</sup>Catalyst **9**. <sup>c</sup>*p*-Xylene solvent. <sup>d</sup>Yield determined by GC-FID. ....35

**Figure 3.3** Urea and lithium catalyzed C–H insertion reactions. Isolated yield after column chromatography. <sup>a</sup>Yield determined by NMR using an internal standard. <sup>b</sup>Catalyst **4** <sup>c</sup>LiHMDS base in cyclohexane solvent. <sup>d</sup>Catalyst **5**. <sup>e</sup>LiOtBu base in 1,2-DCE solvent. ....36

**Figure 3.4** Urea catalyzed C–H insertion reactions of  $\beta$ -ketoester derived vinyl triflates. Isolated yield after column chromatography. <sup>a</sup>10 equiv LiH. ....37

**Figure 3.5** Mechanism of urea promoted C–H insertion. a) Nature of C–C bond formation of vinylogous acyl triflates. Ar = *p*-tolyl. b,c) Mechanistic studies. d) Proposed catalytic cycle of reaction. Ar = 3,5-bis(CF<sub>3</sub>)phenyl. ....39

## CHAPTER FOUR

**Figure 4.1** C–C bond formations via Lewis acid-WCA catalysis. a) Intramolecular C–H insertion reactions from vinyl triflates via Li-WCA catalysis. b) This work: Medium-sized ring formation via Li-WCA catalysis. ....46

**Figure 4.2** Commercial drugs with *exo*-alkene on a 7-membered ring. ....47

**Figure 4.3** Scope of Li-WCA catalyzed medium-sized ring formation. The reactions were performed on 0.05 mmol scale unless otherwise specified. All yields were isolated yields unless specified. All structures were characterized by NMR. The structures of **5**, **9**, **12**, **13**, **16** and **17** were also characterized by microED.....50

**Figure 4.4** a) Possible mechanistic pathways. b) Computational investigation of the medium-sized ring formation of vinyl cations. c) Influence of –OMe position on the medium-sized ring formation. d) Mechanistic study for Path 1 & Path 2. The yield was determined by NMR with an internal standard. e) Mechanistic study for Path 3. The ratio was determined by FD–MS. \*All computations were performed with  $\omega$ B97X-D/def2-TZVPP/SMD(*o*-dichlorobenzene) //  $\omega$ B97X-D/def2-SVP/SMD(*o*-dichlorobenzene) at 413.15 K.....52

## CHAPTER FIVE

**Figure 5.1** Previous work and this study. a) Hofer-Moest electrochemical oxidation. b) this research: electrochemical fluorination of alkenyl boronates via vinyl carbocations. 60

**Figure 5.2** Scope of alkenyl boronic ester electrochemical fluorination. Isolated yields. <sup>a</sup>3 equiv of TBAF on 1 mmol scale. <sup>b</sup>Isolated as a 9:1 mixture of fluoride:styrene. <sup>c</sup>+0.8 V vs SCE. n.d.=not detected. ....65

**Figure 5.3** Mechanistic experiments to probe for vinyl carbocation reactivity. a) Elimination reactivity suggesting vinyl carbocation intermediate. b) Unsymmetric alkenyl boronic ester reactivity. c) Friedel-Crafts reactivity with N-Me pyrrole. d) C–H Insertion reactivity. Isolated yields. <sup>a</sup>Yield determined by <sup>1</sup>H NMR with an internal standard. <sup>b</sup>Ratio of styrene olefin isomers determined by GC-FID.....66

**Figure 5.4** Mechanistic experiments to probe for vinyl radical intermediate. a) Cyclic voltammogram of the tetrabutylammonium salt of **1** in 0.1 M TBABF<sub>4</sub> MeCN at 100 mV/s. First and second oxidative waves and +1.8 V of typical reaction highlighted. b) Styrene products observed in the presence of *n*PrSD. c) Change of arylation regioselectivity at lower applied potential. <sup>a</sup>Propane thiol prepared at 77% deuteration as determined by <sup>1</sup>H NMR. <sup>b</sup>Yields determined by <sup>1</sup>H NMR with an internal standard. *n*PrSD=deuterium incorporated *n*-propyl thiol. ....68

**Figure 5.5** a) Predicted initial oxidation. b) Proposed mechanism of boronate fluorination. Calculated HOMO and oxidation potential using (uM06-2X/6-311++G(d,p) cpcm=acetonitrile // uM06-2X/6-31+G(d,p) cpcm=acetonitrile). ....70

## CHAPTER SIX

**Figure 6.1** Allylboration versus homoallylation with cyclopropanated allylboron reagents. ....80

**Figure 6.2** Cyclopropylcarbinylation and mechanistic study.....82

**Figure 6.3** Cyclopropylcarbinylation versus homoallylation with *cis*-phenyl reagent **13**.  
.....83

**Figure 6.4** Homoallylation with *trans*-methyl reagent **3**.....84

**Figure 6.5** Reversal of the cyclopropylcarbinylation/homoallylation selectivity by electronic tuning.....86

**Figure 6.6** Calculated reaction pathways of phenyl-substituted boronate **13**. ....90

**Figure 6.7** Calculated reaction pathways of methyl-substituted boronate **3**. ....91

## CHAPTER SEVEN



<b>Figure 7.1</b> a) Generation of iminyl radicals via N–O bond homolysis. b) Access to pyrroline derivative with vicinal stereocenters. c) Radical NHC catalysis. d) Diastereoselective iminoacylation of trisubstituted olefin.....	94
<b>Figure 7.2</b> Prospective catalytic cycle.....	96
<b>Figure 7.3</b> Scope of aldehydes. <sup>a</sup> .....	99
<b>Figure 7.4</b> Scope of oximes. <sup>b</sup> .....	101
<b>Figure 7.5</b> Synthetic transformation of <b>9</b> . <sup>a</sup> .....	103
<b>Figure 7.6</b> Experimental mechanistic studies. ....	105
<b>Figure 7.7</b> Computational mechanistic studies. ....	107
<b>Figure 7.8</b> Diastereoselective amidoacylation of olefins. <sup>a</sup> .....	109

## CHAPTER EIGHT

<b>Figure 8.1</b> Use of cyclopropyl containing substrates. a) To implement selectivity in HAT-based C–H bond functionalization procedures. b) To probe mechanisms. ....	123
<b>Figure 8.2</b> Structures of the substrates investigated in this work.....	126
<b>Figure 8.3</b> Difference in activation free energies ( $\Delta\Delta G^\ddagger$ , in kcal mol <sup>-1</sup> ) for HAT from the $\alpha$ - and $\beta$ - C–H bonds in <b>S1</b> , <b>S2</b> , <b>S4</b> and <b>S5</b> by ETFDO: computational and experimental studies. ....	131
<b>Figure 8.4</b> Computed activation free energy difference ( $\Delta\Delta G^\ddagger$ , in kcal mol <sup>-1</sup> ) for HAT from the C–H bonds of <b>S3</b> by ETFDO. ....	131
<b>Figure 8.5</b> Energetics of C–H bond oxidation of <b>S3</b> promoted by ETFDO. ....	132
<b>Figure 8.6</b> Computed and experimental activation free energy difference ( $\Delta\Delta G^\ddagger$ , in kcal mol <sup>-1</sup> ) for HAT from the C–H bonds of <b>S7</b> and <b>S8</b> to ETFDO. ....	133
<b>Figure 8.7</b> Energetics of C–H bond oxidation of <b>S8</b> promoted by ETFDO. ....	134

<b>Figure 8.8</b> Normalized site-selectivities and diastereoselectivities observed in the hydroxylation of bicyclo[n.1.0]alkanes <b>S1</b> , <b>S2</b> , <b>S4</b> and <b>S5</b> promoted by ETFDO. ....	136
<b>Figure 8.9</b> a) Charge distribution of <b>S8-Int1</b> by CM5 calculations. b) Spin density of hypothetical triplet radical pair <b>S8-Int1a</b> . ....	145
<b>Figure 8.10</b> Normalized site-selectivities observed in the oxygenation of 1,1-dimethylcyclohexane ( <b>S6</b> ), spiro[2.5]octane ( <b>S7</b> ) and 6- <i>tert</i> -butylspiro[2.5]octane ( <b>S8</b> ) promoted by ETFDO. ....	148
<b>Figure 8.11</b> Transition state structures and structural analysis in C–H bond activation of bicyclo[3.1.0]hexane <b>S1</b> . ....	150
<b>Figure 8.12</b> Transition state structures and structural analysis in C–H bond activation of bicyclo[4.1.0]heptane <b>S2</b> . ....	151
<b>Figure 8.13</b> Transition state structures and structural analysis in C–H bond activation of bicyclo[5.1.0]octane <b>S4</b> . ....	152
<b>Figure 8.14</b> Transition state structures and structural analysis in C–H bond activation of bicyclo[6.1.0]nonane <b>S5</b> . ....	153
<b>Figure 8.15</b> Transition state and intermediate structures in the oxygenation with 1-methylbicyclo[4.1.0]heptane <b>S3</b> . ....	154
<b>Figure 8.16</b> Transition state and intermediate structures in the oxygenation with spiro[2.5]octanes <b>S7</b> . ....	155
<b>Figure 8.17</b> Transition state and intermediate structures in the oxygenation with 6-( <i>tert</i> -butyl)spiro[2.5]octanes <b>S8</b> . ....	156
<b>Figure 8.18</b> Energy profile in the oxygenation with spiro[2.5]octanes <b>S7</b> . ....	157

## LIST OF SCHEMES

### CHAPTER EIGHT

<b>Scheme 8.1</b> Oxygenation of spiro[2.5]octane and 6- <i>tert</i> -butylspiro[2.5]octane promoted by manganese-oxo species.....	124
<b>Scheme 8.2</b> Mechanism of oxygenation by dioxiranes. ....	125
<b>Scheme 8.3</b> Oxygenation of bicyclo[n.1.0]alkanes (n = 3-6) ( <b>S1-S5</b> ) promoted by ETFDO.....	127
<b>Scheme 8.4</b> Oxygenation of 1,1-dimethylcyclohexane ( <b>S6</b> ) and of spiro[2.5]octanes ( <b>S7</b> and <b>S8</b> ) promoted by ETFDO.....	128
<b>Scheme 8.5</b> Oxygenation of <i>cis</i> -bicyclo[4.1.0]heptan-2-ol ( <b>P2a-OH</b> ) and <i>trans</i> -bicyclo[4.1.0]heptan-2-ol ( <b>P2b-OH</b> ). Conversion and product yields were determined by GC and averaged over two independent experiments. a) Reaction conditions: <b>P2a-OH</b> or <b>P2b-OH</b> 1 eq, oxone 1 eq, NaHCO <sub>3</sub> 4 eq, 1,1,1-trifluoro-2-butanone 0.2 eq, HFIP/H <sub>2</sub> O (3:1), Bu <sub>4</sub> NHSO <sub>4</sub> 0.05 eq, T = 0 °C, 3 h. b) <b>P2a-OH</b> 1 eq, <b>P2b-OH</b> 1 eq, oxone 1 eq, NaHCO <sub>3</sub> 4 eq, 1,1,1-trifluoro-2-butanone 0.2 eq, HFIP/H <sub>2</sub> O (3:1), Bu <sub>4</sub> NHSO <sub>4</sub> 0.05 eq, T = 0 °C, 6 h. <sup>a</sup> rsm: recovered starting material. ....	129
<b>Scheme 8.6</b> Oxygenation of <i>trans</i> -6- <i>tert</i> -butylspiro[2.5]octan-2-ol ( <b>P8a-OH</b> ) and <i>cis</i> -6- <i>tert</i> -butylspiro[2.5]octan-2-ol ( <b>P8c-OH</b> ). Conversion and product yields were determined by GC and averaged over two independent experiments. a) Reaction conditions: <b>P8a-OH</b> or <b>P8c-OH</b> 1 eq, oxone 1 eq, NaHCO <sub>3</sub> 4 eq, 1,1,1-trifluoro-2-butanone 0.2 eq, HFIP/H <sub>2</sub> O (3:1), Bu <sub>4</sub> NHSO <sub>4</sub> 0.05 eq, T = 0 °C, 3 h. b) <b>P8a-OH</b> 1 eq, <b>P8c-OH</b> 1 eq, oxone 1 eq, NaHCO <sub>3</sub> 4 eq, 1,1,1-trifluoro-2-butanone 0.2 eq, HFIP/H <sub>2</sub> O (3.0:1.0), Bu <sub>4</sub> NHSO <sub>4</sub> 0.05 eq, T = 0 °C, 6 h. <sup>a</sup> rsm: recovered starting material.....	129

<b><i>Scheme 8.7</i></b> Proposed mechanism for the oxygenation of <b>S2</b> promoted by cytochrome P450 enzymes. <sup>15a</sup> .....	139
<b><i>Scheme 8.8</i></b> Proposed mechanistic pathways for the oxygenation of <b>S3</b> promoted by ETFDO.....	141
<b><i>Scheme 8.9</i></b> Proposed mechanism for the oxygenation of <b>S7</b> and <b>S8</b> promoted by ETFDO.....	147

## LIST OF TABLES

### CHAPTER THREE

**Table 3.1** Optimization of C–H insertion reactions with hydrogen-bonding catalysts. ....33

### CHAPTER FOUR

**Table 4.1** Optimization of the reaction conditions to build medium-sized rings. ....48

### CHAPTER FIVE

**Table 5.1** Optimization of fluorination from vinyl trifluoroborate **1** and pinacol boronate **3**. Isolated yields. <sup>a</sup>Formed *in situ* from the pinacol boronic ester. <sup>b</sup><sup>19</sup>F NMR yield with fluorobenzene as an internal standard. <sup>c</sup>Added 50 mg mol sieves, MeCN distilled over CaH<sub>2</sub> and dried over mol sieves. TBAT=tetrabutyl ammonium difluorotriphenyl silicate, TMAF=tetramethyl ammonium fluoride. n.d.=not detected. ....63

### CHAPTER SEVEN

**Table 7.1** Optimization and control studies.<sup>a</sup>.....98

## ACKNOWLEDGEMENTS

"Give all your worries and cares to God, for he cares about you." (Peter 5:7) holds a special place in my heart as my cherished Bible verse and a guiding principle that shapes my life. Despite embarking on my educational journey later in life, I entered graduate school with unwavering confidence, entrusting all my anxieties to God and believing that I could overcome any obstacles. Approaching my studies and projects with utmost dedication, I found immense happiness, joy, and personal growth. This invaluable opportunity brought fulfillment and pushed me to surpass my limits, ultimately leading to the completion of my doctoral thesis statement—a significant milestone in my life. This acknowledgment is a testament to my gratitude towards all the professors, committees, and individuals who have played an integral role in my growth and accomplishments.

The primary catalyst behind my unwavering commitment and enthusiasm throughout my graduate school journey is the invaluable guidance of two esteemed professors, Professor Ken Houk and Professor Hosea Nelson, who exposed me to a vast realm of knowledge within the field of Chemistry.

Professor Ken Houk has a special place in my heart as he recognized my potential and consistently encouraged collaborative research, granting me opportunities to explore various captivating subjects. Through his generosity in sharing valuable UCLA heritage books and papers instrumental to my research, I witnessed his open-mindedness and passion for academia, inspiring me to approach scholarly pursuits with the same fervor. The individual meetings with

Professor Ken Houk provided a platform for him to impart insightful guidance, enabling me to systematically refine my papers and work with meticulous attention to detail. Under his mentorship, I have acquired an unyielding thirst for knowledge, propelling me on an enduring journey of personal and intellectual growth. Furthermore, Professor Ken Houk demonstrated exceptional personal support, treating my affairs like his own. While preparing the NIW (National Interest Waiver) green card application for myself and my family, he wrote strong recommendation letters. He showed a genuine interest in every aspect, ensuring smooth progress at every step. Additionally, during the Thanksgiving holiday, he graciously invited the entire lab and our families, creating a warm and inclusive atmosphere that made the holiday truly memorable.

Professor Hosea Nelson has been instrumental in shaping my current position. Upon completing my undergraduate studies, I decided to pursue graduate school. I submitted my application and resume, which he evaluated with utmost optimism, recognizing my potential. During my graduate research, Professor Hosea Nelson introduced me to the computational organic chemistry field, enabling me to see the big picture. Despite Professor Hosea Nelson's transition to Caltech, I could maintain continuous mentorship from him and the Nelson Lab, which afforded me an environment of profound intellectual stimulation and motivation. By diligently crafting preparatory materials for group meetings, I have significantly enhanced my practical aptitude as a chemist, equipping myself with the necessary skills to excel in real-world applications. Professor Hosea Nelson's incisive and resolute counsel has fostered within me a humble appreciation for the profound revelations and educational experiences that abound within the demanding realm of chemistry.

Expressing my deepest gratitude once again to my advisors, I would like to extend my thanks to Professor Neil Garg and Professor Alexander Spokoyny for taking the time out of their busy schedules to provide me with comprehensive support and advice on matters related to my education, academic plans, establishments, and activities.

I am profoundly grateful for the presence of like-minded individuals traversing a similar path and sharing comparable aspirations. The immeasurable strength and motivation I have derived from this realization are beyond words. Despite the limited face-to-face interactions due to the pandemic, the presence of the Houk Lab and Nelson Lab members stands as the most treasured gift I have received over the past five years. Thanks to all of you, I have been able to attribute my continuous growth and dedication toward positively impacting my peers and the global community to the collective contributions of each member. I extend my heartfelt appreciation for enabling me to engage in perpetual learning. While the significance of my academic journey and pursuit of a degree remains profound, I am equally grateful for the privilege of encountering exceptional individuals like you.

First, my heartfelt thanks go to Xiangyang Chen. I assimilated important research techniques and logical frameworks in computational chemistry from her. Moreover, she introduced me to a collaborative opportunity with Dr. Jiannan Zhao, laying the groundwork for Chapter 7 of this thesis. Next, I thank Tyler Benton, Cooper Jamieson, Arka Sengupta, Selbi Nuryyeva, and Gina Ga Young Lee. As I began to focus on computational chemistry in the Houk lab, they provided me with fundamental skills in various computational chemistry methods. Tyler and Gina familiarized me with the Hoffman2 cluster, Gaussian, and CREST. Cooper and Arka guided me



to run Progdyn MD simulations, and Selbi demonstrated complex radical calculations. These skills, which I further honed, proved invaluable for numerous projects throughout my doctoral journey and formed the foundation of this thesis. My appreciation extends to my fellow Houk lab colleagues: Huiling Shao, Meng Duan, Pengchen Ma, Qingyang Zhao, Panpan Chen, Billy Treacy, and Lisa Boatner. I truly enjoyed our spontaneous conversations on random topics in the office and during group activities. I appreciated the cheerful and friendly lab environment.

Next, I must thank Stasik Popov. When I was a young graduate student, he mentored me even if he was not officially assigned as a mentor. His intellect and kindness have left a lasting impression on me during graduate school. I remember his patient training for my first glovebox work, which took nearly two hours to set up only three reactions. Moreover, his guidance during my second-year presentation was instrumental. His support during my early years in graduate school was indispensable. My appreciation extends to Ben Wigman, who taught me various experimental techniques for vinyl cation chemistry, which proved invaluable for my experimental work in the Nelson group. Ben's sense of humor and friendly manner brightened the lab atmosphere. I want to thank Sepand Nistanaki. During my candidacy exam preparation, Sepand identified a flaw in my proposal and devoted his time to helping me craft a solid proposal. I want to thank Lee Joon Kim. She taught me the concept of MicroED during the pandemic, and I could learn a general workflow of this cutting-edge technology. I am grateful to Jessica Burch, Christopher Jones, and Chloe William, who contributed to making a friendly lab environment in the Nelson group. I must also thank my close friend, Steven (Zhenqi) Zhao. Our shared experiences as international students allowed us to understand each other's situations in our academic and personal lives. Spending time with him often relieves stress amid work and life pressures. I wish to thank Alex Bagdasarian, Brian Shao, and Sydnee Green. During my initial

year as a novice graduate student, I frequently encountered challenges while operating the lab equipment. However, the experienced individuals in the lab generously assisted me, allowing me to correct my errors and enhance my proficiency in handling the equipment.

I consider myself incredibly fortunate as I reflect upon my journey, acknowledging the countless individuals who have played climacteric roles in my success. Among them, two individuals stand out as the motivation who thrust my growth. The first is Professor F. Dean Toste, whose wholehearted support and contribution revitalized my ambition to study chemistry when I was on the threshold of giving up after not receiving admission to graduate school in 2017. His guidance paved the way for me to pursue a doctoral program at UCLA, where I am now blessed to collaborate with outstanding researchers. The second person I am deeply thankful for is Nick Y. Shin, whose genuine assistance has been the cornerstone of my journey. Nick proved to be an irreplaceable companion, leaving me with unforgettable memories while offering incalculable support in my chemistry career. Specifically, his guidance in preparing my statement of purpose for graduate school was immeasurable, playing a significant role in my journey.

Throughout my graduate years, I have encountered and connected with numerous people, each with unique personalities and life experiences. Their kind-hearted help and love have encouraged personal growth within me, provoking me to spread the same kindness and contribute to the positive transformation of those around me. In addition to these influential figures, I have been lucky to meet innumerable other benefactors whose impact on my life is indescribable. As a result, I now feel a deep inclination not only to receive assistance but also to offer support, actively contributing to the betterment of others' lives and catalyzing meaningful change.

Lastly, I humbly extend this honor and moment to my cherished family. To my esteemed parents, Taeyoung Lee and Kyung Soon Lee, who have consistently supported their son's belated career transition and wholeheartedly waited for his endeavors while studying abroad, I express my profound gratitude and utmost love. I sincerely appreciate the unwavering guidance that my mom and dad provided, serving as constant sources of inspiration and fostering a lifelong commitment to learning. Your tremendous support has been a source of solace and encouragement, uplifting me through moments of elation and discouragement. Furthermore, I sincerely acknowledge and thank my in-laws, who reside distantly but continuously exhibit understanding and take pride in their son-in-law, even amidst the constraints of a busy schedule that may limit communication. I am very grateful to my wife and son. My wife, Minjeong Park, is my unwavering supporter during this journey, serving as my haven in times of stress. Her belief in me enabled me to reach this accomplishment I never thought possible. Throughout this demanding journey, she embraced the challenges of our daily life, often prioritizing my needs over hers. Her true love was light in the darkness, leading me back when I felt lost. My son, Eden Hyun Lee, reminded me of the world beyond chemistry research through his smiles and the purity of his joy. His presence motivated me to strive harder and to shape my family's future. He was an unending source of happiness and inspiration, always bringing me back to what is truly important in life. I am genuinely grateful for being embraced as part of the family. This bond has gained even greater significance during my graduate school journey. I will forever cherish the deep love and grace bestowed upon me by parents, striving to live in a manner that reflects my heartfelt appreciation. Moreover, the thought of my dear departed grandmother and grandfather, Okju Moon and Gapsu Lee, brings me immense joy, envisioning them looking down upon me with approving smiles from the heavens.

## BIOGRAPHICAL SKETCH

### Education:

#### University of California, Los Angeles

Los Angeles, CA

Ph.D. Candidate in Chemistry, 2023

M.S. in Chemistry, 2020

Research advisors: Professor Kendall N. Houk and Professor Hosea M. Nelson

#### University of California, Berkeley

Berkeley, CA

B.S. in Chemistry, 2016

Research advisor: Professor F. Dean Toste

### Professional and Academic Experience:

#### Graduate Research Assistant

University of California, Los Angeles

2018–2023

Advisors: Professor Kendall N. Houk and Professor Hosea M. Nelson

- Utilized computational quantum mechanical modeling methods such as Density Functional Theory (DFT) and Molecular Dynamics (MD) simulations to understand the behavior and reactivities of short-lived carbocation and radical intermediates
- Investigated C–H insertion and Friedel–Crafts reactions of vinyl carbocation intermediates via computational and experimental methods
- Explored the norbornyl cation and its generation in Winstein-Trifan solvolysis via modern computational techniques
- Collaborated with Professor Isaac J. Krauss (Brandeis University), Professor Jiannan Zhao (Dalian University of Technology), and Professor Massimo Bietti (University of Rome, Tor Vergata) to elucidate complex reaction mechanisms with computational modeling

#### Graduate Teaching Assistant

University of California, Los Angeles

2018–2022

- CHEM 144 (Practical and Theoretical Introductory Organic Synthesis)
- CHEM 136 (Organic Structural Methods)
- CHEM 14CL (General and Organic Chemistry Laboratory II)
- CHEM 14D (Organic Reactions and Pharmaceuticals)
- CHEM 30CL (Organic Chemistry Laboratory II)

#### Visiting Student Researcher

California Institute of Technology

2021–2022

#### Medicinal Chemist Intern

Genentech, Inc.

2017

- Formulated a synthetic process for highly branched dendrimer drug conjugates
- Optimized the synthetic route to active pharmaceutical ingredients

#### Undergraduate Research Assistant

University of California, Berkeley

2016–2017

Advisor: Professor F. Dean Toste

- Investigated strategies for stabilizing Oxo-Re catalyst to achieve high yield in the aqueous adipic acid synthesis
- Synthesized isotopically labeled compounds for KIE studies and prepared vicinal diol starting materials for investigating Hammett correlation

### Honors and Awards:

Graduate Dean's Scholar Award	2018
Excellence in Chemistry Fellowship	2018

### Publications:

- [9] Galeotti, M.<sup>†</sup>; Lee, W.<sup>†</sup>; Sisti, S.; Casciotti, M.; Salamone, M.; Houk, K. N.; Bietti, M. "Divergent Radical and Cationic Pathways in C(sp<sup>3</sup>)-H Bond Oxygenation of Bicyclic and Spirocyclic Hydrocarbons Bearing Cyclopropane Moieties promoted by Dioxiranes," *Manuscript in preparation*. (<sup>†</sup>Authors contributed equally)
- [8] Lee, W.; Benton, T.; Sengupta, A.; Houk, K. N. "Molecular Dynamics of the Norbornyl Cation and Its Generation in Winstein-Trifan Solvolysis: The timing of  $\sigma$ -Bridging Establishes Anchimeric Assistance," *Manuscript in preparation*.
- [7] Zhao, Z.; Popov, S.; Lee, W.; Burch, J. E.; Delgadillo, D. A.; Kim, L. J.; Shahgholi, M.; Houk, K. N.; Nelson, H. M. "Accessing Medium-sized Rings via Vinyl Carbocation Intermediates," *Manuscript submitted*.
- [6] Lee, W.; Nelson, H. M.; Houk, K. N. "Computational Exploration of the Nature of Li<sup>+</sup>-Ureide Anion Catalysis on Formation of Highly Reactive Vinyl Carbocations and Subsequent C-C Bond Forming Reactions," *J. Org. Chem.*, **2023**, *88*, 3403–3408.
- [5] Liu, W.-D.<sup>†</sup>; Lee, W.<sup>†</sup>; Shu, H.; Xiao, C.; Chen, X.; Houk, K. N.; Zhao, J. "Diastereoselective Radical Aminoacylation of Olefins through N-Heterocyclic Carbene Catalysis," *J. Am. Chem. Soc.*, **2022**, *144*, 22767–22777. (<sup>†</sup>Authors contributed equally)
- [4] Lee, W.<sup>†</sup>; Polyak, D.<sup>†</sup>; Xu, B.; Houk, K. N.; Krauss, I. J. "A Mechanistic Switch from Homoallylation to Cyclopropylcarbinylation of Aldehydes," *Org. Lett.*, **2022**, *24*, 4660–4664. (<sup>†</sup>Authors contributed equally)
- [3] Wigman, B.; Lee, W.; Wei, W.; Houk, K. N.; Nelson, H. M. "Electrochemical Fluorination of Vinyl Boronates Through Donor-Stabilized Vinyl Carbocation Intermediates," *Angew. Chem. Int. Ed.*, **2022**, e202113972.
- [2] Bagdasarian, A. L.; Popov, S.; Wigman, B.; Wei, W.; Lee, W.; Nelson, H. M. "Urea-Catalyzed Vinyl Carbocation Formation Enables Mild Functionalization of Unactivated C-H Bonds," *Org. Lett.*, **2020**, *22*, 7775–7779.
- [1] Larson, R.; Samant, A.; Chen, J.; Lee, W.; Bohn, M.; Ohlmann, D.; Zuend, S.; Toste, F. D. "Hydrogen Gas-Mediated Deoxydehydration/Hydrogenation of Sugar Acids: Catalytic Conversion of Glucarates to Adipates," *J. Am. Chem. Soc.*, **2017**, *139*, 14001–14004.

## CHAPTER ONE

### **Molecular Dynamics of the Norbornyl Cation and Its Generation in Winstein-Trifan Solvolysis: The Timing of $\sigma$ -Bridging Establishes Anchimeric Assistance**

#### **1.1 Contributions**

This is an unpublished work by Lee, W., Benton, T. R., Sengupta, A., Houk, K. N. As a computational organic chemist, I contributed to finding the timing of *exo*- and *endo*-solvolysis in the implicit acetic acid solvent, understanding the dynamic behavior of 2-norbornyl cation in the solvent at ambient temperature, and obtaining the energy profile of the solvolyses. Furthermore, I wrote the manuscript under the guidance of Professor Kendall N. Houk.

#### **1.2 Abstract**

Molecular dynamics simulations have been performed for the solvolyses of *exo*- and *endo*-norbornyl brosylate and for the “nonclassical”  $\sigma$ -bridged norbornyl cation in acetic acid solution. This modeling of the 1949 Winstein-Trifan experiment confirms that *exo*-solvolysis is accompanied by  $\sigma$ -bridging, while *endo*-solvolysis is not; it occurs eventually in a dynamically stepwise fashion. Simulations of the norbornyl cation showed typical vibrations due to zero-point and thermal vibrations, but no tendency to sample localized “classical cation” geometries.

#### **1.3 Introduction**

Bridged cations are now a widely accepted type of carbocation intermediates.<sup>1</sup> It was not always so! In 1949, Winstein and Trifan reported the acetolysis of *exo*- and *endo*-2-norbornyl brosylates.

They observed a 350-times faster rate of *exo*- than of *endo*-solvolysis. Only the racemic *exo*-2-norbornyl acetate product was formed (**Figure 1.1a**).<sup>2</sup> The authors proposed a three-center two-electron bonding structure of 2-norbornyl cation (**Figure 1.1b**), and its formation during solvolysis only by backside C–C “anchimeric assistance” in the *exo*-solvolysis. A plane of symmetry in the delocalized carbonium ion allows the attack of acetate at C<sub>1</sub> and C<sub>2</sub>, giving the racemic *exo*-norbornyl acetate. Moreover, anchimeric assistance of the C<sub>1</sub>–C<sub>6</sub>  $\sigma$ -bond toward  $\sigma^*$  anti-bonding orbital between C<sub>2</sub> and the leaving group’s oxygen was proposed to explain the faster rate of 2-*exo*-norbornyl brosylate. Roberts, who coined the term *nonclassical* cations on the basis of extensive scrambling occurring in <sup>13</sup>C labeling experiments, proposed the bridged 2-norbornyl cation might be viewed as a 3-fold symmetric nortricyclonium ion.<sup>3</sup> In the early 1960s, Brown began to publish objections to the Winstein interpretations, and instead invoked equilibrating “classical” cations to rationalize racemization and steric effects to explain the greater rate of *exo*-solvolysis (**Figure 1.1c**).<sup>4,5</sup> Meanwhile, Olah *et al.* employed nuclear magnetic resonance (NMR) methods to observe 2-norbornyl cation in magic acid solutions (SbF<sub>5</sub>/SbF<sub>5</sub>-SO<sub>2</sub>/SbF<sub>5</sub>-SO<sub>2</sub>ClF-SO<sub>2</sub>F<sub>2</sub>).<sup>6</sup> They discovered the equilibria of hydride and alkyl shifts to be frozen out at –158 °C (**Figure 1.1d**). The structure of the 2-norbornyl cation was proposed to be a symmetrically bridged structure **1** or a structure in rapid equilibrium ( $\leq 3$  kcal/mol) between localized cations **2** and **3**. The results obtained at –268 °C by Yannoni *et al.* indicated the single-minimum bridged structure or equilibrating between the classical cations through extremely low energy barrier ( $< 0.2$  kcal/mol).<sup>7</sup> Saunders *et al.* used isotopic perturbation methods to demonstrate that the 2-norbornyl cation is a single and symmetric structure.<sup>8</sup> Schleyer, Schreiner, Schaefer, *et al.* compared the stability of the symmetrically bridged (C<sub>s</sub>) structure **1** and classical structure **2** and **3** with *ab initio* quantum mechanical methods, showing the significant

stabilization of the symmetric 2-norbornyl cation and that the classical structure is not a minima.<sup>9,10</sup>

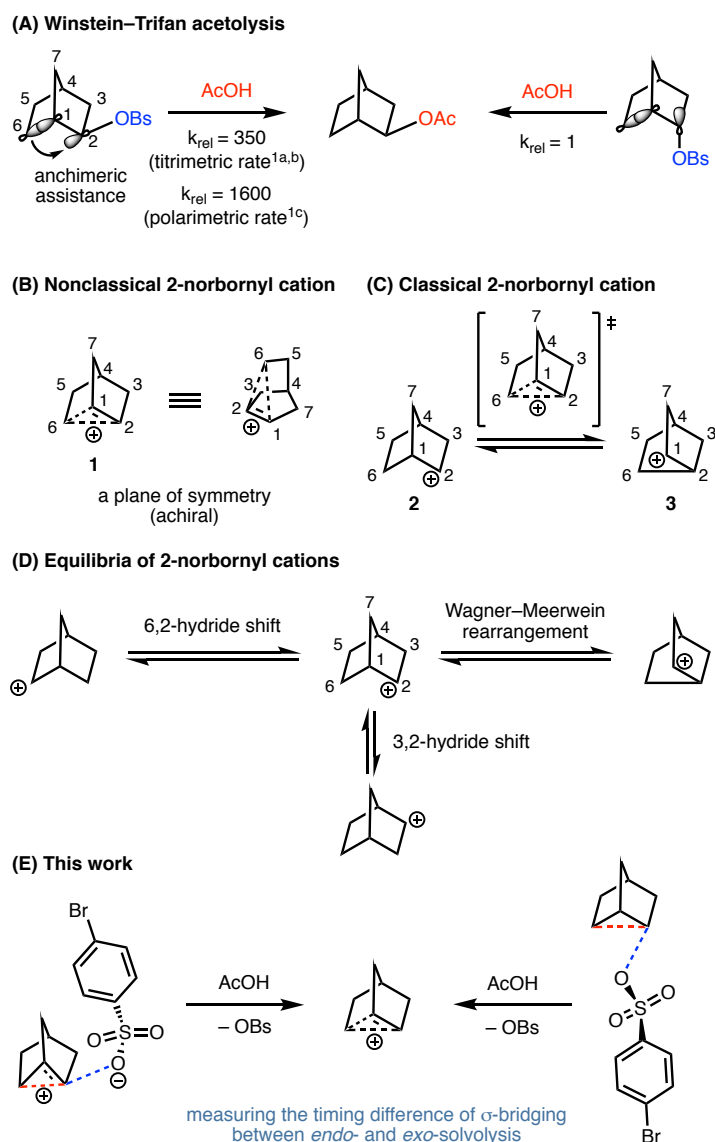


**Figure 1.1** a) Winstein-Trifan acetolysis. b) Nonclassical 2-norbornyl cation. c) Classical 2-norbornyl cation. d) Equilibria of 2-norbornyl cations. e) This work.

Meyer, Krossing, *et al.* decisively confirmed the symmetrically bridged structure of the 2-norbornyl cation via X-ray crystallography.<sup>11</sup> List and co-workers demonstrated enantiocontrol over the nonclassical 2-norbornyl cation with imidodiphosphorimidate catalysts, all due to a homochiral anion.<sup>12</sup> We undertook a study of the Winstein-Trifan solvolysis using modern



molecular dynamics techniques. We also studied the dynamic behavior of the norbornyl cation in solution.

#### 1.4 Computational Methods

All density functional theory (DFT) computations were performed with Gaussian 16.<sup>13</sup> Geometry optimizations were performed at the M06-2X/6-311+g(d,p) level of theory.<sup>14</sup> Frequency calculations were carried out at the same level of theory used for geometry optimization to characterize stationary points as minima or saddle points on the potential energy surface (PES) and to obtain thermal Gibbs free energies at 298 K. The SMD solvation model accounted for the effect of AcOH.<sup>15</sup> Intrinsic reaction coordinate (IRC) calculations were used to verify that a transition state (TS) connects the reactant and product on the PES. The 3D molecular structures were visualized by CYLView<sup>16</sup> and PyMol. MD simulations were performed at the M06-2X/6-31G(d)/SMD=AcOH level of theory. The ProgDyn/Gaussian interface developed by Singleton *et al.* was employed to perform trajectory simulations.<sup>17</sup> Quasiclassical trajectories were initialized near the saddle point region of the PES with a normal-mode sampling method (**Figure 1.2**).

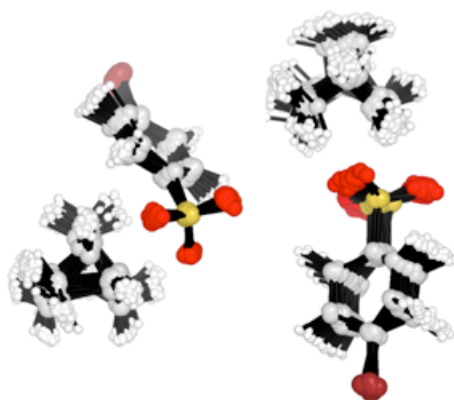


**Figure 1.2** Transition state ensembles of *exo*- and *endo*-solvvolysis.

This method involves adding zero-point and thermal energy for each real normal mode in the TS and obtaining a Boltzmann distribution by randomly sampling a set of geometries and velocities. The transition state ensemble was propagated for 500 fs until the formation of the bridged norbornyl cation. The time step for integration is 1 fs.

## 1.5 Results and Discussion

We evaluated the energies of forming norbornyl cation from *exo*- and *endo*-norbornyl brosylate

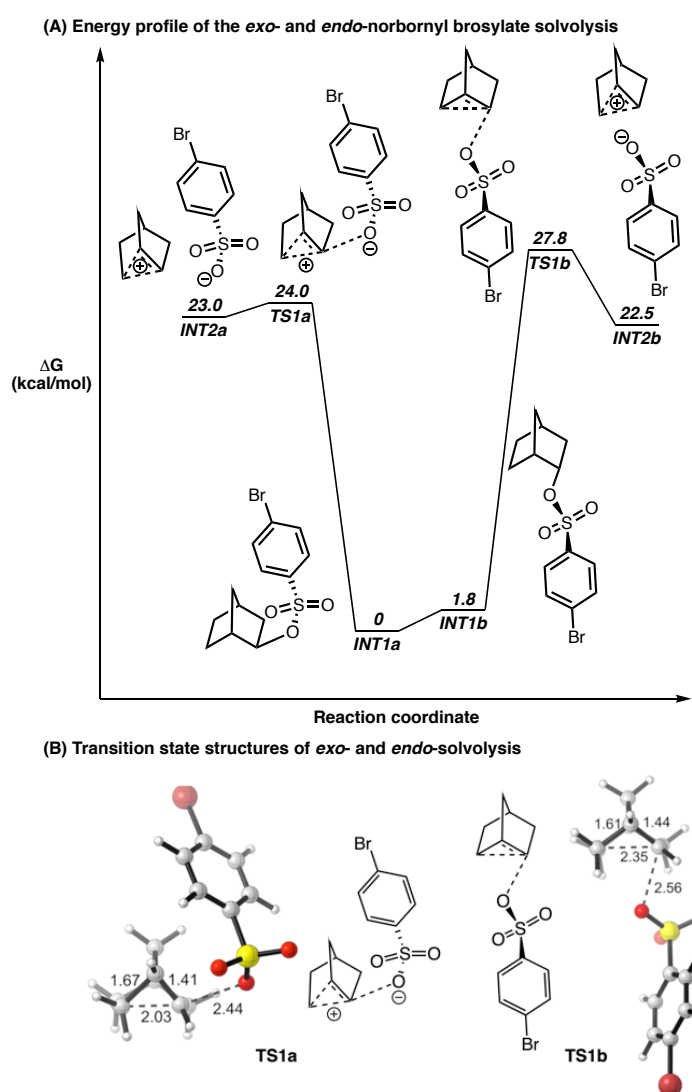


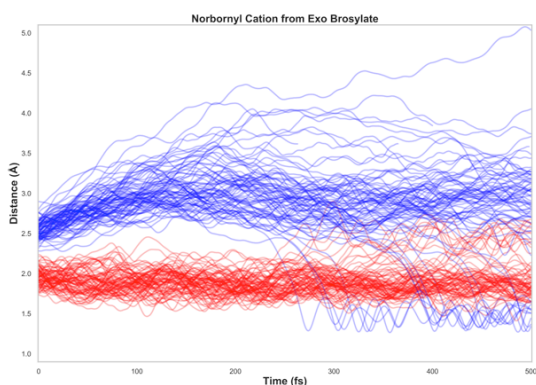
**Figure 1.3** a) Energy profile of the *exo*- and *endo*-norbornyl brosylate solvolysis. b) Transition state structures of *exo*- and *endo*-solvolysis.

with M06-2X/6-311+G(d,p)/SMD=AcOH (**Figure 1.3a**). *Exo*-norbornyl brosylate **INT1a** is slightly more stable than *endo*-norbornyl brosylate **INT1b**. The ionization of *exo*-norbornyl brosylate **TS1a** occurs at a free energy of 24.0 kcal/mol, while **TS1b** for *endo*-norbornyl brosylate ionization takes place at 27.8 kcal/mol. The ionization of *exo*-norbornyl brosylate is favored by 3.8 kcal/mol. This computational result resembles the original titrimetric ratio ( $k_{\text{exo}}/k_{\text{endo}} = 350$ ,  $\sim 3.5$  kcal/mol) obtained by Winstein and Trifan.<sup>2</sup> The transition state structures of **TS1a** and **TS1b** are shown in **Figure 1.3b**. Anchimeric assistance helps the ionization of norbornyl cation from *exo*-norbornyl brosylate.<sup>2</sup> Note 2.03 Å and 2.35 Å of C<sub>2</sub>–C<sub>6</sub> in **TS1a** and **TS1b** respectively. The bond distance of C<sub>2</sub>–C<sub>6</sub> in *exo*-solvolysis **TS1a** shows the substantial form of the bridged bond.  $\sigma$  orbital of C<sub>2</sub>–C<sub>6</sub> bond donates electron density into  $\sigma^*$  orbital of C<sub>2</sub>–O anti-bond through anti-periplanar interactions. The rate of *exo*-solvolysis in the formation of 2-norbornyl carbocation is improved by anchimeric assistance. In contrast, the interactions do not exist in the *endo*-norbornyl solvolysis **TS1b**. Additionally, the steric strain invoked by Brown is not noticeably observed in either *exo*-solvolysis **TS1a** or *endo*-solvolysis **TS1b**. In the case of *exo*-solvolysis **TS1a**, the distance between oxygen in the leaving group and the nearest hydrogen in C<sub>3</sub> is 2.48 Å. The distance between the oxygen and the closest hydrogen in C<sub>6</sub> for *endo*-solvolysis **TS1b** is 2.23 Å.

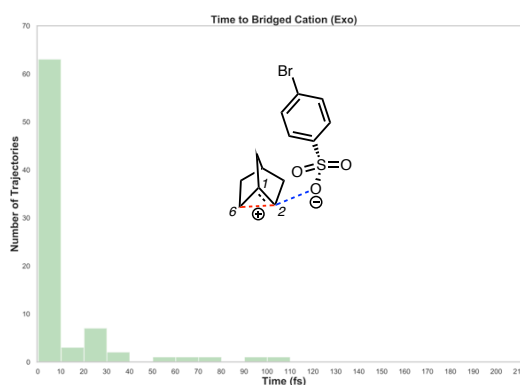
In order to study the timing of  $\sigma$ -bridging, we employ Singleton's Progdyn program package, which enables quasiclassical molecular dynamics simulations with DFT (M06-2X/6-31g(d)/SMD=AcOH). We measure the time to the formation of a bridged C<sub>6</sub>–C<sub>2</sub> bond from *exo*- and *endo*-solvolysis transition states. The bridging distance is determined as 2.00 Å, reported by Schreiner *et al.*<sup>18</sup> According to Eyring's transition state theory, the pre-exponential factor,  $kT/h$ , is defined by the rate of translational motion of atoms. A time of 60 fs is the lifetime of a

transition state at room temperature to form a bond between two atoms with thermal energy. We consider the formation of bridged bond (2.00 Å) to be dynamically concerted if the time is  $\leq 60$  fs. Conversely, if the time is  $> 60$  fs, it is considered as dynamically stepwise process. We ran 80 trajectories of the simulations with *exo*-transition states. As shown in **Figure 1.4a**, most of the trajectories showed the formation of the bridged bond at the beginning of the simulations.

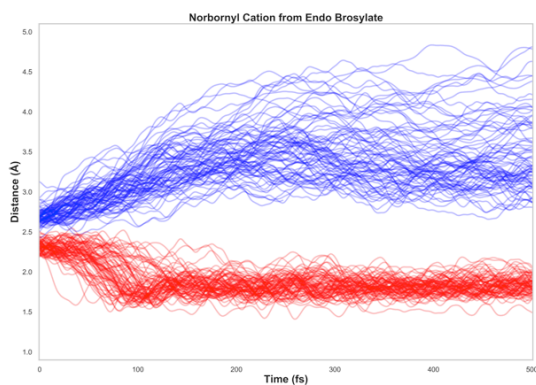
(A) Plot of C<sub>6</sub>-C<sub>2</sub> and C<sub>2</sub>-O during *exo*-solvolysis simulations



(B) Histogram of trajectory time-to-bridging (*exo*)



(C) Plot of C<sub>6</sub>-C<sub>2</sub> and C<sub>2</sub>-O during *endo*-solvolysis simulations



(D) Histogram of trajectory time-to-bridging (*endo*)

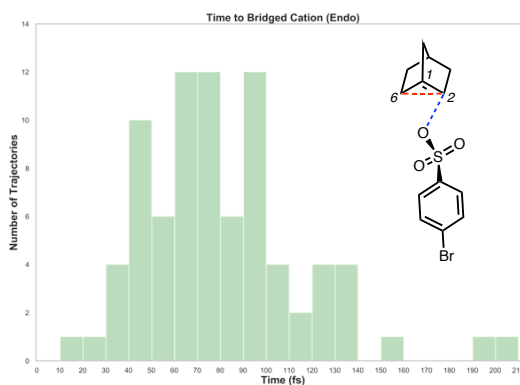


**Figure 1.4** a) Plot of C<sub>6</sub>-C<sub>2</sub> and C<sub>2</sub>-O bonds during *exo*-solvolysis simulations. b) Histogram of trajectory time-to-bridging (*exo*). c) Plot of C<sub>6</sub>-C<sub>2</sub> and C<sub>2</sub>-O bonds during *endo*-solvolysis simulations. d) Histogram of trajectory time-to-bridging (*endo*).

Seventy-six trajectories show the dynamically concerted formation of bridged cations ( $\leq 60$  fs, **Figure 1.4b**), and only four trajectories showed the dynamically stepwise formation of bridged cations ( $> 60$  fs, **Figure 1.4b**). The average of the timing of the bridged bond formation from

*exo*-solvolysis transition states is  $9.1 \pm 40.4$  fs. On average, the solvolysis of *exo*-norbornyl brosylate occurs through the dynamically concerted process. 81 trajectories of the molecular dynamics with *endo*-solvolysis transition states are simulated. **Figure 1.4c** shows the noticeable change in C<sub>6</sub>–C<sub>2</sub> bond distance at  $80.9 \pm 68.1$  fs. As shown in **Figure 1.4d**, fifty-eight trajectories show the dynamically stepwise formation of bridged cations ( $> 60$  fs), and twenty-three trajectories present the dynamically concerted process of forming the cations ( $\leq 60$  fs). The average time to form a bridged C<sub>6</sub>–C<sub>2</sub> bond from *endo*-transition states is  $80.9 \pm 68.1$  fs, which is likely a dynamically stepwise process. The solvolysis of *endo*-norbornyl brosylate is significantly slower than *exo*-solvolysis. Interestingly, ion-recombination is also observed in the simulations of *exo*-solvolysis. 14 trajectories showed the covalent bond reformation (C<sub>2</sub>–O) after the formation of a bridged C<sub>6</sub>–C<sub>2</sub> bond. Note that C<sub>2</sub>–O bond distance is decreased to  $\sim 1.5$  Å as shown in **Figure 1.4a**. Recombination occurs because of the low energy gap ( $\Delta G = 1.0$  kcal/mol) between INT2a and TS1a (**Figure 1.3a**).

We also investigated the behavior of norbornyl cation in acetic acid solvent at ambient temperature (**Figure 1.5a**). We simulated the molecular dynamics of ground state norbornyl cation with 29 trajectories (500 fs for each trajectory). The average bond distance of C<sub>6</sub>–C<sub>1</sub> and C<sub>6</sub>–C<sub>2</sub> is  $1.82 \pm 0.2$  Å. C<sub>6</sub> is symmetrically bonded to C<sub>1</sub> and C<sub>2</sub> through a partial sigma bond. Also, the broad dispersion of bond length data of C<sub>6</sub>–C<sub>1</sub> and C<sub>6</sub>–C<sub>2</sub> is observed, which is raised by the bond stretch of bridged C–C bonds. The selected bond lengths of the bridged carbon bonds, ranging from 1.50 Å to 2.39 Å with a bin size of 0.01 Å, show a broad distribution statistically. 86.3 % of these bond lengths fall within the range of 1.70 to 1.99 Å, while the remaining 13.7% are found outside of this range. In addition to analysis of the bridged bonds, an average bond length of C<sub>2</sub>–C<sub>1</sub> is  $1.40 \pm 0.1$  Å, indicating partial double-bond character.

Additionally, we performed the molecular dynamics with norbornane to compare its sigma bonds with the partial sigma bonds of the 2-norbornyl cation (**Figure 1.5b**). We simulated twenty-six trajectories (500 fs for each trajectory).

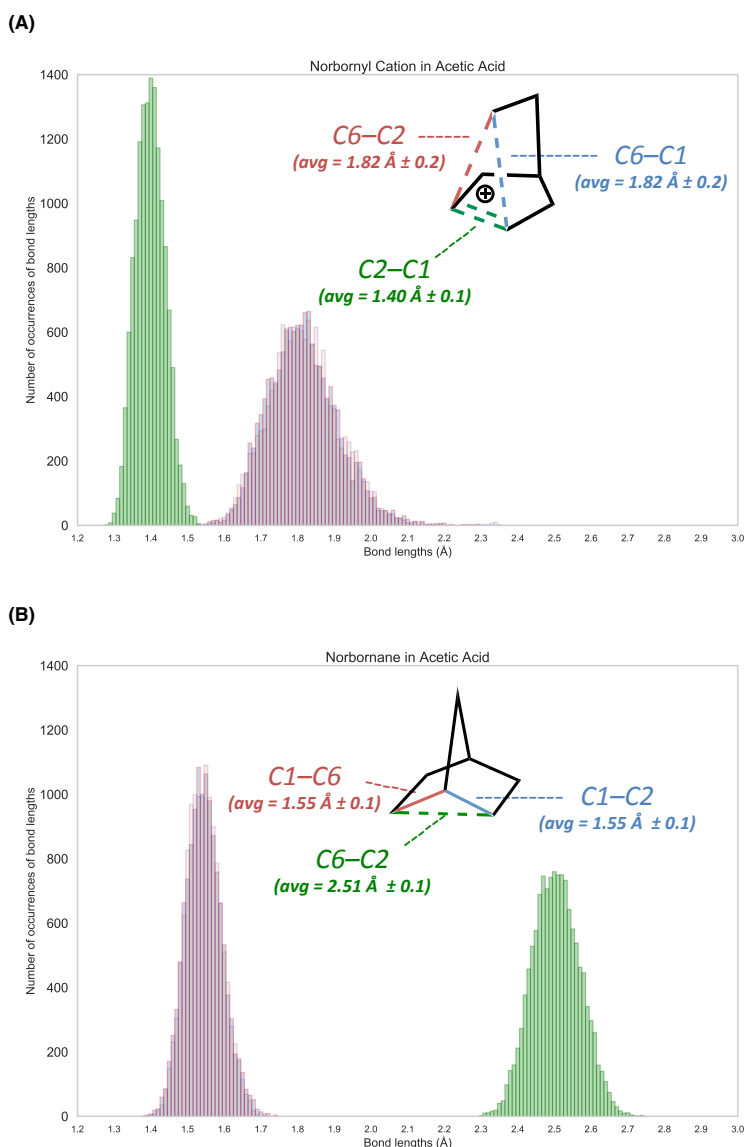


**Figure 1.5** a) Histogram graph of selected bond lengths during 2-norbornyl cation 500 fs simulations (29 trajectories). b) Histogram graph of selected bond lengths during norbornane 500 fs simulations (26 trajectories).

The narrow dispersion of bond length data of C<sub>6</sub>-C<sub>1</sub> and C<sub>2</sub>-C<sub>1</sub> is found,  $1.55 \pm 0.1$  Å. The selected bond lengths of the sigma carbon bonds, ranging from 1.30 Å to 1.79 Å with a bin

interval of 0.01 Å, show a narrow-ranging distribution. 99.8 % of these bond lengths fall from 1.40 Å to 1.69 Å. The strength of a typical sigma bond is stronger than a partial sigma bond because the electron density is concentrated along with the perfect internuclear axis of the carbon atoms. The difference in bond strength is clearly observed in the graphical and quantitative analysis. The analysis of the bond lengths through molecular dynamics features a three-center two-electron bond in a 2-norbornyl cation. Conclusively, the average bond lengths of C<sub>6</sub>-C<sub>1</sub>, C<sub>6</sub>-C<sub>2</sub>, and C<sub>1</sub>-C<sub>2</sub> match with the X-ray structure reported by Meyer and Krossing *et al.*<sup>11</sup> Schleyer's computational work showed that the bond distance of C<sub>6</sub>-C<sub>1</sub> in the classical 2-norbornyl cation is 1.55 Å.<sup>9</sup> Our simulations find that only 0.06% of either C<sub>6</sub>-C<sub>1</sub> or C<sub>6</sub>-C<sub>2</sub> bond can be equal or less than 1.55 Å, which is necessary to form the classical 2-norbornyl cation. Moreover, the bridged bond distance in the nonclassical 2-norbornyl cation is likely the same as that observed in the ion pair structures obtained from the solvolysis simulations. Therefore, classical 2-norbornyl cations are practically never obtained.

## 1.6 Conclusion

We have revisited Winstein-Trifan solvolysis with DFT and Progdyn MD simulations. The energy difference between *exo*- and *endo*-solvolysis matches Winstein-Trifan's original kinetics. Importantly, we have discovered that forming the C<sub>6</sub>-C<sub>2</sub> bridged bond from the *exo*-solvolysis transition state ensemble occurs at  $9.1 \pm 40.4$  fs (dynamically concerted) and that formation from *endo*-solvolysis happens at  $80.9 \pm 68.1$  fs (dynamically stepwise). Furthermore, we have confirmed an average plane of symmetry in the nonclassical 2-norbornyl cation by analyzing the dynamic behavior under implicit acetic acid solvent at ambient temperature. The solution

structure of norbornyl cation is the same as that in the X-ray crystal structure and shows negligible geometries resembling the putative classical norbornyl cation.



## 1.7 References

- (1) (a) Anslyn, E. V.; Dougherty, D. A. *Modern Physical Organic Chemistry*; University Science Books: Herndon, VA, **2006**, pp 661–666. (b) Vogel, P.; Houk, K. N. *Organic Chemistry: Theory, Reactivity and Mechanisms in Modern Synthesis*; Wiley-VCH: Weinheim, Germany, **2019**, pp 308–312. (c) Naredla, R. R.; Klumpp, D. A. Contemporary Carbocation Chemistry: Applications in Organic Synthesis. *Chem. Rev.* **2013**, *113*, 6905–6948; see especially pp 6907.
- (2) (a) Winstein, S.; Trifan, D. S. The Structure of the Bicyclo [2,2,1]2-Heptyl (Norbonyl) Carbonium Ion. *J. Am. Chem. Soc.* **1949**, *71*, 2953. (b) Winstein, S.; Trifan, D. S. Neighboring Carbon and Hydrogen. X. Solvolysis of *endo*-Norbonyl Arylsulfonates<sup>1,2,3</sup>. *J. Am. Chem. Soc.* **1952**, *74*, 1147–1154. (C) Winstein, S.; Clippinger, E.; Howe, R.; Vogelfanger, E. The Nonclassical Norbonyl Cation<sup>1</sup>. *J. Am. Chem. Soc.* **1965**, *87*, 376–377.
- (3) (a) Roberts, J. D.; Lee, C. C. The Nature of the Intermediate in the Solvolysis of Norbonyl Derivatives<sup>1,2</sup>. *J. Am. Chem. Soc.* **1951**, *73*, 5009–5010. (b) Roberts, J. D.; Mazur, R. H. The Nature of the Intermediate in Carbonium Ion-Type Interconversion Reactions of Cyclobutyl, Cyclopropylcarbinyl, and Allylcarbinyl Derivatives<sup>1</sup>. *J. Am. Chem. Soc.* **1951**, *73*, 3542–3543.
- (4) (a) Brown, H. C. (with comments by Schleyer, P. v. R.) *The Nonclassical Ion Problem*; Plenum: New York, **1977**. (b) Brown, H. C.; Morgan, K. J.; Chloupek, F. J. Structural Effects in Solvolytic Reactions. I. The Role of Equilibrating Cations in Carbonium Ion Chemistry. Nature of the Intermediates Involved in the Solvolysis of Symmetrically Substituted  $\beta$ -Phenylethyl Derivatives<sup>1</sup>. *J. Am. Chem. Soc.* **1965**, *87*, 2137–2153. (c) Brown, H. C. The Energy of the Transition States and the Intermediate Cation in the Ionization of 2-Norbonyl Derivatives. Where is the Nonclassical Stabilization Energy?. *Acc. Chem. Res.* **1983**, *16*, 432–440. (d) Brown, H. C.; Chloupek, F. J.; Rei, M-H. Rates of Solvolysis of the *p*-Nitrobenzoates of *exo-endo*

Tertiary Norborneols. A Critical Examination of the *exo-endo* Rate Ratio as a Basis for the Postulated Nonclassical Structure of the Norbornyl Cation. *J. Am. Chem. Soc.* **1964**, *86*, 1248–1250.

(5) (a) Olah, G. A. My Search for Carbocations and Their Role in Chemistry (Nobel Lecture). *Angew. Chem. Int. Ed.* **1995**, *34*, 1393–1405. (b) Olah, G. A.; Schleyer, P. v. R.; Eds. In *Carbonium Ions*; Wiley-Interscience: New York, **1968–1976**; Vols. I–IV; (c) Olah, G. A. *Carbocations and Electrophilic Reactions*; Verlag Chemie: Weinheim, **1974**. (d) Olah, G. A.; Prakash, G. K. S.; Sommer, J. *Superacids*; Wiley-Interscience: New York, **1985**. (e) Olah, G. A.; Molnár, Á. *Hydrocarbon Chemistry*; Wiley-Interscience: New York, **1995**. (f) Olah, G. A.; Prakash, G. K. S.; Williams, R. E.; Field, L. D.; Wade, K. *Hypercarbon Chemistry*; Wiley-Interscience: New York, **1987**.

(6) (a) Schleyer, P. v. R.; Watts, W. E.; Fort, R. C.; Comisarow, M. B.; Olah, G. A. Stable Carbonium Ions. X.<sup>1</sup> Direct Nuclear Magnetic Resonance Observation of the 2-Norbornyl Cation. *J. Am. Chem. Soc.* **1964**, *86*, 5679–5680. (b) Saunders, M.; Schleyer, P. v. R.; Olah, G. A. Stable Carbonium Ions. XI.<sup>1</sup> The Rate of Hydride Shifts in the 2-Norbornyl Cation. *J. Am. Chem. Soc.* **1964**, *86*, 5680–5681. (c) Olah, G. A.; Prakash, G. K. S.; Arvanaghi, M.; Anet, F. A. L. High-Field <sup>1</sup>H and <sup>13</sup>C NMR Spectroscopic Study of the 2-Norbornyl Cation<sup>1a</sup>. *J. Am. Chem. Soc.* **1982**, *104*, 7105–7108. (d) Olah, G. A.; Prakash, G. K. S.; Saunders, M. Conclusion of the classical-nonclassical ion controversy based on the structural study of the 2-norbornyl cation. *Acc. Chem. Res.* **1983**, *16*, 440–448.

(7) (a) Yannoni, C. S.; Macho, V.; Myhre, P. C. Carbon-13 NMR Spectra of Carbonium Ions in the Solid State: The 2-Norbornyl Cation. *J. Am. Chem. Soc.* **1982**, *104*, 907–909. (b) Yannoni, C.

- S.; Macho, V.; Myhre, P. C. Resolved  $^{13}\text{C}$  NMR Spectra of Carbonium Ions at Cryogenic Temperatures. The Norbornyl Cation at 5 K. *J. Am. Chem. Soc.* **1982**, *104*, 7380–7381.
- (8) (a) Saunders, M.; Kates, M. R. Deuterium Isotope Effect on the Carbon-13 NMR Spectrum of the Bicyclo[2.2.1]heptyl Cation. Nonclassical Norbornyl Cation. *J. Am. Chem. Soc.* **1980**, *102*, 6867–6868. (b) Saunders, M.; Kates, M. R. Isotopic Perturbation Effects on a Single Averaged NMR Peak: Norbornyl Cation. *J. Am. Chem. Soc.* **1983**, *105*, 3571–3573. (c) Saunders, M.; Johnson, C. S., Jr. Effects of Tunneling on NMR Spectra. The Question of Heavy Atom Tunneling in Norbornyl Cations Reexamined. *J. Am. Chem. Soc.* **1987**, *109*, 4401–4402.
- (9) Schleyer, P. v. R.; Sieber, S. The Classical 2-Norbornyl Cation Rigorously Defined *Ab Initio*. *Angew. Chem. Int. Ed.* **1993**, *32*, 1606–1608 and earlier references cited therein.
- (10) Schreiner, P. R.; Severance, D. L.; Jorgensen, W. L.; Schleyer, P. v. R.; Schaefer, H. F., III Energy Difference between the Classical and the Nonclassical 2-Norbornyl Cation in Solution. A Combined *ab Initio*-Monte Carlo Aqueous Solution Study. *J. Am. Chem. Soc.* **1995**, *117*, 2663–2664.
- (11) Scholz, F.; Himmel, D.; Heinemann, F. W.; Schleyer, P. v. R.; Meyer, K.; Krossing, I. Crystal Structure Determination of the Nonclassical 2-Norbornyl Cation. *Science* **2013**, *341*, 62–64.
- (12) Properzi, R.; Kaib, P. S. J.; Leutzsch, M.; Pupo, G.; Mitra, R.; De, C. K.; Song, L.; Schreiner, P. R.; List, B. Catalytic Enantiocontrol over a Non-Classical Carbocation. *Nat. Chem.* **2020**, *12*, 1174–1179.
- (13) Frisch, M. J.; Trucks, G. W.; Schlegel, H. B.; Scuseria, G. E.; Robb, M. A.; Cheeseman, J. R.; Scalmani, G.; Barone, V.; Petersson, G. A.; Nakatsuji, H.; Li, X.; Caricato, M.; Marenich, A. V.; Bloino, J.; Janesko, B. G.; Gomperts, R.; Mennucci, B.; Hratchian, H. P.; Ortiz, J. V.;

Izmaylov, A. F.; Sonnenberg, J. L.; Williams-Young, D.; Ding, F.; Lipparini, F.; Egidi, F.; Goings, J.; Peng, B.; Petrone, A.; Henderson, T.; Ranasinghe, D.; Zakrzewski, V. G.; Gao, J.; Rega, N.; Zheng, G.; Liang, W.; Hada, M.; Ehara, M.; Toyota, K.; Fukuda, R.; Hasegawa, J.; Ishida, M.; Nakajima, T.; Honda, Y.; Kitao, O.; Nakai, H.; Vreven, T.; Throssell, K.; Montgomery, J. A., Jr.; Peralta, J. E.; Ogliaro, F.; Bearpark, M. J.; Heyd, J. J.; Brothers, E. N.; Kudin, K. N.; Staroverov, V. N.; Keith, T. A.; Kobayashi, R.; Normand, J.; Raghavachari, K.; Rendell, A. P.; Burant, J. C.; Iyengar, S. S.; Tomasi, J.; Cossi, M.; Millam, J. M.; Klene, M.; Adamo, C.; Cammi, R.; Ochterski, J. W.; Martin, R. L.; Morokuma, K.; Farkas, O.; Foresman, J. B.; Fox, D. J. Gaussian, Inc.: Wallingford, CT, **2016**.

(14) Zhao, Y.; Truhlar, D. G. The M06 Suite of Density Functionals for Main Group Thermochemistry, Thermochemical Kinetics, Noncovalent Interactions, Excited States, and Transition Elements: Two New Functionals and Systematic Testing of Four M06-Class Functionals and 12 Other Functionals. *Theor. Chem. Acc.* **2008**, *120*, 215–241.

(15) Marenich, A. V.; Cramer, C. J.; Truhlar, D. G. Universal Solvation Model Based on Solute Electron Density and on a Continuum Model of the Solvent Defined by the Bulk Dielectric Constant and Atomic Surface Tensions. *J. Phys. Chem. B* **2009**, *113*, 6378–6396.

(16) Legault, C. Y. *CYLview*, 1.0b; Universite' de Sherbrooke, **2009**; <http://www.cylview.org>.

(17) Ussing, B. R.; Hang, C.; Singleton, D. A. Dynamic Effects on the Periselectivity, Rate, Isotope Effects, and Mechanism of Cycloadditions of Ketenes with Cyclopentadiene. *J. Am. Chem. Soc.* **2006**, *128*, 7594–7607.

(18) Schreiner, P. R.; Schleyer, P. v. R.; Schaefer, H. F., III Why the Classical and Nonclassical Norbornyl Cations Do Not Resemble the 2-*endo*- and 2-*exo*-Norbornyl Solvolysis Transition States<sup>1,‡</sup>. *J. Org. Chem.*, **1997**, *62*, 4216–4228.

## CHAPTER TWO

### Computational Exploration of the Nature of Li<sup>+</sup>-Ureide Anion Catalysis on Formation of Highly Reactive Vinyl Carbocations and Subsequent C–C Bond Forming Reactions

#### 2.1 Contributions

This is an author manuscript from the publication: Lee, W.; Nelson, H. M.; Houk, K. N. Computational Exploration of the Nature of Li<sup>+</sup>-Ureide Anion Catalysis on Formation of Highly Reactive Vinyl Carbocations and Subsequent C–C Bond Forming Reactions. *J. Org. Chem.* **2023**, 88, 3403–3408. <https://doi.org/10.1021/acs.joc.2c02178>. The project involved a joint effort between the laboratories of my advisors, Professor Kendall N. Houk and Professor Hosea M. Nelson. As a computational organic chemist, I focused on understanding the role of Li<sup>+</sup>-ureide anion catalysis on vinyl cation C–H insertion reactions and investigating their underlying mechanisms.

#### 2.2 Abstract

The mechanisms of the C–H insertion reactions of vinyl carbocations formed by heterolysis of vinyl trifluoromethanesulfonates (triflates) by catalytic lithiated 1,3-bis[3,5bis(trifluoromethyl)phenyl]urea (Li<sup>+</sup>-ureide) have been studied with ωB97X-D density functional theory (DFT). The ionization promoted by the Li<sup>+</sup>-ureide forms a metastable intimate ion pair complex of Li<sup>+</sup>-ureide-triflate anion and vinyl cation. The relative thermodynamic stabilities of isomeric alkyl cations are impacted by ion-pairing with the Li<sup>+</sup>-ureide-triflate anion. We show that the C–H insertion reaction of the vinyl cation intermediate is the rate-determining

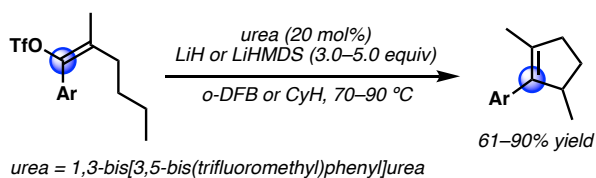
step, and explain the effect of the aryl substituents on the formation of the vinyl cation and its C–H insertion reactivity as well as the regioselectivity of C–H activation by the vinyl cation.

### 2.3 Introduction

Silylium Lewis-acid catalyzed heterolysis of vinyl triflates to form highly reactive vinyl cations, which can undergo high-yielding C–H insertion and Friedel-Crafts reactions, in non-polar solvents were reported by Nelson and Houk in 2018.<sup>1</sup> Although the ionization strategy using high temperature, protic solvents, and stoichiometric acids for vinyl cation generation had been studied by Grob<sup>2</sup>, Hanack<sup>3</sup>, Rappoport<sup>4</sup>, and Stang<sup>5</sup>, the formation of vinyl cations in non-polar hydrocarbon solvents is a recent discovery. Silylium Lewis-acid catalysts do ionize vinyl triflates, but Lewis basic heteroatoms or heterocycles interfere with the catalytic activity of silylium catalysts. In order to overcome the limitation raised by the electrophilicity of the strong Lewis acid catalyst, milder Lewis-acid lithium cations coordinated to weakly-coordinating anions (WCA), such as tetrakis(pentafluorophenyl) borate were discovered.<sup>6</sup> In efforts to further broaden the utility of this method, we investigated more easily accessible catalysts capable of ionizing vinyl triflates. Recently, we found Li<sup>+</sup>-ureide (LiUr) catalyst **1** to be a competent Lewis acid for the heterolysis of vinyl triflates to produce vinyl cations that subsequently undergo C–C bond forming reactions (**Figure 2.1**).<sup>7</sup>

Vinyl carbocations are produced by the heterolysis that forms triflate coordinated to LiUr catalyst **1**. Although there have been many studies of anion-binding catalysts and their effect on the reaction mechanism of various chemical transformations<sup>8a-e</sup>, only a few examples have shown lithium amide catalysts as anion acceptors.<sup>7,8f</sup>

a)  $\text{Li}^+$ -ureide-catalyzed vinyl cation formation and its C–H insertion reaction



b) Computationally-optimized structure of the dimer of the lithium salt of the urea

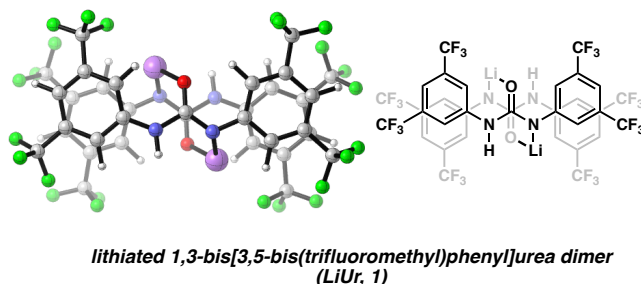


**Figure 2.1** a)  $\text{Li}^+$ -ureide-catalyzed vinyl carbocation formation and its C–C bond forming reactions. b) Structure of the dimer of the lithium salt of the urea optimized by DFT computations.

Thus, we were unsure of the exact role of the catalyst and its influence in ion-pairing with carbocations, which prompted our computational mechanistic studies to explore the nature of  $\text{Li}^+$ -ureide catalysis and the subsequent reactivity of vinyl carbocations. Our work has shown how a complex anion interacts with a cation and the product-determining transition states, hypotheses previously only speculated on. We provide a detailed step-by-step vision of the role of  $\text{Li}^+$ -ureide on promoting reactions and controlling selectivities. We propose a structure of the active catalyst and show computationally how it can influence cationic reaction pathways.

## 2.4 Computational Methods

Density functional theory (DFT) computations were performed with Gaussian 16.<sup>9</sup> The  $\omega\text{B97X-D}$  functional was used to optimize molecular geometries.<sup>10</sup> The 6-31G(d,p) basis set was employed when the number of atoms is greater than 60. Single point energies were obtained with the 6-311+G(d,p) basis set. The 6-311+G(d,p) basis set was used for optimization when the

number of atoms is less than 60. A cyclohexane solvent of low dielectric constant<sup>11</sup> was employed in the experiment with pyridine vinyl triflate **2**.<sup>7</sup> Thus, geometry optimizations and single point calculations were completed in the gas phase. In order to characterize the stationary points on the potential energy surface and obtain thermal Gibbs free energy, frequency calculations were performed at the same level of theory used for geometry optimization. Gibbs free energies were corrected using GoodVibes, which corrects the vibrational frequencies via a quasi-harmonic approximation, as proposed by Grimme.<sup>12</sup> CYLview was used to visualize molecular structures.<sup>13</sup>

## 2.5 Results and Discussion

While nuclear magnetic resonance spectroscopy of Li<sup>+</sup>-ureide **1** indicated the presence of lithiate<sup>7</sup>, attempts at identifying a solid state structure of Li<sup>+</sup>-ureide **1** by crystallographic means were unsuccessful. Thus, a computationally-optimized ( $\omega$ B97X-D/6-31G(d,p)) dimeric Li<sup>+</sup>-ureide (LiUr) structure **1** is employed in our mechanistic studies (**Figure 2.1b**). Aggregation of lithium amides is well known, and we adopted this dimer as a simple model of potential catalytic aggregates.<sup>14,15</sup>

The proposed catalytic cycle is shown in **Figure 2.2**. The mechanism involves the formation of active Li<sup>+</sup>-ureide catalyst **1**, which catalyzes heterolysis of vinyl triflate **2** to form vinyl cation **3**, insertion of cation into a C–H bond, and deprotonation of tertiary cation **4** to produce **5**.



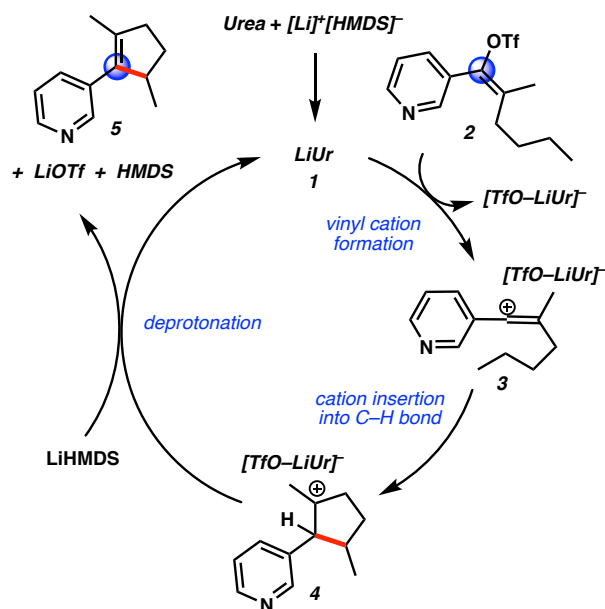


**Figure 2.2** Proposed reaction mechanism.

We computationally explored the overall reaction mechanism with LiUr catalyst **1** and pyridine vinyl triflate **2**, which gives product **5** in 80% yield. Gibbs free energies (in kcal/mol) are obtained at 298.15 K, and the energetics are summarized in **Figure 2.3**, assuming the dimeric lithium ureide is the catalyst. The coordination of LiUr catalyst **1** to vinyl triflate substrate **6** leads to a complex **7**. This coordination is computed to be favorable by 14.4 kcal/mol. Cleavage of the C–O bond gives ion-pairing complex **9** (–1.0 kcal/mol), with TS **8** at 1.3 kcal/mol. There is a negligible barrier for the reversible formation of complex **7** from ion-pairing complex **9**.

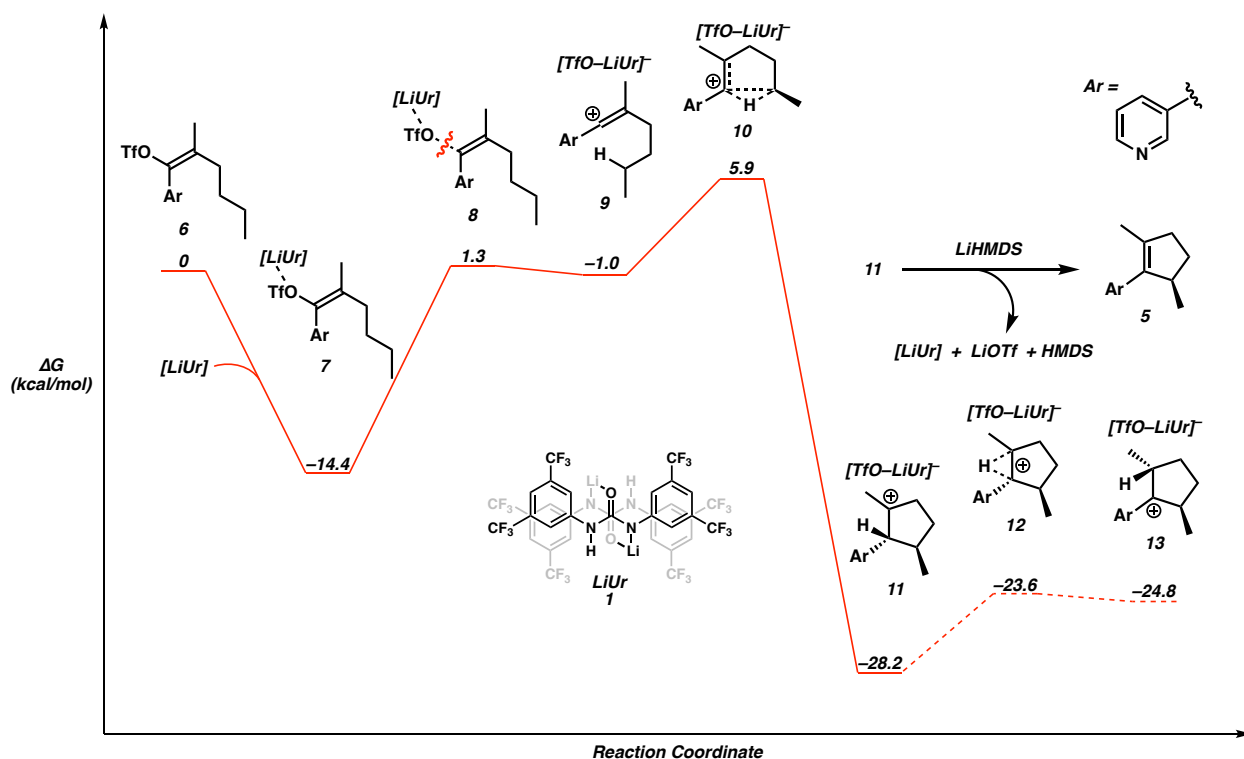


**Figure 2.3** Computational investigation of the overall reaction process with  $\omega$ B97X-D/6-311+G(d,p) //  $\omega$ B97X-D/6-31G(d,p) in the gas phase at 298.15 K.

As shown in **Figure 2.4**, a contact of 3.06 Å between  $\text{Li}^+$ -ureide-triflate anion and vinyl cation is observed in ion-pairing complex **9**. An intimate ion pair, which was originally introduced by Winstein, is seen in this structure.<sup>16</sup> A concerted C–H insertion occurs via TS **10** at 5.9 kcal/mol to form **11** (–28.2 kcal/mol). The C–H insertion step is the rate-determining step.<sup>17</sup> The transition state **10** computed for this reaction is shown in **Figure 2.4**. Note the transition state is essentially a hydride abstraction, but the generation of the alkene with its  $\pi$  bond directly interacting with the secondary cation vacant orbital leads to the insertion product **11** with no additional barrier. This is a two-stage concerted process. Finally, a highly exergonic deprotonation by excess LiHMDS forms product **5**.

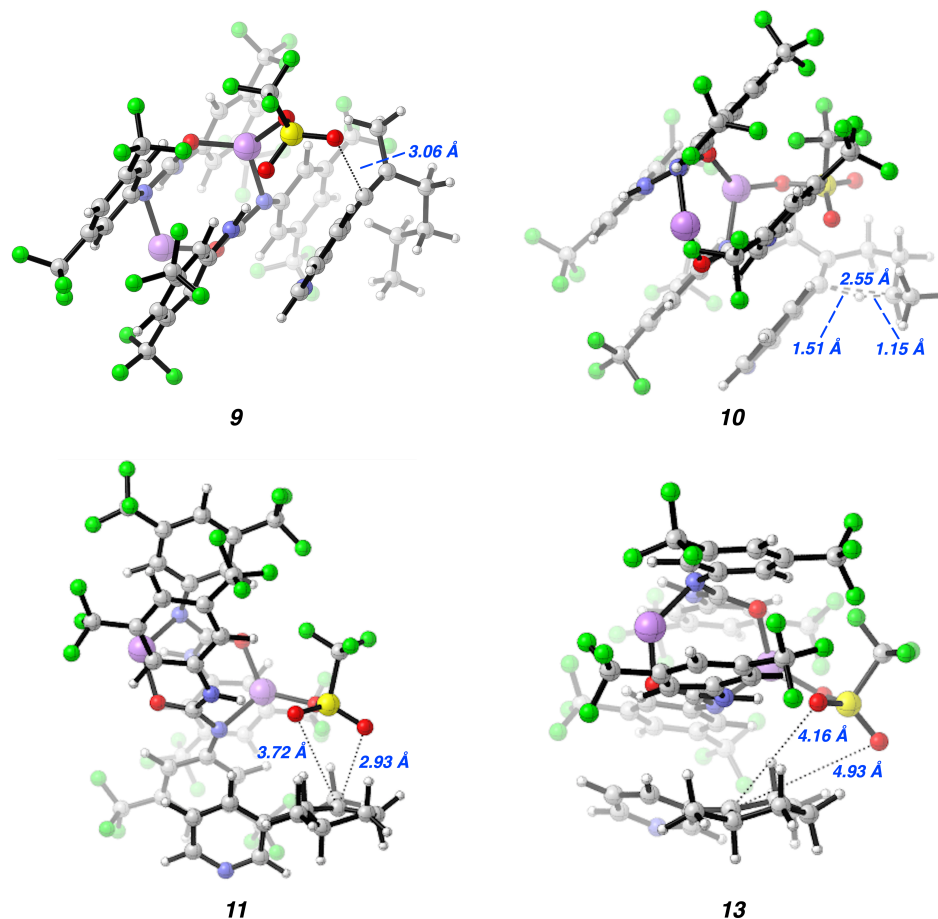
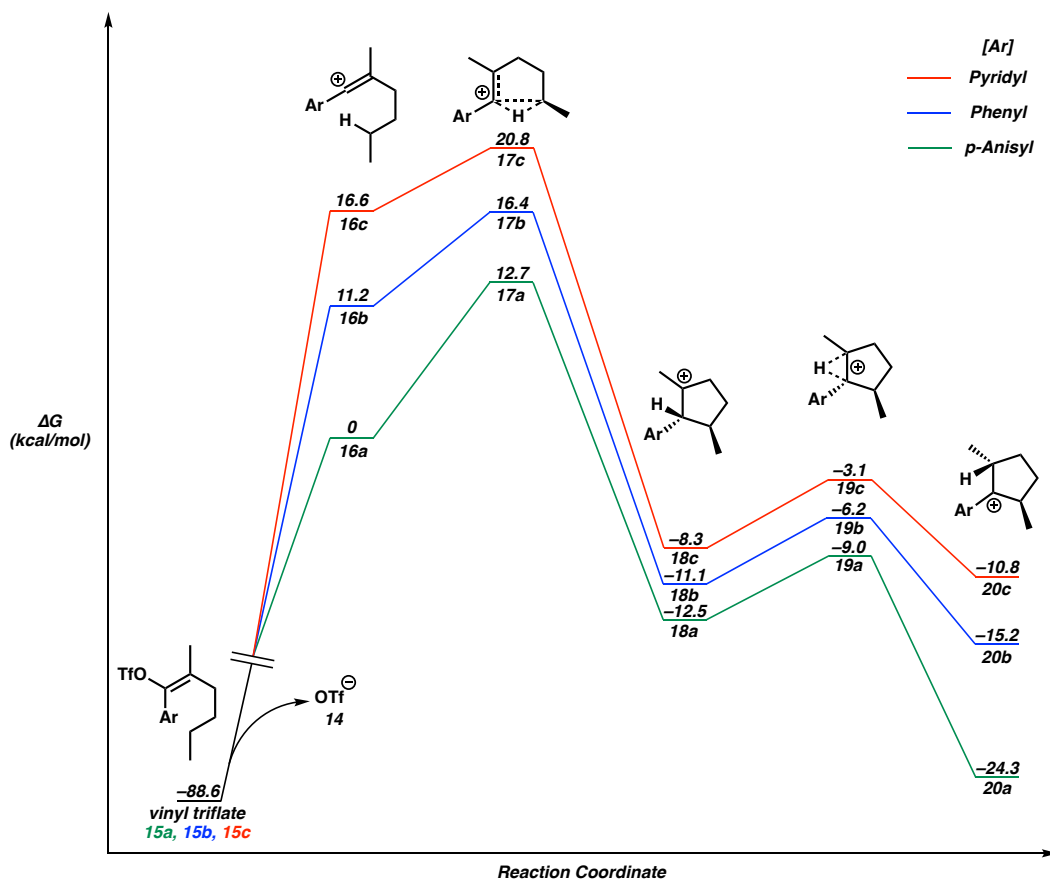


**Figure 2.4** 3-D structures of complex **9**, **11**, **13** and C–H insertion transition state **10**.

We find that the hydride shift from **11** to **13** is thermodynamically unfavorable in the ion pair even though **13** is a benzylic carbocation. As shown in **Figure 2.4**, distances from oxygens that consist of negatively charged ions to a positively charged carbon atom in complex **11** are 3.72 Å and 2.93 Å. On the other hand, in complex **13**, distances between anionic oxygens and a cationic carbon of 4.16 Å and 4.93 Å. Structural analysis exhibits the ion-pair interactions are stronger in complex **11**. Calculations on these reactions in the absence of a counter anion show that pyridine benzylic cation **20c** is more stable than tertiary cation **18c** by 2.5 kcal/mol (**Figure 2.5a**). The relative stabilities of the tri-coordinated carbocations are changed by the effect of ion pairing. Thus, we propose that the deprotonation step occurs directly from **11**.

a) Electronic effects of aryl groups in C–H insertion reactions



b) Investigation on regioselectivity in C–H activation by vinyl cation

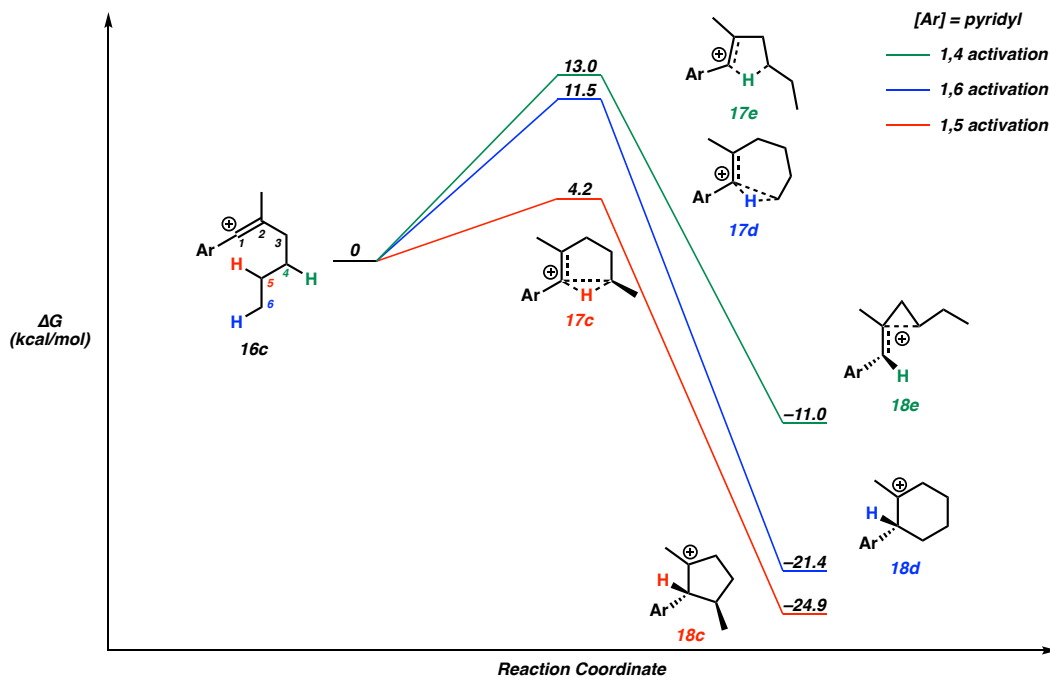


**Figure 2.5** Computational studies of the vinyl cation reactivity in the absence of counter anion with  $\omega$ B97X-D/6-311+G(d,p) in the gas phase at 298.15K.

Computational model substrates (Ar = *p*-anisyl and phenyl) were employed to evaluate the electronic effects in the C–H insertion reaction (**Figure 2.5a**, Gibbs free energies in kcal/mol). Triflate affinity energies, which measure the energy to generate the vinyl cation from the triflate, are utilized as a reference to compare the energetics of the ions. As shown in **Figure 2.5a**, vinyl cation **16** undergoes the concerted C–H insertion reaction via TS **17** to generate tertiary carbocation **18**, which is followed by 1,2-hydride shift through TS **19** in order to form benzylic cation **20**. IRC calculations of TS **17** predicted the concerted C–H insertion pathway. The activation energy barriers of the C–H insertion reactions are affected by the stability of vinyl cation intermediates. With the relatively electron-withdrawing pyridyl group, the vinyl cation intermediate is less stabilized than by phenyl or anisyl. The activation energy barrier for C–H insertion reaction is lowest with pyridyl and higher with phenyl and anisyl (**Figure 2.5a**).

The regioselectivity in C–H activation by the vinyl carbocation was also studied (**Figure 2.5b**). The two-stage concerted process (**17d**, 11.5 kcal/mol) forms 6-membered ring **18d**. The process generates the primary cation vacant orbital through the 1,6-hydride abstraction in the first stage. The generation of the primary cation is more difficult than the generation of the secondary cation, which is observed in **17c** in the formation of 5-membered ring **18c**. The reaction is possible, but the competing reaction pathway **17c** (4.2 kcal/mol) is kinetically favored.

Moreover, we attempted computational location of the transition state for formation of 4-membered ring, but the computational studies predict formation of the bridged cation **18e** via concerted 1,4-hydride abstraction **17e** (13.0 kcal/mol). This hypothetical pathway is less favorable than formation of **17c**.

## 2.6 Conclusion

We have investigated the mechanism of a vinyl carbocation C–H insertion reaction with a dimeric  $\text{Li}^+$ -ureide catalyst. We show that the catalyst not only generates vinyl carbocations from vinyl triflates, but forms an ion pair of the cation with  $\text{Li}^+$ -ureide triflate anion rather than the ureide anion proposed before.<sup>7</sup> Because of the reversible nature of the catalyzed heterolysis, the subsequent C–H insertion step can be the rate-determining step. In previous work, the heterolysis is rate-determining, because ionization of 1-cyclohexenyl triflate is slow due to the non-linear geometry forced on the cyclohexenyl *sp*-hybridized cation.<sup>1,17</sup> By contrast, the ionization of substrates that can form aryl-substituted linear vinyl cations is easier, and the rate of C–H insertion can be influenced by aryl substituents. The reactivity difference of anisyl, phenyl, and pyridyl vinyl cations in C–H insertion reactions has been measured theoretically in this work. We have also explained why the formation of five-membered ring product through the C–H insertion reaction is favored over four- and six-membered ring formation.<sup>7</sup> Finally, our groups have described an enantioselective vinyl cation C–H insertion reaction.<sup>18</sup> Our studies of vinyl carbocations generated from  $\text{Li}^+$ -ureide catalyst provide further evidence for the nature of ion pairs generated in these reactions.

## 2.7 References

- (1) Popov, S.; Shao, B.; Bagdasarian, A. L.; Benton, T. R.; Zou, L.; Yang, Z.; Houk, K. N.; Nelson, H. M. Teaching an old carbocation new tricks: intermolecular C–H insertion reactions of vinyl cations. *Science* **2018**, *361*, 381–387.
- (2) Grob, C. A.; Cseh, G. Die Solvolyse von  $\alpha$ -Bromstyrolen Substitution am ungesättigten trigonalen Kohlenstoffatom. *Helv. Chim. Acta* **1964**, *47*, 194–203.
- (3) (a) Hanack, M. Vinyl Cations in Solvolysis Reactions. *Acc. Chem. Res.* **1970**, *3*, 209–216. (b) Hanack, M. Stabilized Vinyl Cations. *Acc. Chem. Res.* **1976**, *9*, 364–371. (c) Hanack, M. Mechanistic and Preparative Aspects of Vinyl Cation Chemistry. *Angew. Chem., Int. Ed. Engl.* **1978**, *17*, 333–341.
- (4) (a) Rappoport, Z.; Gal, A. Vinylic Cations from Solvolysis. I. Trianisylvinyl halide system. *J. Am. Chem. Soc.* **1969**, *91*, 5246–5254. (b) Rappoport, Z.; Apeloig, Y. Vinylic cations from solvolysis. II. Stereochemistry of the SN1 reaction of 1,2-dianisyl-2-phenylvinyl halides. *J. Am. Chem. Soc.* **1969**, *91*, 6734–6742. (c) Rappoport, Z.; Kaspi, J. Vinylic cations from solvolysis. III. Solvolysis of triarylvinyl arylsulfonates in aqueous acetone. *J. Am. Chem. Soc.* **1970**, *92*, 3220–3221. (d) Rappoport, Z.; Kaspi, J. Vinylic cations from solvolysis. XVIII. Unusual solvent effects and external ion return in the solvolysis of several vinylic compounds in aqueous trifluoroethanol. *J. Am. Chem. Soc.* **1974**, *96*, 4518–4530.
- (5) (a) Vinyl Cations; Stang, P.; Rappoport, Z.; Hanack, M.; Subramanian, L. R., Eds.; Academic Press: New York, 1979. (b) Dicoordinated Cations; Rappoport, Z.; Stang, P. J., Eds.; Wiley: New York, 1997. (c) Stang, P. J.; Summerville, R. Preparation and solvolysis of vinyl trifluoromethanesulfonates. I. evidence for simple alkylvinyl cation intermediates. *J. Am. Chem. Soc.* **1969**, *91*, 4600–4601. (d) Stang, P. J.; Anderson, A. G. Preparation and chemistry of

vinyl triflates. 16. mechanism of alkylation of aromatic substrates. *J. Am. Chem. Soc.* **1978**, *100*, 1520–1525.

(6) Wigman, B.; Popov, S.; Bagdasarian, A. L.; Shao, B.; Benton, T. R.; Williams, C. G.; Fisher, S. P.; Lavallo, V.; Houk, K. N.; Nelson, H. M. Vinyl carbocations generated under basic conditions and their intramolecular C–H insertion reactions. *J. Am. Chem. Soc.* **2019**, *141*, 9140–9144.

(7) Bagdasarian, A. L.; Popov, S.; Wigman, B.; Wei, W.; Lee, W.; Nelson, H. M. Urea-catalyzed vinyl carbocation formation enables mild functionalization of unactivated C–H bonds. *Org. Lett.* **2020**, *22*, 7775–7779.

(8) (a) Seidel, D. The Anion-Binding Approach to Catalytic Enantioselective Acyl Transfer. *Synlett* **2014**, *25*, 783–794. (b) Zhang, Z.; Schreiner, P. R. (Thio)urea organocatalysis—What can be learnt from anion recognition?. *Chem. Soc. Rev.*, **2009**, *38*, 1187–1198. (c) Beckendorf, S.; Asmus, S.; García Mancheño, O. H-Donor Anion Acceptor Organocatalysis—The Ionic Electrophile Activation Approach. *ChemCatChem* **2012**, *4*, 926–936. (d) Brak, K.; Jacobsen, E. N. Asymmetric Ion-Pairing Catalysis. *Angew. Chem., Int. Ed.* **2013**, *52*, 534–561. (e) Visco, M. D.; Attard, J.; Guan, Y.; Mattson, A. E. Anion-binding catalyst designs for enantioselective synthesis. *Tetrahedron Lett.* **2017**, *58*, 2623–2628. (f) Sharma, H. A.; Essman, J. Z.; Jacobsen, E. N. Enantioselective catalytic 1,2-boronate rearrangements. *Science* **2021**, *374*, 752–757.

(9) Frisch, M. J.; Trucks, G. W.; Schlegel, H. B.; Scuseria, G. E.; Robb, M. A.; Cheeseman, J. R.; Scalmani, G.; Barone, V.; Petersson, G. A.; Nakatsuji, H.; Li, X.; Caricato, M.; Marenich, A. V.; Bloino, J.; Janesko, B. G.; Gomperts, R.; Mennucci, B.; Hratchian, H. P.; Ortiz, J. V.; Izmaylov, A. F.; Sonnenberg, J. L.; Williams-Young, D.; Ding, F.; Lipparini, F.; Egidi, F.; Goings, J.; Peng, B.; Petrone, A.; Henderson, T.; Ranasinghe, D.; Zakrzewski, V. G.; Gao, J.;



Rega, N.; Zheng, G.; Liang, W.; Hada, M.; Ehara, M.; Toyota, K.; Fukuda, R.; Hasegawa, J.; Ishida, M.; Nakajima, T.; Honda, Y.; Kitao, O.; Nakai, H.; Vreven, T.; Throssell, K.; Montgomery, J. A., Jr.; Peralta, J. E.; Ogliaro, F.; Bearpark, M. J.; Heyd, J. J.; Brothers, E. N.; Kudin, K. N.; Staroverov, V. N.; Keith, T. A.; Kobfayashi, R.; Normand, J.; Raghavachari, K.; Rendell, A. P.; Burant, J. C.; Iyengar, S. S.; Tomasi, J.; Cossi, M.; Millam, J. M.; Klene, M.; Adamo, C.; Cammi, R.; Ochterski, J. W.; Martin, R. L.; Morokuma, K.; Farkas, O.; Foresman, J. B.; and Fox, D. J. *Gaussian 16*; Gaussian, Inc.: Wallingford, CT, **2016**.

(10) Chai, J.-D.; Head-Gordon, M. Long-range corrected hybrid density functionals with damped atom–atom dispersion corrections<sup>†</sup>. *Phys. Chem. Chem. Phys.* **2008**, *10*, 6615–6620.

(11) Richards, T. W.; Shipley, J. W. The dielectric constants of typical aliphatic and aromatic hydrocarbons, cyclohexane, cyclohexanone, and cyclohexanol. *J. Am. Chem. Soc.* **1919**, *41*, 2002–2012.

(12) (a) Grimme, S. Supramolecular binding thermodynamics by dispersion-corrected density functional theory. *Chem. Eur. J.* **2012**, *18*, 9955–9964; (b) Luchini, G.; Alegre-Requena J. V.; Guan, Y.; Funes-Ardoiz, I.; Paton, R. S. (2019). GoodVibes: *GoodVibes 3.0.1* DOI: 10.5281/zenodo.595246.

(13) Legault, C. Y. *CYLview*, 1.0b; Universite' de Sherbrooke, **2009**; <http://www.cylview.org>.

(14) (a) Reich, H. J. Role of organolithium aggregates and mixed aggregates in organolithium mechanisms. *Chem. Rev.* **2013**, *113*, 7130–7178. (b) Harrison-Marchand, A.; Mongin, F. Mixed aggregate (MAA): a single concept for all dipolar organometallic aggregates. 1. structural data. *Chem. Rev.* **2013**, *113*, 7470–7562.

(15) Williard, P. G.; Salvino, J. M. Synthesis, isolation, and structure of an LDA-THF complex. *J. Org. Chem.* **1993**, *58*, 1–3.

(16) Winstein, S.; Clippinger, E.; Fainberg, A. H.; Heck, R.; Robinson, G. C. Salt effects and ion pairs in solvolysis and related reactions. III.<sup>1</sup> common ion rate depression and exchange of anions during acetolysis<sup>2,3</sup>. *J. Am. Chem. Soc.* **1956**, *78*, 328–335.

(17) The measurement of  $k_H/k_D$  of the C–H insertion reaction of a cyclohexenyl vinyl triflate with cyclohexane and cyclohexane- $d_{12}$  is 0.96, implying that formation of the strained cyclohexenyl vinyl cation is rate-determining.<sup>1</sup> By contrast, in the example in Figure 3, the cation will be formed more readily and the C–H insertion reaction will be slower. We expect a normal kinetic isotope effect.

(18) Nistanaki, S. K.; Williams, C. G.; Wigman, B.; Wong, J. J.; Haas, B. C.; Popov, S.; Werth, J.; Sigman, M. S.; Houk, K. N.; Nelson, H. M. Catalytic asymmetric C–H insertion reactions of vinyl carbocations. *Science* **2022**, *378*, 1085–1091.

## CHAPTER THREE

### Urea-Catalyzed Vinyl Carbocation Formation Enables Mild Functionalization of Unactivated C–H Bonds

#### 3.1 Contributions

This is an author manuscript from the publication: Bagdasarian, A. L.; Popov, S.; Wigman, B.; Wei, W.; Lee, W.; Nelson, H. M. Urea-Catalyzed Vinyl Carbocation Formation Enables Mild Functionalization of Unactivated C–H Bonds. *Org. Lett.* **2020**, *22*, 7775–7779.

<https://doi.org/10.1021/acs.orglett.0c01745>. As a synthetic organic chemist, I conducted experiments to develop Li<sup>+</sup>-ureide catalysis and new substrate classes for intramolecular C–H insertion reactions of vinyl cations.

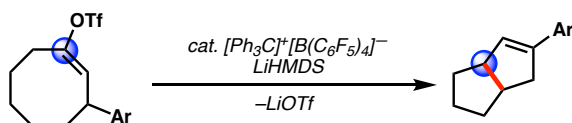
#### 3.2 Abstract

Herein we report the 3,5-bistrifluoromethylphenyl urea-catalyzed functionalization of unactivated C–H bonds. In this system, the urea catalyst mediates the formation of high-energy vinyl carbocations that undergo facile C–H insertion and Friedel–Crafts reactions. We introduce a new paradigm for these privileged scaffolds where the combination of hydrogen-bonding motifs and strong bases affords highly active Lewis acid catalysts capable of ionizing strong C–O bonds. Despite the highly Lewis-acidic nature of these catalysts that enables triflate abstraction from sp<sup>2</sup> carbons, these newly found reaction conditions allow for the formation of heterocycles and tolerate highly Lewis-basic heteroaromatic substrates. This strategy showcases the potential utility of dicoordinated vinyl carbocations in organic synthesis.

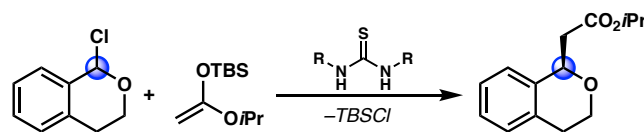
### 3.3 Introduction

As evidenced by the elegant and pervasive metal carbenoid chemistry in the literature, forging C–C bonds via C–H insertion reactions is a powerful strategy in organic synthesis.<sup>1,2</sup> Here, the transition metal tempers the highly reactive nature of the neutral dicoordinate carbon center, facilitating selective and controlled reactivity. Recently our group has shown that vinyl carbocations can participate in C–H insertion reactions that are mechanistically complementary to classical carbenoid insertion chemistry.<sup>3,4</sup> While previous studies from our group and others have demonstrated that these species undergo facile C–C bond-forming reactions, all catalytic systems reported thus far have utilized expensive, hygroscopic, and specialized weakly coordinating anion (WCA) salts that are often difficult to functionalize and establish structure-function relationships (**Figure 3.1a**).<sup>5</sup>

**a** *Li<sup>+</sup>-catalyzed transannular C–H functionalization*  
Wigman, *J. Am. Chem. Soc.*, 2019



**b** *Thiourea-catalyzed enantioselective alkylation*  
Reisman, *J. Am. Chem. Soc.*, 2008



**c** *Urea-catalyzed functionalization of inert C–H bonds*  
*This research*

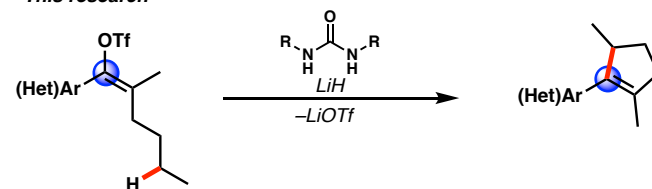


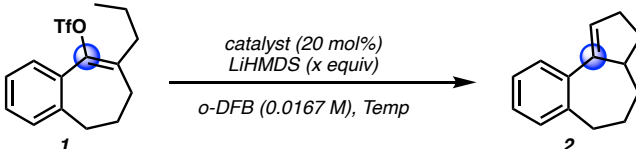
**Figure 3.1** Vinyl cation insertion reactions and hydrogen-bond donor catalysts. a) Lithium-promoted intramolecular C–H insertion reactions of vinyl cations. b) Chiral thiourea-catalyzed additions to oxocarbenium cations via chloride abstraction. c) Functionalization of unactivated C–H bonds catalyzed by ureas.

In an effort to identify more easily accessible and modular catalysts for these powerful transformations, we looked towards hydrogen-bonding catalysts, such as thioureas. These readily available and highly tunable scaffolds have found success in promoting the formation of cationic intermediates.<sup>6,7</sup> Specifically we were inspired by Reisman and Jacobsen's use of thioureas to generate resonance-stabilized tricoordinate carbocations that engage in highly-selective bond-forming processes (**Figure 3.1b**).<sup>8</sup> The same group later showed that squaramides, combined with trimethylsilyl triflate (TMSOTf), enhance the electrophilicity of the silicon center via triflate binding.<sup>9</sup> Inspired by these studies, we sought to apply an analogous mode of ionization to vinyl triflates, which would provide vinyl cations capable of C–C bond-forming reactions. Herein, we report the successful realization of this hypothesis where the combination of urea scaffolds and Li-bases catalyzes C–H functionalization and Friedel–Crafts reactions through intermediate vinyl cations (**Figure 3.1c**).

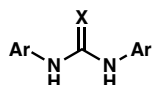
### 3.4 Results and Discussion

We began proof-of-concept studies in the context of the C–H insertion reactions of propylated benzosuberonyl triflate **1** (**Table 3.1**).<sup>5</sup> We hypothesized that a hydrogen-bonding catalyst could ionize its vinyl triflate, and the ensuing vinyl carbocation would insert into the terminal CH<sub>3</sub> group of the tethered propyl chain to give product **2**. Initially, the use of Schreiner's thiourea **3** gave neither conversion to the desired product **2**, nor consumption of starting material **1**. We rationalized that a stronger Lewis acid was needed to promote the ionization. Based on our previous studies, we hypothesized that deprotonation of the urea would yield a lithiated species sufficiently Lewis acidic to ionize an enol triflate, revealing the potent vinyl carbocation.<sup>5,10,11</sup> To our delight, we found that the addition of a stoichiometric amount of lithium

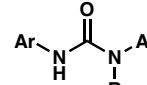
hexamethyldisilazide (LiHMDS) to this reaction mixture resulted in a high yielding C–H insertion reaction, giving tricycle **2** in 78% yield (entry 2). The urea and squaramide analogs (**4** and **5** respectively) of Schreiner’s catalyst were also competent catalysts for this transformation, yielding the desired product in 96% and 72% yield, respectively (entries 3 and 4). This catalytic system was also effective at lower temperatures and with lower equivalents of base (entries 5 and 6). Performing the reaction without any urea catalyst (**4**) yielded negligible amounts of desired product (entry 7). These experiments showcase the necessity of both the hydrogen-bonding catalyst and the lithium base. Additionally, performing this reaction with catalytic lithiated urea **4-Li** gave the desired product in 86% yield, suggesting that this is on, or accessible through, the active catalytic cycle (entry 8).



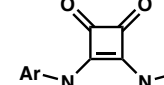
entry	catalyst	LiHMDS equiv	Temp (°C)	yield
1	<b>3</b>	none	30	0%
2	<b>3</b>	1.5	30	78%
3	<b>4</b>	1.5	30	96%
4	<b>5</b>	1.5	30	72%
5	<b>4</b>	1.5	-40	93%
6	<b>4</b>	1.2	30	96%
7	none	1.2	30	3%
8	<b>4-Li</b>	1.2	30	86%
9	<b>6</b>	1.2	30	3%
10	<b>7</b>	1.2	30	79%
11	<b>8</b>	1.2	30	9%
12	<b>9</b>	1.2	30	19%



**3:** X = S, Ar = 3,5-bisCF<sub>3</sub>C<sub>6</sub>H<sub>3</sub>



**4:** X = O, Ar = 3,5-bisCF<sub>3</sub>C<sub>6</sub>H<sub>3</sub>



**5:** Ar = 3,5-bisCF<sub>3</sub>C<sub>6</sub>H<sub>3</sub>

**6:** X = O, Ar = 2-CF<sub>3</sub>C<sub>6</sub>H<sub>4</sub>      **9:** Ar = 3,5-bisCF<sub>3</sub>C<sub>6</sub>H<sub>3</sub>      R = Me

**7:** X = O, Ar = 3-CF<sub>3</sub>C<sub>6</sub>H<sub>4</sub>      **4-Li:** Ar = 3,5-bisCF<sub>3</sub>C<sub>6</sub>H<sub>3</sub>      R = Li

**8:** X = O, Ar = 4-CF<sub>3</sub>C<sub>6</sub>H<sub>4</sub>

**Table 3.1** Optimization of C–H insertion reactions with hydrogen-bonding catalysts.

Having found that urea catalyst **4** afforded the desired product in the highest yield, we next explored the effect of catalyst substitution on the product outcome. Probing monosubstituted trifluoromethyl urea catalysts (**6–8**) revealed the importance of a *meta*-trifluoromethyl group (79% yield for entry 10 vs. 3–9% yield for entries 9 and 11).<sup>12</sup> Lastly, the N-methylated catalyst **9** delivered the desired product in a meager 19% yield, highlighting the importance of having both N–H hydrogen-bond donors (entry 12).

To further develop the scope of this reaction, urea-catalyzed Friedel–Crafts reactions of vinyl triflates were explored. Here, we decided to use the optimized reaction conditions from the above insertion chemistry as a starting point. We found a large scope of both triflates and arenes to be tolerant of this transformation. A silylated pyrrole gave moderate selectivity for vinylation of the C3 position (**Figure 3.2a, 10**).<sup>13</sup> Electron deficient vinyl triflates were tolerated, reacting with anisoles and xylenes in moderate to good yields (52–76%, **11–13**). The trifluoromethylated vinyl triflate also reacted with benzene or a bromobenzene derivative yielding vinylated arenes in high yields (**14–15**). More electron rich aromatic nucleophiles, such as dimethoxybenzene, underwent smooth coupling with a variety of halogenated vinyl triflates in good yields (**16–18**). There was minimal decrease in efficiency when performing the reaction on 1-gram scale with the iodinated vinyl triflate, giving styrene **18** in 64% yield. Furthermore, cyclooctenyl triflate **19** was observed to undergo a transannular C–H insertion, Friedel–Crafts cascade with 4-methylanisole giving alkylated arene **20** in 57% yield (**Figure 3.2b**). Here, two C–C bonds, a 5,5-fused ring system, and a quaternary carbon center were all forged in a single step. Notably, all of the reactions outlined in **Figure 3.2** were performed on the bench and required neither scrupulous drying of substrates nor catalysts.

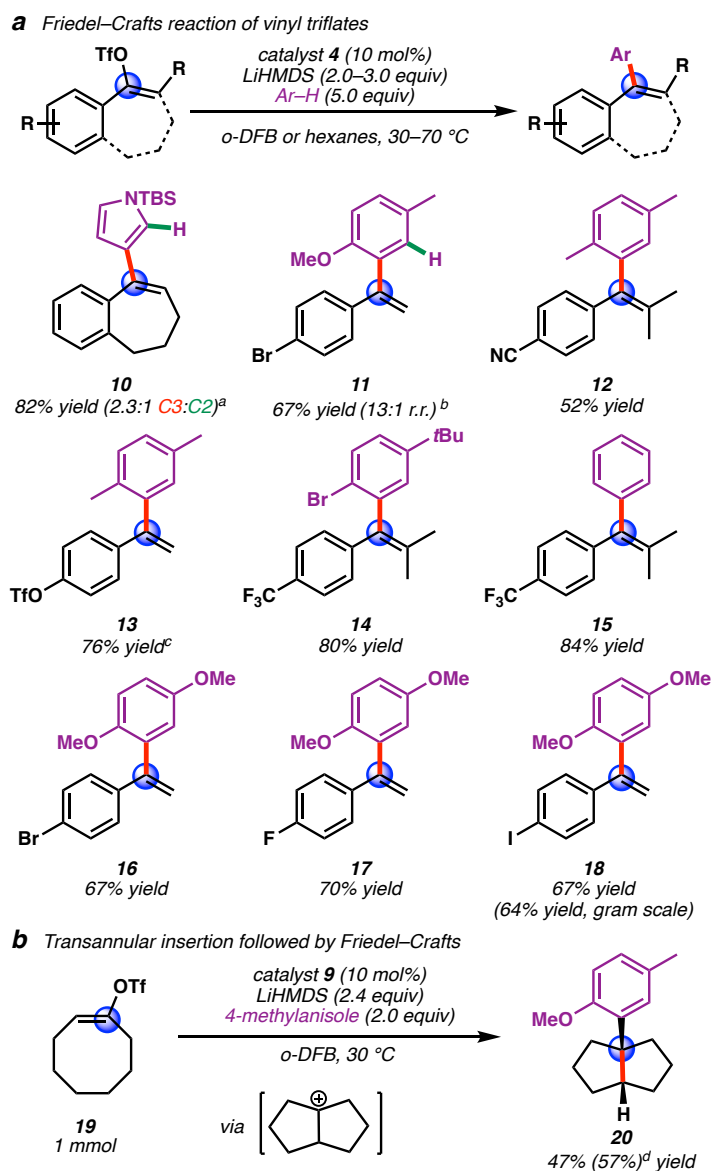


**Figure 3.2** Urea catalyzed Friedel–Crafts reactions. Isolated yield after column chromatography a) Scope of vinyl triflates and arenes. b) C–H insertion, Friedel–Crafts cascade. <sup>a</sup>10 equiv arene. <sup>b</sup>Catalyst **9**. <sup>c</sup>*p*-Xylene solvent. <sup>d</sup>Yield determined by GC-FID.

We then sought to validate our hypothesis that these readily accessible organocatalysts were able to tolerate various functional groups in the context of vinyl cation C–H insertion reactions. To explore the functional group tolerance, a variety of alkylated styrenyl triflates were prepared (**Figure 3.3**).



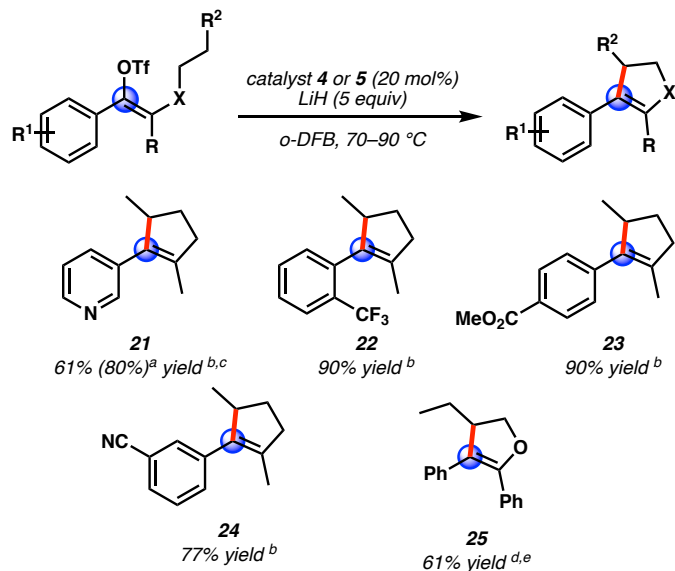


**Figure 3.3** Urea and lithium catalyzed C–H insertion reactions. Isolated yield after column chromatography. <sup>a</sup>Yield determined by NMR using an internal standard. <sup>b</sup>Catalyst **4** <sup>c</sup>LiHMDS base in cyclohexane solvent. <sup>d</sup>Catalyst **5**. <sup>e</sup>LiOtBu base in 1,2-DCE solvent.

We were quite pleased to find that a substrate bearing a pyridine substituent was competent in this transformation, yielding cyclopentenyl pyridine **21** in 61 % yield. Substrates bearing electron-withdrawing substituents, however, resulted in products with poor olefin isomer ratios.<sup>14</sup> Upon further optimization, we discovered that utilization of LiH allowed for high-yielding reactions with excellent olefin selectivity for these substrates (**22–24**). Moreover LiOtBu was also a competent base for this transformation, allowing for the formation of dihydrofuran **25** in 61 % yield, via insertion into an ether tether. To the best of our knowledge, this example showcases the first heterocycle synthesis from a C–H insertion reaction of a vinyl cation. Furthermore, the variety of Li-bases used for these transformations highlights the modularity of this system as well as the importance of both the hydrogen-bonding catalyst and base. Inspired by the successful synthesis of ester **23**, we posited that we could also form aryl cyclopentene derivatives via C–H insertion reactions of vinylogous acyl triflates derived from butylated  $\beta$ -ketoesters (**Figure 3.4**).

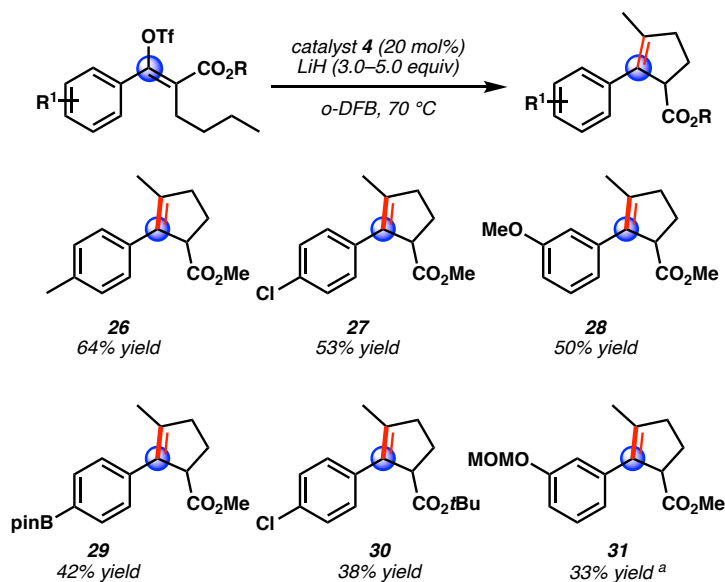


**Figure 3.4** Urea catalyzed C–H insertion reactions of  $\beta$ -ketoester derived vinyl triflates. Isolated yield after column chromatography. <sup>a</sup>10 equiv LiH.

These substrates are good candidates because they are readily accessible from corresponding  $\beta$ -ketoesters, they would yield highly functionalized cyclopentenes, and they are natively heteroatom-rich, providing a further test of the compatibility of this catalytic system. Under the standard LiHMDS conditions, we found no conversion to the desired product, likely due to the electrophilicity of (vinylogous) esters as well as recent reports describing ester functionalization with LiHMDS.<sup>15,16</sup>

We found that using LiH as the base allowed for productive transformations. Methyl, halogen substituents, boronic esters and methyl ethers were all tolerated, yielding the ester products **26–29** in 42–64% yield. Notably, under these basic conditions, acid-sensitive functional groups such as a methoxymethyl (MOM) ether protected phenol or *tert*-butyl ester remained intact, yielding cyclized products **30** and **31** in 38% and 33% yield, respectively. We observed the exclusive formation of the  $\beta,\gamma$ -unsaturated products; we attribute this to the increased stability of these products in comparison to the  $\alpha,\beta$ -unsaturated products, likely due to allylic strain.<sup>14</sup>

With the information derived from our initial scope studies, we began our investigation into the mechanism of this transformation. During our studies of the vinylogous acyl triflates we consistently noticed small amounts of olefinic products in our crude reaction mixtures. Careful purification of the reaction mixture derived from tolyl triflate **32** provided  $\gamma$ -lactone **33** in 16% yield (**Figure 3.5a**). We attribute formation of this byproduct to the intermediate vinyl cation **34** undergoing a 1,5-hydride shift generating secondary carbocation **35**. This putative intermediate can then undergo a facile 1,2-hydride shift to yield secondary carbocation **36** followed by trapping by the pendant ester yielding the lactone product. This overall “rebound”-type mechanism has been proposed by Stang, Hanack, Olah, Mayr, Caple, and others.<sup>17</sup> To further support this mechanistic hypothesis, we synthesized propylated triflate **37**. Under the reaction conditions, neither the desired insertion product nor lactone byproducts were observed (**Figure 3.5b**). We attribute this to the inherent difficulty in the formation of primary carbocation **38**. These mechanistic findings stand in stark contrast with those of previously observed vinyl cation C–H insertion reactions of propylated benzosuberonyl triflates (e.g. **1**, **Table 3.1**) and previously disclosed silylium mediated transformations that proceed through a concerted C–H insertion process.<sup>5</sup> The reason for this mechanistic divergence is unclear at this time.

To investigate if the lithiated urea catalyst was the active Lewis acid, we exposed substrate **32** to a stoichiometric amount of the lithiated urea catalyst, synthesized through deprotonation of urea **4** with LiHMDS.<sup>14</sup> This gave the desired product in 23% yield with LiOTf observed by <sup>7</sup>Li and <sup>19</sup>F NMR (**Figure 3.5c**). On the basis of these results, we propose that the lithiated urea **4-Li** is the active species responsible for triflate ionization, although other possibilities such as a dilithiated urea or simply a triflate abstraction by parent urea **4** can not be ruled out (**Figure 3.5d**).<sup>5</sup>

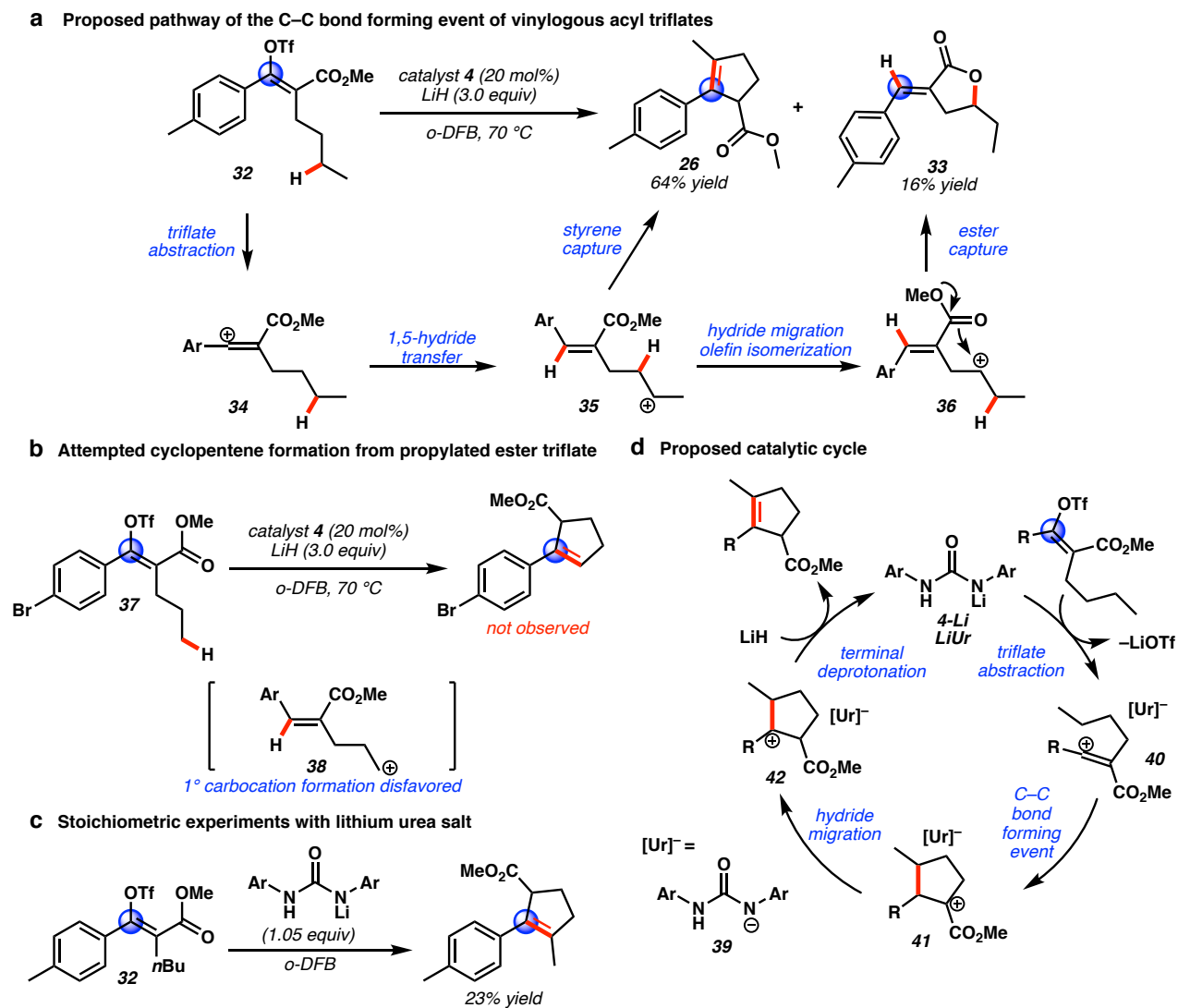


**Figure 3.5** Mechanism of urea promoted C–H insertion. a) Nature of C–C bond formation of vinylogous acyl triflates. Ar = *p*-tolyl. b,c) Mechanistic studies. d) Proposed catalytic cycle of reaction. Ar = 3,5-bis(CF<sub>3</sub>)phenyl.

We posit that the lithiated urea catalyst **4-Li** can abstract a triflate from the substrate and produce vinyl cation **40**. This can then undergo the C–C bond-forming event yielding  $\alpha$ -ester cation **41** followed by a hydride migration to give benzylic cation **42** and deprotonation to give the product, concurrently forming LiOTf and regenerating the catalyst. In the case of the vinylogous acyl triflate substrates, we posit that C–C bond formation is a stepwise process, proceeding

through the pathway outlined in **Figure 3.5a**. For the Friedel-Crafts reactions that are performed with LiHMDS, we posit that a similar mechanism is operative.

### **3.5 Conclusion**

In conclusion, we disclose a novel application of hydrogen-bonding scaffolds, where 3,5-bistrifluoromethylphenyl ureas catalyze C–C bond-forming reactions of vinyl triflates under strongly basic conditions. In the presence of these catalysts, the proposed reactive dicoordinate carbocation intermediates undergo facile C–H insertion and Friedel–Crafts reactions in good to excellent yield. This strategy demonstrates the utility of vinyl carbocation reactions and introduces easily accessible and modular catalysts for these transformations.

### 3.6 References

- (1) (a) Doyle, M. P.; Duffy, R.; Ratnikov, M.; Zhou, L. Catalytic carbene insertion into C–H bonds. *Chem. Rev.* **2010**, *110*, 704–724. (b) He, J.; Wasa, M.; Chan, K. S. L.; Shao, Q.; Yu, J.-Q. Palladium-catalyzed transformations of alkyl C–H bonds. *Chem. Rev.* **2017**, *117*, 8754–8786. (c) Davies, H. M. L.; Du Bois, J.; Yu, J.-Q. C–H Functionalization in organic synthesis. *Chem. Soc. Rev.* **2011**, *40*, 1855–1856. (d) Liao, K.; Pickel, T. C.; Boyarskikh, V.; Bacsá, J.; Musaev, D. G.; Davies, H. M. L. Site-selective and stereoselective functionalization of non-activated tertiary C–H bonds. *Nature* **2017**, *551*, 609–613. (e) Liao, K.; Yang, Y.-F.; Li, Y.; Sanders, J. N.; Houk, K. N.; Musaev, D. G.; Davies, H. M. L. Design of catalysts for site-selective and enantioselective functionalization of non-activated primary C–H bonds. *Nature Chem.* **2018**, *10*, 1048–1055.
- (2) (a) Davies, H. M. L.; Beckwith, R. E. J. Catalytic enantioselective C–H activation by means of metal-carbenoid-induced C–H insertion. *Chem. Rev.* **2003**, *103*, 2861–2904. (b) Ma, C.; Fang, P.; Mei, T.-S. Recent advances in C–H functionalization using electrochemical transition metal catalysis *ACS Catalysis* **2018**, *8*, 7179–7189. (c) Wan, J. P.; Gan, L.; Liu, Y. Transition metal-catalyzed C–H bond functionalization in multicomponent reactions: a tool toward molecular diversity. *Org. Biomol. Chem.* **2017**, *15*, 9031–9043
- (3) Shao, B.; Bagdasarian, A. L.; Popov, S.; Nelson, H. M. Arylation of hydrocarbons enabled by organosilicon reagents and weakly coordinating anions. *Science* **2017**, *355*, 1403–1407.
- (4) Popov, S.; Shao, B.; Bagdasarian, A. L.; Benton, T. R.; Zhou, L.; Yang, Z.; Houk, K. N.; Nelson, H. M. Teaching an old carbocation new tricks: intermolecular C–H insertion reactions of vinyl cations *Science* **2018**, *361*, 381–387.
- (5) Wigman, B.; Popov, S.; Bagdasarian, A. L.; Shao, B.; Benton, T. R.; Williams, C. G.; Fisher, S. P.; Lavallo, V.; Houk, K. N.; Nelson, H. M. Vinyl carbocations generated under basic

conditions and their intramolecular C–H insertion reactions. *J. Am. Chem. Soc.* **2019**, *141*, 9140–9144.

(6) (a) Doyle, A. G.; Jacobsen, E. N. Small-molecule H-bond donors in asymmetric catalysis. *Chem. Rev.* **2007**, *107*, 5713–5743. (b) Schreiner, P. R.; Witkopp, A. *Org. Lett.* **2002**, *4*, 217–220.

c) Kotke, M.; Schreiner, P. R.; *Tetrahedron* **2006**, *62*, 434–439.

(7) Knowles, R. R.; Jacobsen, E. N. Attractive noncovalent interactions in asymmetric catalysis: links between enzymes and small molecule catalysts. *Proc. Natl. Acad. Sci.* **2010**, *107*, 20678–20685.

(8) Reisman, S. E.; Doyle, A. G.; Jacobsen, E. N. Enantioselective thiourea-catalyzed additions to oxocarbenium ions. *J. Am. Chem. Soc.* **2008**, *130*, 7198–7199.

(9) Banik, S. M.; Levina, A.; Hyde, A. M.; Jacobsen, E. N. Lewis acid enhancement by hydrogen-bond donors for asymmetric catalysis. *Science* **2017**, *358*, 761–764.

(10) Jakab, G.; Tancon, C.; Zhang, Z.; Lippert, K. M.; Schreiner, P. R. (Thio)urea organocatalysts equilibrium acidities in DMSO. *Org. Lett.* **2012**, *14*, 1724–1727.

(11) Ni, X.; Li, X.; Wang, Z.; Cheng, J.-P. Squaramide equilibrium acidities in DMSO. *Org. Lett.* **2014**, *16*, 1786–1789.

(12) Lippert, K. M.; Hof, K.; Gerbig, D.; Ley, D.; Hausmann, H.; Guenther, S.; Schreiner, P. R. *Eur. J. Org. Chem.* **2012**, *30*, 5919–5927.

(13) Simchen, G.; Majchrzak, M. W. Friedel-Crafts acylation of 1-tert-butyldimethylsilylpyrrole, a very short and simple route to 3-substituted pyrroles. *Tetrahedron Lett.* **1985**, *26*, 5035–5036.

(14) See Supplementary Information for details in the adapted article.

(15) Li, G.; Szostak, M. Highly selective transition-metal-free transamidation of amides and amidation of esters at room temperature. *Nat. Commun.* **2018**, *9*, 1–8.

- (16) Li, G.; Ji, C.-L.; Hong, X.; Szostak, M. Highly chemoselective, transition-metal-free transamidation of unactivated amides and direct amidation of alkyl esters by N–C/O–C cleavage. *J. Am. Chem. Soc.* **2019**, *141*, 11161–11172.
- (17) a) Hargrove, R. J.; Stang, P. J. Solvolysis of medium ring size cycloalkenyl triflates : a comparison of relative rates vs ring size *Tetrahedron* **1976**, *32*, 37–41. b) Olah, G. A.; Mayr, H. Stable carbocations. 198. Formation of allyl cations via protonation of alkynes in magic acid solution. Evidence for 1,2-hydrogen and alkyl shifts in the intermediate vinyl carbocations *J. Am. Chem. Soc.* **1976**, *98*, 7333–7340. c) Kanishev, M. I.; Shegolev, A. A.; Smit, W. A.; Caple, R.; Kelner, M. J. 1,5-hydride shifts in vinyl cation intermediates produced upon the acylation of acetylenes *J. Am. Chem. Soc.* **1979**, *101*, 5660–5671. d) Lamparter, E.; Hanack, M. Vinylkationen, VI solvolyse von 1-cyclononenyl- und 1-cyclodeceny-trifluormethansulfonat *Eur. J. Inorg. Chem.* **1972**, *105*, 3789–3793.



## CHAPTER FOUR

### Accessing Medium-sized Rings via Vinyl Carbocation Intermediates

#### 4.1 Contributions

This is an unpublished work by Zhao, Z., Popov, S., Lee, W., Burch, J. E., Delgadillo, D. A., Kim, L. J., Shahgholi, M., Houk, K. N., Nelson, H. M. This project was a collaborative work between the laboratories of my advisors, Professor Kendall N. Houk and Professor Hosea M. Nelson. As a computational organic chemist, I conducted all computational experiments while Zhenqi (Steven) Zhao carried out the majority of the experimental work. Zhenqi (Steven) Zhao received experimental assistance from Stasik Popov, Jessica E. Burch, David A. Delgadillo, Lee Joon Kim, and Mona Shahgholi.

#### 4.2 Abstract

Medium-sized rings (8–11 membered cycles) are often more challenging to synthesize than smaller rings (5–7 membered cycles) due to ring strain. Herein, we report a catalytic method for forming 8- and 9-membered rings that proceeds via the intramolecular Friedel–Crafts reactions of vinyl carbocation intermediates. These reactive species are generated catalytically through the ionization of vinyl toluenesulfonates by a Lewis acidic lithium cation/weakly coordinating anion salt.

#### 4.3 Introduction

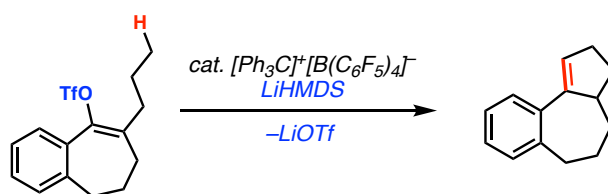
Cyclic structural motifs are ubiquitous in natural products, pharmaceuticals, and other industrially relevant compositions of matter.<sup>1,2</sup> Amongst them, 5- and 6-membered rings are the most common cyclic structures due to their ease of preparation.<sup>3,4</sup> In contrast, medium-sized rings (8–11 membered rings) are often more difficult to access, where methods commonly utilized to forge 6- or 5-membered rings fail. Unlike macrocycles ( $\geq 12$ -membered rings), medium-sized rings suffer from torsional and transannular strain; therefore, their annulation reactions can be less favorable and sluggish.<sup>3–7</sup> As a result, medium-sized rings appear less in synthetic molecules, hindering their utility across a broad swath of applications.

Despite their challenging formation, compounds with medium-sized rings are abundant in natural products.<sup>8,9</sup> For some bioactive compounds bearing medium-sized cyclic motifs, it has been proposed that the unique balance of structural rigidity and broad conformational space enables higher binding affinities to biological targets relative to small ring analogs.<sup>10</sup> Despite these facts, the number of methods for medium-sized ring formation remains limited in organic synthesis. Ring expansion from smaller rings is widely used to generate medium-sized rings; however, these reactions need careful design depending on the structure of the medium-sized ring desired and usually require several synthetic steps towards well-poised, smaller ring precursors.<sup>11</sup> For direct annulation methods, catalytic ring-closing metatheses and cross-coupling reactions are the most common, but precious noble metals such as palladium and ruthenium are required as catalysts.<sup>12,13</sup> Medium-sized ring formation through radical intermediates has also been reported, although stoichiometric radical sources are commonly used.<sup>12,13</sup> As a result, it is still of great interest to develop catalytic and metal-free annulation reactions to access medium-sized rings. In recent years, our group has developed various platforms to generate vinyl carbocation intermediates.<sup>14–18</sup> The most prominent method is Lewis acid-weakly coordinating anion (WCA)

catalysis, where vinyl trifluoromethanesulfonates (vinyl triflates) are ionized to form kinetically persistent vinyl carbocation intermediates.<sup>14,15</sup> These reactive species can then engage in C–H insertion (**Figure 4.1a**) and intermolecular Friedel–Crafts reactions. In this manuscript, we report that vinyl carbocations can also be used to forge challenging medium-sized ring systems (**Figure 4.1b**).

**A. Intramolecular C–H insertion from vinyl triflates via Li-WCA catalysis**

Wigman, *J. Am. Chem. Soc.*, **2019**



**B. Medium-sized ring formation from vinyl tosylates via Li-WCA catalysis**

*This research*

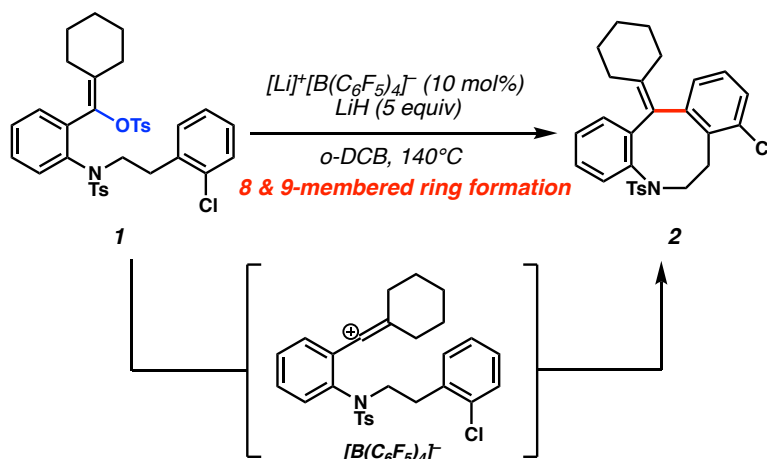


**Figure 4.1** C–C bond formations via Lewis acid-WCA catalysis. a) Intramolecular C–H insertion reactions from vinyl triflates via Li-WCA catalysis. b) This work: Medium-sized ring formation via Li-WCA catalysis.

#### 4.4 Results and Discussion

Vinyl triflates have served as vinyl carbocation precursors in previous studies.<sup>14–16</sup> However, due to the difficulty in preparing pure samples of electron-rich vinyl triflates, we investigated vinyl toluenesulfonates (vinyl tosylates).<sup>19</sup> As such, vinyl tosylate **1** was selected as our model

substrate. A sulfonamide was introduced into the aniline-derived scaffold to protect the Lewis basic amine moiety, a common functional group in many bioactive molecules.<sup>20,21</sup> We proposed that vinyl tosylate **1** would transform to tetrahydroazocine **2** under Li-WCA catalysis. Medium-sized ring **2** features an *exo*-alkene on the 8-membered ring, which is reminiscent of commercial drugs pizotifen,<sup>22</sup> amitriptyline,<sup>23</sup> and cyproheptadine,<sup>24</sup> albeit these are comprised of more readily prepared 7-membered rings (**Figure 4.2**). The established route to these drugs features a key intramolecular Friedel–Crafts acylation of a carboxylic acid to forge their core 7-membered ring. As there are few reports to build larger medium-sized rings via Friedel–Crafts acylation,<sup>25,26</sup> our complementary method provides access to underexplored chemical space via vinyl carbocation intermediates.

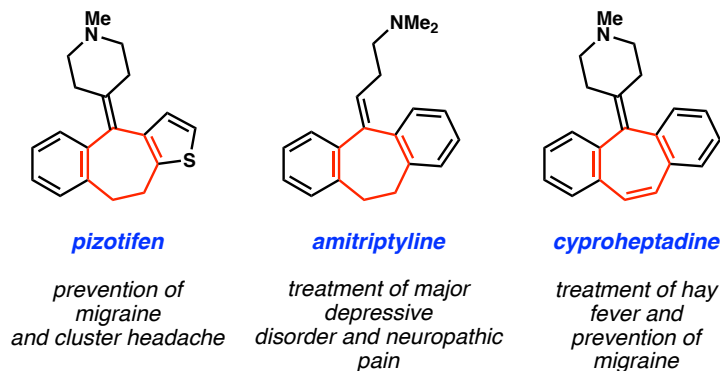
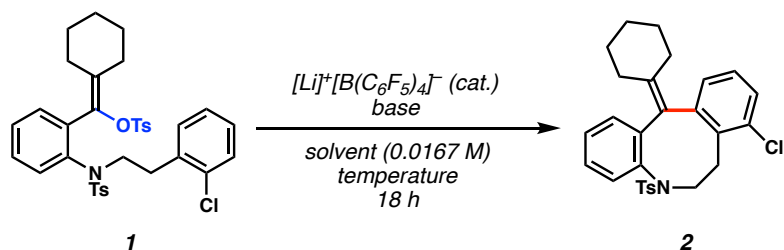


**Figure 4.2** Commercial drugs with *exo*-alkene on a 7-membered ring.

Recognizing that electron-deficient arenes are sluggish nucleophiles, we questioned if electrophilic vinyl cation species could engage them in Friedel–Crafts reactions. Therefore, we began optimization with vinyl tosylate **1** to study the Friedel–Crafts reactions with electrophilic vinyl cation species (**Table 4.1**). When vinyl tosylate **1** was subjected to 10 mol% of lithium tetrakis(pentafluorophenyl)borate ([Li]<sup>+</sup>[B(C<sub>6</sub>F<sub>5</sub>)<sub>4</sub>]<sup>-</sup>) (**3**) in 1,2-dichlorobenzene (*o*-DCB) at 140 °C, tetrahydroazocine **2** was formed in 40% yield (entry 1).



entry	catalyst (mol%)	base (equiv)	solvent	temperature (°C)	yield (%)
1	<b>3*</b> (10)	none	<i>o</i> -DCB	140	40
<b>2</b>	<b>3*</b> (10)	<b>LiH (5)</b>	<b><i>o</i>-DCB</b>	<b>140</b>	<b>74</b>
3	<b>3*</b> (10)	LiHMDS (1.5)	<i>o</i> -DCB	140	21
4	None	LiH (5)	<i>o</i> -DCB	140	n.d.
5	<b>3*</b> (5)	LiH (5)	<i>o</i> -DCB	140	49
6	<b>3*</b> (1)	LiH (5)	<i>o</i> -DCB	140	24
7	<b>3*</b> (10)	LiH (5)	<i>o</i> -DFB	92	n.d.
8	<b>3*</b> (10)	LiH (5)	mesitylene	140	50
9	<b>3*</b> (10)	LiH (5)	DMF	140	n.d.
10	<b>4</b> (10)	LiH (5)	<i>o</i> -DCB	140	19
11	<b>4</b> (10)	LiHMDS (1.5)	<i>o</i> -DCB	140	n.d.

\*Catalyst **3** is  $[\text{Li}]^+[\text{B}(\text{C}_6\text{F}_5)_4]^-$ .

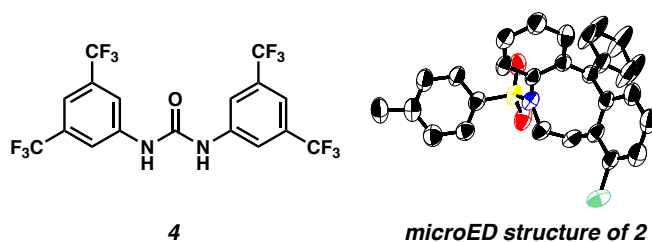


**Table 4.1** Optimization of the reaction conditions to build medium-sized rings.

The structure of product **2** was confirmed using microcrystal electron diffraction (microED).<sup>27</sup> Since a significant amount of starting material remained after long reaction times (entry 1), we hypothesized that adding a lithium base could help regenerate the lithium catalyst and improve

the reaction yield. Indeed, adding an excess of LiH increased the yield to 74% (entry 2). In contrast, the presence of lithium bis(trimethylsilyl)amide (LiHMDS), which was used in previous reports,<sup>15,16</sup> was detrimental to the reaction, forming the product in 21% yield (entry 3). Performing the reaction without  $[\text{Li}]^+[\text{B}(\text{C}_6\text{F}_5)_4]^-$  did not provide any tetrahydroazocine **2** (entry 4). Lower loadings of  $[\text{Li}]^+[\text{B}(\text{C}_6\text{F}_5)_4]^-$  gave lower yields of the product (entries 5,6), highlighting the essential role of  $[\text{Li}]^+[\text{B}(\text{C}_6\text{F}_5)_4]^-$  in this catalytic cyclization. Solvents other than *o*-DCB were also examined but were found inferior (entries 7–9). Hydrogen bonding catalyst **4**, which our group had previously applied in the ionization of vinyl triflates, gave diminished yields (entries 10,11).<sup>16</sup>

With the optimized conditions, we set out to explore the substrate scope. First, we tested various ring sizes. Similar to vinyl tosylate **1**, the substrate with a non-substituted aryl nucleophile also gave the 8-membered ring product in moderate yield (**Figure 4.3, 5**). A 9-membered ring was also formed under this system giving tetrahydroazonine **6** with a yield of 82%. However, 10-membered ring formation proved difficult, as hexahydroazecine **7** was not observed under the reaction conditions. We also found that the sulfonamide could be replaced with other functional groups. For example, thioether **8** was obtained with a moderate yield of 46%, and medium-sized carbocycle **9** could be synthesized in 81% yield. The 9-membered ring ether **10** could be produced in 65% yield with an electron-rich arene as the nucleophile. However, we found difficulty forming medium ring ether **11** from its corresponding vinyl tosylate. Substitution effects on the aryl nucleophile were also studied. Phenyl groups with the dimethylamino and methoxy groups could give the 8-membered ring products with good yields (**12** and **13**). Notably, *tert*-butyldimethylsilyl (TBS) protected phenol was also tolerated under the reaction conditions as 79% yield of **14** was obtained. Unfortunately, when the strong electron-withdrawing group

trifluoromethyl was present on the aryl group, product **15** was not formed. With a weak electron withdrawing group, such as bromine, the medium-sized ring product **16** could be obtained smoothly in 79% yield. Furthermore, heterocycles could also be used in the reaction. Thiophene was tolerated, yielding the 8-membered ring product **17** and **18** in 73% and 85% yield, respectively. In addition, tetrahydroazocine **5** was formed with 66% yield on the preparative scale of 1 mmol (0.4 g).

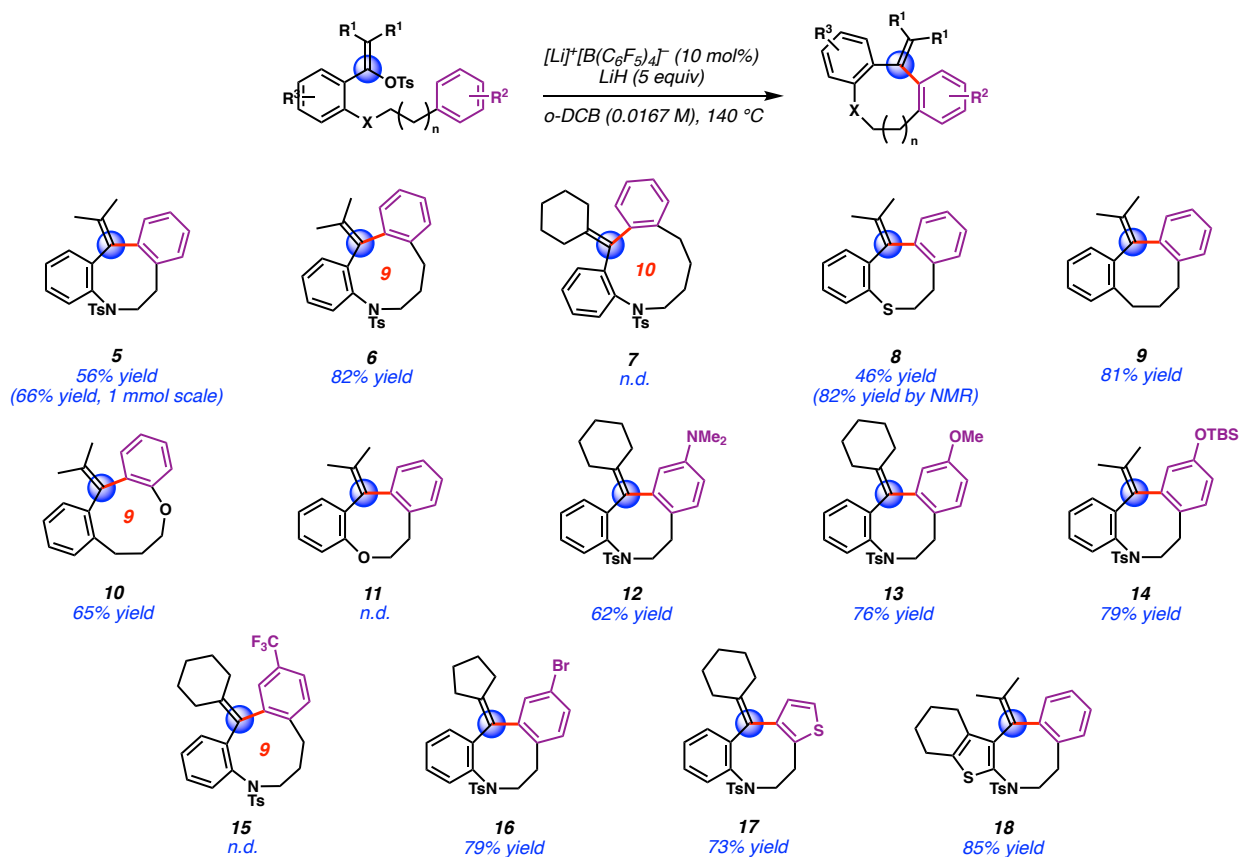


**Figure 4.3** Scope of Li-WCA catalyzed medium-sized ring formation. The reactions were performed on 0.05 mmol scale unless otherwise specified. All yields were isolated yields unless specified. All structures were characterized by NMR. The structures of **5**, **9**, **12**, **13**, **16** and **17** were also characterized by microED.

Because forming medium-sized rings through direct cyclization is challenging, we decided to study the reaction mechanism further. Lithium-WCA catalysis systems employing

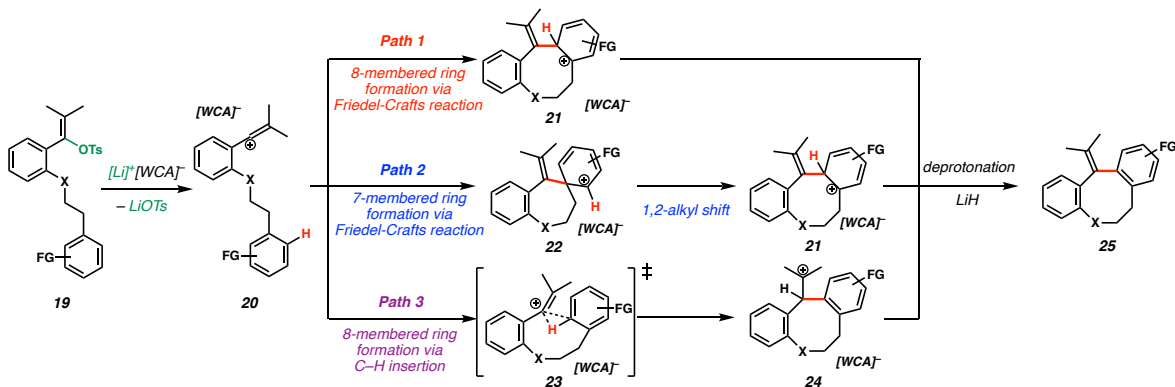
[Li]<sup>+</sup>[B(C<sub>6</sub>F<sub>5</sub>)<sub>4</sub>]<sup>-</sup> have been demonstrated to ionize vinyl sulfonates to vinyl cations.<sup>15</sup> Here, we

proposed three possible pathways in forming 8-membered ring **25** from the vinyl cation **20** (**Figure 4.4a**). **Path 1** is a conventional Friedel–Crafts reaction of the vinyl cation where the medium-sized ring intermediate **21** is formed in one step. In **Path 2**, the vinyl cation reacts with the aromatic p-system at the *ipso* carbon to form a 7-membered ring in **22**, which often harbors less ring strain than the corresponding 8-membered ring. A 1,2-shift of the alkyl group then occurs to expand the ring to give intermediate **21**. Alternatively, in **Path 3**, a concerted insertion of the vinyl cation into an aryl C–H bond is operative, mechanistically analogous to the insertion of vinyl cations into alkyl C–H bonds.<sup>14–16</sup>

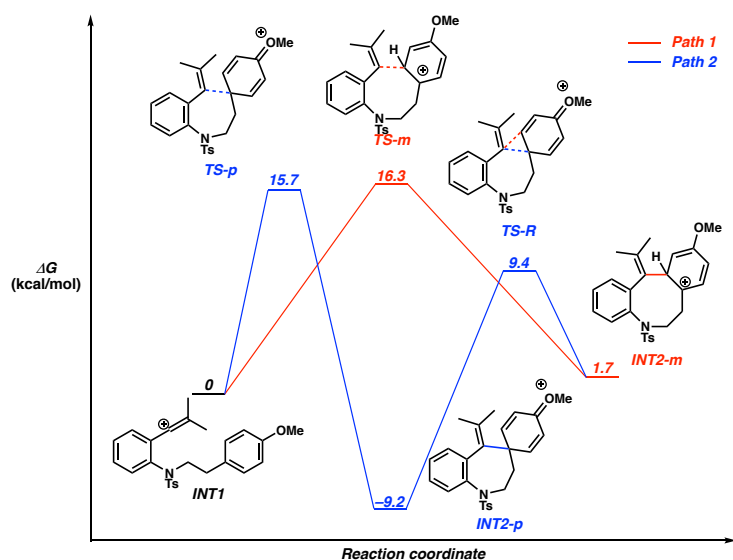
In order to differentiate the potential mechanisms of **Path 1** and **Path 2**, these proposed pathways were evaluated by density functional theory (DFT) calculations (**Figure 4.4b**). **INT1** can undergo the hypothetical Friedel–Crafts reaction via **TS-m** (16.3 kcal/mol) to form 8-membered ring **INT2-m** (**Path 1**). For the other putative mechanism shown in **Path 2**, **INT1** goes through seven-membered ring formation via **TS-p** (15.7 kcal/mol) and subsequent 1,2-alkyl shift **TS-R** (9.4 kcal/mol). Potentially owing to ring strain and stabilization from oxonium resonance, arenium **INT2-p** is thermodynamically more stable than **INT2-m**. The alkyl shift of **INT2-p** is energetically feasible, given that the deprotonation step is not attainable from **INT2-p**. These calculations support the anisyl substituent (**13**, **Figure 4.3**) proceeding through either **Path 1** or **Path 2** since  $\Delta\Delta G^\ddagger$  is only 0.6 kcal/mol. Because of the small energy difference between **Path 1** and **Path 2**, we carried out further computations to probe the influence of electronic effects (**Figure 4.4c**).



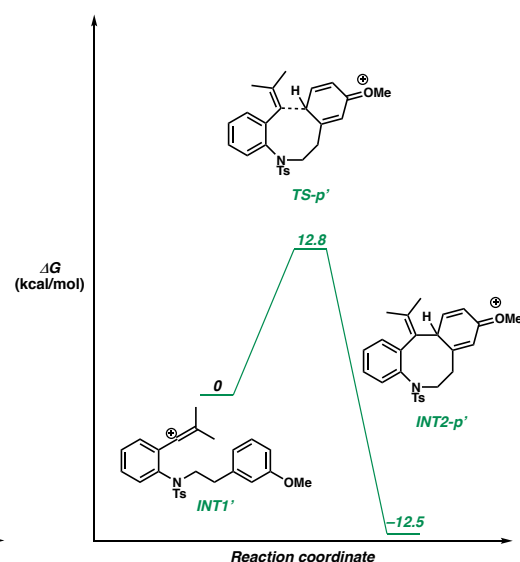
A. Possible mechanistic pathways of the medium-sized ring formation



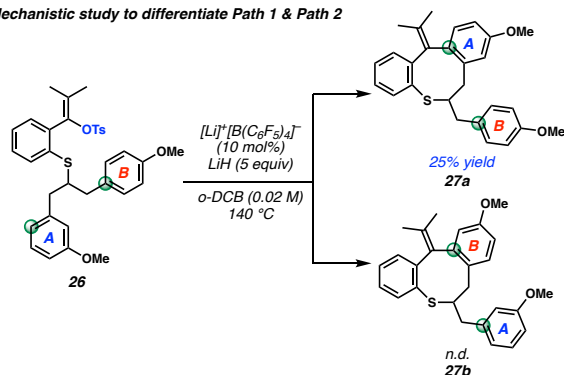
B. Computational studies on 7- vs 8-membered ring formations



C. Influence of -OMe position on 8-membered ring formation



D. Mechanistic study to differentiate Path 1 & Path 2



E. Mechanistic study to differentiate Path 1 & Path 3

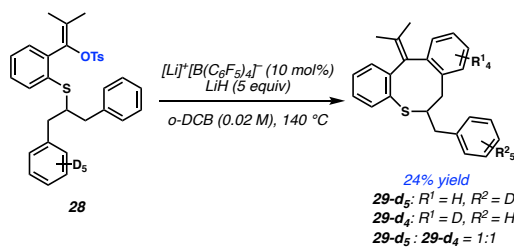


**Figure 4.4** a) Possible mechanistic pathways. b) Computational investigation of the medium-sized ring formation of vinyl cations. c) Influence of -OMe position on the medium-sized ring formation. d) Mechanistic study for Path 1 & Path 2. The yield was determined by NMR with an internal standard. e) Mechanistic study for Path 3. The ratio was determined by FD-MS.

\*All computations were performed with  $\omega$ B97X-D/def2-TZVPP/SMD(*o*-dichlorobenzene) //  $\omega$ B97X-D/def2-SVP/SMD(*o*-dichlorobenzene) at 413.15 K.

Here, we found that the formation of 8-membered ring **INT1'** originating from the electron-rich carbon *para* to methoxy group was considerably favorable relative to both **Path 1** and **Path 2** from **INT1**, suggesting a strong electronic bias in **INT1**. Therefore, vinyl tosylate **26** was designed to experimentally probe the influence of electronic effects on mechanism (**Figure 4.4d**). Tosylate **26** has two aromatic nucleophiles (green balls highlight the most nucleophilic positions). If **Path 1** were operative, arene A would incorporate into the product (**27a**, **Figure 4.4c**). Conversely, if 7-membered ring formation occurred first, as in **Path 2**, ring B would incorporate into the cyclic scaffold (**27b**). Interestingly, tosylate **26** favored the formation of **27a** in 25% yield, although the reaction led to a complex mixture. Various analytical techniques including NMR and LC-MS suggested this was the major cyclization product.

From these calculations and experiments, direct C–H insertion (**Path 3**) could not be excluded. Thus, we prepared vinyl tosylate **28** to probe the feasibility of **Path 3** (**Figure 4.4e**). Under the standard reaction condition, a mixture of **29-d<sub>5</sub>** and **29-d<sub>4</sub>** was obtained with a distribution of roughly 1:1. This result was inconsistent with **Path 3**, where a primary KIE in the putative product-determining step would provide a larger ratio between **29-d<sub>5</sub>** and **29-d<sub>4</sub>**. Overall, the reactions of vinyl tosylates **26** (**Figure 4.4c**) and **28** (**Figure 4.4e**) both support **Path 1** as a potential reaction mechanism, consistent with canonical Friedel–Crafts reactivity.

## 4.5 Conclusion

In conclusion, we have discovered a novel method to access medium-sized rings via vinyl carbocation intermediates. Vinyl tosylates are used as the precursor and ionized into vinyl carbocations under the Li-WCA catalysis system. It is followed by an intramolecular Friedel–

Crafts reaction with aryl nucleophiles to form medium-sized rings. These discoveries further demonstrate the application of vinyl cations in chemical synthesis.

## 4.6 References

- (1) Brown, D. G.; Wobst, H. J. A Decade of FDA-Approved Drugs (2010–2019): Trends and Future Directions. *J. Med. Chem.* **2021**, *64*, 2312–2338.
- (2) Nicolaou, K. C.; Edmonds, D. J.; Bulger, P. G. Cascade Reactions in Total Synthesis. *Angew. Chem. Int. Ed.* **2006**, *45*, 7134–7186.
- (3) Casadei, M. A.; Galli, C.; Mandolini, L. Ring-closure reactions. 22. Kinetics of cyclization of diethyl (.omega.-bromoalkyl)malonates in the range of 4- to 21-membered rings. Role of ring strain. *J. Am. Chem. Soc.* **1984**, *106*, 1051–1056.
- (4) Galli, C.; Illuminati, G.; Mandolini, L.; Tamborra, P. Ring-closure reactions. 7. Kinetics and activation parameters of lactone formation in the range of 3- to 23-membered rings. *J. Am. Chem. Soc.* **1977**, *99*, 2591–2597.
- (5) Gol'dfarb, Y. I.; Belen'kii, L. I. *Russ. Chem. Rev.* **1960**, *29*, 214–235.
- (6) Wiberg, K. B. The Concept of Strain in Organic Chemistry. *Angew. Chem. Int. Ed. Engl.* **1986**, *25*, 312–322.
- (7) Grossel, M. *Alicyclic Chemistry*; Oxford University Press: New York, **2006**, pp. 20–22 and pp. 43–50.
- (8) Shiina, I. Total Synthesis of Natural 8- and 9-Membered Lactones: Recent Advancements in Medium-Sized Ring Formation. *Chem. Rev.* **2007**, *107*, 239–273.
- (9) Hussain, A.; Yousuf, S. K.; Mukherjee, D. Importance and synthesis of benzannulated medium-sized and macrocyclic rings (BMRs). *RSC Adv.* **2014**, *4*, 43241–43257.
- (10) Romines, K. R.; Watenpaugh, K. D.; Tomich, P. K.; Howe, W. J.; Morris, J. K.; Lovasz, K. D.; Mulichak, A. M.; Finzel, B. C.; Lynn, J. C. Use of Medium-Sized Cycloalkyl Rings To

Enhance Secondary Binding: Discovery of a New Class of Human Immunodeficiency Virus (HIV) Protease Inhibitors. *J. Med. Chem.* **1995**, *38*, 1884–1891.

(11) Clarke, A. K.; Unsworth, W. P. A happy medium: the synthesis of medicinally important medium-sized rings *via* ring expansion. *Chem. Sci.* **2020**, *11*, 2876–2881.

(12) Majumdar, K. C. Regioselective formation of medium-ring heterocycles of biological relevance by intramolecular cyclization. *RSC Adv.* **2011**, *1*, 1152–1170.

(13) Yet, L. Metal-Mediated Synthesis of Medium-Sized Rings. *Rev.* **2000**, *100*, 2963–3008.

(14) Popov, S.; Shao, B.; Bagdasarian, A. L.; Benton, T. R.; Zou, L.; Yang, Z.; Houk, K. N.; Nelson, H. M. Teaching an old carbocation new tricks: intermolecular C–H insertion reactions of vinyl cations. *Science* **2018**, *361*, 381–387.

(15) Wigman, B.; Popov, S.; Bagdasarian, A. L.; Shao, B.; Benton, T. R.; Williams, C. G.; Fisher, S. P.; Lavallo, V.; Houk, K. N.; Nelson, H. M. Vinyl carbocations generated under basic conditions and their intramolecular C–H insertion reactions. *J. Am. Chem. Soc.* **2019**, *141*, 9140–9144.

(16) Bagdasarian, A. L.; Popov, S.; Wigman, B.; Wei, W.; Lee, W.; Nelson, H. M. Urea-catalyzed vinyl carbocation formation enables mild functionalization of unactivated C–H bonds. *Org. Lett.* **2020**, *22*, 7775–7779.

(17) Wigman, B.; Lee, W.; Wei, W.; Houk, K. N.; Nelson, H. M. Electrochemical Fluorination of Vinyl Boronates through Donor-Stabilized Vinyl Carbocation Intermediates. *Angew. Chem. Int. Ed.* **2022**, *61*, e202113972.

(18) Nistanaki, S. K.; Williams, C. G.; Wigman, B.; Wong, J. J.; Hass, B. C.; Popov, S.; Werth, J.; Sigman, M. S.; Houk, K. N.; Nelson, H. M. Catalytic asymmetric C–H insertion reactions of vinyl carbocations. *Science*, **2022**, *378*, 1085–1091.

- (19) Yates, K.; Périé, J. Solvolysis of arylvinyl bromides and tosylates. *J. Org. Chem.* **1974**, *39*, 1902–1908.
- (20) Capasso, C.; Supuran, C. T. Sulfa and trimethoprim-like drugs - antimetabolites acting as carbonic anhydrase, dihydropteroate synthase and dihydrofolate reductase inhibitors. *J. Enzym. Inhib. Med. Chem.* **2014**, *29*, 379–387.
- (21) Puccetti, L.; Fasolis, G.; Vullo, D.; Chohan, Z. H.; Scozzafava, A.; Supuran, C. Carbonic anhydrase inhibitors. Inhibition of cytosolic/tumor-associated carbonic anhydrase isozymes I, II, IX, and XII with Schiff's bases incorporating chromone and aromatic sulfonamide moieties, and their zinc complexes. *Bioorg. Med. Chem. Lett.* **2005**, *15*, 3096–3101.
- (22) Standal, J. E. Pizotifen as an antidepressant. *Acta. Psychiatr. Scand.* **1977**, *56*, 276–279.
- (23) Couch, J. R.; Hassanein, R. S. Amitriptyline in migraine prophylaxis. *Arch. Neurol.* **1979**, *36*, 695–699.
- (24) De Bruyne, P.; Christiaens, T.; Boussery, K.; Mehuys, E.; Van Winkel, M. Are antihistamines effective in children? A review of the evidence. *Arch. Dis. Child.* **2017**, *102*, 56–60.
- (25) Metternich, J. B.; Artiukhin, D. G.; Holland, M. C.; von Bremen-Kühne, M.; Neugebauer, J.; Gilmour R. Photocatalytic *E* → *Z* Isomerization of Polarized Alkenes Inspired by the Visual Cycle: Mechanistic Dichotomy and Origin of Selectivity. *J. Org. Chem.* **2017**, *82*, 9955–9977.
- (26) Schubert, W. M.; Sweeney, W. A.; Latourette, H. K. Spectroscopic and Other Properties of Large Ring Mono- and Dimeric Benzocyclanones Prepared by a High-dilution Friedel-Crafts Reaction<sup>1</sup>. *J. Am. Chem. Soc.* **1954**, *76*, 5462–5466.

(27) Jones, C. G.; Martynowycz, M. W.; Hattne, J.; Fulton, T. J.; Stoltz, B. M.; Rodriguez, J. A.; Nelson, H. M.; Gonen, T. The CryoEM Method MicroED as a Powerful Tool for Small Molecule Structure Determination. *ACS Cent. Sci.* **2018**, *4*, 1587–1592.

## CHAPTER FIVE

### Electrochemical Fluorination of Vinyl Boronates Through Donor-Stabilized Vinyl Carbocation Intermediates

#### 5.1 Contributions

This is an author manuscript from the publication: Wigman, B.; Lee, W.; Wei, W.; Houk, K. N.; Nelson, H. M. Electrochemical Fluorination of Vinyl Boronates Through Donor-Stabilized Vinyl Carbocation Intermediates. *Angew. Chem. Int. Ed.* **2022**, *61*, e202113972.

<https://doi.org/10.1002/anie.202113972>. As a computational organic chemist, I carried out all computational experiments while Benjamin Wigman performed the majority of the experimental work. Benjamin Wigman received experimental assistance from Wenjing Wei.

#### 5.2 Abstract

The electrochemical generation of vinyl carbocations from alkenyl boronic esters and boronates is reported. Using easy-to-handle nucleophilic fluoride reagents, these intermediates are trapped to form fully substituted vinyl fluorides. Mechanistic studies support the formation of dicoordinated carbocations through sequential single-electron oxidation events. Notably, this electrochemical fluorination features fast reaction times and Lewis-acid free conditions. This transformation provides a complementary method to access vinyl fluorides with simple fluoride salts such as TBAF.

#### 5.3 Introduction



Carbocations, a common synthon in synthetic organic chemistry logic, have been studied for more than 100 years.<sup>1</sup> While the reactivities and properties of alkyl carbocations have been the main focus of these studies, highly reactive vinyl carbocations and their ensuing bond-forming reactions have been the subject of far fewer research efforts. Nonetheless, vinyl cations have been isolated and characterized in the solid state,<sup>2a,b</sup> revealing their remarkable linear geometry, and have been generated by a variety of conditions including solvolysis,<sup>2c</sup> photolysis,<sup>2d-f</sup> leaving group abstraction,<sup>2g-j</sup> and alkyne protonation/transition metal-activation.<sup>2k,l</sup> With the exceptions of photolysis, which requires high energy UV light, and solvolysis which requires high temperatures, vinyl cation generation often relies on potent Lewis or Brønsted acids that can be poisoned by heteroatoms and requires rigorous air-free handling. At the outset of the current study, we hypothesized that these reactive intermediates could instead be generated via consecutive single-electron oxidation events, analogous to the Hofer-Moest electrochemical oxidation of alkyl carboxylates to alkyl carbocations (**Figure 5.1a**).<sup>3a,b</sup>

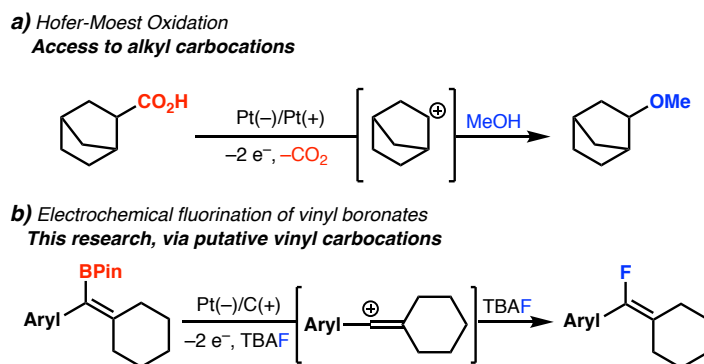


**Figure 5.1** Previous work and this study. a) Hofer-Moest electrochemical oxidation. b) this research: electrochemical fluorination of alkenyl boronates via vinyl carbocations.

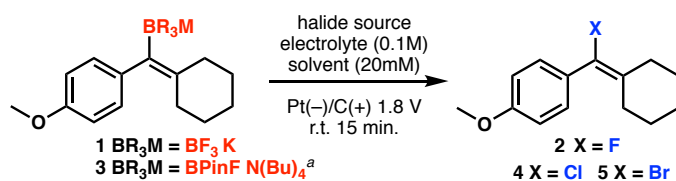
Electrochemical oxidation has become a powerful strategy to generate a variety of reactive cationic intermediates, as is demonstrated in the cation pool method.<sup>3c,d</sup> This unconventional approach to generating these high-energy species could allow for milder and less stringent reaction conditions, perhaps enabling the discovery of new chemical transformations. Here, we

report our initial studies in this area, where alkenyl boronates are converted to vinyl fluorides electrochemically through nucleophilic trapping of vinyl carbocation intermediates (**Figure 5.1b**). While vinyl fluorides have well established syntheses, including but not limited to Wittig olefination reactions, addition to alkynes and allenes, and transition metal-catalyzed cross-coupling reactions, we believe this report serves as a complementary and potentially divergent method to gain access to a variety of vinyl halides as well as other olefinic products due to the vinyl carbocation generated.<sup>4</sup>

#### 5.4 Results and Discussion

Inspired by the Hofer-Moest oxidation and reports of generation of alkyl carbocations from redox-active esters,<sup>3,5</sup> attempts at oxidation of carboxylate derivatives by means of various photochemical, electrochemical, and chemical processes provided intractable mixtures of products that gave no evidence for vinyl carbocation formation.<sup>6</sup> We turned to other redox active groups, particularly trifluoroborates (**Table 5.1**) since these are known to undergo single electron oxidation.<sup>7</sup> We were gratified to find that electrolysis in an undivided cell of vinyl trifluoroborate **1** with a platinum cathode and carbon anode at a constant working potential of +1.8V vs SCE in dichloromethane (DCM) with tetrabutylammonium fluoride trihydrate (TBAF) as a trapping agent produced vinyl fluoride **2** in 42% yield by <sup>19</sup>F NMR (**Table 5.1**, entry 1) after only 15 minutes. The styrenyl position was key for reactivity, as non-styrenyl boronates were not competent for this transformation.<sup>6</sup> In this solvent, however, the vinyl chloride product was also observed in 20% yield by <sup>1</sup>H NMR, presumably from reduction of DCM to produce the chloride anion. Switching the solvent to tetrahydrofuran (THF) or dimethylformamide (DMF) (entries 2,3) led to trace or no product respectively; ultimately use of acetonitrile (MeCN) yielded vinyl

fluoride **2** in 65% isolated yield with no vinyl chloride impurity (entry 4). We also examined vinyl pinacol boronate **3**, as more electron-rich boronates have been demonstrated to have a profound effect on the oxidation potential of the substrate.<sup>8</sup> Pinacol boronate (BPinF) **3** was generated *in situ* from the starting pinacol boronic ester: <sup>11</sup>B NMR studies indicated that the boronate was fully formed in solution with 3 equivalents of TBAF.<sup>6</sup> We believe the anionic boronate complex to be the redox active intermediate, as without this fluoride additive no reaction occurs. Subjecting this pinacol boronate (**3**) to the reaction conditions yielded vinyl fluoride **2** in a slightly increased 70% isolated yield (entry 5). Other electrolytes, fluoride sources, and equivalents of TBAF led to diminished yield (entries 6–12). The remaining mass balances for these reactions are ketone and enone products, the latter presumably arising from oxidation of the ketone, which we attribute to water quenching of a vinyl carbocation intermediate.<sup>6</sup> It is noteworthy that this reaction does not need to be carried out under rigorously anhydrous conditions, likely due to the high nucleophilicity of the fluoride anion. We believe water to serve as the sacrificial oxidant, and attempts to perform the reaction under water-free conditions resulted in incomplete conversion of the starting material (entry 13). Importantly, we found that analogous conditions could be used to produce vinyl chloride **4** and bromide **5** simply by substituting TBAF with TBACl or TBABr (entries 14,15).<sup>6</sup> With these results in hand, we began to explore the scope of this reaction. Initial efforts focused on utilizing electron rich arenes, such as the *p*-anisole substituent of boronate **3**, that would stabilize putative carbocation intermediates. Strongly electron-donating substituents produced vinyl fluorides **6–9** in 50–82% yield (**Figure 5.2**).



Entry	Starting Material	Solvent	Electrolyte (0.1 M)	Halide Source (equiv)	Yield
1	1	DCM	TBABF <sub>4</sub>	TBAF•(H <sub>2</sub> O) <sub>3</sub> (5 equiv)	42% <sup>b</sup>
2	1	THF	TBABF <sub>4</sub>	TBAF•(H <sub>2</sub> O) <sub>3</sub> (5 equiv)	<5% <sup>b</sup>
3	1	DMF	TBABF <sub>4</sub>	TBAF•(H <sub>2</sub> O) <sub>3</sub> (5 equiv)	n.d.
4	1	MeCN	TBABF <sub>4</sub>	TBAF•(H <sub>2</sub> O) <sub>3</sub> (5 equiv)	65%
5	3	MeCN	TBABF <sub>4</sub>	TBAF•(H <sub>2</sub> O) <sub>3</sub> (5 equiv)	70%
6	3	MeCN	TBABF <sub>4</sub>	TBAF•(H <sub>2</sub> O) <sub>3</sub> (3 equiv)	62%
7	3	MeCN	TBABF <sub>4</sub>	TBAF•(H <sub>2</sub> O) <sub>3</sub> (2 equiv)	50%
8	3	MeCN	TBABF <sub>4</sub>	TMAF•(H <sub>2</sub> O) <sub>4</sub> (5 equiv)	49%
9	3	MeCN	TBABF <sub>4</sub>	TBAF•(tBuOH) <sub>4</sub> (5 equiv)	58%
10	3	MeCN	TBABF <sub>4</sub>	KF+18-Crown-6 (10 equiv)	n.d.
11	3	MeCN	TBABF <sub>4</sub>	TBAT (5 equiv)	40% <sup>b</sup>
12	3	MeCN	TBAPF <sub>6</sub>	TBAF•(H <sub>2</sub> O) <sub>3</sub> (5 equiv)	54% <sup>b</sup>
13	3	MeCN	TBABF <sub>4</sub>	TBAF•(H <sub>2</sub> O) <sub>3</sub> (5 equiv)	19% <sup>b,c</sup>
14	3	MeCN	TBABF <sub>4</sub>	TBACl (6 equiv)	68%
15	1	MeCN	TBABr	—	57%

**Table 5.1** Optimization of fluorination from vinyl trifluoroborate **1** and pinacol boronate **3**. Isolated yields. <sup>a</sup>Formed *in situ* from the pinacol boronic ester. <sup>b</sup><sup>19</sup>F NMR yield with fluorobenzene as an internal standard. <sup>c</sup>Added 50 mg mol sieves, MeCN distilled over CaH<sub>2</sub> and dried over mol sieves. TBAT=tetrabutyl ammonium difluorotriphenyl silicate, TMAF=tetramethyl ammonium fluoride. n.d.=not detected.

Vinyl fluoride **7** was also isolated in good yield utilizing only three equivalents of TBAF on 1 mmol scale. Alkenyl boronic esters bearing *meta* substituents and an *ortho* or *para* donor were also tolerated, yielding vinyl fluorides **10** and **11** in 59% and 47% yield respectively.

Additionally, novel fluoro-analogue **12** of chlorotrianisene, a nonsteroidal estrogen,<sup>9a</sup> was generated in 60% yield. Other appended ring sizes and alkyl chains also led to production of the vinyl fluoride (**13–16**). Constant voltage conditions were key to produce electron-rich aniline fluoride product **16**.

Less electron donating substituents were tolerated, but led to incomplete conversion even at higher applied potentials (**17–19**). Notably, these N–H containing compounds are not tolerated under routine Lewis acid promoted vinyl carbocation formation, but are commonly seen in natural products and drug molecules.<sup>2,9b</sup> The boronic ester bearing a simple phenyl ring did not lead to formation of vinyl fluoride **20**, even under forcing conditions.

Throughout our scope studies we observed that only electron-rich arenes were competent in this transformation. Yields increased with decreasing Hammett  $\sigma_p$  parameter, suggesting that there was a carbocation formed at the carbon once bearing the boronic ester. The trend of decreasing yield, **6**>**13**>**17**>**19**, with corresponding  $\sigma_p$  values of  $-0.81 < -0.27 < -0.17 < 0.00$  for the respective *para* donor substituents, was observed.<sup>10</sup> Additionally, if a *meta*-methoxy group were present on the arene, an electron-withdrawing substituent with  $\sigma_m = +0.12$ , **21** was not formed.<sup>6,10</sup> This trend suggested the formation of a carbocation intermediate, and so we carried out further mechanistic studies to investigate the intermediacy of a vinyl carbocation.

First we probed for canonical vinyl carbocation reactivity. One classic mode of reactivity of vinyl carbocations is E1 elimination to form alkyne products.<sup>11</sup> Upon subjection of vinyl boronic ester **22** to the reaction conditions, alkyne **23**, the product of E1 elimination of putative vinyl carbocation **24**, was observed in moderate yield (**Figure 5.3a**). A similar elimination occurs with trisubstituted alkenyl boronic esters to yield alkyne.<sup>6</sup> This does however limit the substrates for fluorination to tetrasubstituted alkenyl boronates.

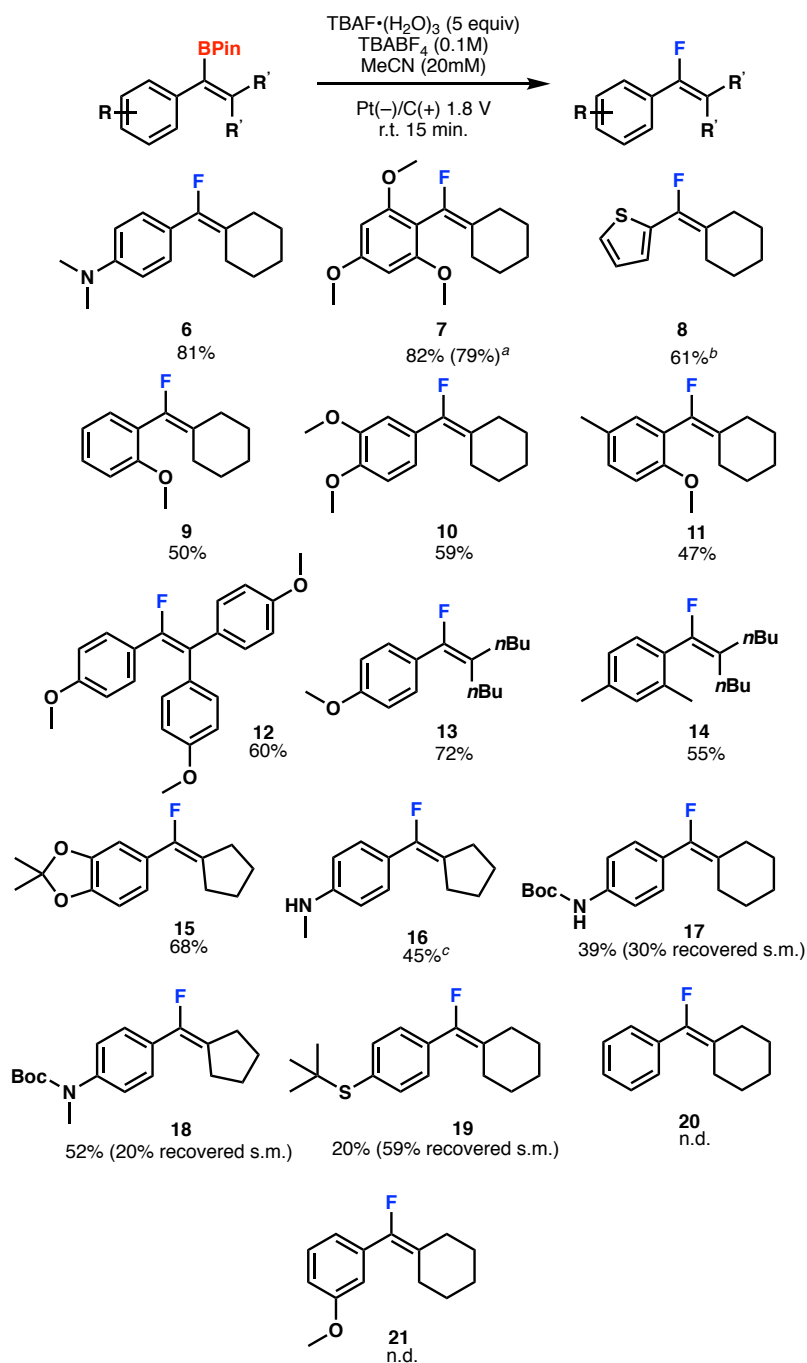


**Figure 5.2** Scope of alkenyl boronic ester electrochemical fluorination. Isolated yields. <sup>a</sup>3 equiv of TBAF on 1 mmol scale. <sup>b</sup>Isolated as a 9:1 mixture of fluoride:styrene. <sup>c</sup>+0.8 V vs SCE. n.d.=not detected.

In order to rule out production of this alkyne from a vinyl fluoride intermediate, styrenyl fluoride **25** was prepared and subjected to the reaction conditions. No conversion to the alkyne was observed and the starting material was recovered in quantitative yield.

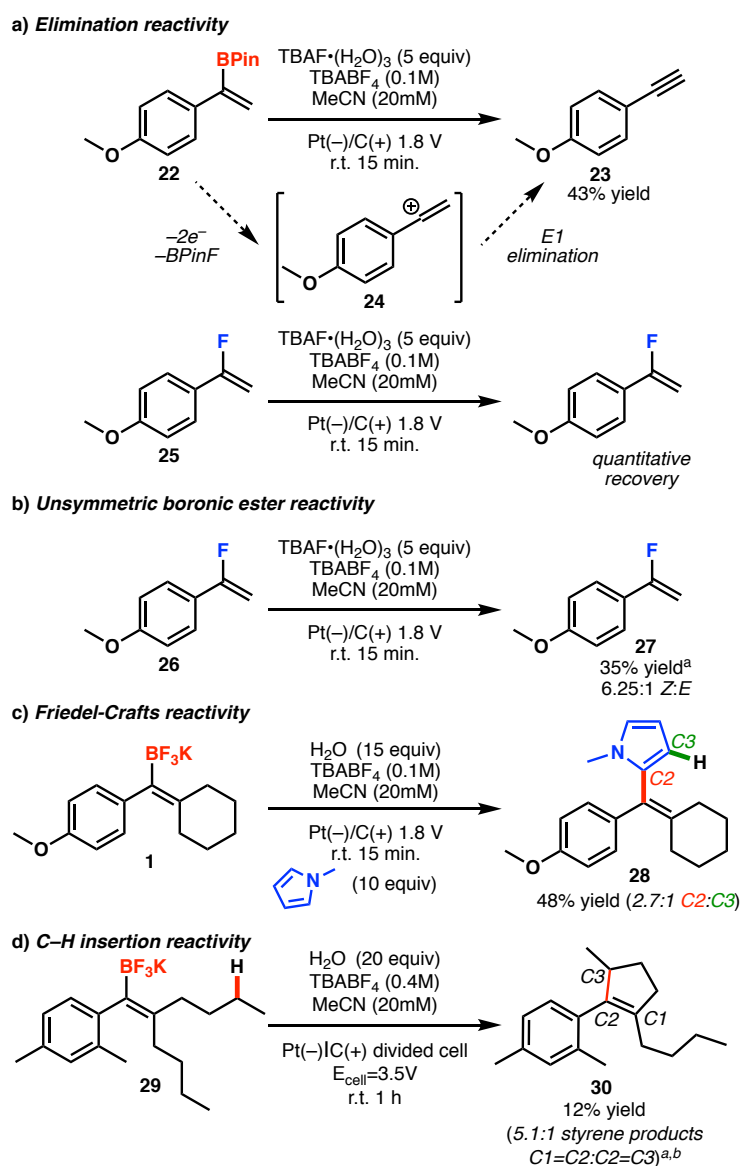


**Figure 5.3** Mechanistic experiments to probe for vinyl carbocation reactivity. a) Elimination reactivity suggesting vinyl carbocation intermediate. b) Unsymmetric alkenyl boronic ester reactivity. c) Friedel-Crafts reactivity with N-Me pyrrole. d) C–H Insertion reactivity. Isolated yields. <sup>a</sup>Yield determined by <sup>1</sup>H NMR with an internal standard. <sup>b</sup>Ratio of styrene olefin isomers determined by GC-FID.

To probe the intermediacy of a linear vinyl carbocation intermediate, unsymmetric alkenyl boronic ester **26** was prepared as a single isomer. Subjection of this material to the reaction conditions yielded a mixture of *Z:E* vinyl fluoride products **26** in a 6.25:1 ratio (**Figure 5.3b**) This supports fluoride nucleophilic attack of a linear intermediate as opposed to other stereo retentive pathways.

Vinyl carbocations are also known to undergo C–C bond forming reactions with arene nucleophiles.<sup>2,11</sup> To explore Friedel-Crafts reactivity, **1** was subjected to the reaction conditions in the presence of 10 equivalents of electron rich N-Me pyrrole instead of TBAF. Pyrrole nucleophiles have been observed to trap similar *p*-anisole substituted vinyl carbocations generated by photolysis.<sup>2d</sup> In the event, arylated products **28** were produced in a 2.7:1 ratio in 48% yield (**Figure 5.3c**). This product ratio further supports a vinyl carbocation intermediate as opposed to a radical intermediate, as such radical additions are reported to exclusively form C2 addition products.<sup>12</sup>

C–C bond forming reactions via intramolecular C–H insertion reactions have also been observed in several studies of vinyl carbocations.<sup>2g-k</sup> In order to probe for this type of reactivity the trifluoroborate salt **29** with appended alkyl chains was prepared and subjected to electrolysis in a divided cell. In the presence of fluoride these products were not observed, and so the pre-activated trifluoroborate was used. Gratifyingly, we observed production of the C–H insertion products **30** as a mixture of olefin isomers, albeit in low yield (**Figure 5.3d**). This diminished yield is due to the subsequent decomposition of the electron-rich tetrasubstituted styrene products under the oxidative conditions.<sup>6</sup>

To further investigate the mechanistic pathway to the proposed vinyl carbocation we performed cyclic voltammetry experiments. The tetrabutylammonium salt of **1** showed two irreversible



oxidative events at +1.12 V and +1.56 V vs SCE (**Figure 5.4a**).<sup>6</sup> This experiment demonstrated evidence for a two-electron oxidation process; additionally, bulk electrolysis coulometry at a constant potential of 1.8 V vs SCE further confirmed this with a calculated Faradaic efficiency for two-electrons per boronate substrate of 73%.<sup>6</sup>

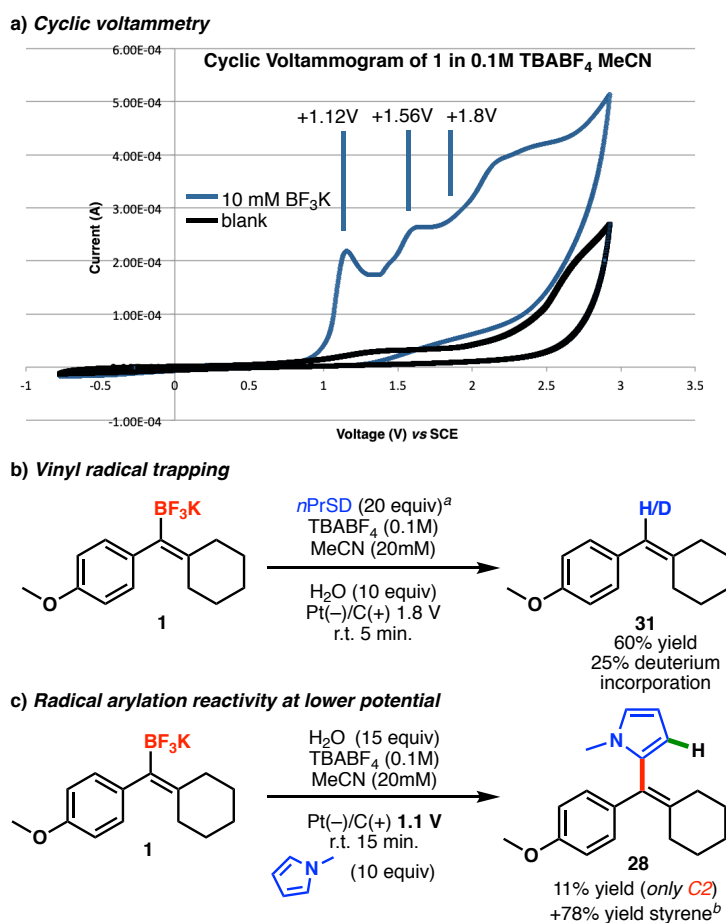


**Figure 5.4** Mechanistic experiments to probe for vinyl radical intermediate. a) Cyclic voltammogram of the tetrabutylammonium salt of **1** in 0.1 M TBABF<sub>4</sub> MeCN at 100 mV/s. First and second oxidative waves and +1.8 V of typical reaction highlighted. b) Styrene products observed in the presence of *n*PrSD. c) Change of arylation regioselectivity at lower applied potential. <sup>a</sup>Propane thiol prepared at 77% deuteration as determined by <sup>1</sup>H NMR. <sup>b</sup>Yields determined by <sup>1</sup>H NMR with an internal standard. *n*PrSD=deuterium incorporated *n*-propyl thiol.

We hypothesized that the initial oxidation would yield a vinyl radical, as is proposed for the oxidation of a variety alkyl trifluoroborates.<sup>13</sup> In order to probe for this intermediate,

trifluoroborate **1** was subjected to the reaction conditions in the presence of deuterated H/D-atom donor propane thiol (**Figure 5.4b**). Deuterium incorporation exclusively at the styrene position (**31**) was observed supporting the intermediacy of a vinyl radical. To determine if this radical intermediate was generated at the lower potential, trifluoroborate **1** was subjected to constant voltage electrolysis in the presence of N-methyl pyrrole at +1.1 V vs SCE (**Figure 5.4c**).

At this potential different regioselectivity was observed compared to at +1.8 V (**Figure 5.3b**); only the C2 arylation product was observed suggesting the presence of a radical.<sup>12</sup> Furthermore, at this lower potential no vinyl fluoride products were observed in the presence of TBAF.<sup>5</sup>

With these combined experiments supporting the intermediacy of a vinyl radical after the first oxidation at +1.1 V vs SCE, we propose the sequential ECE-type oxidation mechanism in **Figure 5.5**. DFT calculations were performed to further understand the initial oxidation event. Initial *in silico* oxidation of the calculated HOMO of trifluoroborate anion **32** yielded delocalized radical cation **33**, in good agreement with experimental data at a calculated potential of +1.04 V vs SCE (**Figure 5.5a**). We propose that this can subsequently eliminate BF<sub>3</sub> to yield vinyl radical **34** that undergoes a second oxidation to yield vinyl carbocation **35** (**Figure 5.5b**). In the case of the pinacol boronic esters, an equivalent of BPin-F is produced that was observed by <sup>19</sup>F and <sup>11</sup>B NMR.<sup>6</sup> This carbocation intermediate can be trapped by nucleophilic fluoride in solution to furnish vinyl fluoride product **2**.

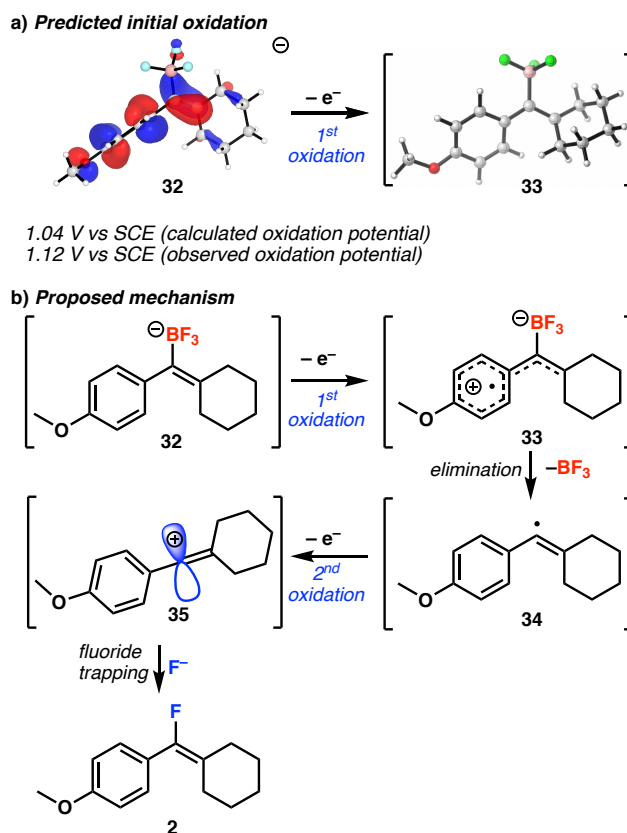


**Figure 5.5** a) Predicted initial oxidation. b) Proposed mechanism of boronate fluorination. Calculated HOMO and oxidation potential using (uM06-2X/6-311++G(d,p) cpcm=acetonitrile // uM06-2X/6-31+G(d,p) cpcm=acetonitrile).

## 5.5 Conclusion

In conclusion, we report the novel generation of vinyl carbocations via a mild electrochemical potential; from a synthetic standpoint the products of these reactions have potential application in medicinal chemistry. Vinyl fluorides have been demonstrated to be effective enol mimics,<sup>14</sup> are considered bioisosteres of the peptide bond,<sup>15</sup> and fluorinated drug compounds can often display exquisite pharmacokinetic properties and binding affinity compared to the parent C–H containing compound.<sup>16</sup> While there are several reports of conversion of aryl boronates to aryl fluorides, these reaction conditions commonly rely on the use of electrophilic fluorine reagents and silver salts.<sup>17</sup> The use of easy-to-handle nucleophilic fluoride reagents has recently been reported

for generation of aryl fluorides from aryl boronates, but there are few examples of the conversion of alkenyl boronates to vinyl fluorides.<sup>17,18</sup> Moreover, vinyl fluorides are often synthesized from alkynes, yielding di- or tri-substituted alkene products, while methods to access fully substituted vinyl fluorides typically require prefunctionalized fluorination reagents.<sup>4,19,20</sup> This electrochemical method features short reaction times in moderate to good yield. Additionally, mechanistic studies support the intermediacy of a vinyl radical followed by a second oxidation to a vinyl cation; this evidence suggests that electrochemical oxidation may be a viable strategy to access dicoordinate vinyl carbocations, emerging intermediates in organic synthesis.<sup>21</sup>

## 5.6 References

- (1) (a) Olah, G. A. 100 Years of carbocations and their significance in chemistry. *J. Org. Chem.* **2001**, *66*, 5943–5957. (b) Naredla, R. R.; Klumpp, D. A. Contemporary carbocation chemistry: applications in organic synthesis. *Chem. Rev.* **2013**, *113*, 6905–6948.
- (2) (a) Müller, T.; Juhasz, M.; Reed, C. A. The X-ray structure of a vinyl cation. *Angew. Chem., Int. Ed.* **2004**, *43*, 1543–1546. (b) Bismuto, A.; Nichol, G. S.; Duarte, F.; Cowley, M. J.; Thomas, S. P. Characterization of the zwitterionic intermediate in 1,1-carboboration of alkynes. *Angew. Chem., Int. Ed.* **2020**, *59*, 12731–12735. (c) Pfeifer, W. D.; Bahn, C. A.; Schleyer, P. v. R.; Bocher, S.; Harding, E. C.; Hummel, K.; Hanack, M.; Stang, P. J. Behavior of bent vinyl cations generated by solvolysis of cyclic trifluoromethanesulfonates. *J. Am. Chem. Soc.* **1971**, *93*, 1513–1516. (d) Byrne, P. A.; Kobayashi, S.; Würthwein, E. –U.; Ammer, J.; Mayr, H. Why are vinyl cations sluggish electrophiles? *J. Am. Chem. Soc.* **2017**, *139*, 1499–1511. (e) Kitamura, T.; Kobayashi, S.; Taniguchi, H. Photochemistry of vinyl halides. Vinyl cation from photolysis of 1,1-diaryl-2-halopropenes. *J. Org. Chem.* **1982**, *47*, 2323–2328. (f) Slegt, M.; Grohnheid, R.; van der Vlugt, D.; Ochiai, M.; Okuyama, T.; Zuilhof, H.; Overkleeft, H. S.; Loder, G. Photochemical generation of six- and five-membered cyclic vinyl cations. *J. Org. Chem.* **2006**, *71*, 2227–2235. (g) Biermann, U.; Koch, R.; Metzger, J. O. Intramolecular concerted insertion of vinyl cations into C–H bonds: hydroalkylating cyclization of alkynes with alkyl chloroformates to give cyclopentanes. *Angew. Chem., Int. Ed.* **2006**, *45*, 3076–3079. (h) Cleary, S. E.; Hensinger, M. J.; Brewer, M. Remote C–H insertion of vinyl cations leading to cyclopentenones. *Chem. Sci.* **2017**, *8*, 6810–6814. (i) Popov, S.; Shao, B.; Bagdasarian, A. L.; Benton, T. R.; Zou, L.; Yang, Z.; Houk, K. N.; Nelson, H. M. Teaching an old carbocation new tricks: intermolecular C–H insertion reactions of vinyl cations. *Science* **2018**, *361*, 381–387. (j) Wigman, B.; Popov, S.;

Bagdasarian, A. L.; Shao, B.; Benton, T. R.; Fisher, S. P.; Lavallo, V.; Houk, K. N.; Nelson, H. M. Vinyl carbocations generated under basic conditions and their intramolecular C–H insertion reactions. *J. Am. Chem. Soc.* **2019**, *141*, 9140–9144. (k) Zhang, F.; Das, S.; Walkinshaw, A. J.; Casitas, A.; Taylor, M.; Suero, M. G.; Gaunt, M. J. Cu-catalyzed cascades to carbocycles: union of diaryliodonium salts with alkenes and or alkynes exploiting remote carbocations. *J. Am. Chem. Soc.* **2014**, *136*, 8851–8854. (l) Schroeder, S.; Strauch, C.; Gaelings, N.; Niggemann, M. Vinyl triflimides—a case of assisted vinyl cation formation. *Angew. Chem., Int. Ed.* **2019**, *58*, 5119–5123.

(3) (a) Hofer, H.; Moest, M. Mitteilung aus dem electrochemischen laboratorum der königl, technischen hochschule zu münchen. *Justus Liebigs Ann. Chem.* **1902**, *323*, 284–323. (b) Corey, E. J.; Bauld, N. L.; La Londe, R. T.; Casanova, J. Jr.; Kaiser, E. T. Generation of cationic carbon by anodic oxidation of carboxylic acids. *J. Am. Chem. Soc.* **1960**, *82*, 2645–2646. (c) Yoshida, J.-I.; Shimizu, A.; Hayashi, R. Electrogenenerated cationic reactive intermediates: the pool method and further advances. *Chem. Rev.* **2018**, *118*, 4702–4730. (d) Okajima, M.; Soga, K.; Nokami, T.; Suga, S.; Yoshida, J.-I. Oxidative generation of diarylcarbenium ion pools. *Org. Lett.* **2006**, *8*, 5005–5007.

(4) (a) Lei, X.; Dutheuil, G.; Pannecoucke, X.; Quirion, J.-C. A facile and mild method for the synthesis of terminal bromofluoroolefins via diethylzinc-promoted Wittig reaction. *Org. Lett.* **2006**, *8*, 5005–5007. (b) Pomeisl, K.; Cejka, J.; Kvicala, J.; Paleta, O. Synthesis of 3-fluorofuran-2(5H)-ones based on *Z/E* photoisomerisation and cyclisation of 2-fluoro-4-hydroxybut-2-enoates. *Eur. J. Org. Chem.* **2007**, 5917–5925. (c) Van der Veken, P.; Kertesz, I.; Senten, K.; Haemers, A.; Augustyns, K. Synthesis of (*E*)- and (*Z*)-fluoro-olefin analogues of potent dipeptidyl peptidase IV inhibitors. *Tetrahedron Lett.* **2003**, *44*, 6231–6234. (d) Zapata, A. J.; Gu,

Y. H.; Hammond, G. B. The first  $\alpha$ -fluoroallenylphosphonate, the synthesis of conjugated fluoroenynes, and the stereoselective synthesis of vinylfluorophosphonates using a new multifunctional fluorine-containing building block. *J. Org. Chem.* **2000**, *65*, 227–234. (e) Chevrie, D.; Lequeux, T.; Demoute, J. P.; Pazenok, S. A convenient one-step synthesis of fluoroethylidene derivatives. *Tetrahedron Lett.* **2003**, *44*, 8127–8130. (f) Zhu, L. G.; Ni, C. F.; Zhao, Y. C.; Hu, J. B. 1-*tert*-Butyl-1*H*-tetrazol-5-yl fluoromethyl sulfone (TBTSO<sub>2</sub>CH<sub>2</sub>F): a versatile fluoromethylidene synthon and its use in the synthesis of monofluorinated alkenes via Julia–Kocienski olefination. *Tetrahedron* **2010**, *66*, 5089–5100. (g) Ghosh, A. K.; Banerjee, S.; Sinha, S.; Kang, S. B.; Zajc, B.  $\alpha$ -Fluorovinyl Weinreb amides and  $\alpha$ -fluoroenones from a common fluorinated building block. *J. Org. Chem.* **2009**, *74*, 3689–3697. (h) Lin, J.; Welch, J. T. The stereoselective construction of fluoroalkenoates via the Peterson olefination reaction using *tert*-butyl  $\alpha$ -fluoro- $\alpha$ -(trialkylsilyl)acetates. *Tetrahedron Lett.* **1998**, *39*, 9613–9616. (i) Yoshimatsu, M.; Murase, Y.; Itoh, A.; Tanabe, G.; Muraoka, O. *Z*-selective or stereospecific alkenylation reaction: a novel synthetic method for  $\alpha$ -fluoro- $\alpha,\beta$ -unsaturated esters. *Chem. Lett.* **2005**, *34*, 998–999. (j) Usuki, Y.; Iwaoka, M.; Tomoda, S. A new synthesis of  $\alpha$ -fluoro- $\alpha,\beta$ -unsaturated ketones and esters based on organoselenium methodology. *J. Chem. Soc. Chem. Commun.* **1992**, 1148–1150. (k) Sano, K.; Fukuhara, T.; Hara, S. Regioselective synthesis of  $\beta$ -fluoro- $\alpha,\beta$ -unsaturated ketones by the reaction of  $\beta$ -diketones with DFMB. *J. Fluorine Chem.* **2009**, *130*, 708–713. (l) Dolensky, B.; Kirk, K. L. New Building Blocks for Fluorinated Bioimidazole Derivatives II: Preparation of  $\beta$ -Fluorouracanic Acids. *J. Org. Chem.* **2002**, *67*, 3468–3473. (m) Landelle, G.; Champagne, P. A.; Barbeau, X.; Paquin, J.-F. Stereocontrolled approach to bromofluoroalkenes and their use for the synthesis of tri- and tetrasubstituted fluoroalkenes. *Org. Lett.* **2009**, *11*, 681–684. (n) Dutheil, G.; Couve-Bonnaire, S.; Pannecoucke,

X. Synthesis of tetrasubstituted  $\alpha$ -fluoroenones. *Tetrahedron* **2009**, *65*, 6034–6038. (o) Luo, H. Q.; Hu, X. H.; Loh, T.-P. Highly stereocontrolled synthesis of fluorinated 2,6-*trans* dihydropyrans via Prins cyclization. *Tetrahedron Lett.* **2010**, *51*, 1041–1043. (p) for an in depth review see: Landelle, G.; Bergeron, B.; Turcotte-Savard, M.-O.; Paquin, J.-F. Synthetic approaches to monofluoroalkenes. *Chem. Soc. Rev.* **2011**, *40*, 2867–2908.

(5) Webb, E. W.; Park, J. B.; Cole, E. L.; Donnelly, D. J.; Bonacorsi, S. J.; Ewing, W. R.; Doyle, A. G. Nucleophilic (radio)fluorination of redox-active esters via radical polar crossover enabled by photoredox catalysis. *J. Am. Chem. Soc.* **2020**, *142*, 9493–9500.

(6) See Supplementary Information for details in the adapted article.

(7) (a) Suzuki, J.; Tanigawa, M.; Inagi, S.; Fuchigami, T. Electrochemical oxidation of organotrifluoroborate compounds. *ChemElectroChem*, **2016**, *3*, 2078–2083. (b) Horris, J. H.; Gysling, H. J.; Reed, D. Electrochemistry of boron compounds *Chem. Rev.* **1985**, *85*, 51–76. (c) Molander, G. A.; Colombel, V.; Braz, V. A. Direct alkylation of heteroaryls using potassium alkyl and alkoxymethyltrifluoroborates. *Org. Lett.* **2011**, *13*, 1852–1855. (d) Neufeldt, S. R.; Seigerman, C. K.; Sanford, M. S. Mild palladium-catalyzed C–H alkylation using potassium alkyltrifluoroborates in combination with MnF<sub>3</sub>. *Org. Lett.* **2013**, *15*, 2302–2305. (e) Lee, H. G.; Chung, T. D.; Go, S. Y.; Chung, H.; Shin, S. J.; An, S.; Youn, J. H.; Im, T. Y.; Kim, J. Y. A unified synthetic strategy to introduce heteroatoms via electrochemical functionalization of alkyl organoboron reagents. *ChemRxiv*. **2021**, <https://doi.org/10.33774/chemrxiv-2021-bvfl1>.

(8) Lennox, A. J. J.; Nutting, J. E.; Stahl, S. S. Selective electrochemical generation of benzylic radicals enabled by ferrocene-based electron transfer mediators. *Chem. Sci.* **2018**, *9*, 356–361.

(9) (a) Luniwal, A.; Jetson, R.; Erhardt, P. *Analogue-based drug discovery*. Wiley:Hoboken, 2012; pp. 165–185. (b) Kerru, N.; Gummidi, L.; Maddila, S.; Gangu, K. K.; Jonnalagadda, S. B.



A Review on Recent Advances in Nitrogen-Containing Molecules and Their Biological Applications *Molecules* **2020**, *25*, 1909.

(10) Hansch, C.; Leo, A.; Taft, R. W. A survey of Hammett substituent constants and resonance and field parameters. *Chem. Rev.* **1991**, *91*, 165–195. (Note:  $\sigma_p$  value for –SMe and –NHCO<sub>2</sub>Me substituents used)

(11) (a) Stang, P. J.; Rappoport, Z.; Hanack, M.; Subramanian, L. R. *Vinyl Cations*; Academic Press, 1979. (b) Rappoport, Z.; Shulman, P.; Thuval, M. Vinylic cations from solvolysis. 26. Solvolysis of 9-( $\alpha$ -chlorovinyl)anthracene and selectivity of the derived ion. *J. Am. Chem. Soc.* **1978**, *100*, 7041–4051.

(12) (a) Kocaoğlu, E.; Karaman, M. A.; Tokogöz, H.; Talaz, O. Transition-metal catalyst free oxidative radical arylation of N-methylpyrrole. *ACS Omega*, **2017**, *2*, 5000–5004. (b) Li, Z.; Gandon, V.; Bour, C. Bimolecular vinylation of arenes by vinyl cations. *Chem. Comm.* **2020**, *56*, 6507–6510. (c) Suleymanov, A. A.; Doll, M.; Ruggi, A.; Scopelliti, R.; Fadaei-Tirani, F. Synthesis of tetraarylethene luminogens by C–H vinylation of aromatic compounds with triazenes. *Angew. Chem., Int. Ed.* **2019**, *59*, 9957–9961.

(13) Matsui, J. K.; Lang, S. B.; Heitz, D. R.; Molander, G. A. Photoredox-mediated routes to radicals: the value of catalytic radical generation in synthetic methods development. *ACS Catal.* **2017**, *7*, 2563–2575.

(14) Burkhardt, J. P.; Weintraub, P. M.; Gates, C. A.; Resvick, R. J.; Vaz, R. J.; Friedrich, D.; Angelastro, M. R.; Bey, P.; Peet, N. P. Novel steroidal vinyl fluorides as inhibitors of steroid C<sub>17(20)</sub> lyase. *Bioorg. Med. Chem.* **2002**, *10*, 929–934.

(15) (a) Wermuth, C. G.; Aldous, D.; Raboisson, P.; Rognan, D. *The practice of medicinal chemistry*. 4<sup>th</sup> edition; Academic Press: Oxford, 2015; pp. 210–212. (b) Chandrakumar, N. S.;

Yonan, P. K.; Stapelfeld, A.; Svage, M.; Rorbacher, E.; Contreras, P. C.; Hammond, D. Preparation and opioid activity of analogues of the analgesic dipeptide 2,6-dimethyl-1-tyrosyl-N-(3-phenylpropyl)-D-alaninamide. *J. Med. Chem.* **1992**, *35*, 223–233.

(16) (a) Wang, J.; Roselló, M. S.; Aceña, J. L.; Pozo, C. D.; Sorochinsky, A. E.; Fustero, S.; Soloshonok, V. A.; Liu, H. Fluorine in pharmaceutical industry: fluorine-containing drugs introduced to the market in the last decade (2001-2011). *Chem. Rev.* **2014**, *114*, 2432–2506. (b) Meanwell, N. A. Fluorine and fluorinated motifs in the design and application of bioisosteres for drug design. *J. Med. Chem.* **2018**, *61*, 5822–5880.

(17) (a) Furuya, T.; Ritter, T. Fluorination of boronic acids mediated by silver(I) triflate. *Org. Lett.* **2009**, *11*, 2860–2863. (b) Ye, Y.; Sanford, M. S. Mild copper-mediated fluorination of aryl stannanes and aryl trifluoroborates. *J. Am. Chem. Soc.* **2013**, *135*, 4648–4651. (c) Fier, P. S.; Luo, J.; Hartwig, J. F. Copper-mediated fluorination of arylboronate esters. Identification of a copper(III) fluoride complex. *J. Am. Chem. Soc.* **2013**, *135*, 2552–2559.

(18) Ye, Y.; Schimler, S. D.; Hanley, P. S.; Sanford, M. S. Cu(OTf)<sub>2</sub>-mediated fluorination of aryltrifluoroborates with potassium fluoride. *J. Am. Chem. Soc.* **2013**, *135*, 16292–16295.

(19) Okoromoba, O. E.; Han, J.; Hammond, G. B.; Xu, B. Designer HF-based fluorination reagent: highly regioselective synthesis of fluoroalkenes and *gem*-difluoromethylene compounds from alkynes. *J. Am. Chem. Soc.* **2014**, *136*, 14381–14384.

(20) (a) Drouin, M.; Hamel, J.-D.; Paquin, J.-F. Synthesis of monofluoroalkanes: a leap forward. *Synthesis* **2018**, *50*, 881–955. (b) Yanai, H.; Taguchi, T. Synthetic methods for fluorinated olefins. *Eur. J. Org. Chem.* **2011**, 5939–5954. (c) McCarthy, J. R.; Matthews, D. P.; Stemerick, D. M.; Huber, E. W.; Bey, P.; Lippert, B. J.; Snyder, R. D.; Sunkara, P. S. Stereospecific method to *E* and *Z* terminal fluoro olefins and its application to the synthesis of 2'-deoxy-2'-

fluoromethylene nucleosides as potential inhibitors of ribonucleoside diphosphate reductase. *J. Am. Chem. Soc.* **1991**, *113*, 7439–7440. (d) Burton, D. J.; Greenlimb, P. E. Fluoro olefins. VII. preparation of terminal vinyl fluorides. *J. Org. Chem.* **1975**, *40*, 2796–2800.

(21) Niggemann, M.; Gao, S. Are vinyl cations finally coming of age? *Angew. Chem., Int. Ed.* **2018**, *57*, 16942–16944.

## CHAPTER SIX

### A Mechanistic Switch from Homoallylation to Cyclopropylcarbinylation of Aldehydes

#### 6.1 Contributions

This is an author manuscript from the publication: Lee, W.; Polyak, D.; Xu, B.; Houk, K. N.; Krauss, I. J. A Mechanistic Switch from Homoallylation to Cyclopropylcarbinylation of Aldehydes. *Org. Lett.* **2022**, 24, 4660–4664. <https://doi.org/10.1021/acs.orglett.2c01790>. This project was a collaborative work between the laboratories of Professor Kendall N. Houk at the University of California, Los Angeles and Professor Isaac J. Krauss at Brandeis University. Daniel Polyak and I are co-first authors of this publication. I conducted all computational experiments while Daniel Polyak and Bokai Xu performed the experimental work.

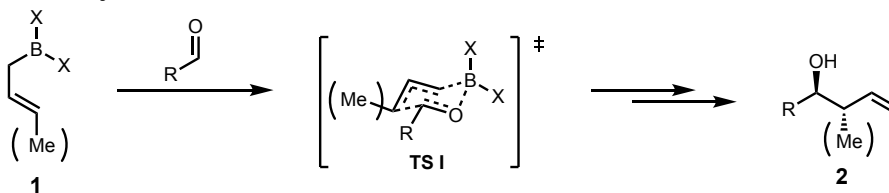
#### 6.2 Abstract

Cyclopropanated allylboration reagents participate in homoallylation reactions of aliphatic and aromatic aldehydes, generating allylic-substituted alkenes that are difficult to produce via other methods. In studying the effect of cyclopropane substituents, we discovered that an aryl substituent completely changes the outcome to cyclopropylcarbinylation, as if the cyclopropylcarbinylyl fragment were transferred intact. However, density functional theory computation suggested a novel mechanism involving ring opening and reclosure, which is supported by experimental evidence.

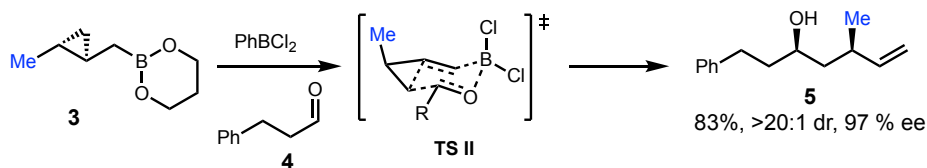
#### 6.3 Introduction

Allylboration and crotylboration of aldehydes are well studied reactions, and a variety of asymmetric variants have been developed, taking advantage of well organized closed transition states that result in predictable stereochemical outcomes (**Figure 6.1**).<sup>1</sup> However, homoallylation and homocrotylation reactions are less developed.<sup>2</sup> Our group has prepared cyclopropanated allylboration reagents (cyclopropylcarbinylboronates), which homoallylate aldehydes through Zimmerman-Traxler transition states<sup>3</sup> that are apparently analogous to allylboronates (**TS-I**, **TS-II**).<sup>4</sup>

**allylation/crotylation:**



**homocrotylation with alkyl substituents (previous work):**



**anomalous cyclopropylcarbinylation with Ph substituent:**

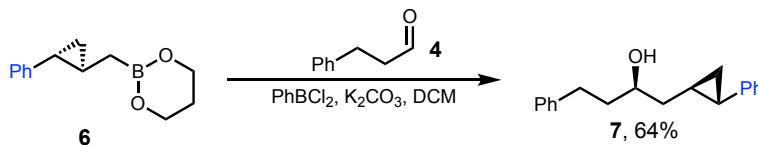


**Figure 6.1** Allylboration versus homoallylation with cyclopropanated allylboron reagents.

During the course of a substituent scope investigation (see the preceding manuscript), we observed an anomalous result that has led us to a revised mechanistic hypothesis.<sup>5</sup> While substitution of an alkyl group at the  $\gamma$  position of the boronate has led to alkyl-containing “homocrotylation” products with high stereospecificity (**Figure 6.1**), we were surprised to observe that substitution of a phenyl group at this position led to cyclopropylcarbinylation (**6**  $\rightarrow$

7). Herein, we present mechanistic evidence that this transformation occurs through cyclopropane ring opening and reclosure.

#### 6.4 Results and Discussion

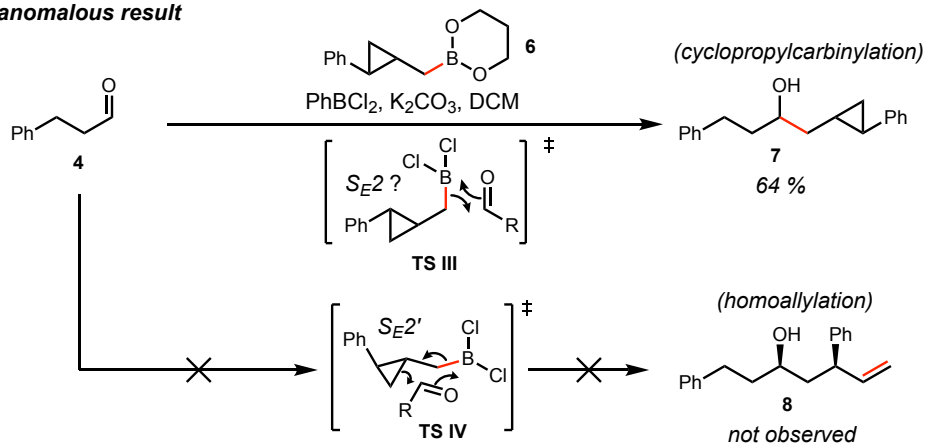
To explore potential mechanisms for this anomalous result, we undertook density functional theory (DFT) calculations ( $\omega$ B97X-D/6-311++G(d,p)/SMD (CH<sub>2</sub>Cl<sub>2</sub>))<sup>6</sup> (**Figure 6.2**).

Interestingly, the dichloroborane intermediate **6'** derived from PhBCl<sub>2</sub> activation of **6** was predicted to react through modified Zimmerman-Traxler transition state **TS-V**, in which the cyclopropane breaks and reforms in a concerted asynchronous fashion. To test this prediction experimentally, we prepared the deuterium-labeled reagent **6-d<sub>2</sub>**. Consistent with the DFT-predicted mechanism, the deuterated methylene in the cyclopropane of boronate **6-d<sub>2</sub>** was replaced by a nondeuterated methylene in the cyclopropane of product **7-d<sub>2</sub>**. To assign the relative stereochemistry of **7**, a crystalline analog was prepared; *p*-nitrobenzaldehyde (**11**) reacted in good yield and was further derivatized as nitrophenylcarbamate **12**. The X-ray crystal structure of **12** showed that the relative stereochemistry of the cyclopropylcarbinylation product was consistent with the DFT-predicted mechanism, in which the aldehyde substituent is oriented equatorially in the chair transition state **TS-V**.

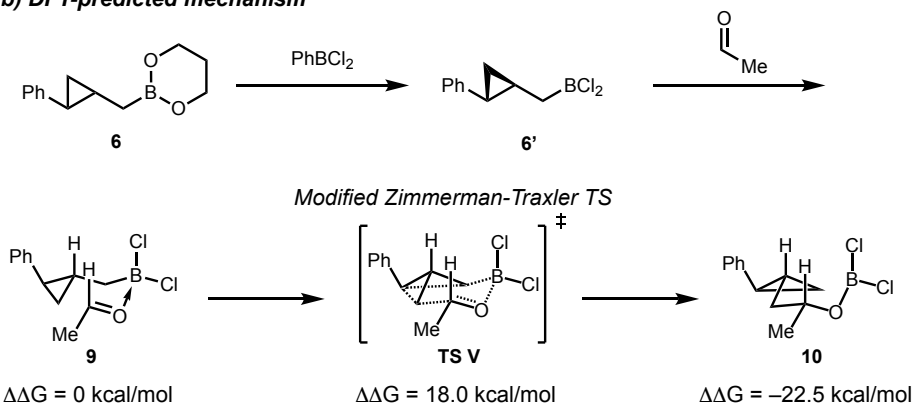
To further study the effect of the aromatic substituent, we prepared a *cis* analog of **6-d<sub>2</sub>** (**13**, **Figure 6.3a**). This reagent afforded the analogous cyclopropylcarbinylation product **14**, but in this case as a 2.3:1 *cis/trans* cyclopropane mixture. Interestingly, some homoallylation product **15** was also obtained, as well as a small amount of 1,1-disubstituted alkene **16**. The position of the deuterium labels was again consistent with a cyclopropane opening/closing mechanism, but,

in this case, the presence of hydride shift product **16** and some *cis*→*trans* isomerization of the cyclopropane suggested a carbocationic intermediate.

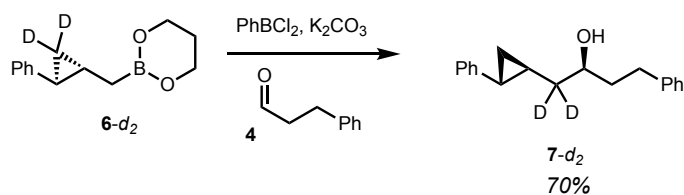
**a) anomalous result**



**b) DFT-predicted mechanism**



**c) isotope labeling study**



**d) confirmation of relative stereochemistry**

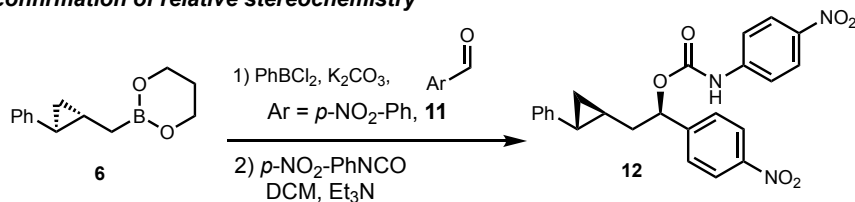
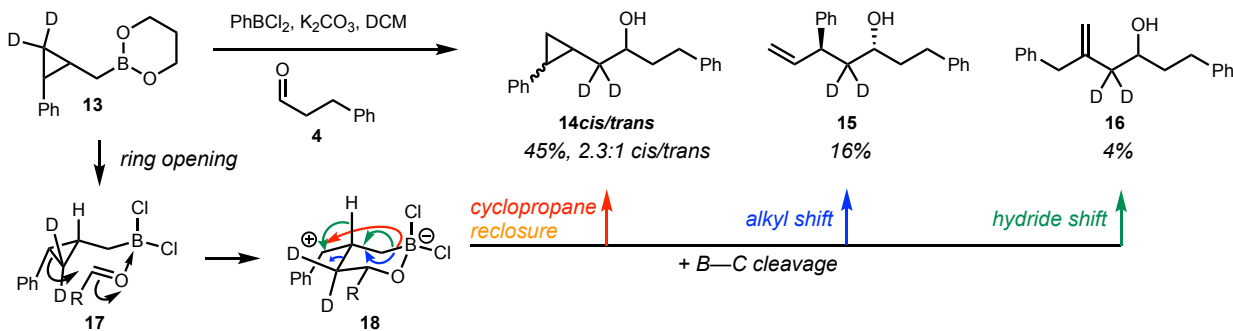


**Figure 6.2** Cyclopropylcarbylation and mechanistic study.

In fact, DFT calculations ( $\omega$ B97X-D/6-311++G(d,p)/SMD ( $\text{CH}_2\text{Cl}_2$ )) (**Figure 6.3b**) also predicted the cationic intermediate.

**a) deuterium labeling studies**



**b) computational studies**

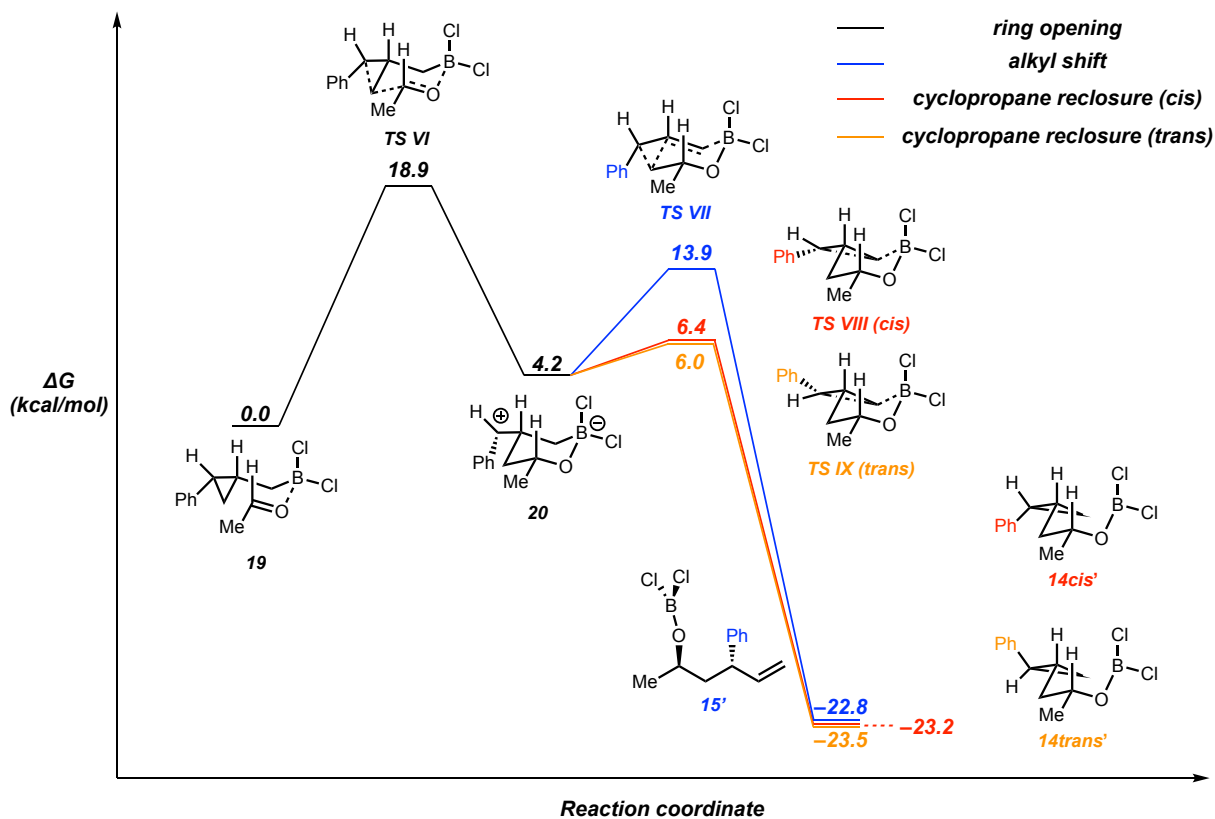


**Figure 6.3** Cyclopropylcarbylation versus homoallylation with *cis*-phenyl reagent **13**.

According to the calculations, *cis* reagent **13** reacts through a slightly higher initial activation barrier than *trans* reagent **6** ( $\Delta G = 18.9$  kcal/mol vs 18.0 kcal/mol); however, instead of a



barrierless reclosure of the cyclopropane, the *cis* reagent recloses the ring through a second energy maximum **TS-VIII** ( $\Delta G = 6.4$  kcal/mol), to afford **14cis**. The benzylic carbocation intermediate **20** ( $\Delta G = 4.2$  kcal/mol) between these two maxima can alternatively reclose cyclopropane with concomitant rotation of the phenyl ring (**TS-IX**,  $\Delta G = 6.0$  kcal/mol) to afford **14trans**. To form the observed minor homoallylation product **15**, cation **20** is predicted to undergo a concerted carbon migration/B–C bond cleavage step (**TS-VII**,  $\Delta G = 13.9$  kcal/mol). To probe the mechanistic factors that could favor homoallylation versus cyclopropylcarbinylation pathways, we used analogous DFT calculations ( $\omega$ B97X-D/6-311++G(d,p)/SMD ( $\text{CH}_2\text{Cl}_2$ )) to evaluate the reaction pathway of known methyl-substituted reagent (**3**, **Figure 6.4a**).

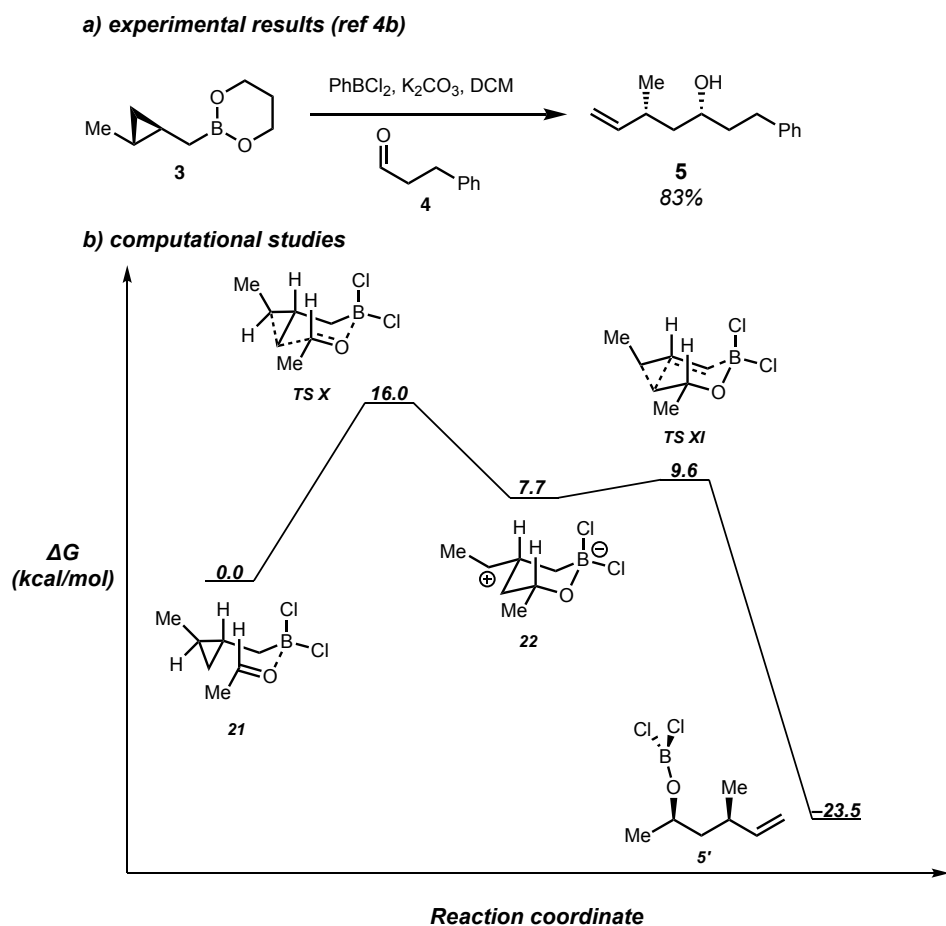


**Figure 6.4** Homoallylation with *trans*-methyl reagent **3**.

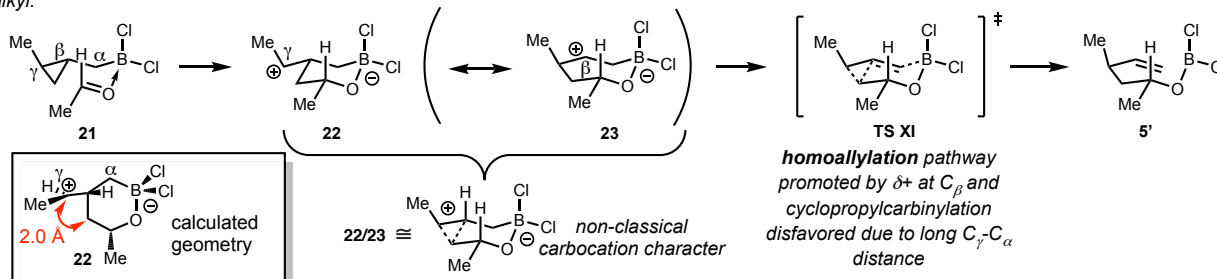
Although previous DFT calculations in the gas phase had suggested a concerted transition state (**TS II**, **Figure 6.1**),<sup>4b</sup> the current computational method, including a solvation model, suggested a two-step pathway. After a ring opening transition state **TS X** ( $\Delta G = 16.0$  kcal/mol; see **Figure 6.4b**) that is slightly lower in energy than **TS V**, a carbocation intermediate **22** is formed at 7.7 kcal/mol, but, in this case, the alkyl shift/B–C cleavage step (**TS-XI**) has a lower barrier than that in the *cis*-phenyl analogue ( $\Delta\Delta G = 1.9$  kcal/mol versus 9.7 kcal/mol; see **Figures 6.3b** and **6.4b**). In **22**, the secondary carbocation center is only 2.0 Å from the methylene to which it was previously bonded (as opposed to 2.4 Å for benzylic carbocation **20**) and the adjacent methine carbon is distorted from a tetrahedral geometry. Together, these measurements suggest some non-classical character in this carbocation; i.e., **22** leans toward an alkyl shift along the trajectory leading to the observed homoallylation product **5'** (**Figure 6.5a**). Therefore, the homoallylation preference observed with alkyl-substituted reagents may reflect the tendency of the initially formed carbocation to undergo alkyl shift ( $2^\circ \rightarrow 2^\circ$ ), whereas benzylic cation **20** is more stable than secondary alkyl cation **24** and lacks this tendency, favoring attack by the B–C electron pair directly at the benzylic carbocation. Note that the DFT calculations overestimate the energy of homoallylation pathway compared with cyclopropylcarbinylation (**Figures 6.6** and **6.7** in **6.7 Supplementary Information**) both for phenyl and methyl substituents; the observed homoallylation/cyclopropylcarbinylation ratios (1:2.8 for **15/14** and only homoallylation for **5**) are higher than those expected from the calculated energies. However, the calculations are qualitatively consistent with the observation that homoallylation is more favored with the alkyl substituent versus aryl.

Based on the calculated geometry for *cis*-phenyl derived intermediate **20**, we noted that some destabilization may result from steric interactions between the phenyl ring and the methylene

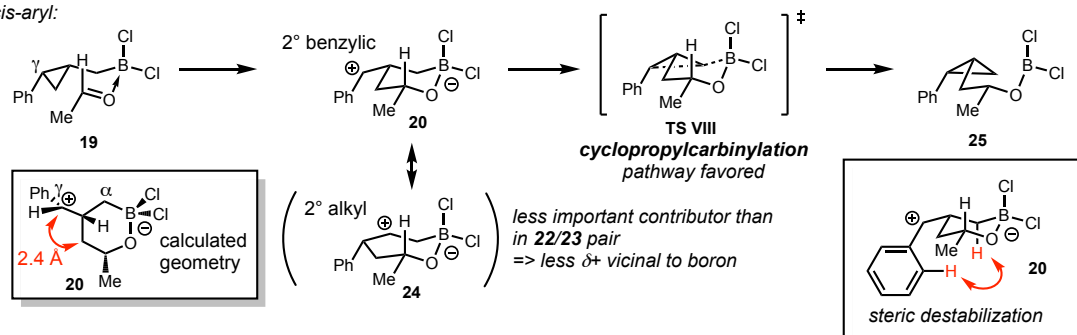
attached to boron (**Figure 6.5a**, red hydrogens); we hypothesized that this destabilization may contribute to disfavoring cyclopropylcarbinylation with **13**, but not *trans* reagent **6**.

**a) structural analysis and selectivity hypothesis**

alkyl:



cis-aryl:



**b) reversal of cyclopropylcarbinylation/homoallylation selectivity**

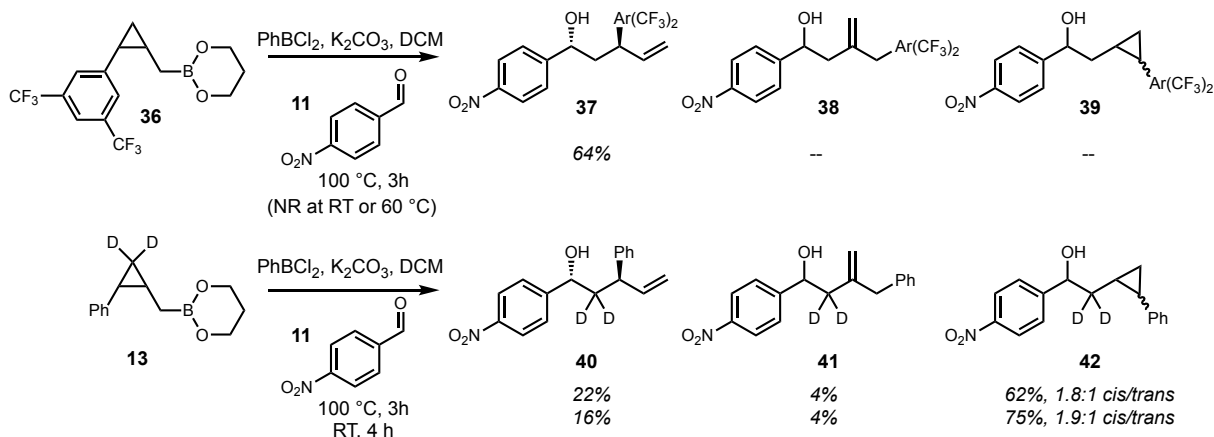


**Figure 6.5** Reversal of the cyclopropylcarbinylation/homoallylation selectivity by electronic tuning.

To test whether further destabilization of the benzylic cation could shift the balance in favor of homoallylation, we prepared the boronate analogue **36** containing electron-poor arene (**Figure 6.5b**). Although heating was required for any reaction to occur with nitrobenzaldehyde (**11**),

homoallylation product **37** was isolated exclusively with 64% yield, with no cyclopropylcarbinylation product **39** or hydride-shift-derived **38**. By comparison, **13** afforded 62% cyclopropylcarbinylation product **42** with the same aldehyde. Control experiments with **13** showed that temperature was not responsible for the change in selectivity.

## 6.5 Conclusion

In summary, we have discovered and mechanistically characterized a selectivity switch that occurs in alkyl- versus aryl-substituted cyclopropylcarbinyboron reagents. Whereas alkyl substituents are compatible with homoallylation, aromatic substituents alter the course of the reaction, promoting cyclopropylcarbinylation through a ring-opening/ring-closing mechanism, and this effect can be reversed with electron withdrawing arene substituents. Together with computational studies, these data suggest that the balance between these two pathways is dependent on the stabilization of cationic character on the cyclopropane carbon  $\gamma$  to boron.

## 6.6 References

- (1) (a) Yamamoto, Y.; Asao, N., Selective reactions using allylic metals. *Chem. Rev.* **1993**, *93*, 2207–2293; (b) Denmark, S. E.; Fu, J., Catalytic Enantioselective Addition of Allylic Organometallic Reagents to Aldehydes and Ketones. *Chem. Rev.* **2003**, *103*, 2763–2794; (c) Lachance, H.; Hall, D. G., Allylboration of Carbonyl Compounds. *Org. React.* **2009**, *73*, DOI: 10.1002/0471264180.or073.01.
- (2) (a) Sato, Y.; Takimoto, M.; Hayashi, K.; Katsuhara, T.; Takagi, K.; Mori, M., Novel Stereoselective Cyclization via  $\pi$ -Allylnickel Complex Generated from 1,3-Diene and Hydride Nickel Complex. *J. Am. Chem. Soc.* **1994**, *116*, 9771–9772; (b) Kimura, M.; Ezo, A.; Shibata, K.; Tamaru, Y., Novel and Highly Regio- and Stereoselective Nickel-Catalyzed Homoallylation of Benzaldehyde with 1,3-Dienes. *J. Am. Chem. Soc.* **1998**, *120*, 4033–4034; (c) Kimura, M.; Fujimatsu, H.; Ezo, A.; Shibata, K.; Shimizu, M.; Matsumoto, S.; Tamaru, Y., Nickel-Catalyzed Homoallylation of Aldehydes and Ketones with 1,3-Dienes and Complementary Promotion by Diethylzinc or Triethylborane. *Angew. Chem., Int. Ed.* **1999**, *38*, 397–400; (d) Sato, Y.; Takimoto, M.; Mori, M., Further Studies on Nickel-Promoted or -Catalyzed Cyclization of 1,3-Diene and a Tethered Carbonyl Group. *J. Am. Chem. Soc.* **2000**, *122*, 1624–1634; (e) Kimura, M.; Ezo, A.; Tanaka, S.; Tamaru, Y., Nickel-Catalyzed Homoallylation of Aldehydes in the Presence of Water and Alcohols. *Angew. Chem., Int. Ed.* **2001**, *40*, 3600–3602; (f) Sato, Y.; Sawaki, R.; Saito, N.; Mori, M., Nickel-Catalyzed Intermolecular Coupling of 1,3-Dienes and Aldehydes via Transmetalation of Nickelacycles with Diisobutylaluminum Acetylacetonate. *J. Org. Chem.* **2002**, *67*, 656–662; (g) Kimura, M.; Ezo, A.; Mori, M.; Iwata, K.; Tamaru, Y., Regio- and Stereoselective Nickel-Catalyzed Homoallylation of Aldehydes with 1,3-Dienes. *J.*

*Am. Chem. Soc.* **2006**, *128*, 8559–8568; (h) Li, H.; Wu, J.; Luo, J.; Dai, W.-M., A Concise Total Synthesis of Amphidinolide T2. *Chem. - Eur. J.* **2010**, *16*, 11530–11534.

(3) Zimmerman, H. E.; Traxler, M. D., The Stereochemistry of the Ivanov and Reformatsky Reactions. I. *J. Am. Chem. Soc.* **1957**, *79*, 1920–1923.

(4) (a) Pei, W.; Krauss, I. J., Homoallylboration and Homocrotylboration of Aldehydes. *J. Am. Chem. Soc.* **2011**, *133*, 18514–18517; (b) Lin, H.; Pei, W.; Wang, H.; Houk, K. N.; Krauss, I. J., Enantioselective Homocrotylboration of Aliphatic Aldehydes. *J. Am. Chem. Soc.* **2013**, *135*, 82–85; (c) Dugas, G. J.; Lam, Y.-h.; Houk, K. N.; Krauss, I. J., Boron Carboxylate Catalysis of Homoallylboration. *J. Org. Chem.* **2014**, *79*, 4277–4284; (d) Lin, H.; Tian, L.; Krauss, I. J., Enantioselective syn and anti Homocrotylation of Aldehydes: Application to the Formal Synthesis of Spongidepsin. *J. Am. Chem. Soc.* **2015**, *137*, 13176–13182; (e) Tian, L.; Krauss, I. J., Stereoselective Homocrotylation of Aldehydes: Enantioselective Synthesis of Allylic-Substituted Z/E-Alkenes. *Org. Lett.* **2018**, *20*, 6730–6735.

(5) Polyak, D.; Xu, B.; Krauss, I. J., Homoallylboration of Aldehydes: Stereoselective Synthesis of Allylic-Substituted Alkenes and E-Alkenes. *Org. Lett.*, DOI: 10.1021/acs.orglett.2c01789.

(6) (a) Chai, J.-D.; Head-Gordon, M., Long-range corrected hybrid density functionals with damped atom–atom dispersion corrections. *Phys. Chem. Chem. Phys.* **2008**, *10*, 6615–6620; (b) Marenich, A. V.; Cramer, C. J.; Truhlar, D. G., Universal Solvation Model Based on Solute Electron Density and on a Continuum Model of the Solvent Defined by the Bulk Dielectric Constant and Atomic Surface Tensions. *J. Phys. Chem. B* **2009**, *113*, 6378–6396.

## 6.7 Supplementary Information

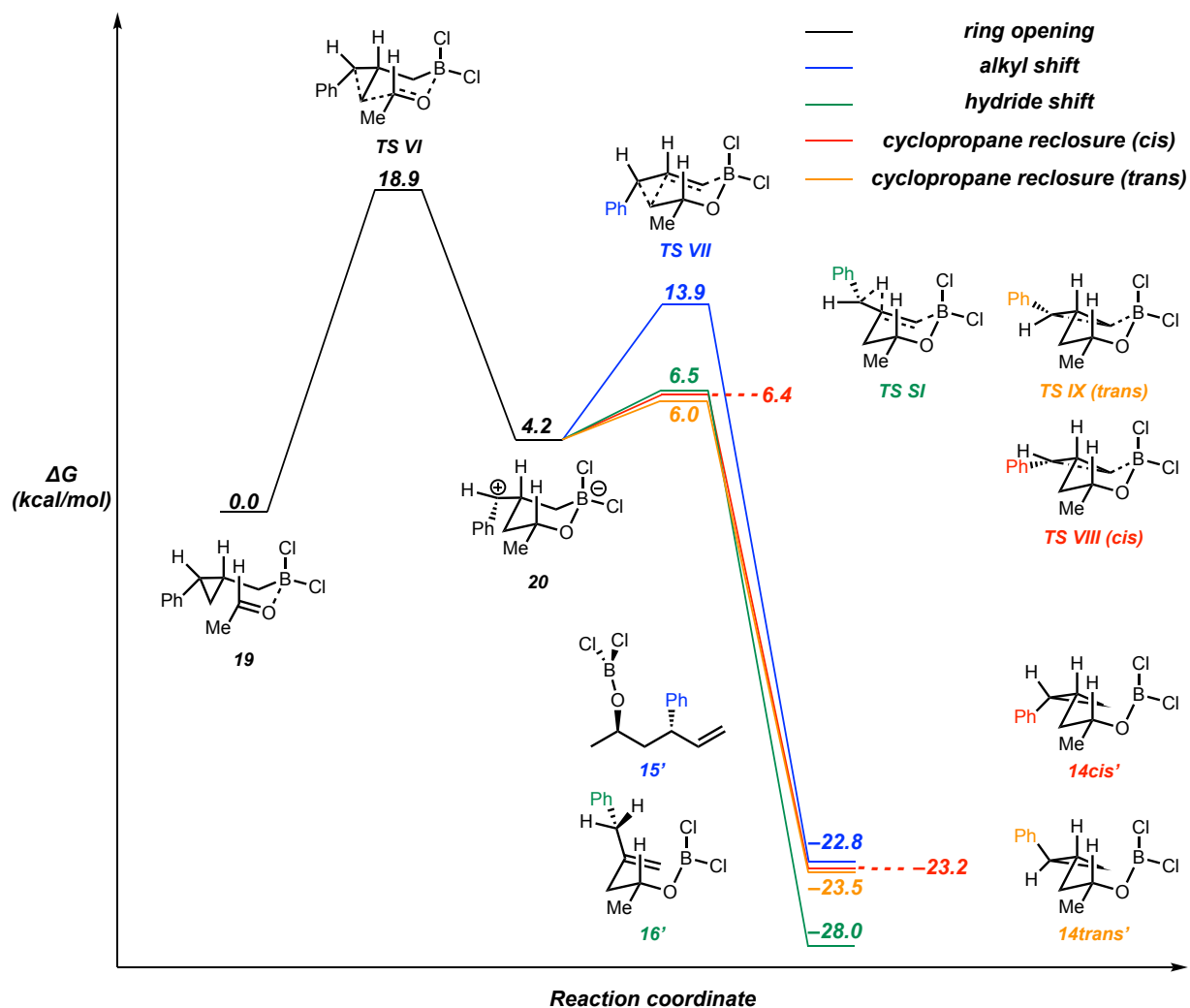


**Figure 6.6** Calculated reaction pathways of phenyl-substituted boronate **13**.

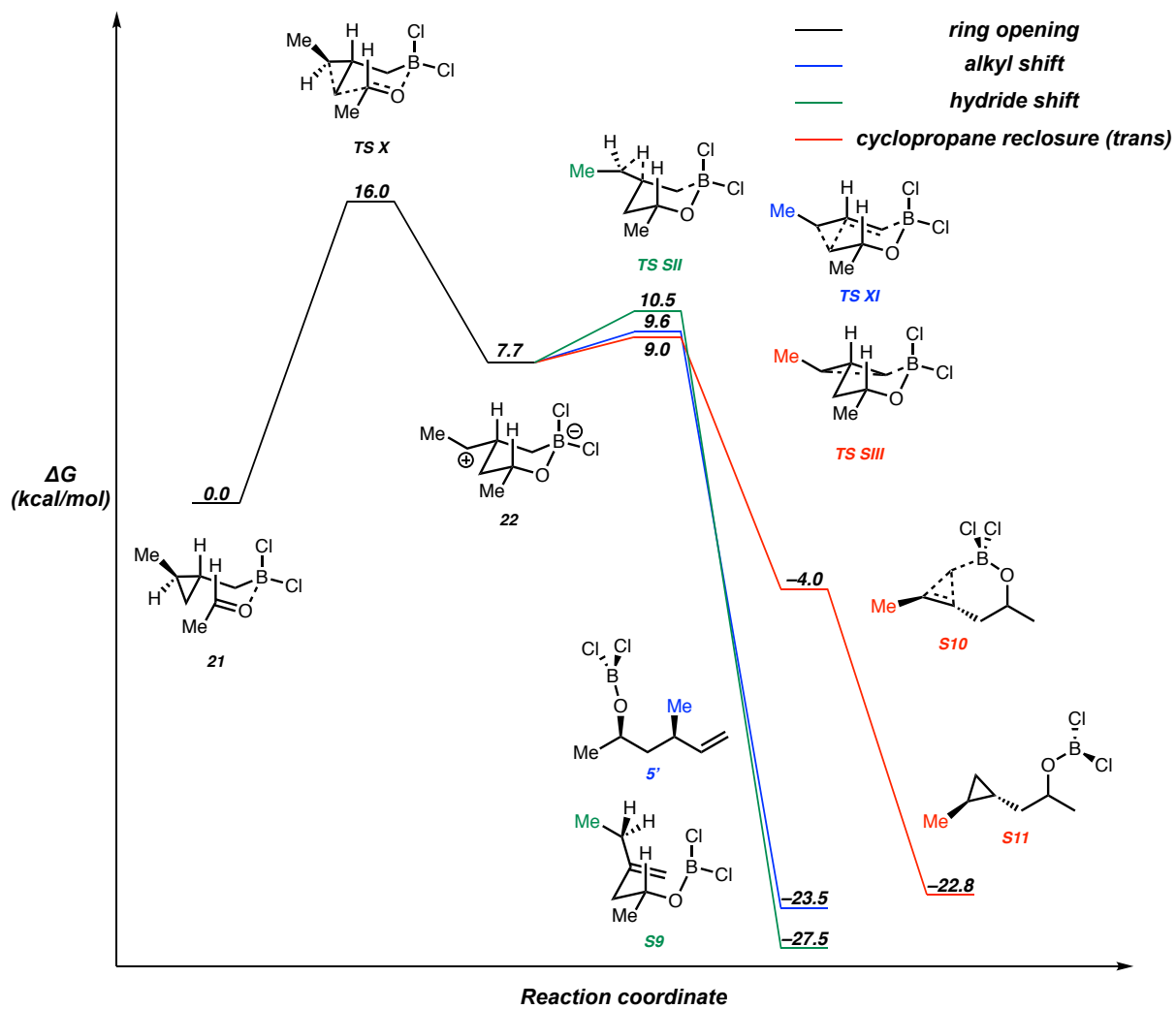


**Figure 6.7** Calculated reaction pathways of methyl-substituted boronate **3**.



## CHAPTER SEVEN

### Diastereoselective Radical Aminoacylation of Olefins through N-Heterocyclic Carbene Catalysis

#### 7.1 Contributions

This is an author manuscript from the publication: Liu, W.-D.; Lee, W.; Shu, H.; Xiao, C.; Xu, H.; Chen, X.; Houk, K. N.; Zhao, J. Diastereoselective Radical Aminoacylation of Olefins through N-Heterocyclic Carbene Catalysis. *J. Am. Chem. Soc.* **2022**, *144*, 22767–22777. <https://doi.org/10.1021/jacs.2c11209>. This project was a collaborative work between the laboratories of Professor Kendall N. Houk at the University of California, Los Angeles and Professor Jiannan Zhao at the Dalian University of Technology. Wen-Deng Liu and I are the co-first authors of this publication. I conducted all computational experiments while Wen-Deng Liu carried out the majority of the experimental work. Postdoctoral fellow Dr. Xiangyang Chen contributed to the analysis of the computational results. Wen-Deng Liu received experimental assistance from Hanyu Shu, Chuyu Xiao, and Huiwei Xu.

#### 7.2 Abstract

There have been significant advancements in radical-mediated reactions through covalent-based organocatalysis. Here we present the generation of iminyl- and amidyl radical via N-heterocyclic carbene (NHC) catalysis, enabling diastereoselective aminoacylation of trisubstituted alkenes. Different from photoredox catalysis, single electron transfer from the deprotonated Breslow intermediate to *O*-aryl hydroxylamine generates an NHC-bound ketyl radical, which undergoes

diastereocontrolled cross coupling with the prochiral C-centered radical. This operationally simple method provides a straightforward access to a variety of pyrroline and oxazolidinone heterocycles with vicinal stereocenters (77 examples, up to >19:1 d.r.). Electrochemical studies of the acyl thiazolium salts support our reaction design and highlight the reducing ability of Breslow-type derivatives. A detailed computational analysis of this organocatalytic system suggests that radical-radical coupling is the rate-determining step, in which  $\pi$ - $\pi$  stacking interaction between the radical intermediates subtly control the diastereoselectivity.

### 7.3 Introduction

Nitrogen-centered radicals are versatile reactive intermediates with broad applications in the synthesis of N-containing heterocycles,<sup>1,2</sup> which are ubiquitous structural motifs in natural products and pharmaceuticals.<sup>3</sup> Pre-functionalized oximes are excellent precursors for iminyl radicals owing to their weak N–O bond.<sup>2,4</sup> To supplement the classical methods for N–O bond cleavage via microwave<sup>4a</sup> (>160 °C) or UV irradiation,<sup>4b,c</sup> recent developments in the field of photoredox catalysis<sup>2,5</sup> provided an attractive way to access iminyl radicals from oxime ethers<sup>6</sup> and acyl oximes<sup>7</sup> under mild conditions (**Figure 7.1a**). These N radicals may undergo 5-exo-trig cyclization onto tethered alkenes, providing access to pyrrolines (**Figure 7.1b**).<sup>6,7b</sup> Studer and Leonori have shown, independently, that the resultant C-centered radicals could be intermolecularly captured by Michael acceptors<sup>6b</sup> or SOMOphiles<sup>6c</sup> to form C–C, C–N, and C–halide bonds. However, daunting challenges remain in the cyclization with 1,2-disubstituted alkenes, which generated a prochiral carboncentered radical.<sup>6a-c</sup> The diastereoselectivity is not controlled in the following radical-involved process due to nominal interaction between the photocatalyst and radical-based intermediates, which undergo reaction with minimal activation

barriers. One of the key breakthroughs in this field can be traced to a recent report by Yu and co-workers, who achieved diastereoselective imination of this type by careful selection of vinyl boronic acid as the radical acceptor.<sup>8</sup>

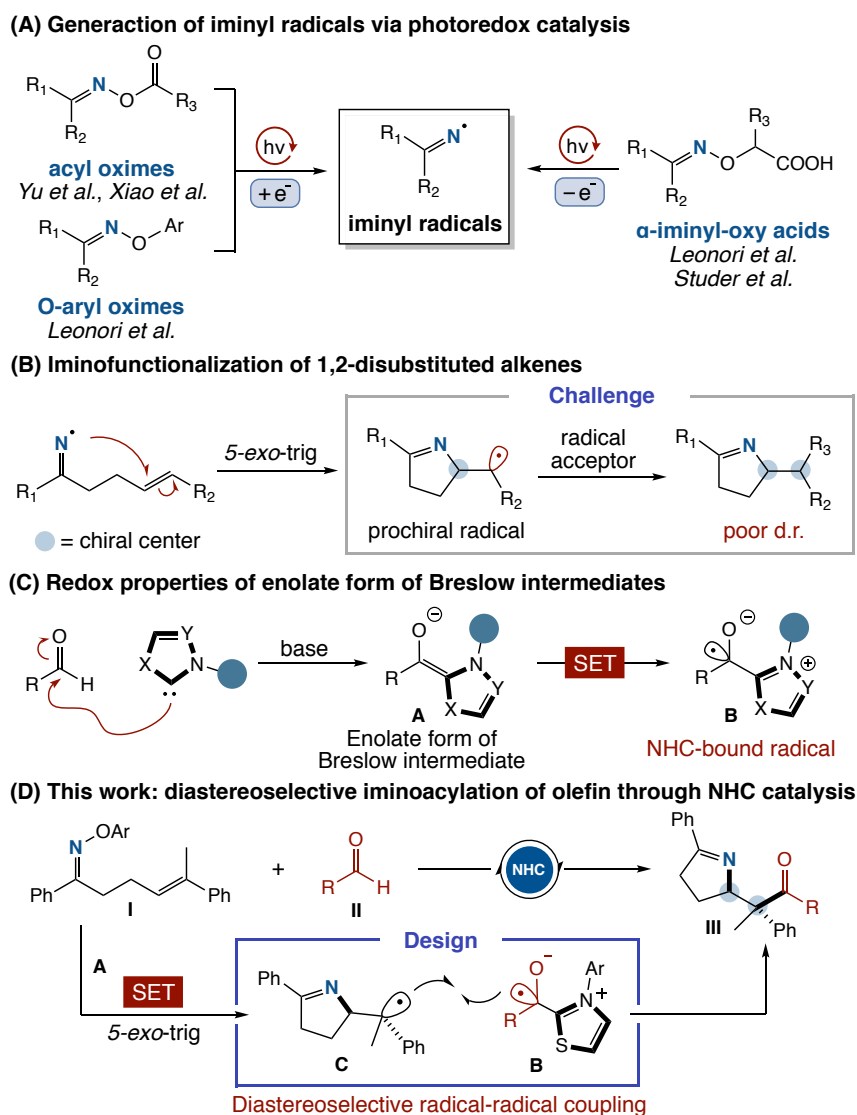


**Figure 7.1** a) Generation of iminyl radicals via N–O bond homolysis. b) Access to pyrroline derivative with vicinal stereocenters. c) Radical NHC catalysis. d) Diastereoselective iminoacylation of trisubstituted olefin.

In this context, the development of an appropriate catalytic system capable of controlling diastereoselectivity in radical–radical coupling reactions is highly desirable and would be of great synthetic importance. In contrast to the use of a photoredox catalyst, we envisioned that

covalent-based organocatalysis could provide an opportunity to control the stereochemistry in radical-involved reactions<sup>9</sup> due to the strong interaction between the catalyst and the reactant. N-Heterocyclic carbenes (NHCs) are well-known as nucleophilic organocatalysts<sup>10</sup> for the umpolung of aldehydes via Breslow intermediates.<sup>11</sup> Moving from traditional ionic chemistry logic to a radical approach, recent electrochemical<sup>12</sup> and methodological studies<sup>13,14</sup> revealed that the reduction potential of deprotonated Breslow intermediate **A** was sufficiently negative to perform single electron transfer (SET) with various single electron acceptors, such as TEMPO,<sup>14a</sup> nitro compounds,<sup>14c-f</sup> and polyhalides<sup>14g,h</sup> (**Figure 7.1c**). Pioneering studies from Ohmiya's group reported NHC-catalyzed radical decarboxylative coupling of aldehydes with redox-active esters, allowing for the rapid assembly of functionalized ketones.<sup>15</sup> In these processes, the deprotonated Breslow intermediate **A** can serve as both a single electron donor and an acyl radical equivalent for subsequent C–C bond formation. In the past few years, the synthetic potential of NHC radical catalysis was significantly extended to a number of SET-mediated transformation processes.<sup>16-18</sup> It is worthwhile mentioning that this attractive strategy provides the possibility for stereocontrolled radical reactions, since the NHC catalyst is associated with the C-centered radical **B** through a covalent bond.

Herein, based on the above hypothesis, we report the development of an NHC-catalyzed process capable of generating N-centered radicals and achieving diastereoselective aminoacylation under metal- and light-free conditions. As illustrated in **Figure 7.1d**, single electron reduction of oxime ether **I** by the electron-rich Breslow intermediate **A** triggered the formation of C-centered radical **C** after 5-exo-trig cyclization. We envisioned that the resulting NHC-bound ketyl radical **B** could differentiate competing stereomeric transition states of the prochiral radical **C** and allow diastereoselective radical–radical coupling. This organocatalytic protocol afforded access to

functionalized pyrrolines, which can be further transformed to interesting oxazinanone and indolizidine heterocycles. Moreover, we recognized an opportunity for amidyl radical generation and used them in diastereoselective amidoacylation of tethered alkenes.<sup>2,19</sup> Integrated experimental and computational studies revealed that the precise stereocontrol is attributed to steric hindrance on the NHC organocatalyst and  $\pi$ - $\pi$  stacking interaction between radicals **B** and **C**.

## 7.4 Results and Discussion

**Reaction Development.** We envisioned a prospective catalytic cycle for the NHC-catalyzed olefin iminoacylation as shown in **Figure 7.2**.

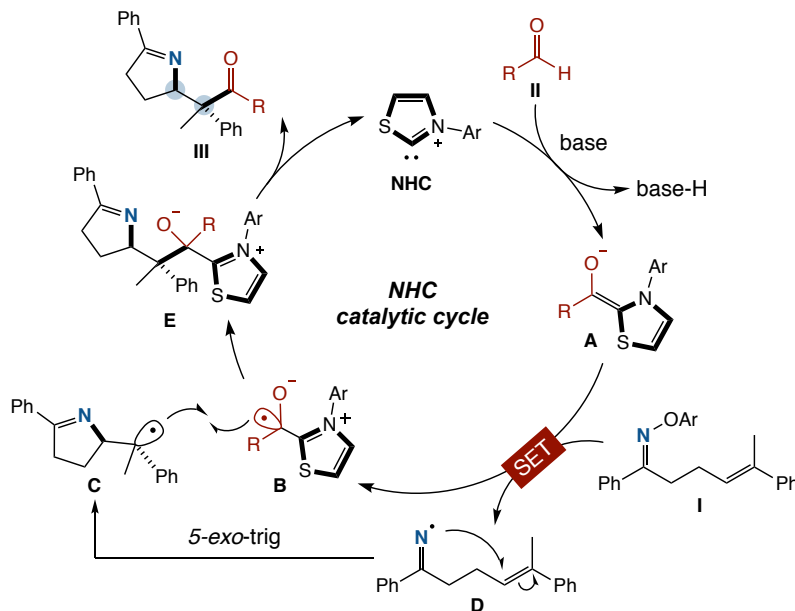
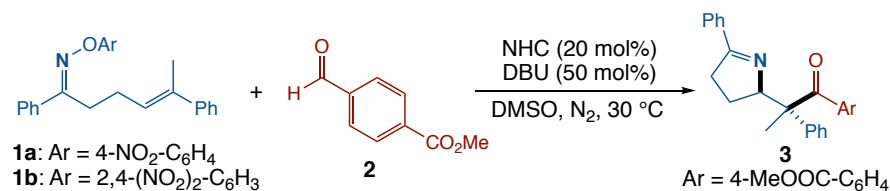


**Figure 7.2** Prospective catalytic cycle.

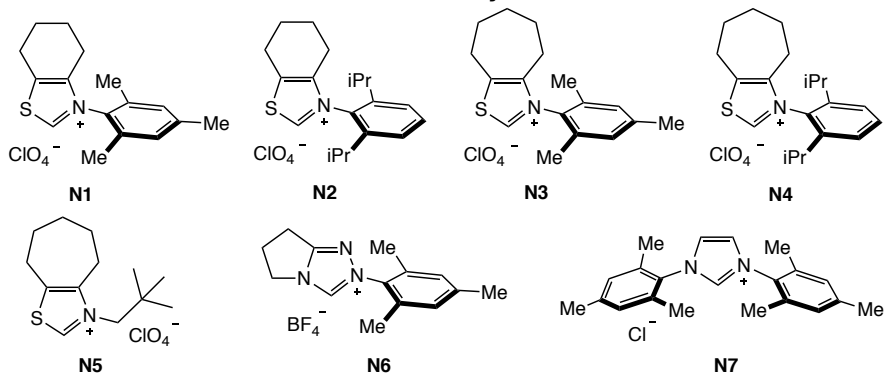
We anticipated that the deprotonated Breslow intermediate **A** would be generated from a thiazolium-type NHC and aldehyde **II** in the presence of a base. The subsequent SET event between the enolate **A** and oxime ether **I** would produce the ketyl radical **B** and iminyl radical **D** after homolysis of the N–O bond. Next, in accord with literature precedent,<sup>6,7b</sup> we expected the

iminyl radical **D** to perform 5-*exo*-trig cyclization to furnish a new C–N bond and the prochiral C-centered radical **C**, which would undergo diastereoselective radical cross-coupling with **B**. Finally, elimination of NHC from intermediate **E** would regenerate the organocatalyst and afford the desired pyrroline product **III** with vicinal stereocenters.

Inspired by Leonori's pioneering studies on the electron-poor *O*-aryl oximes,<sup>6a</sup> we began our reaction condition optimization with NO<sub>2</sub>-substituted oxime **1a** due to its ease of SET reduction (**Table 7.1**). Initially, the iminoacylation reaction with aromatic aldehyde **2** was performed in the presence of DBU and *N*-2,4,6-trimethylphenyl-substituted six-membered ring fused thiazolium salt **N1** (20 mol%). As shown in **Table 7.1**, we were pleased to find that the desired pyrroline **3** was obtained in good yield with 5:1 d.r. (entry 1). Encouraged by this result, the diastereoselective iminoacylation was evaluated by other NHC precursors. Gratifyingly, diisopropyl substituted thiazolium salt **N2** significantly improved the diastereoselectivity, furnishing **3** in 79% yield with >19:1 d.r. (**Table 7.1**, entry 2). Further investigation of the backbone moiety revealed that the seven-membered ring fused thiazolium salt **N4** was more efficient, increasing the yield to 91% as well as retaining the excellent diastereoselectivity (**Table 7.1** entry 4). The *N*-neopentyl-substituted **N5** showed comparable reactivity, but it induced lower diastereoselectivity (entry 5). Other NHCs bearing triazolium (**N6**) or imidazolium (**N7**) structures were ineffective under otherwise identical conditions (entries 6 and 7). The substituent on the *O*-aryl oxime was also critical for this reaction. When 2,4-dinitro-substituted aryl oxime **1b** was subjected to the reaction conditions, **3** was formed in much lower yield (entry 8 versus entry 4). Further evaluation of the solvents led to inferior yield (entries 9–11). Pleasingly, the amount of NHC precatalyst could be reduced to 5 mol% without any loss in the yield and diastereoselectivity (entry 12).



### NHC Catalysts

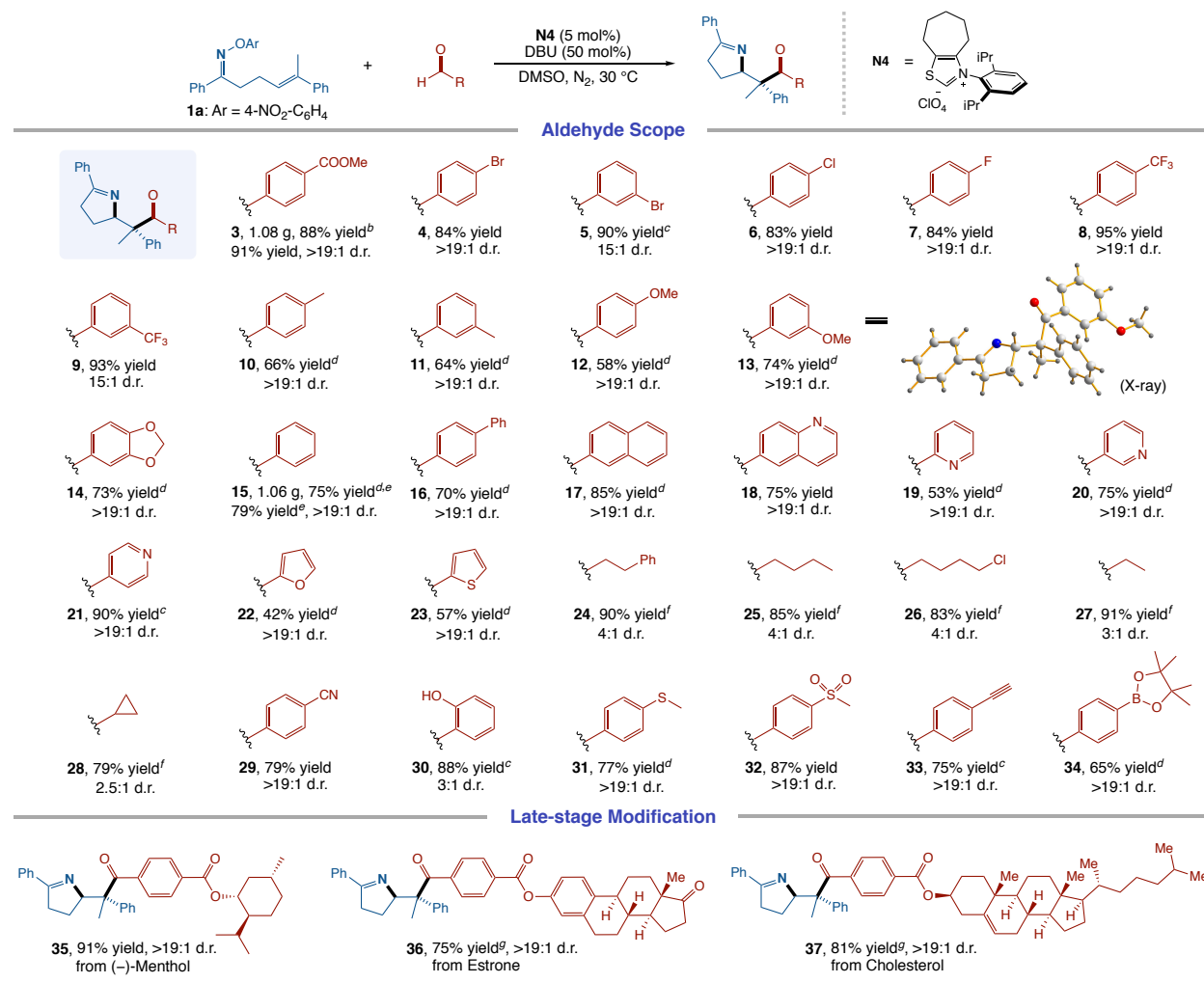


entry	NHC catalyst	solvent	yield (%) <sup>b</sup>	d.r. <sup>c</sup>
1	<b>N1</b>	DMSO	68	5:1
2	<b>N2</b>	DMSO	79	>19:1
3	<b>N3</b>	DMSO	51	5:1
4	<b>N4</b>	DMSO	91	>19:1
5	<b>N5</b>	DMSO	92	2.5:1
6	<b>N6</b>	DMSO	trace	-
7	<b>N7</b>	DMSO	trace	-
8 <sup>d</sup>	<b>N4</b>	DMSO	28	>19:1
9	<b>N4</b>	DMF	68	>19:1
10	<b>N4</b>	CH <sub>3</sub> CN	35	>19:1
11	<b>N4</b>	CH <sub>2</sub> Cl <sub>2</sub>	42	>19:1
12 <sup>e</sup>	<b>N4</b>	DMSO	91	>19:1

<sup>a</sup>Reactions were carried out with **1a** (0.1 mmol), **2** (0.15 mmol), NHC catalyst (20 mol%) and DBU (0.5 equiv) in 1.0 mL of solvent at 30 °C for 12 h. <sup>b</sup>Yields of isolated products. <sup>c</sup>Diastereomeric ratio (d.r.) values were determined by <sup>1</sup>H NMR. <sup>d</sup>**1b** was used instead of **1a**. <sup>e</sup>5 mol % **N4** was used.

**Table 7.1** Optimization and control studies.<sup>a</sup>

**Substrate Scope.** With the optimized conditions in hand, we next explored the generality of the iminoacylation of trisubstituted alkenes. The observed excellent diastereoselectivity led us to first examine the reaction of *O*-aryl oxime **1a** with various aldehydes (**Figure 7.3**).



<sup>a</sup>Reaction conditions: *O*-aryl oxime **1a** (0.1 mmol), aldehyde (1.5 equiv), NHC precatalyst **N4** (5 mol %), DBU (50 mol %) in DMSO (1.0 mL) at 30 °C for 12 h. Isolated product yields. Diastereomeric ratio (d.r.) values were determined by <sup>1</sup>H NMR. <sup>b</sup>3.0 mmol of **1a** was used. <sup>c</sup>10 mol % of catalyst was used. <sup>d</sup>20 mol % of catalyst was used. <sup>e</sup>4.0 mmol of **1a** was used. <sup>f</sup>Reaction was performed with NHC precatalyst **N5** (20 mol %) and Cs<sub>2</sub>CO<sub>3</sub> (50 mol %) at 60 °C. <sup>g</sup>Reaction was performed in DMSO/CH<sub>2</sub>Cl<sub>2</sub> (4.0 mL, v/v = 1:1).

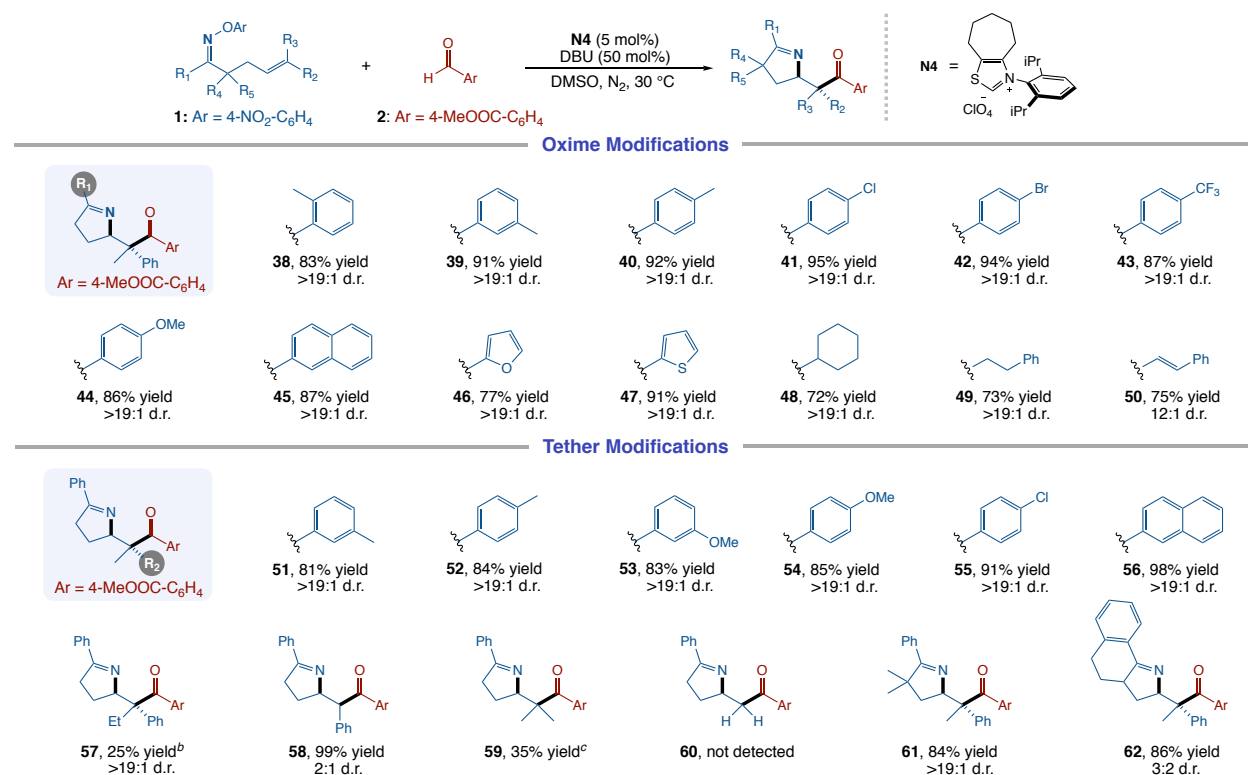
**Figure 7.3** Scope of aldehydes.<sup>a</sup>



To our delight, the developed NHC catalyzed radical reaction was effective over a wide range of aryl aldehydes to furnish the pyrroline products **3–23** in satisfying yields with excellent diastereoselectivity. It needs to be mentioned that the outcome was influenced a little by the electronic nature of the substituents on the aromatic ring. Generally, electron-deficient aryl aldehydes gave the desired products (**3–9**) with better yield and lower catalyst loading than the electron-rich ones (**10–14**). Additionally, the relative stereochemistry of the functionalized pyrroline was established by X-ray diffraction analysis of **13**. The diastereoselective transformation also proceeded smoothly with naphthyl (**17**) and various heteroaryl aldehydes such as substituted quinoline (**18**), pyridine (**19–21**), furan (**22**), and thiophene (**23**). In addition to aromatic aldehydes, we found that this strategy is amenable to aliphatic aldehydes (**24–28**) employing less sterically demanding **N5** instead of **N4**.<sup>15c</sup> Notably, diverse functionalities including nitrile, thioether, alkyne, and boronic ester were all competent (**29–34**). The broad functional group compatibility of the reaction encouraged us to investigate its practicality for late-stage functionalization of natural products. (–)-Menthol, estrone, and cholesterol-derived aldehydes were all compatible with the reaction conditions, providing the corresponding products (**35–37**) in 75–91% yield with complete diastereoselectivity. Furthermore, this iminoacylation reaction can be conducted on a gram scale, enabling the practical synthesis of pyrroline derivatives. The synthesis of pyrroline **3** and **15** was scaled up to give 1.1 gram of product in 88% and 75% yield, respectively.

Having investigated the aldehyde scope, we were interested in exploring the synthetic robustness of this diastereoselective iminoacylation reaction with other iminyl radical precursors. To this end, a variety of oxime ethers were prepared, and tested with the NHC catalyzed reaction. As

shown in **Figure 7.4**, the steric and electronic properties of the substituents on the aryl group ( $R_1$ ) had a slight influence on the reaction outcomes (**38–44**).



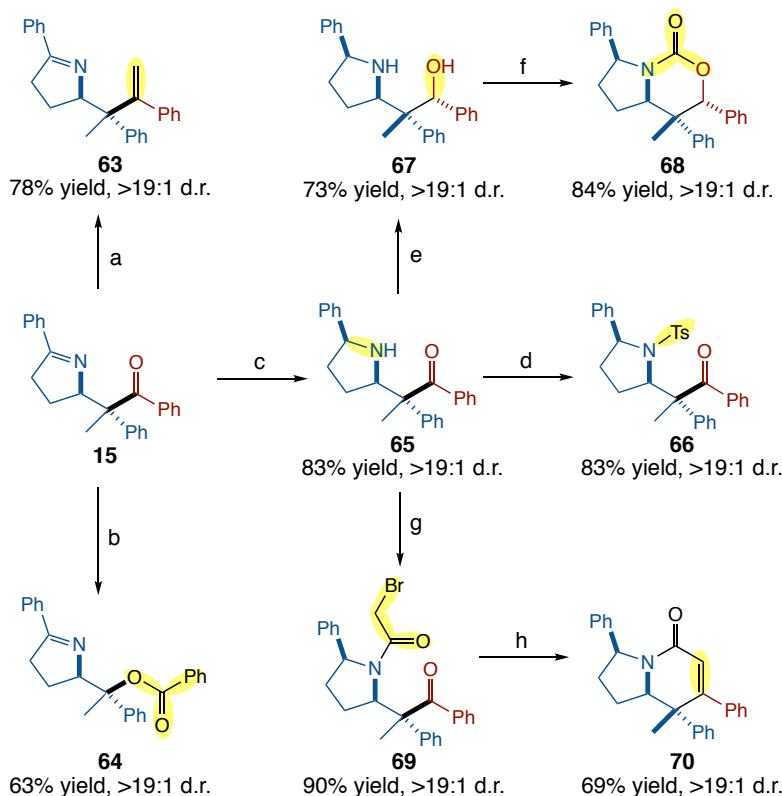
<sup>a</sup>See Figure 7.3. Isolated yields. Diastereomeric ratio (d.r.) values were determined by <sup>1</sup>H NMR.  
<sup>b</sup>20 mol % of catalyst was used. <sup>c</sup>50 mol% of Cs<sub>2</sub>CO<sub>3</sub> was used instead of DBU.

**Figure 7.4** Scope of oximes.<sup>b</sup>

Fused-ring, furan and thiophene-substituted oximes were viable substrates for producing the cyclic products in good yields with >19:1 d.r. (**45–47**). Notably, the catalyst system was also effective with alkyl and alkenyl-based substrates (**48–50**). With respect to the pendant alkene moiety, a variety of trisubstituted olefins with different substituents on the aromatic ring ( $R_2$ ) were successfully accommodated (**51–56**). For the substrates containing disubstituted olefin (**58**), diastereoselectivity was low due to enolized racemization. Dimethyl substituted alkene could also be used as an acceptor, albeit with lower yield for the target **59**. Unfortunately, oxime with terminal double bond (**60**) was not successful, presumably due to the instability of the primary

radical generated by cyclization. In addition, oxime substrates that contain *gem*-dimethyl substituents at the alpha-position of the C=N double bond ( $R_4 = R_5 = \text{Me}$ ), worked smoothly to deliver product **61** in high yield. When tetralin oxime was used, tricyclic product **62** was obtained in 84% yield, albeit with lower diastereoselectivity.

**Synthetic Applications.** To further demonstrate the synthetic utility of this reaction, the conversion of product **15** into various derivatives was examined. As shown in **Figure 7.5**, the functionalized pyrroline derivative **15** can further participate in several carbonyl-based transformations, including the Wittig reaction to form alkene **63**, and Baeyer-Villiger oxidation to afford carboxylic ester **64**. Hydrogenation of the imine offers opportunities to generate pyrrolidine derivatives. The pyrrolidine derivative **65** could be converted into 3-amino alcohol **67** under reductive conditions. Cyclization of **67** with 1,1'-carbonyldiimidazole (CDI) in THF at reflux temperature gave the 1,3-oxazinan-2-one derivative **68** in 84% yield without any loss of diastereoselectivity. The structure of cycloadduct **68** was unambiguously confirmed by an X-ray crystallographic analysis. Furthermore, acylation of **65** followed by ring-closing Wittig reaction yielded the indolizidine derivative **70**, which is an important framework of many natural products.<sup>20</sup>



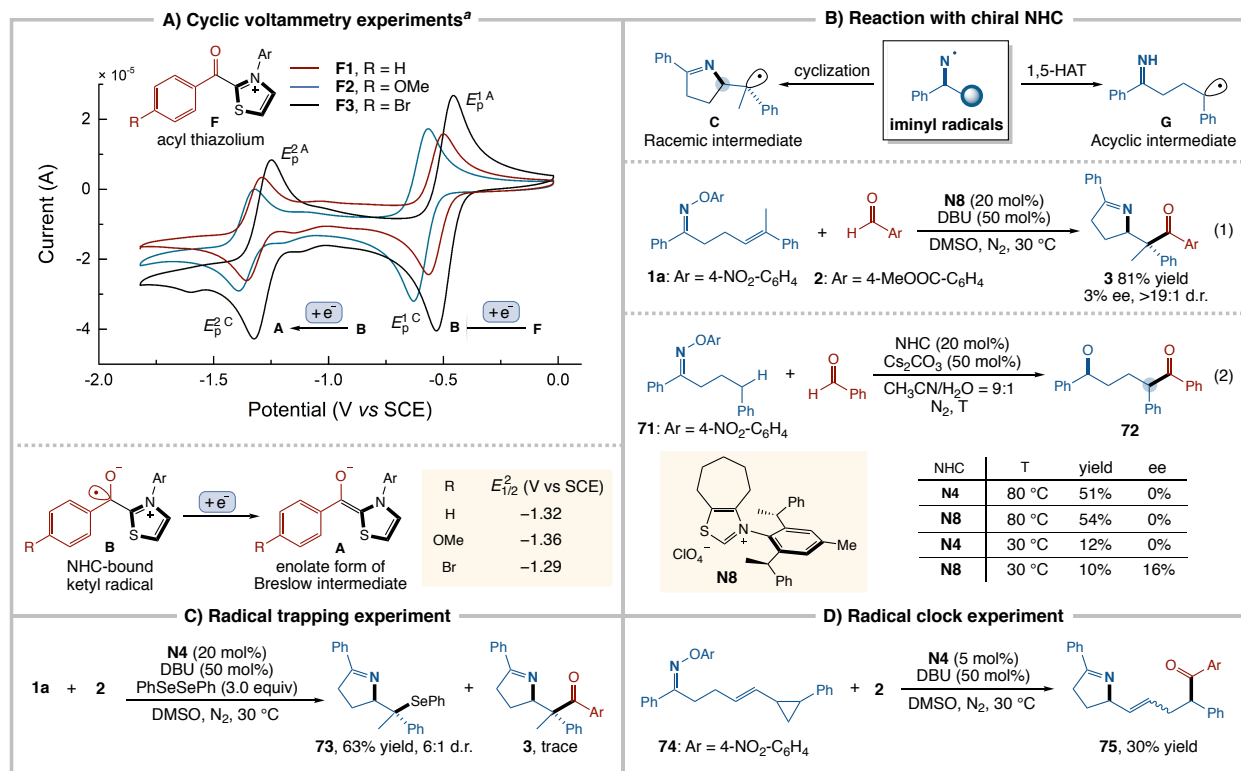
<sup>a</sup>Reaction conditions: (a)  $\text{PPh}_3\text{CH}_3\text{Br}$ ,  $n\text{-BuLi}$ , THF,  $-78\text{ }^\circ\text{C}$  to r.t.; (b)  $m\text{-CPBA}$ ,  $\text{NaHCO}_3$ ,  $\text{CH}_2\text{Cl}_2$ , r.t.; (c) 10% Pd/C,  $\text{H}_2$  (1 atm.), EtOAc, r.t.; (d) TsCl,  $\text{Et}_3\text{N}$ ,  $\text{CH}_2\text{Cl}_2$ , r.t.; (e)  $\text{NaBH}_4$ , MeOH,  $0\text{ }^\circ\text{C}$  to r.t.; (f) CDI, THF, reflux; (g) bromoacetyl bromide,  $\text{Et}_3\text{N}$ ,  $\text{CH}_2\text{Cl}_2$ ,  $0\text{ }^\circ\text{C}$  to r.t.; and (h)  $\text{PPh}_3$ , THF, r.t., then NaH, THF.

**Figure 7.5** Synthetic transformation of 9.<sup>a</sup>

**Experimental Investigations on the Reaction Pathways.** Upon exploration of the diastereoselective iminoacylation to display broad scope and high synthetic applicability, we were encouraged to investigate mechanistic details (**Figure 7.6**). In order to investigate the redox properties of Breslow-type derivatives, a series of acyl thiazoliums **F** were synthesized for cyclic voltammetry studies.<sup>21</sup> As shown in **Figure 7.6a**, scan of **F1** in  $\text{CH}_3\text{CN}$  containing 0.1 M  $n\text{Bu}_4\text{NPF}_6$  produced two successive reversible reduction waves. It features a reversible first reduction wave at  $E_{1/2}^1 = -0.53\text{ V}$  versus SCE, which corresponds to the reduction of **F1** to ketyl radical **B1**. Importantly, further single-electron reduction of persistent radical **B1** afforded

enolate **A1** with significantly lower potential ( $E_{1/2}^2[\mathbf{B1/A1}] = -1.32$  V vs SCE). The electronic properties of the substituents on the aryl group had a slight influence on the reduction potentials ( $E_{1/2}^2[\mathbf{B2/A2}] = -1.36$  V vs SCE;  $E_{1/2}^2[\mathbf{B3/A3}] = -1.29$  V vs SCE). These results highlight the strong reducing ability of Breslow-type derivatives, thus making the ground-state SET with oxime ether **1a** ( $E_{p/2}[\mathbf{1a/1a}^{\cdot-}] = -1.04$  V vs SCE) exergonic ( $\Delta G_{\text{SET}} \approx -5$  kcal mol<sup>-1</sup>).<sup>22,23</sup>

To further probe the involvement of NHC-bound ketyl radical **B**, a chiral NHC precatalyst **N8**<sup>16f</sup> was tested under the reaction conditions (**Figure 7.6b**). We envisioned this may facilitate the enantioselective iminoacylation of olefins. However, the coupling product **3** was obtained as a racemic mixture (eq 1), presumably due to the influence of a racemic stereocenter in the coupling partner **C**. Thus, we prepared oxime **71**, and tested it with benzaldehyde and **N8** (eq 2). In this case, we proposed that the iminyl radical would undergo intramolecular 1,5-hydrogen atom abstraction (HAT) rather than cyclization, delivering the acyclic radical **G**.<sup>2c,2g</sup> As the result, 1,5-dione **72** was isolated with 16% ee. This outcome supports our hypothesis of the formation of the NHC-bound ketyl radical **B** and its participation in the radical–radical coupling step. Meanwhile, a radical trapping experiment was conducted (**Figure 7.6c**). In the presence of 3.0 equiv of PhSeSePh, the standard reaction of **1a** and **2** furnished the selenide **73** in 63% yield. Moreover, oxime ether **74**, which bears a 2-phenylcyclopropyl group, was synthesized as a radical clock (**Figure 7.6d**). In this event, the NHC catalyzed reaction gave the expected fragmentation product **75** as a mixture of diastereomers. Pleasingly, two of the isomers were isolated in 30% yield and fully characterized, which provided strong support for the formation of the C-centered radical **C**.



<sup>a</sup>Cyclic voltammetry of 1 mM **F** in CH<sub>3</sub>CN with 0.1 M *n*Bu<sub>4</sub>NPF<sub>6</sub> electrolyte at a 100 mVs<sup>-1</sup> rate. Each voltammogram was obtained independently.

**Figure 7.6** Experimental mechanistic studies.

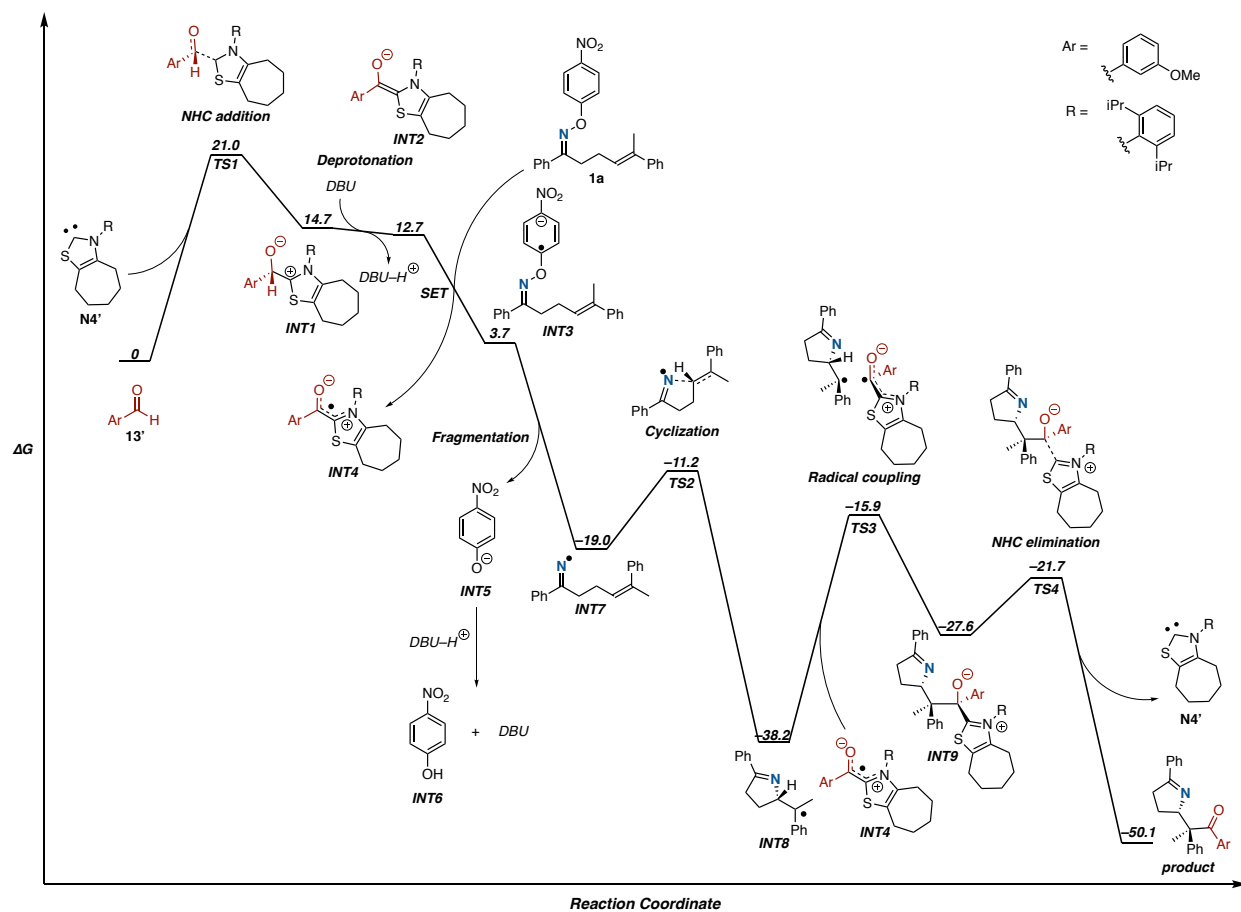
**Computational Studies.** To better understand the mechanistic details, energy profiles of the proposed pathways were evaluated by density functional theory (DFT) calculations (**Figure 7.7**). Addition of NHC catalyst **N4'** to *m*-anisaldehyde **13'** occurs via **TS1** (21.0 kcal/mol) to form **INT1**, which is further deprotonated by DBU to form Breslow intermediate **INT2** and DBU-H<sup>+</sup>. Oxime **1a** and Breslow intermediate **INT2** undergo SET to generate reduced oxime **INT3** and oxidized Breslow intermediate **INT4**. Then, fragmentation occurs from radical anion of oxime **INT3** to produce N-radical intermediate **INT7** and phenoxide **INT5** that forms phenol **INT6** by protonation with DBU-H<sup>+</sup>. N-radical intermediate **INT7** cyclizes via **TS2** (-11.2 kcal/mol) in order to form cyclized radical intermediate **INT8**. Oxidized Breslow intermediate **INT4**, which was generated by SET, undergoes coupling with cyclized radical intermediate **INT8** via **TS3** (-

15.9 kcal/mol) to produce coupling intermediate **INT9**. NHC elimination via **TS4** (−21.7 kcal/mol) from intermediate **INT9** generates product and regenerates NHC catalyst **N4'**. The overall reaction progress is exergonic by 50.1 kcal/mol. Based on the computational results, the radical coupling step is the rate-determining step. While radical coupling often occurs with very low barriers, both of these radicals are stabilized and sterically hindered.

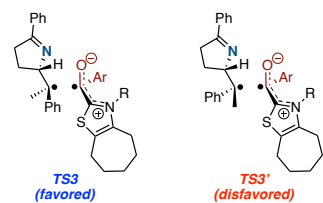
Since the radical coupling step is the rate-determining step, cyclized radical intermediate **INT8** or oxidized Breslow intermediate **INT4** can be trapped by radical traps such as PhSeSePh. As shown in **Figure 7.6c**, experimental mechanistic studies observed radical trapping of cyclized radical intermediate **INT8** by PhSeSePh. Both computational and experimental studies support that the rate-determining step is the radical coupling step.

In addition to describing the overall reaction pathway, we explored the origin of diastereoselectivity in the radical coupling. We found **TS3**, which forms the experimental product that is confirmed by X-ray crystallography, and **TS3'** forming its diastereomer (**Figure 7.7**). **TS3** is favored by 1.5 kcal/mol compared to **TS3'**, which is close to the experimental outcome (>19:1 d.r, approximately 1.7 kcal/mol). We think that the energy difference between **TS3** and **TS3'** is caused by favorable  $\pi$ - $\pi$  interactions, likely mainly dispersive attraction between phenyl of the cumene substructure and thiazole of the NHC substructure in **TS3** (**Figure 7.7c**). In contrast to **TS3**,  $\pi$ - $\pi$  interactions are not involved in **TS3'** (**Figure 7.7e**). **TS3'** is a perfectly staggered conformation as is generally favorable, but **TS3** can bring the two aromatics into appropriate attractive distances. For the validation of our hypothesis of  $\pi$ - $\pi$  interaction involvement in the diastereoselectivity-determining step, we conducted single point calculations of **TS3a** and **TS3a'** with the phenyl substituent replaced by H (**Figure 7.7d**).

A) Energy profile of the overall reaction

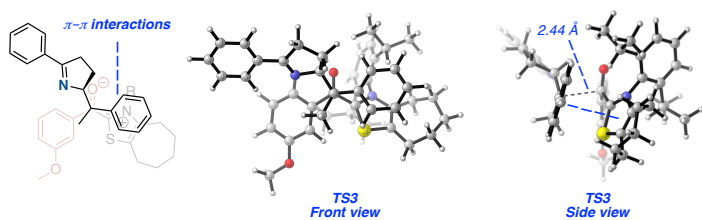


B) Comparison between computational and experimental results

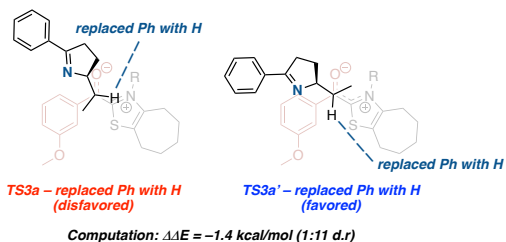


Experiment:  $\Delta\Delta G > 1.7$  kcal/mol ( $>19:1$  d.r)  
Computation:  $\Delta\Delta G = 1.5$  kcal/mol ( $13:1$  d.r)

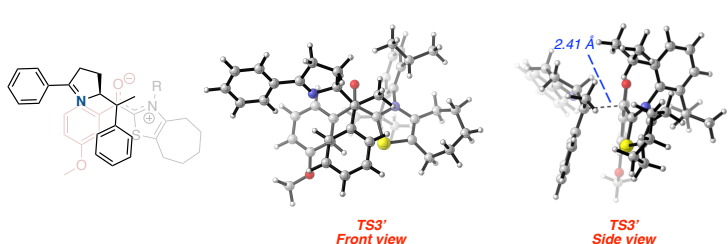
C) Structure of TS3



D) Energy difference between TS3 and TS3' in the absence of Ph



E) Structure of TS3'



<sup>a</sup>Computational studies are performed with (u)ωB97X-D/def2-tzvpp/SMD=DMSO//((u)ωB97X-D/def2-svp/SMD=DMSO at 298.15K. The unit of Gibbs free energies is kcal/mol.

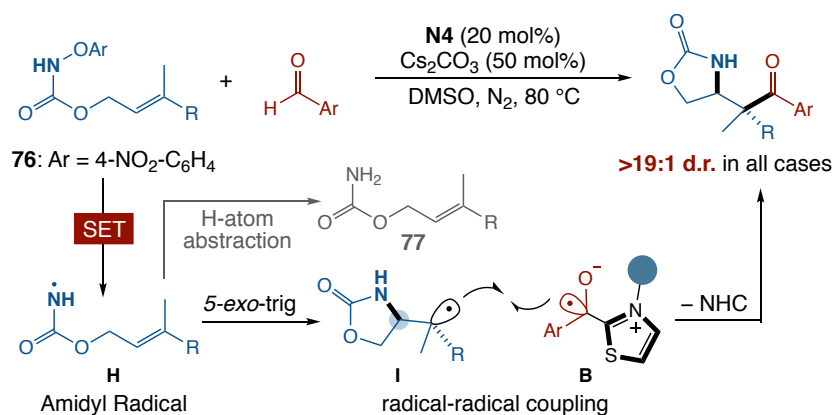
Figure 7.7 Computational mechanistic studies.



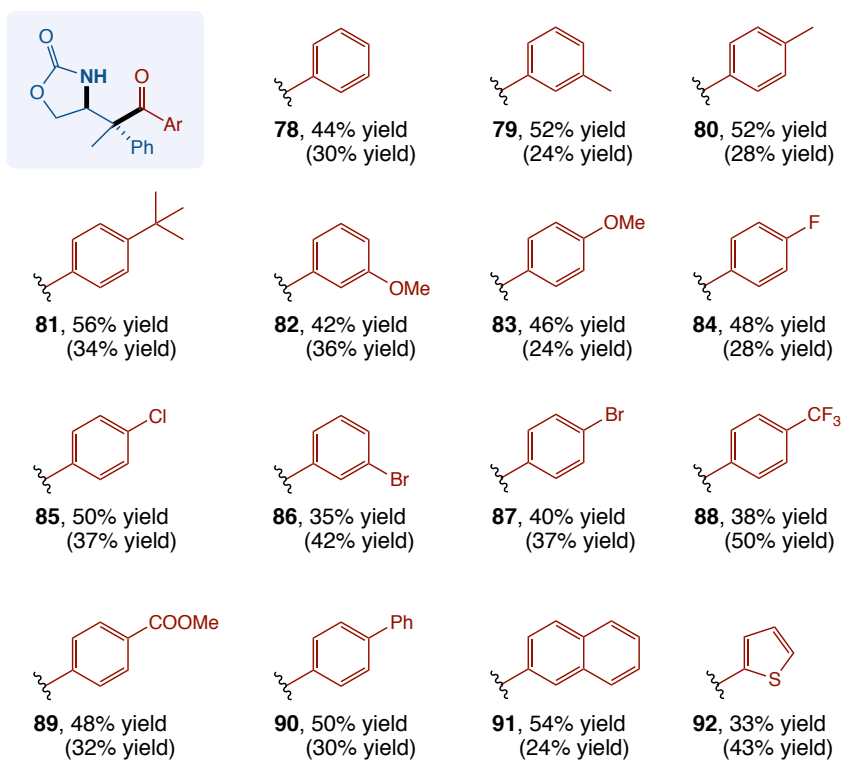
Here, **TS3a** became disfavored by 1.4 kcal/mol due to the unfavorable eclipsed structure. It shows that the role of  $\pi$ - $\pi$  interactions by the phenyl substituent is important to control the selectivity. Thus, we suggest  $\pi$ - $\pi$  interactions contribute to lower the energy of **TS3** relative to **TS3'**.

**Further Classes of Reactivity.** Building on the mechanistic understanding of this NHC-catalyzed radical reaction, we decided to evaluate whether this strategy could be applied to the generation of amidyl radicals. Gratifyingly, the diastereoselective amidoacylation of olefins was achieved (**Figure 7.8**). We hypothesized that electron-poor aryloxy-amide **76a** (R = Ph,  $E_{1/2} = -0.97$  V vs SCE) would be an ideal amidyl radical precursor.<sup>19b,d</sup> Upon SET reduction and homolysis of the N–O bond, the amidyl radical **H** is expected to undergo 5-*exo*-trig cyclization. The resultant C-centered radical **I** subsequently engages in radical–radical coupling with **B** to form the desired oxazolidinone derivative and regenerate the NHC catalyst. We anticipated that the NHC-bound ketyl radical **B** would differentiate the stereochemistry of **I**, affording the cyclic carbamate with excellent diastereoselectivity.

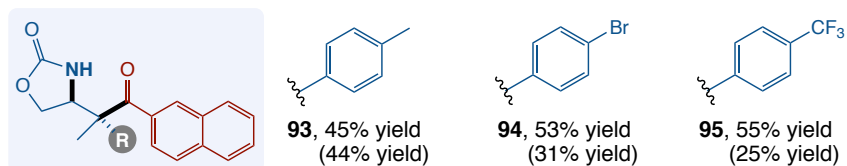
The desired transformation was feasible to afford the coupling product by employing reaction conditions similar to the ones presented above. However, we realized that the amidyl radical may undergo HAT to provide the amide byproduct **77** owing to its electrophilic nature.<sup>24</sup> This competing pathway led to a decrease in the formation of amidoacylation products. Scope investigation demonstrated that a series of aldehydes bearing electron-rich or electron-deficient groups at the para- and meta-positions were compatible with the reaction, giving **78–90** in good yields. Additionally, the oxazolidinone **91** generated from 2-naphthaldehyde afforded single crystal, enabling X-ray structure determination to confirm the relative stereochemistry.



### Aldehyde Scope



### Tether Modifications



<sup>a</sup>Reaction conditions: *O*-aryl carbamate **76** (0.2 mmol), aldehyde (1.5 equiv), NHC precatalyst **N4** (20 mol %), Cs<sub>2</sub>CO<sub>3</sub> (50 mol %) in DMSO (2.0 mL) at 80 °C for 12 h. Isolated product yields. Diastereomeric ratio (d.r.) values were determined by <sup>1</sup>H NMR. Yields of the amide byproduct are given in parentheses.

**Figure 7.8** Diastereoselective amidoacylation of olefins.<sup>a</sup>

In regard to the R on the alkene moiety in **76**, several phenyl rings were applicable to the reaction. Importantly, we obtained oxazolidinone derivatives with excellent diastereoselectivity, further demonstrating the significance of this organocatalytic system.

## 7.5 Conclusion

In summary, we have developed a synthetic method for the diastereoselective iminoacylation and amidoacylation of trisubstituted alkenes under covalent-based NHC radical catalysis. Central to the success of this strategy is the formation of a thiazolium derived Breslow intermediate with proper sterics, which not only promotes single-electron transfer but also controls the diastereoselectivity. This approach provides ready access to functionalized pyrrolines, which are easily elaborated to the synthesis of pyrrolidines. The combined experimental and computational investigations of this organocatalytic system provide an understanding of how diastereoselective radical–radical coupling occurs and suggest that the radical coupling step is the diastereoselectivity- and rate-determining step. A series of acyl thiazoliums, the most oxidized Breslow-type derivatives, were synthesized for cyclic voltammetry studies, indicating redox potentials as negative as  $-1.36$  V versus SCE. Further application of this strategy to enantioselective radical-involved transformations is anticipated in view of the tremendous success of chiral NHC in asymmetric organocatalysis.

## 7.6 References

- (1) For selected reviews, see: (a) Kitamura, M.; Narasaka, K. Catalytic Radical Cyclization of Oximes Induced by One-Electron Transfer. *Bull. Chem. Soc. Jpn.* **2008**, *81*, 539–547. (b) Zard, S. Z. Recent Progress in the Generation and Use of Nitrogen-Centred Radicals. *Chem. Soc. Rev.* **2008**, *37*, 1603–1618. (c) Walton, J. C. The Oxime Portmanteau Motif: Released Heteroradicals Undergo Incisive EPR Interrogation and Deliver Diverse Heterocycles. *Acc. Chem. Res.* **2014**, *47*, 1406–1416. (d) Walton, J. C. Functionalised Oximes: Emergent Precursors for Carbon-, Nitrogen- and Oxygen-Centred Radicals. *Molecules* **2016**, *21*, 63.
- (2) For recent reviews, see: (a) Chen, J.-R.; Hu, X.-Q.; Lu, L.-Q.; Xiao, W.-J. Visible Light Photoredox-Controlled Reactions of N-Radicals and Radical Ions. *Chem. Soc. Rev.* **2016**, *45*, 2044–2056. (b) Xiong, T.; Zhang, Q. *Chem. Soc. Rev.* **2016**, *45*, 3069–3087. (c) Davies, J.; Morcillo, S. P.; Douglas, J. J.; Leonori, D. Hydroxylamine Derivatives as Nitrogen-Radical Precursors in Visible-Light Photochemistry. *Chem. Eur. J.* **2018**, *24*, 12154–12163. (d) Jiang, H.; Studer, A. Chemistry With N-Centered Radicals Generated by Single-Electron Transfer-Oxidation Using Photoredox Catalysis. *CCS Chem.* **2019**, *1*, 38–49. (e) Yu, X.-Y.; Zhao, Q.-Q.; Chen, J.; Xiao, W.-J.; Chen, J.-R. When Light Meets Nitrogen-Centered Radicals: From Reagents to Catalysts. *Acc. Chem. Res.* **2020**, *53*, 1066–1083. (f) Song, C.; Shen, X.; Yu, F.; He, Y.; Yu, S. Generation and Application of Iminyl Radicals from Oxime Derivatives Enabled by Visible Light Photoredox Catalysis. *Chin. J. Org. Chem.* **2020**, *40*, 3748–3759. (g) Kwon, K.; Simons, R. T.; Nandakumar, M.; Roizen, J. L. Strategies to Generate Nitrogen-Centered Radicals That May Rely on Photoredox Catalysis: Development in Reaction Methodology and Applications in Organic Synthesis. *Chem. Rev.* **2022**, *122*, 2353–2428. (h) Pratley, C.; Fenner,

S.; Murphy, J. A. Nitrogen-Centered Radicals in Functionalization of  $sp^2$  Systems: Generation, Reactivity, and Applications in Synthesis. *Chem. Rev.* **2022**, *122*, 8181–8260.

(3) (a) Welsch, M. E.; Snyder, S. A.; Stockwell, B. R. Privileged Scaffolds for Library Design and Drug Discovery. *Curr. Opin. Chem. Biol.* **2010**, *14*, 347–361. (b) Vitaku, E.; Smith, D. T.; Njardarson, J. T. Analysis of the Structural Diversity, Substitution Patterns, and Frequency of Nitrogen Heterocycles among U.S. FDA Approved Pharmaceuticals. *J. Med. Chem.* **2014**, *57*, 10257–10274.

(4) For recent selected examples, see: (a) Markey, S. J.; Lewis, W.; Moody, C. J. A New Route to  $\alpha$ -Carbolines Based on  $6\pi$ -Electrocyclization of Indole-3-alkenyl Oximes. *Org. Lett.* **2013**, *15*, 6306–6308. (b) Mikami, T.; Narasaka, K. Photochemical Transformation of  $\gamma,\delta$ -Unsaturated Ketone *O*-(*p*-Cyanophenyl)oximes to 3,4-Dihydro-2*H*-pyrrole Derivatives. *Chem. Lett.* **2000**, 338–339. (c) McBurney, R. T.; Walton, J. C. Dissociation or Cyclization: Options for a Triad of Radicals Released from Oxime Carbamates. *J. Am. Chem. Soc.* **2013**, *135*, 7349–7354.

(5) For selected reviews, see: (a) Narayanam, J. M. R.; Stephenson, C. R. J. Visible Light Photoredox Catalysis: Applications in Organic Synthesis. *Chem. Soc. Rev.* **2011**, *40*, 102–113. (b) Prier, C. K.; Rankic, D. A.; MacMillan, D. W. C. Visible Light Photoredox Catalysis with Transition Metal Complexes: Applications in Organic Synthesis. *Chem. Rev.* **2013**, *113*, 5322–5363. (c) Skubi, K. L.; Blum, T. R.; Yoon, T. P. Dual Catalysis Strategies in Photochemical Synthesis. *Chem. Rev.* **2016**, *116*, 10035–10074.

(6) (a) Davies, J.; Booth, S. G.; Essafi, S.; Dryfe, R. A. W.; Leonori, D. Visible-Light-Mediated Generation of Nitrogen-Centered Radicals: Metal-Free Hydroimination and Iminohydroxylation Cyclization Reactions. *Angew. Chem. Int. Ed.* **2015**, *54*, 14017–14021. (b) Jiang, H.; Studer, A. Iminyl-Radicals by Oxidation of  $\alpha$ -Imino-oxy Acids: Photoredox-Neutral Alkene

Carboimination for the Synthesis of Pyrrolines. *Angew. Chem. Int. Ed.* **2017**, *56*, 12273–12276.

(c) Davies, J.; Sheikh, N. S.; Leonori, D. Photoredox Imino Functionalizations of Olefins. *Angew. Chem. Int. Ed.* **2017**, *56*, 13361–13365. (d) Usami, K.; Yamaguchi, E.; Tada, N.; Itoh, A.

Visible-Light-Mediated Iminyl Radical Generation from Benzyl Oxime Ether: Synthesis of Pyrroline via Hydroimination Cyclization. *Org. Lett.* **2018**, *20*, 5714–5717.

(7) (a) Jiang, H.; An, X.; Tong, K.; Zheng, T.; Zhang, Y.; Yu, S. Visible-Light-Promoted Iminyl-Radical Formation from Acyl Oximes: A Unified Approach to Pyridines, Quinolines, and Phenanthridines. *Angew. Chem. Int. Ed.* **2015**, *54*, 4055–4059. (b) Cai, S.-H.; Xie, J.-H.; Song, S.;

Ye, L.; Feng, C.; Loh, T.-P. Visible-Light-Promoted Carboimination of Unactivated Alkenes for the Synthesis of Densely Functionalized Pyrroline Derivatives. *ACS Catal.* **2016**, *6*, 5571–5574.

(c) Shu, W.; Nevado, C. Visible-Light-Mediated Remote Aliphatic C–H Functionalizations through a 1,5-Hydrogen Transfer Cascade. *Angew. Chem. Int. Ed.* **2017**, *56*, 1881–1884. (d) Yu, X.-Y.; Chen, J.-R.; Wang, P.-Z.; Yang, M.-N.; Liang, D.; Xiao, W.-J. A Visible-Light-Driven Iminyl Radical-Mediated C–C Single Bond Cleavage/Radical Addition Cascade of Oxime Esters. *Angew. Chem., Int. Ed.* **2018**, *57*, 738–743.

(8) Shen, X.; Huang, C.; Yuan, X.-A.; Yu, S. Diastereoselective and Stereodivergent Synthesis of 2-Cinnamylpyrrolines Enabled by Photoredox-Catalyzed Iminoalkenylation of Alkenes.

*Angew. Chem. Int. Ed.* **2021**, *60*, 9672–9679.

(9) Leifert, D.; Studer, A. The Persistent Radical Effect in Organic Synthesis. *Angew. Chem. Int. Ed.* **2020**, *59*, 74–108.

(10) For selected reviews, see: (a) Enders, D.; Niemeier, O.; Henseler, A. Organocatalysis by N-Heterocyclic Carbenes. *Chem. Rev.* **2007**, *107*, 5606–5655. (b) Hopkinson, M. N.; Richter, C.; Schedler, M.; Glorius, F. An Overview of N-Heterocyclic Carbenes. *Nature* **2014**, *510*, 485–496.

(c) Flanigan, D. M.; Romanov-Michailidis, F.; White, N. A.; Rovis, T. Organocatalytic Reactions Enabled by N-Heterocyclic Carbenes. *Chem. Rev.* **2015**, *115*, 9307–9387. (d) Wang, M. H.; Scheidt, K. A. Cooperative Catalysis and Activation with N-Heterocyclic Carbenes. *Angew. Chem. Int. Ed.* **2016**, *55*, 14912–14922. (e) Chen, X.-Y.; Gao, Z.-H.; Ye, S. Bifunctional N-Heterocyclic Carbenes Derived from L-Pyroglutamic Acid and Their Applications in Enantioselective Organocatalysis. *Acc. Chem. Res.* **2020**, *53*, 690–702. (f) Chen, X.; Wang, H.; Jin, Z.; Chi, Y. R. N-Heterocyclic Carbene Organocatalysis: Activation Modes and Typical Reactive Intermediates. *Chin. J. Chem.* **2020**, *38*, 1167–1202.

(11) (a) Breslow, R. On the Mechanism of Thiamine Action. IV. Evidence from Studies on Model Systems. *J. Am. Chem. Soc.* **1958**, *80*, 3719–3726. (b) Enders, D.; Niemeier, O.; Balensiefer, T. Asymmetric Intramolecular Crossed-Benzoin Reactions by N-Heterocyclic Carbene Catalysis. *Angew. Chem. Int. Ed.* **2006**, *45*, 1463–1467.

(12) (a) Nakanishi, I.; Itoh, S.; Suenobu, T.; Fukuzumi, S. Electron Transfer Properties of Active Aldehydes Derived from Thiamin Coenzyme Analogues. *Chem. Commun.* **1997**, 1927–1928. (b) Nakanishi, I.; Itoh, S.; Suenobu, T.; Fukuzumi, S. Direct Observation of Radical Intermediates While Investigating the Redox Behavior of Thiamin Coenzyme Models. *Angew. Chem. Int. Ed.* **1998**, *37*, 992–994. (c) Nakanishi, I.; Itoh, S.; Fukuzumi, S. Electron-Transfer Properties of Active Aldehydes of Thiamin Coenzyme Models, and Mechanism of Formation of the Reactive Intermediates. *Chem. Eur. J.* **1999**, *5*, 2810–2818. (d) Delfau, L.; Nichilo, S.; Molton, F.; Broggi, J.; Tomás-Mendivil, E.; Martin, D. Critical Assessment of the Reducing Ability of Breslow-type Derivatives and Implications for Carbene-Catalyzed Radical Reactions. *Angew. Chem. Int. Ed.* **2021**, *60*, 26783–26789.

(13) For selected reviews on NHC radical catalysis, see: (a) Ishii, T.; Nagao, K.; Ohmiya, H. Recent Advances in N-Heterocyclic Carbene-based Radical Catalysis. *Chem. Sci.* **2020**, *11*, 5630–5636. (b) Ohmiya, H. N-Heterocyclic Carbene-Based Catalysis Enabling Cross-Coupling Reactions. *ACS Catal.* **2020**, *10*, 6862–6869. (c) Dai, L.; Ye, S. Recent Advances in N-Heterocyclic Carbene-Catalyzed Radical Reactions. *Chin. Chem. Lett.* **2021**, *32*, 660–667. (d) Li, Q.-Z.; Zeng, R.; Han, B.; Li, J.-L. Single-Electron Transfer Reactions Enabled by N-Heterocyclic Carbene Organocatalysis. *Chem. Eur. J.* **2021**, *27*, 3238–3250. (e) Liu, K.; Schwenger, M.; Studer, A. Radical NHC Catalysis. *ACS Catal.* **2022**, *12*, 11984–11999.

(14) (a) Guin, J.; De Sarkar, S.; Grimme, S.; Studer, A. Biomimetic Carbene-Catalyzed Oxidations of Aldehydes Using TEMPO. *Angew. Chem. Int. Ed.* **2008**, *47*, 8727–8730. (b) De Sarkar, S.; Grimme, S.; Studer, A. NHC Catalyzed Oxidations of Aldehydes to Esters: Chemoselective Acylation of Alcohols in Presence of Amines. *J. Am. Chem. Soc.* **2010**, *132*, 1190–1191. (c) White, N. A.; Rovis, T. Enantioselective N-Heterocyclic Carbene-Catalyzed  $\beta$ -Hydroxylation of Enals Using Nitroarenes: An Atom Transfer Reaction That Proceeds via Single Electron Transfer. *J. Am. Chem. Soc.* **2014**, *136*, 14674–14677. (d) White, N. A.; Rovis, T. Oxidatively Initiated NHC-Catalyzed Enantioselective Synthesis of 3,4-Disubstituted Cyclopentanones from Enals. *J. Am. Chem. Soc.* **2015**, *137*, 10112–10115. (e) Li, B.-S.; Wang, Y.; Proctor, R. S. J.; Zhang, Y.; Webster, R. D.; Yang, S.; Song, B.; Chi, Y. R. Carbene-Catalysed Reductive Coupling of Nitrobenzyl Bromides and Activated Ketones or Imines via Single-Electron-Transfer Process. *Nat. Commun.* **2016**, *7*, 12933–12940. (f) Chen, X.-Y.; Chen, K.-Q.; Sun, D.-Q.; Ye, S. N-Heterocyclic Carbene-Catalyzed Oxidative [3 + 2] Annulation of Dioxindoles and Enals: Cross Coupling of Homoenolate and Enolate. *Chem. Sci.* **2017**, *8*, 1936–1941. (g) Yang, W.; Hu, W.; Dong, X.; Li, X.; Sun, J. N-Heterocyclic Carbene Catalyzed  $\gamma$ -



Dihalomethylenation of Enals by Single-Electron Transfer. *Angew. Chem. Int. Ed.* **2016**, *55*, 15783–15786. (h) Wu, X.; Zhang, Y.; Wang, Y.; Ke, J.; Jeret, M.; Reddi, R. N.; Yang, S.; Song, B.-A.; Chi, Y. R. Polyhalides as Efficient and Mild Oxidants for Oxidative Carbene Organocatalysis by Radical Processes. *Angew. Chem. Int. Ed.* **2017**, *56*, 2942–2946.

(15) (a) Ishii, T.; Kakeno, Y.; Nagao, K.; Ohmiya, H. *N*-Heterocyclic Carbene-Catalyzed Decarboxylative Alkylation of Aldehydes. *J. Am. Chem. Soc.* **2019**, *141*, 3854–3858. (b) Ishii, T.; Ota, K.; Nagao, K.; Ohmiya, H. *N*-Heterocyclic Carbene-Catalyzed Radical Relay Enabling Vicinal Alkylacylation of Alkenes. *J. Am. Chem. Soc.* **2019**, *141*, 14073–14077. (c) Kakeno, Y.; Kusakabe, M.; Nagao, K.; Ohmiya, H. Direct Synthesis of Dialkyl Ketones from Aliphatic Aldehydes through Radical *N*-Heterocyclic Carbene Catalysis. *ACS Catal.* **2020**, *10*, 8524–8529. (d) Matsuki, Y.; Ohnishi, N.; Kakeno, Y.; Takemoto, S.; Ishii, T.; Nagao, K.; Ohmiya, H. Aryl Radical-Mediated *N*-Heterocyclic Carbene Catalysis. *Nat. Commun.* **2021**, *12*, 3848.

(16) For selected examples on radical NHC catalysis, see: (a) Li, J.-L.; Liu, Y.-Q.; Zou, W.-L.; Zeng, R.; Zhang, X.; Liu, Y.; Han, B.; He, Y.; Leng, H.-J.; Li, Q.-Z. Radical Acylfluoroalkylation of Olefins through *N*-Heterocyclic Carbene Organocatalysis. *Angew. Chem. Int. Ed.* **2020**, *59*, 1863–1870. (b) Kim, I.; Im, H.; Lee, H.; Hong, S. *N*-Heterocyclic Carbene-Catalyzed Deaminative Cross-Coupling of Aldehydes with Katritzky Pyridinium Salts. *Chem. Sci.* **2020**, *11*, 3192–3197. (c) Gao, Y.; Quan, Y.; Li, Z.; Gao, L.; Zhang, Z.; Zou, X.; Yan, R.; Qu, Y.; Guo, K. Organocatalytic Three-Component 1,2-Cyanoalkylacylation of Alkenes via Radical Relay. *Org. Lett.* **2021**, *23*, 183–189. (d) Yang, H.-B.; Wan, D.-H. C–C Bond Acylation of Oxime Ethers via NHC Catalysis. *Org. Lett.* **2021**, *23*, 1049–1053. (e) Li, Z.; Huang, M.; Zhang, X.; Chen, J.; Huang, Y. *N*-Heterocyclic Carbene-Catalyzed Four-Component Reaction: Chemoselective C<sub>radical</sub>–C<sub>radical</sub> Relay Coupling Involving the Homoenate Intermediate. *ACS*

*Catal.* **2021**, *11*, 10123–10130. (f) Li, Q.-Z.; Zeng, R.; Fan, Y.; Liu, Y.-Q.; Qi, T.; Zhang, X.; Li, J.-L. Remote C(sp<sup>3</sup>)–H Acylation of Amides and Cascade Cyclization via N-Heterocyclic Carbene Organocatalysis. *Angew. Chem. Int. Ed.* **2022**, *61*, e202116629.

(17) For selected reviews on dual NHC/photocatalysis, see: (a) Liu, Q.; Chen, X.-Y. Dual N-Heterocyclic Carbene/Photocatalysis: A New Strategy for Radical Processes. *Org. Chem. Front.* **2020**, *7*, 2082–2087. (b) Mavroskoufis, A.; Jakob, M.; Hopkinson, M. N. Light-Promoted Organocatalysis with N-Heterocyclic Carbenes. *ChemPhotoChem* **2020**, *4*, 5147–5153. (c) Liu, J.; Xing, X.-N.; Huang, J.-H.; Lu, L.-Q.; Xiao, W.-J. Light Opens.; a New Window for N-Heterocyclic Carbene Catalysis. *Chem. Sci.* **2020**, *11*, 10605–10613.

(18) For selected examples on dual NHC/photocatalysis, see: (a) Mavroskoufis, A.; Rajes, K.; Golz, P.; Agrawal, A.; Ruß, V.; Götze, J. P.; Hopkinson, M. N. N-Heterocyclic Carbene Catalyzed Photoenolization/Diels–Alder Reaction of Acid Fluorides. *Angew. Chem. Int. Ed.* **2020**, *59*, 3190–3194. (b) Davies, A. V.; Fitzpatrick, K. P.; Betori, R. C.; Scheidt, K. A. Combined Photoredox and Carbene Catalysis for the Synthesis of Ketones from Carboxylic Acids. *Angew. Chem. Int. Ed.* **2020**, *59*, 9143–9148. (c) Meng, Q.-Y.; Döben, N.; Studer, A. Cooperative NHC and Photoredox Catalysis for the Synthesis of  $\beta$ -Trifluoromethylated Alkyl Aryl Ketones. *Angew. Chem. Int. Ed.* **2020**, *59*, 19956–19960. (d) Liu, M.-S.; Shu, W. Catalytic, Metal-Free Amide Synthesis from Aldehydes and Imines Enabled by a Dual-Catalyzed Umpolung Strategy under Redox-Neutral Conditions. *ACS Catal.* **2020**, *10*, 12960–12966. (e) Liu, K.; Studer, A. Direct  $\alpha$ -Acylation of Alkenes via N-Heterocyclic Carbene, Sulfinate, and Photoredox Cooperative Triple Catalysis. *J. Am. Chem. Soc.* **2021**, *143*, 4903–4909. (f) Meng, Q.-Y.; Lezius, L.; Studer, A. Benzylic C–H Acylation by Cooperative NHC and Photoredox Catalysis. *Nat. Commun.* **2021**, *12*, 2068. (g) Sato, Y.; Goto, Y.; Nakamura, K.; Miyamoto, Y.;

Sumida, Y.; Ohmiya, H. Light-Driven N-Heterocyclic Carbene Catalysis Using Alkylborates. *ACS Catal.* **2021**, *11*, 12886–12892. (h) Bay, A. V.; Fitzpatrick, K. P.; González-Montiel, G. A.; Farah, A. O.; Cheong, P. H.-Y.; Scheidt, K. A. Light-Driven Carbene Catalysis for the Synthesis of Aliphatic and  $\alpha$ -Amino Ketones. *Angew. Chem. Int. Ed.* **2021**, *60*, 17925–17931. (i) Zuo, Z.; Daniliuc, C. G.; Studer, A. Cooperative NHC/Photoredox Catalyzed Ring-Opening of Aryl Cyclopropanes to 1-Aroyloxy-3-Acylated Alkanes. *Angew. Chem. Int. Ed.* **2021**, *60*, 25252–25257. (j) Yu, X.; Meng Q.-Y.; Daniliuc, C. G.; Studer, A. Aroyl Fluorides as Bifunctional Reagents for Dearomatizing Fluoroarylation of Benzofurans. *J. Am. Chem. Soc.* **2022**, *144*, 7072–7079.

(19) For recent examples, see: (a) Miller, D. C.; Choi, G. J.; Orbe, H. S.; Knowles, R. R. Catalytic Olefin Hydroamidation Enabled by Proton-Coupled Electron Transfer. *J. Am. Chem. Soc.* **2015**, *137*, 13492–13495. (b) Davies, J.; Svejstrup, T. D.; Fernandez Reina, D.; Sheikh, N. S.; Leonori, D. Visible-Light-Mediated Synthesis of Amidyl Radicals: Transition Metal-Free Hydroamination and *N*-Arylation Reactions. *J. Am. Chem. Soc.* **2016**, *138*, 8092–8095. (c) Ren, X.; Guo, Q.; Chen, J.; Xie, H.; Xu, Q.; Lu, Z. Visible-Light Promoted Diastereodivergent Intramolecular Oxyamidation of Alkenes. *Chem. Eur. J.* **2016**, *22*, 18695–18699. (d) Fernandez Reina, D.; Dauncey, E. M.; Morcillo, S. P.; Svejstrup, T. D.; Popescu, M. V.; Douglas, J. J.; Sheikh, N. S.; Leonori, D. Visible-Light-Mediated 5-exo-dig Cyclizations of Amidyl Radicals. *Eur. J. Org. Chem.* **2017**, *2017*, 2108–2111. (e) Nguyen, S. T.; Zhu, Q.; Knowles, R. R. PCET-Enabled Olefin Hydroamidation Reactions with *N*-Alkyl Amides. *ACS Catal.* **2019**, *9*, 4502–4507. (f) Zheng, S.; Zhang, S.-Q.; Saednia, B.; Zhou, J.; Anna, J. M.; Hong, X.; Molander, G. A. Diastereoselective Olefin Amidoacylation via Photoredox PCET/Nickel-Dual Catalysis: Reaction Scope and Mechanistic Insights. *Chem. Sci.* **2020**, *11*, 4131–4137.

(20) Michael, J. P. Indolizidine and Quinolizidine Alkaloids. *Nat. Prod. Rep.* **2008**, *25*, 139–165.

(21) Ren, S.-C.; Lv, W.-X.; Yang, X.; Yan, J.-L.; Xu, J.; Wang, F.-X.; Hao, L.; Chai, H.; Jin, Z.; Chi, Y. R. Carbene-Catalyzed Alkylation of Carboxylic Esters via Direct Photoexcitation of Acyl Azolium Intermediates. *ACS Catal.* **2021**, *11*, 2925–2934.

(22) For a ground-state electron transfer between **A1** and **1a**, the Gibbs free energy ( $\Delta G_{\text{SET}}$ ) is expressed by the equation:  $\Delta G_{\text{SET}} = E^{\text{ox}}[\mathbf{B1/A1}] - E^{\text{red}}[\mathbf{1a/1a}^{\bullet-}] + \Delta E_{\text{coulombic}}$ .

(23) (a) Farid, S.; Dinnocenzo, J. P.; Merkel, P. B.; Young, R. H.; Shukla, D.; Guirado, G. Reexamination of the Rehm–Weller Data Set Reveals Electron Transfer Quenching That Follows a Sandros–Boltzmann Dependence on Free Energy. *J. Am. Chem. Soc.* **2011**, *133*, 11580–11587. (b) Buzzetti, L.; Crisenza, G. E. M.; Melchiorre, P. Mechanistic Studies in Photocatalysis. *Angew. Chem. Int. Ed.* **2019**, *58*, 3730–3747.

(24) (a) Sutcliffe, R.; Griller, D.; Lessard, J.; Ingold, K. U. The Structure of Amidyl Radicals. Evidence for the  $\pi$ -Electronic Ground State and for Twist about the Acyl-Nitrogen Bond by Electron Paramagnetic Resonance Spectroscopy. *J. Am. Chem. Soc.* **1981**, *103*, 624–628. (b) Esker, J. L.; Newcomb, M. Chemistry of Amidyl Radicals Produced from N-Hydroxypyridine-2-thione Imidate Esters. *J. Org. Chem.* **1993**, *58*, 4933–4940. (c) Horner, J. H.; Musa, O. M.; Bouvier, A.; Newcomb, M. Absolute Kinetics of Amidyl Radical Reactions. *J. Am. Chem. Soc.* **1998**, *120*, 7738–7748.

## CHAPTER EIGHT

### **Divergent Radical and Cationic Pathways in C(*sp*<sup>3</sup>)-H Bond Oxygenation of Bicyclic and Spirocyclic Hydrocarbons Bearing Cyclopropane Moieties Promoted by Dioxiranes**

#### **8.1 Contributions**

This is an unpublished manuscript by Galeotti, M., Lee, W., Sisti, S., Casciotti, M., Salamone, M., Houk, K. N., Bietti, M. This project was a collaborative work between the laboratories of Professor Kendall N. Houk at the University of California, Los Angeles and Professor Massimo Bietti at the University of Rome, Tor Vergata. Marco Galeotti and I are the co-first authors of this manuscript. As a computational organic chemist, I conducted all computational experiments while Marco Galeotti performed the majority of the experimental work. Marco Galeotti received experimental assistance from Sergio Sisti, Martina Casciotti, and Michela Salamone.

#### **8.2 Abstract**

Through the application of experimental and computational methods, we have investigated mechanisms of the C(*sp*<sup>3</sup>)-H bond oxygenation in bicyclic and spirocyclic hydrocarbons via 3-ethyl-3-(trifluoromethyl)dioxirane (ETFDO). We show the significant influence of hyperconjugative effects on site- and stereo-selective oxygenations. Furthermore, our work demonstrates the presence of cationic intermediates in ETFDO oxygenations. Importantly, this elucidates the involvement of electron transfer pathways in dioxirane-mediated aliphatic C-H bond oxygenations.

### 8.3 Introduction

The cyclopropyl group is an important and versatile motif that, because of its characteristic structural and bonding features,<sup>1</sup> when introduced into organic molecules can modify their properties and provide moreover access to a variety of useful synthetic transformations.

Accordingly, cyclopropane containing molecules are finding increasing application in organic synthesis,<sup>2</sup> in drug development,<sup>3</sup> and as functional molecules in different fields.<sup>4</sup> The cyclopropyl group is also present in several natural products including terpenoids, steroids and alkaloids, among which, many show biological activity and may serve as potential drug leads.<sup>5</sup> A promising approach for structural diversification of cyclopropane containing molecules is represented by C(*sp*<sup>3</sup>)-H bond functionalization, a mainstream topic of modern synthetic chemistry.<sup>6</sup> The presence of cyclopropyl groups has been shown to direct functionalization at adjacent sites via hyperconjugative activation, where overlap between a cyclopropane C-C bonding orbital and the  $\sigma^*$  antibonding orbital of an  $\alpha$ -C-H activates this bond toward functionalization (**Figure 8.1a**), providing a powerful handle to implement site-selectivity in these reactions.<sup>6a</sup>

Concerted insertion or two step hydrogen atom transfer (HAT) strategies are typically amenable for this purpose. In the latter case however, because the intermediate  $\alpha$ -cyclopropyl carbon radicals formed in the HAT step are known to undergo rapid rearrangement,<sup>7</sup> the procedure is limited to the use of reagents that ensure very fast radical capture, preventing competitive unimolecular pathways and delivering the unrearranged functionalized product. Metal-oxo species,<sup>8</sup> dioxiranes,<sup>9</sup> and oxaziridines<sup>10</sup> are examples of such reagents, able to promote stereoretentive C(*sp*<sup>3</sup>)-H oxygenations.

Along these lines, the C–H bond oxygenation of linear, bicyclic and spirocyclic substrates bearing cyclopropane moieties has been studied employing a variety of oxygenation reagents.<sup>11</sup> High selectivity for hydroxylation and/or ketonization at the activated  $\alpha$ -methylenes over other sites has been generally observed. Similar selectivity patterns have been observed in dihalocarbene insertions into the C( $sp^3$ )–H bonds of hydrocarbons bearing cyclopropane moieties.<sup>12</sup>

In the framework of synthetically useful procedures, the full potential of this activation is witnessed by the results obtained by White in the site-selective C–H bond ketonization of a terpenoid derivative,<sup>11f</sup> and by Baran in the site-selective and stereoselective C–H bond hydroxylation employed in an intermediate step of the total synthesis of (+)-phorbol (**Figure 8.1a**).<sup>13</sup> In the former example, hyperconjugation synergistically cooperates with electronic effects to direct oxidation with H<sub>2</sub>O<sub>2</sub> catalyzed by the Fe (*R,R*)-pdp complex, toward the  $\alpha$ -methylene site that, albeit sterically more hindered, is most remote from the carbonyl group. In the latter one, hydroxylation promoted by 3-methyl-3-(trifluoromethyl)dioxirane (TFDO) selectively occurs at the C–H bond of the  $\alpha$ -methylene that is *cis* to the cyclopropane moiety, that is activated by optimal hyperconjugative overlap.

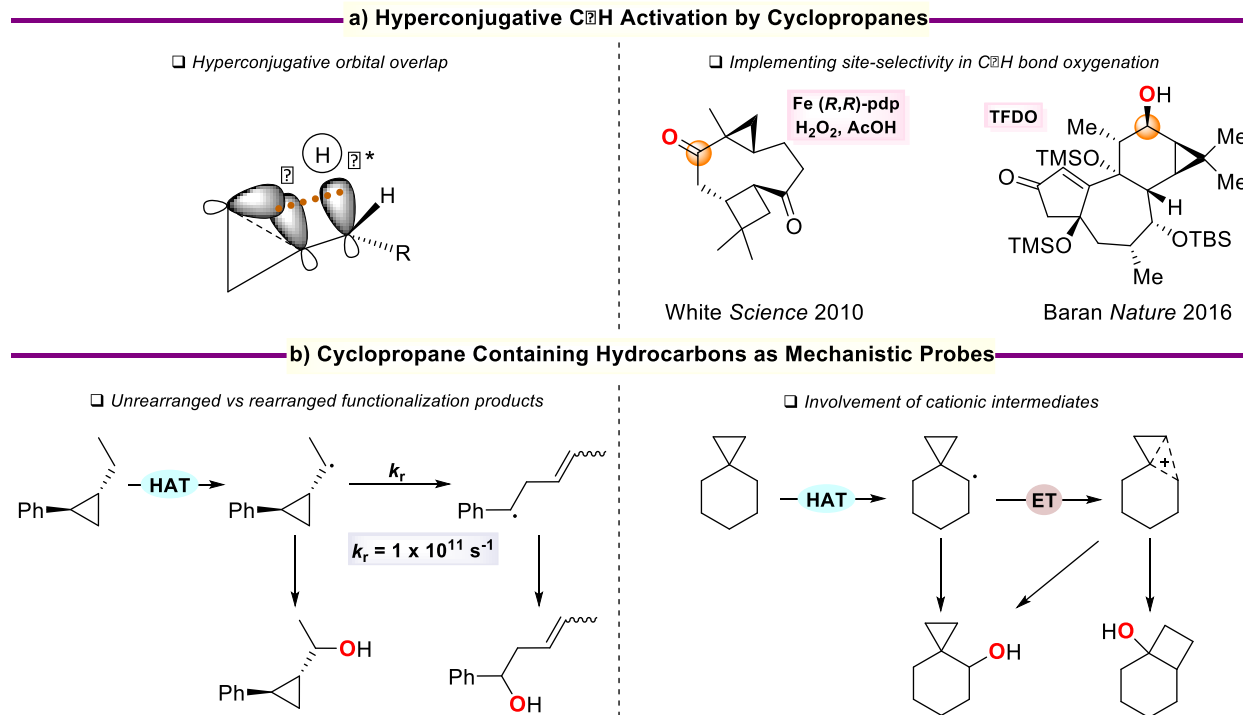


**Figure 8.1** Use of cyclopropyl containing substrates. a) To implement selectivity in HAT-based C–H bond functionalization procedures. b) To probe mechanisms.

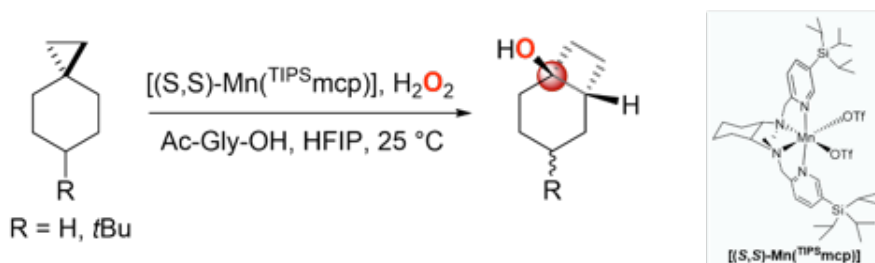
Because of the abovementioned tendency of  $\alpha$ -cyclopropyl carbon radicals to undergo rapid rearrangement,<sup>7</sup> cyclopropane containing substrates are coveted mechanistic probes to study the involvement of radical intermediates in a reaction,<sup>14</sup> to assess the concerted, radical and/or cationic nature of enzymatic and biomimetic reaction mechanisms,<sup>8a,15</sup> as well as to calibrate the rates of competing radical reactions (**Figure 8.1b**). For example, with *trans*-1-ethyl-2-phenylcyclopropane, the carbon radical formed following HAT from the side-chain ethyl group undergoes ring opening with  $k_r = 1 \times 10^{11} \text{ s}^{-1}$ , and this probe has been employed to calibrate the rate constant for recombination of the radical couple formed in the first step of its reaction with dimethyldioxirane (DMDO).<sup>16</sup> A rate constant  $k = 4 \times 10^{12} \text{ s}^{-1}$  has been estimated at room temperature corresponding to a lifetime of the radical couple of 200 fs.

With spiro[2.5]octane, the corresponding  $\alpha$ -cyclopropyl carbon radical undergoes cyclopropane ring-opening with  $k_r = 5 \times 10^7 \text{ s}^{-1}$ .<sup>15a</sup> In the framework of the oxygenation of this substrate



promoted by metal-oxo species,<sup>11f</sup> dioxiranes,<sup>11e</sup> ozone,<sup>11a</sup> and cytochrome P450 enzymes,<sup>15a</sup> no evidence for the formation of products deriving from radical rearrangement has been observed, in line with the relatively low value of  $k_r$  that prevents competition of this pathway with the radical capture or radical recombination steps.

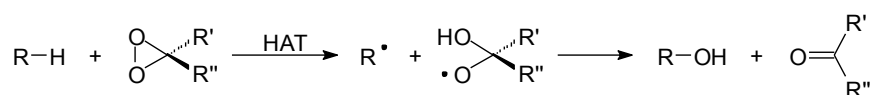
With substrates such as spiro[2.5]octane and bicyclo[4.1.0]heptane (norcarane), the product distribution can also provide information on the possible involvement of cationic intermediates, revealing the occurrence of competitive ET steps.<sup>15a</sup> In the specific case of spiro[2.5]octane, formation of bicyclo[4.2.0]octan-1-ol can provide conclusive evidence for the involvement of a cationic intermediate. To the best of our knowledge, evidence for the formation of rearranged alcohol products has been only obtained in a very recent study on the oxygenation of spiro[2.5]octane and 6-*tert*-butylspiro[2.5]octane promoted by manganese-oxo species where, leveraging on the use of fluorinated alcohol solvents and on catalyst electronics, predominant or exclusive formation of bicyclo[4.2.0]octan-1-ol and *cis*-4-(*tert*-butyl)-bicyclo[4.2.0]octan-1-ol, respectively has been observed (**Scheme 8.1**).<sup>17</sup>



**Scheme 8.1** Oxygenation of spiro[2.5]octane and 6-*tert*-butylspiro[2.5]octane promoted by manganese-oxo species.

Along these lines, by considering that similar mechanistic features are associated to  $\text{C}(sp^3)\text{-H}$  bond oxygenations promoted by metal-oxo species and dioxiranes,<sup>8,18</sup> for which the generally accepted mechanism is described in terms of a HAT step followed by very fast OH rebound (**Scheme 8.2**), and that the oxidizing ability of the intermediate  $\alpha$ -hydroxy alkoxy radical

formed following HAT to the dioxirane can be modulated by careful choice of the precursor ketone as well as by solvent effects, we reasoned that these reagents in combination with fluorinated alcohol solvents could provide the opportunity to probe the (unprecedented) involvement of cationic intermediates in these reactions.



**Scheme 8.2** Mechanism of oxygenation by dioxiranes.

With these concepts in mind, herein we report on the results of a detailed product and computational study on the reactions of 3-ethyl-3-(trifluoromethyl)dioxirane (ETFDO) with a series of bicyclic (**S1-S5**) and spirocyclic (**S7** and **S8**) hydrocarbons bearing cyclopropyl groups, the structures for which are displayed in **Figure 8.2**. In order to obtain additional information, product studies on the reactions with ETFDO have been also extended to 1,1-dimethylcyclohexane (**S6**) and to the diastereomeric alcohol couples **P2a-OH**, **P2b-OH**, **P8a-OH** and **P8c-OH**, the structures for which are also displayed in **Figure 8.2**.

Through this combined approach, new information on the role exerted by cyclopropyl groups on HAT from the C–H bonds of these substrates has been obtained, providing a deeper understanding of the role of hyperconjugative activation on the reactivity, site-selectivity and stereoselectivity observed in these reactions and the first evidence for the involvement of cationic pathways in oxygenation reactions promoted by dioxiranes.

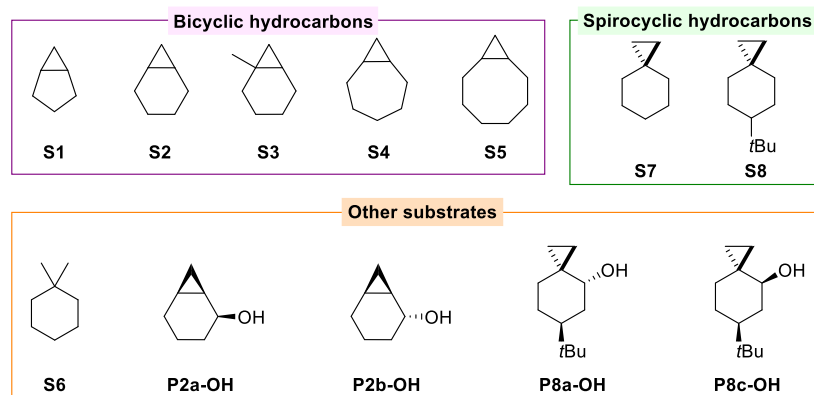
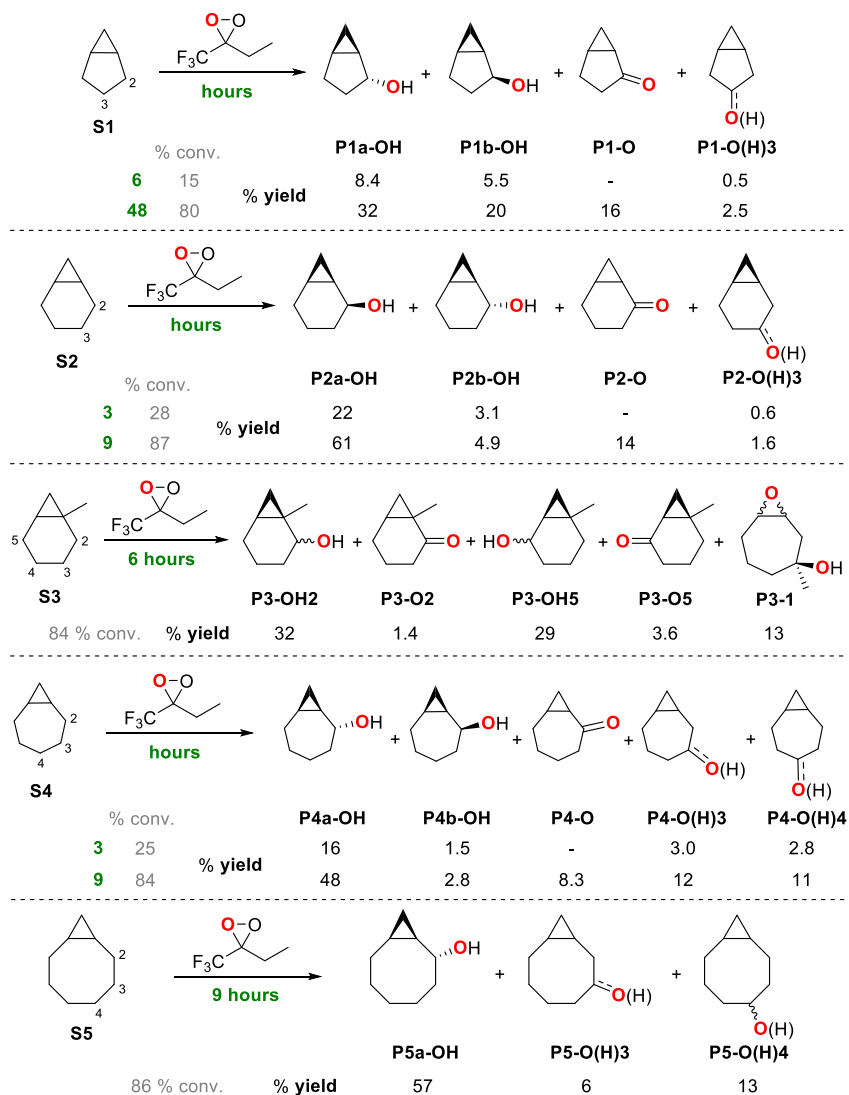


**Figure 8.2** Structures of the substrates investigated in this work.

## 8.4 Experimental and computational results

**Reactions with ETFDO.** Product studies on the reactions of substrates **S1-S8** with in situ generated ETFDO were carried out at  $T = 0\text{ }^{\circ}\text{C}$  in a HFIP/ $\text{H}_2\text{O}$  3:1 solvent mixture containing the substrate (1 eq), oxone (1 eq),  $\text{NaHCO}_3$  (4 eq), 1,1,1-trifluoro-2-butanone (0.2 eq) and  $\text{Bu}_4\text{NHSO}_4$  0.05 eq, according to a previously described procedure.<sup>19</sup>

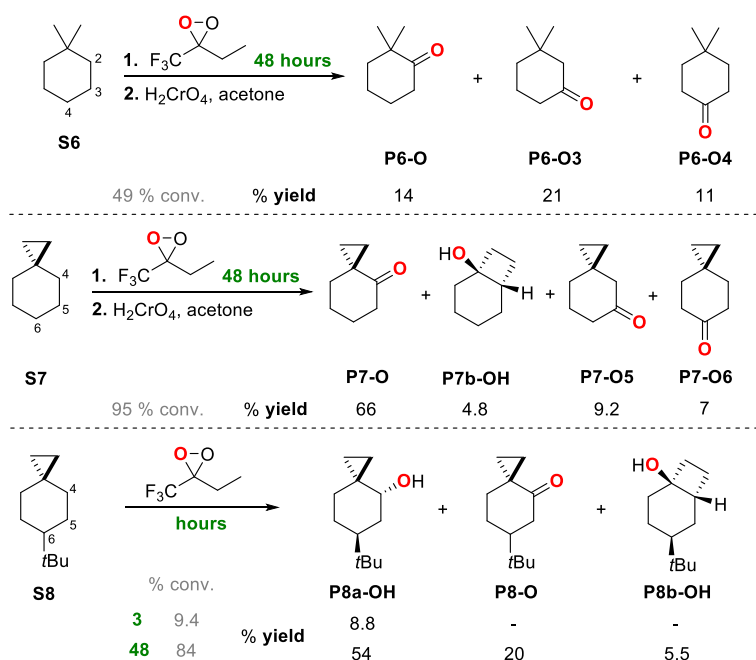
Product yields for the oxygenation of bicyclic hydrocarbons (**S1-S5**) and 1,1-dimethylcyclohexane (**S6**), and of spirocyclic hydrocarbons (**S7** and **S8**) promoted by ETFDO, obtained after reaction optimization, are displayed in **Scheme 8.3** and **Scheme 8.4**, respectively. The two schemes show the results obtained at  $\geq 80\%$  conversion, where total yields of the oxygenation products approach 87%, accompanied by excellent mass balances ( $\geq 90\%$ ). With **S6**, a 49% conversion was observed after 48 h reaction time with a 46% total yield of oxygenation products (**Scheme 8.4**). With substrates **S1**, **S2**, **S4** and **S8**, **Scheme 8.3** and **Scheme 8.4** also display the product yields obtained at low conversion, i.e. under conditions where formation of the ketone product resulting from overoxidation of the first formed alcohols, deriving from hydroxylation at the C–H bonds that are  $\alpha$ - to the cyclopropyl group, is not observed.



**Scheme 8.3.** Oxygenation of bicyclo[n.1.0]alkanes (n = 3-6) (**S1-S5**) promoted by ETFDO.

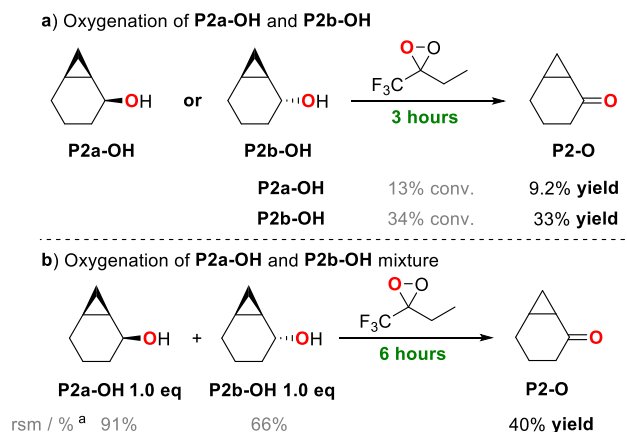
The yield of the minor products deriving from C–H bond oxygenation at remote positions (C-3 for **S1** and **S2**, and C-3, C-4 for **S4** and **S5**) was calculated as the sum of the alcohol and ketone products. In the oxygenation of **S3**, product yields of alcohols at C-2 and C-5 are given in both cases as the sum of the *cis*- and *trans*- isomers (details on the product distributions are reported in the SI). For the oxidation of **S6** and **S7**, product yields were obtained after chromic acid oxidation of the reaction mixture.

In order to obtain additional information, the reaction with ETFDO was also extended to some of the oxygenation products of **S2** and **S8**. The main reaction products **P2a-OH** and **P8a-OH** and the corresponding ketones **P2-O** and **P8-O** were isolated by scale-up ETFDO-mediated oxidation of **S2** and **S8**, respectively. **P2b-OH** and **P8c-OH** (the diastereoisomer of **P8a-OH**, not observed in the reaction of **S8**) were prepared by diastereoselective reduction of the parent ketones **P2-O** and **P8-O**, respectively.



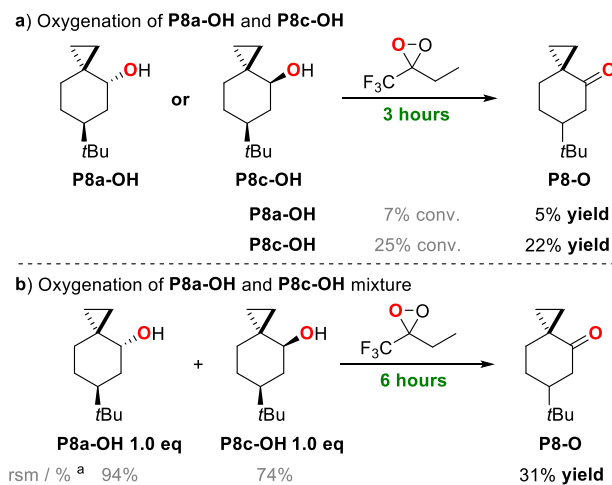
**Scheme 8.4.** Oxygenation of 1,1-dimethylcyclohexane (**S6**) and of spiro[2.5]octanes (**S7** and **S8**) promoted by ETFDO.

Conversions and product yields observed in the oxygenation of the isomeric *cis*- and *trans*-alcohol products **P2a-OH** and **P2b-OH**, deriving from hydroxylation at C-2 of **S2**, promoted by ETFDO are displayed in **Scheme 8.5a**. The results of the substrate competitive oxygenation of a 1:1 mixture of **P2a-OH** and **P2b-OH** promoted by ETFDO are displayed in **Scheme 8.5b**. Conversions and product yields observed in the corresponding experiments carried out on **P8a-OH** and **P8c-OH** are instead displayed in **Scheme 8.6**.



**Scheme 8.5.** Oxygenation of *cis*-bicyclo[4.1.0]heptan-2-ol (**P2a-OH**) and *trans*-bicyclo[4.1.0]heptan-2-ol (**P2b-OH**). Conversion and product yields were determined by GC and averaged over two independent experiments.

a) Reaction conditions: **P2a-OH** or **P2b-OH** 1 eq, oxone 1 eq, NaHCO<sub>3</sub> 4 eq, 1,1,1-trifluoro-2-butanone 0.2 eq, HFIP/H<sub>2</sub>O (3:1), Bu<sub>4</sub>NHSO<sub>4</sub> 0.05 eq, T = 0 °C, 3 h. b) **P2a-OH** 1 eq, **P2b-OH** 1 eq, oxone 1 eq, NaHCO<sub>3</sub> 4 eq, 1,1,1-trifluoro-2-butanone 0.2 eq, HFIP/H<sub>2</sub>O (3:1), Bu<sub>4</sub>NHSO<sub>4</sub> 0.05 eq, T = 0 °C, 6 h. <sup>a</sup>rsm: recovered starting material.



**Scheme 8.6.** Oxygenation of *trans*-6-*tert*-butylspiro[2.5]octan-2-ol (**P8a-OH**) and *cis*-6-*tert*-butylspiro[2.5]octan-2-ol (**P8c-OH**). Conversion and product yields were determined by GC and averaged over two independent experiments.

a) Reaction conditions: **P8a-OH** or **P8c-OH** 1 eq, oxone 1 eq, NaHCO<sub>3</sub> 4 eq, 1,1,1-trifluoro-2-butanone 0.2 eq, HFIP/H<sub>2</sub>O (3:1), Bu<sub>4</sub>NHSO<sub>4</sub> 0.05 eq, T = 0 °C, 3 h. b) **P8a-OH** 1 eq, **P8c-OH** 1 eq, oxone 1 eq, NaHCO<sub>3</sub> 4 eq, 1,1,1-trifluoro-2-butanone 0.2 eq, HFIP/H<sub>2</sub>O (3.0:1.0), Bu<sub>4</sub>NHSO<sub>4</sub> 0.05 eq, T = 0 °C, 6 h. <sup>a</sup>rsm: recovered starting material.

**Computational Studies.** Density functional theory (DFT) computations were performed with Gaussian 16.<sup>20</sup> The (u)ωB97X-D functional was used to optimize molecular geometries.<sup>21</sup> Geometry optimizations were completed with the 6-311++G(d,p) basis set and the SMD solvation model accounting for the effect of H<sub>2</sub>O.<sup>22</sup> Frequency calculations were conducted at the same level of theory used for the geometry optimizations to obtain thermal Gibbs free energies and characterize the stationary points on the potential energy surface. The correct unrestricted wavefunctions were obtained by performing a stability test with the Gaussian keyword *stable=opt*. Gibbs free energies were corrected using Goodvibes, which corrects the vibrational frequencies *via* the approximation for the quasi-harmonic correction, as proposed by Grimme.<sup>23</sup> Intrinsic reaction coordinate (IRC) calculations were performed to verify that a transition state (TS) connects the reactant and the product on the potential energy surface. CYLview was employed to visualize molecular structures.<sup>24</sup>

The computed site-selectivities for C(*sp*<sup>3</sup>)-H bond oxygenation of bicyclo[n.1.0]alkanes **S1**, **S2**, **S4** and **S5** promoted by ETFDO, expressed in terms of the difference in activation free energy ( $\Delta G^\ddagger$ ) between the methylenic C-H bonds of the major ring and the most reactive C<sub>2</sub>-H bond ( $\Delta\Delta G^\ddagger$ , in kcal mol<sup>-1</sup>) are displayed in **Figure 8.3**. As a matter of comparison, the corresponding  $\Delta\Delta G^\ddagger$  values derived from the product distributions displayed in **Figure 8.8** are also shown.

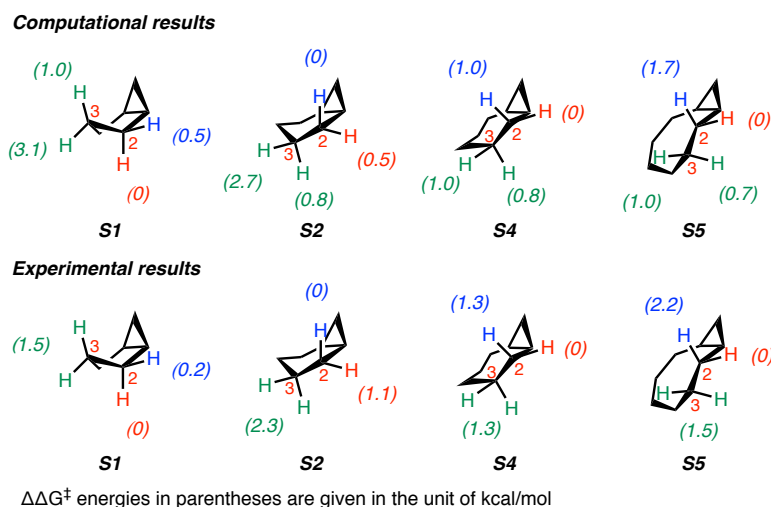
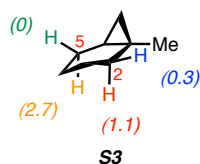


**Figure 8.3** Difference in activation free energies ( $\Delta\Delta G^\ddagger$ , in kcal mol<sup>-1</sup>) for HAT from the  $\alpha$ - and  $\beta$ - C–H bonds in **S1**, **S2**, **S4** and **S5** by ETFDO: computational and experimental studies.

The pertinent transition state structures obtained for these selectivity studies together with the analysis of the hyperconjugation effect on the C<sub>2</sub>–H bonds provided by the fused cyclopropane moiety are shown in **8.7 Supplementary Information** as **Figures 8.11–8.14** for the reactions of substrates **S1**, **S2**, **S4** and **S5**, respectively. The computed site-selectivity for C(*sp*<sup>3</sup>)–H bond oxygenation of 1-methylbicyclo[4.1.0]heptane (**S3**) promoted by ETFDO, expressed in terms of the  $\Delta\Delta G^\ddagger$  between the C<sub>2</sub>–H and C<sub>5</sub>–H bonds and the most reactive C<sub>5</sub>–H bond are displayed in **Figure 8.4**.



$\Delta\Delta G^\ddagger$  energies in parentheses are given in the unit of kcal/mol

**Figure 8.4** Computed activation free energy difference ( $\Delta\Delta G^\ddagger$ , in kcal mol<sup>-1</sup>) for HAT from the C–H bonds of **S3** by ETFDO.

The transition state structures for HAT from the C<sub>2</sub>–H and C<sub>5</sub>–H bonds of **S3** to ETFDO are displayed in **8.7 Supplementary Information** as **Figure 8.15**. The energetics of the



hydroxylation mechanisms for each of the C–H bonds at C-2 and C-5 are displayed in **Figure 8.5**.

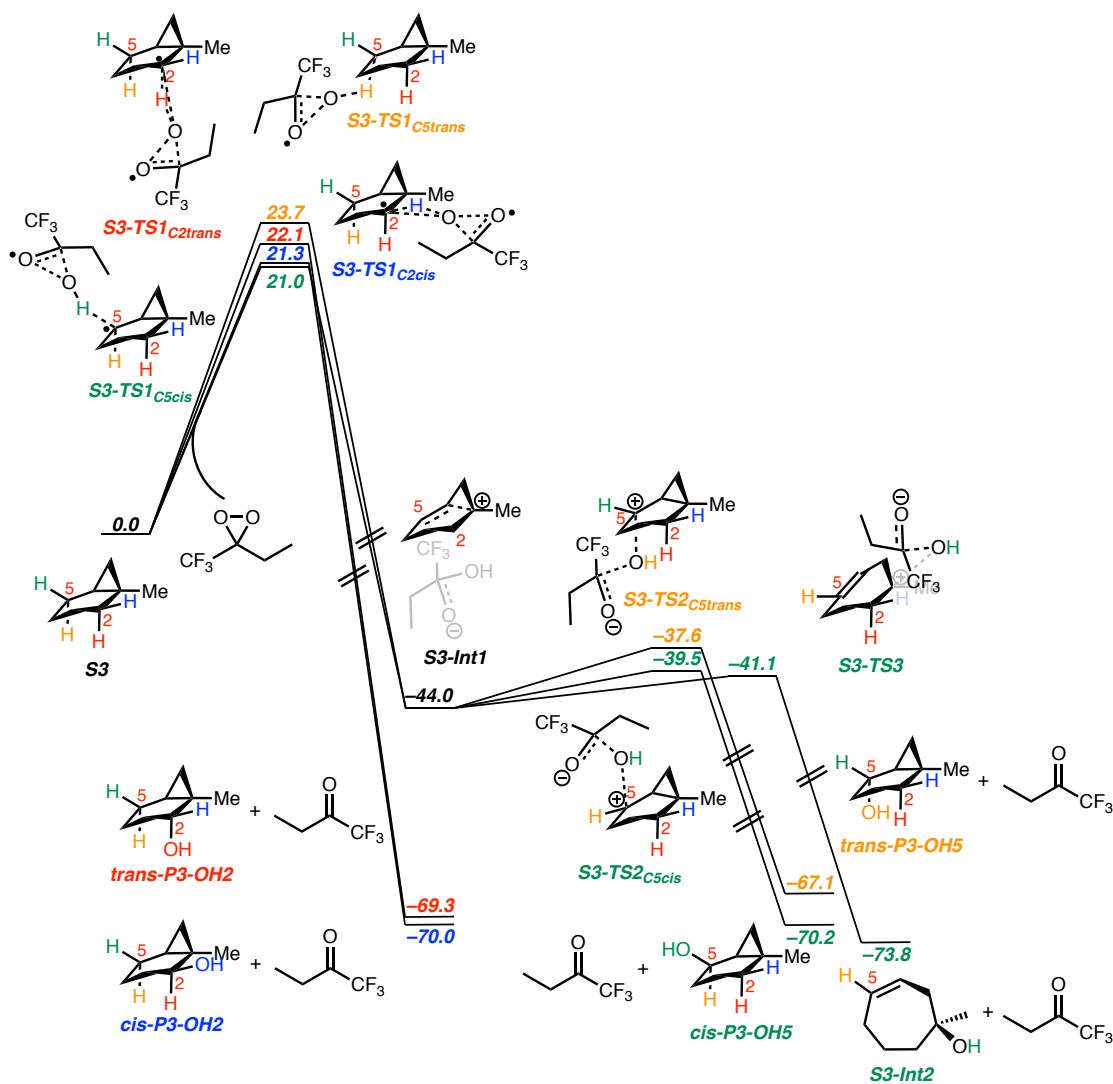


**Figure 8.5** Energetics of C–H bond oxidation of S3 promoted by ETFDO.

The computed site-selectivities for C( $sp^3$ )–H bond oxygenation of spiro[2.5]octanes S7 and S8 promoted by ETFDO, expressed in terms of the  $\Delta\Delta G^\ddagger$  between the methylenic C–H bonds of the six membered ring and the most reactive C<sub>4</sub>–H bond are described in **Figure 8.6**, together with the corresponding  $\Delta\Delta G^\ddagger$  values derived from the product distributions shown in **Scheme 8.4**.

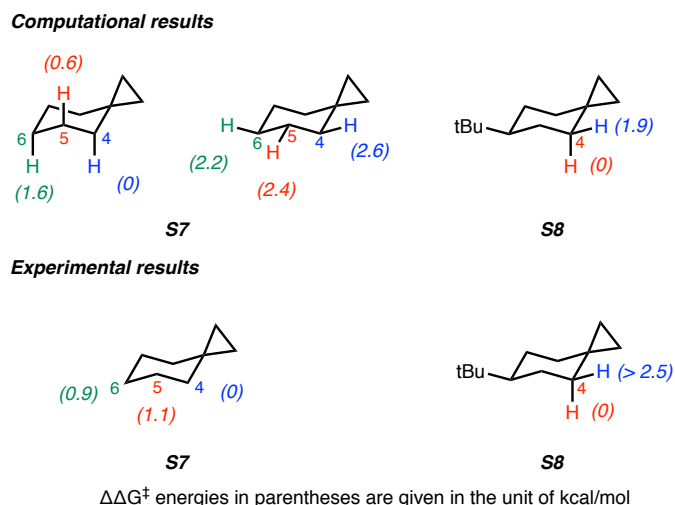


**Figure 8.6** Computed and experimental activation free energy difference ( $\Delta\Delta G^\ddagger$ , in kcal mol<sup>-1</sup>) for HAT from the C–H bonds of **S7** and **S8** to ETFDO.

The transition state structures for HAT from the C<sub>4</sub>–H, C<sub>5</sub>–H and C<sub>6</sub>–H bonds of **S7** and from the C<sub>4</sub>–H bonds of **S8** to ETFDO and the analysis of the hyperconjugation effect on the C<sub>4</sub>–H bonds provided by the spiro-cyclopropane moiety are displayed in **8.7 Supplementary Information** as **Figures 8.16** and **8.17**, respectively. The energetics of the hydroxylation mechanisms for the axial and equatorial C<sub>4</sub>–H bonds of **S8** are displayed in **Figure 8.7**. The corresponding energy profile of the hydroxylation mechanisms for the C<sub>4</sub>–H, C<sub>5</sub>–H and C<sub>6</sub>–H bonds of **S7** are displayed in **8.7 Supplementary Information** as **Figure 8.18**.

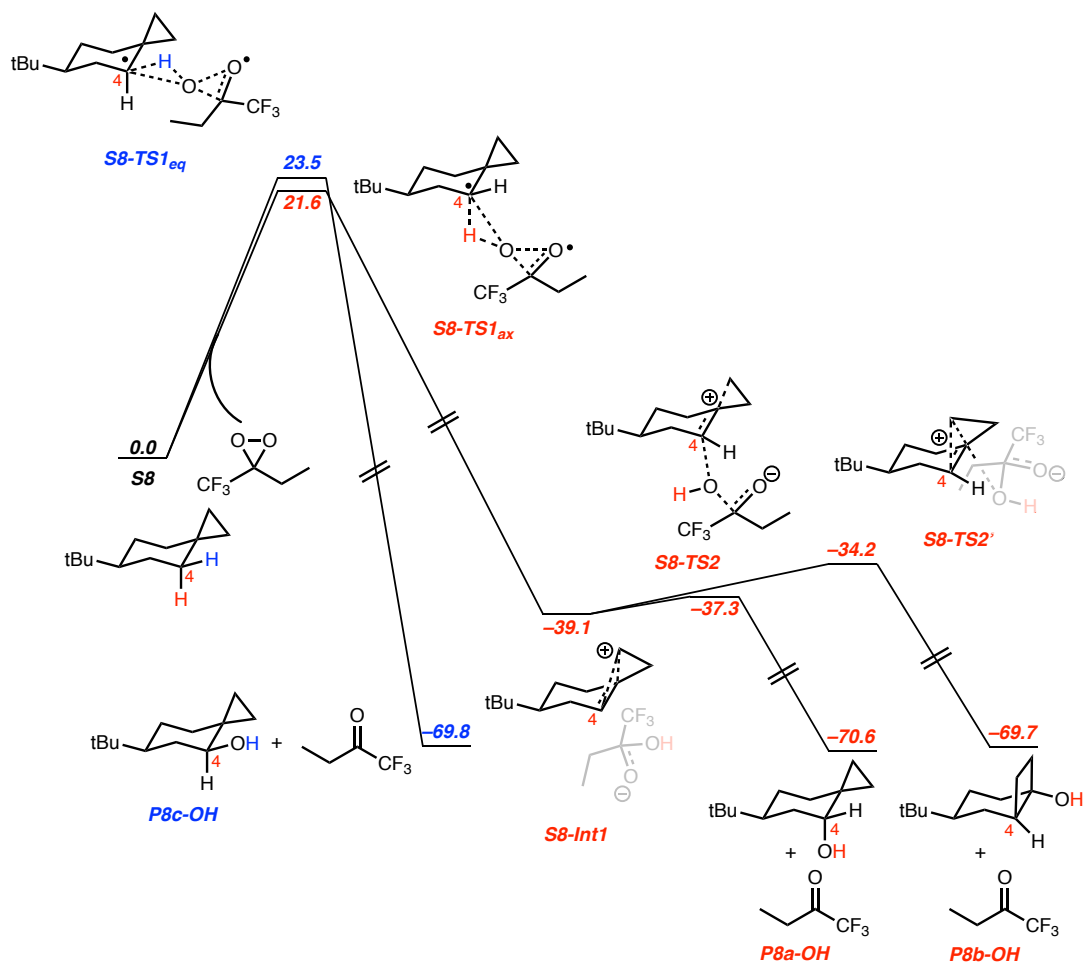


**Figure 8.7** Energetics of C-H bond oxidation of **S8** promoted by ETFDO.

## 8.5 Discussion

**Oxygenation of bicyclic substrates (S1-S5, P2a-OH and P2b-OH).** The results obtained in the C(*sp*<sup>3</sup>)-H bond oxygenation of substrates **S1-S5** promoted by ETFDO are displayed in **Scheme 8.3**. With **S1**, **S2** and **S4** the reactions carried out at low substrate conversion (3-6 hours reaction time, 15-28% conversion) showed in all cases the predominant formation of the diastereomeric alcohol products deriving from C<sub>2</sub>-H bond hydroxylation, accompanied by smaller amounts of products deriving from oxygenation at the other methylenic sites (C-3 for **S1** and **S2**, C-3 and C-4 for **S4**). With all three substrates, no evidence for the formation of the ketone product deriving from overoxidation of the alcohols at C-2, and of products deriving from oxidation of the cyclopropane C-H bonds was observed. The former observation can be accounted for on the basis of the strong hydrogen bond donor (HBD) ability of HFIP that, by engaging in hydrogen bonding with the hydroxyl group of the alcohol products, inverts the polarity of the adjacent C-H bond, deactivating this site toward HAT to the electrophilic ETFDO, thus preventing overoxidation to the ketone.<sup>25</sup> The latter observation reflects the very high BDE of the cyclopropane C-H bonds,<sup>26</sup> that are typically resistant to HAT-based functionalization. By increasing reaction time (48 hours for **S1**, 9 hours for **S2** and **S4**), significantly higher conversions were obtained (80-87%), with formation of sizable amounts of the C-2 ketone in addition to the abovementioned oxygenation products. High product yields (70.5-82.1%) and excellent mass balances (>90%) were observed in all reactions. The product distributions evidence the high site-selectivity obtained in these reactions, with products deriving from oxygenation at C-2 of **S1**, **S2** and **S4** that are formed in 96%, 98% and 72% selectivity, respectively, over those deriving from oxygenation at other sites. A similar outcome was observed in the reaction of **S5** where however, the reaction was carried out for a 9 hour reaction

time (86% conversion, 76% overall product yield), with predominant formation of *trans*-bicyclo[6.1.0]nonan-2-ol (**P5a-OH**) as the exclusive oxygenation product at C-2 in 75% selectivity over those deriving from oxygenation at other sites. These behaviors can be rationalized on the basis of hyperconjugative effects, where overlap between the cyclopropane C–C bonding orbital and the  $\sigma^*$  orbital of the adjacent C<sub>2</sub>–H activates this bond toward HAT (**Figure 8.1a**), accounting for the observed site-selectivities.<sup>6a</sup>

The analysis of the product distributions obtained for **S1**, **S2**, **S4** and **S5**, under conditions where overoxidation of the first-formed alcohols at C-2 is not observed, provides information on the hydroxylation diastereoselectivity. The normalized site-selectivities for hydroxylation of these substrates obtained under these conditions are displayed in **Figure 8.8**, where in particular the *trans/cis* ratios for hydroxylation at C-2 are highlighted.

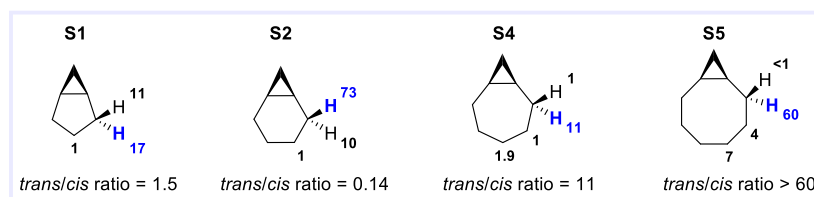


**Figure 8.8** Normalized site-selectivities and diastereoselectivities observed in the hydroxylation of bicyclo[n.1.0]alkanes **S1**, **S2**, **S4** and **S5** promoted by ETFDO.

Preferential hydroxylation of the *trans* C<sub>2</sub>–H bond was observed for **S1**, **S4** and **S5**, with the *trans/cis* ratio that increases with increasing ring size, reaching an upper limit with **S5** for which the product deriving from hydroxylation of the *cis* C<sub>2</sub>–H bond was not detected. Preferential hydroxylation of the *cis* C<sub>2</sub>–H bond was instead observed with **S2** (*trans/cis* = 0.14).

Interestingly, similar diastereoselectivity patterns were observed in dihalocarbene insertions into the C<sub>2</sub>–H bonds of **S1** and **S2** (*trans/cis* = 2.8-4 and 0.23-0.25, respectively),<sup>12</sup> suggesting that the same effects operate in dioxirane hydroxylation and carbene insertion reactions.

The explanation given for the preferential hydroxylation of the *cis* C<sub>2</sub>-H bond observed in the reaction of ETFDO with **S2** can be also put forward to account for the diastereoselectivity observed in the C-H bond oxidation reaction promoted by TFDO, employed in an intermediate step of the total synthesis of (+)-phorbol.<sup>13</sup> Within the bicyclo[4.1.0]heptane substrate motif (**Figure 8.1a**), selective hydroxylation at the α-C-H bond that is *cis* to the cyclopropane moiety was observed.

Strong support to the diastereoselectivities observed in these reactions is provided by the results of computational studies on the oxygenation of **S1**, **S2**, **S4** and **S5** promoted by ETFDO. The activation free energy differences ( $\Delta\Delta G^\ddagger$ ) for HAT from the C<sub>2</sub>-H bonds of these substrates to ETFDO are shown in **Figure 8.3** while the corresponding transition state structures are displayed in **8.7 Supplementary Information** as **Figures 8.11–8.14**.

The computational results for site-selectivity show qualitative agreement with experimental observations. In the reaction of **S1**, the energy difference between *cis* and *trans* C<sub>2</sub>-H bond oxidation is only 0.5 kcal mol<sup>-1</sup>. This difference is small, because hyperconjugation with the cyclopropane ring can activate toward HAT both *cis* and *trans* C<sub>2</sub>-H bonds (**Figure 8.11** in **8.7 Supplementary Information**). Experiments did not differentiate the selectivity between *cis* and *trans* C<sub>3</sub>-H bonds. However, computations predict a preference for oxygenation of the *cis* over *trans* C<sub>3</sub>-H bond ( $\Delta\Delta G^\ddagger = 1.0$  and  $3.1$  kcal mol<sup>-1</sup>, respectively). The effect of hyperconjugation on *trans* C<sub>2</sub>-H bond activation is highlighted in **Figure 8.11** of **8.7 Supplementary Information**. This observation underscores the importance of hyperconjugative interactions in influencing the selectivity of oxygenation reactions.

With **S2**, the computed oxidation site-selectivity follows the order: *cis* C<sub>2</sub>-H ( $\Delta\Delta G^\ddagger = 0$  kcal mol<sup>-1</sup>), *trans* C<sub>2</sub>-H ( $\Delta\Delta G^\ddagger = 0.5$  kcal mol<sup>-1</sup>), and C<sub>3</sub>-H ( $\Delta\Delta G^\ddagger = 0.8$  and  $2.7$  kcal mol<sup>-1</sup>, for *trans* and

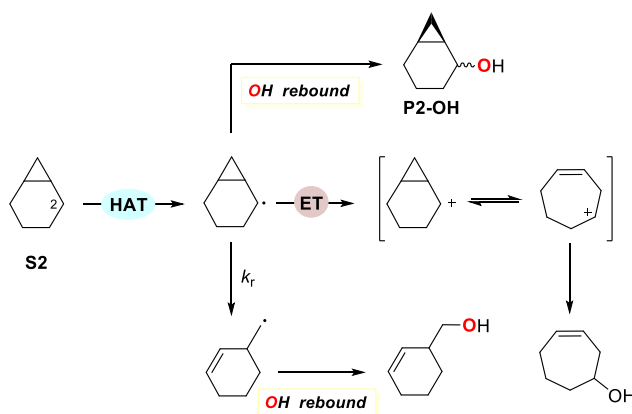
*cis*, respectively). Also with this substrate, the *cis* and *trans* C<sub>3</sub>–H bonds were not differentiated by the experiments. However, the computational results predict that *trans* C<sub>3</sub>–H is favored over *cis* C<sub>3</sub>–H. **Figure 8.12** in **8.7 Supplementary Information** emphasizes the hyperconjugative interaction by the cyclopropyl group when activating the *cis* C<sub>2</sub>–H bond of **S2** toward HAT to ETFDO.

The observation of a stronger hyperconjugative activation of the *cis* C<sub>2</sub>–H bond of **S2** over the *trans* one is also corroborated by the results obtained, under the same experimental conditions, in the oxidation of *cis*- and *trans*-bicyclo[4.1.0]heptan-2-ol (**P2a-OH** and **P2b-OH**, respectively) promoted by ETFDO (**Scheme 8.5a**). With both substrates, exclusive formation of the corresponding ketone product (**P2-O**) in 9.2% and 33% yield, respectively, was observed, indicating that the latter alcohol is 3.6 times more reactive than the former one. **P2b-OH** displays a *cis* C<sub>2</sub>–H bond that benefits from hyperconjugative activation via overlap with the cyclopropane C–C bonding orbitals, whereas with **P2a-OH** the *trans* C<sub>2</sub>–H bond cannot benefit from a similar activation. Additional support is provided by the results obtained in the substrate competitive oxidation of a 1:1 *trans-cis* mixture of bicyclo[4.1.0]heptan-2-ols (**P2a-OH** and **P2b-OH**) promoted by ETFDO (**Scheme 8.5b**). 91% Recovery of **P2a-OH** and 66% recovery of **P2b-OH**, together with an overall 40% yield of **P2-O** were obtained, indicating that the latter alcohol is 3.8 times more reactive than the former one, showing an excellent agreement between the two experiments.

With **S4** and **S5**, the *trans* C<sub>2</sub>–H bond ( $\Delta\Delta G^\ddagger = 0$  kcal mol<sup>-1</sup>) is the most activated toward HAT to ETFDO. With **S4**, similar activation free energy differences are computed for the *cis* C<sub>2</sub>–H, *trans* C<sub>3</sub>–H and *cis* C<sub>3</sub>–H bonds ( $\Delta\Delta G^\ddagger = 1.0, 0.8$  and  $1.0$  kcal mol<sup>-1</sup>, respectively). With **S5**, site-selectivity follows the order: *trans* C<sub>3</sub>–H, *cis* C<sub>3</sub>–H, *cis* C<sub>2</sub>–H (with  $\Delta\Delta G^\ddagger = 0.7, 1.0$  and  $1.7$  kcal

mol<sup>-1</sup>, respectively). With both substrates, the computational results are again in good agreement with the experimental findings. **Figures 8.13 and 8.14** in **8.7 Supplementary Information** highlight the hyperconjugative interaction between the *trans* C<sub>2</sub>-H bond of **S4** and **S5** and the Walsh orbital of the fused cyclopropane ring.

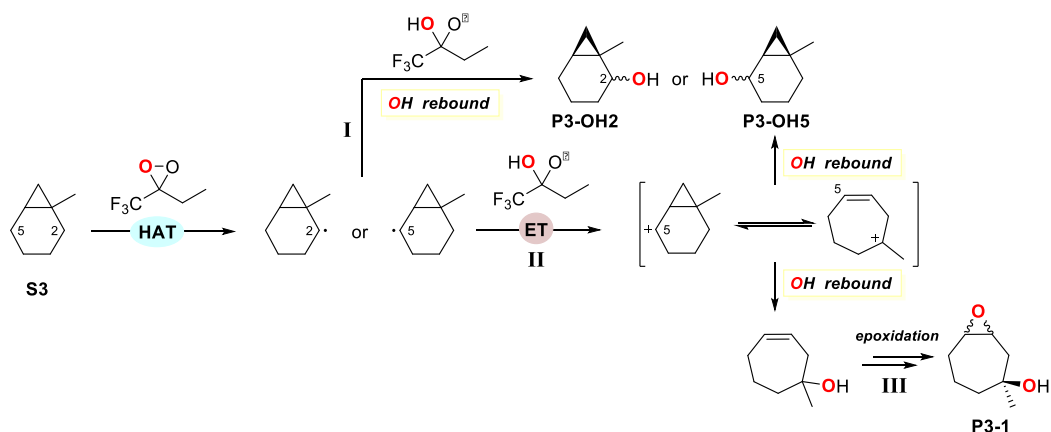
Among the bicyclo[n.1.0]alkane series, the oxygenation of 1-methylbicyclo[4.1.0]heptane (**S3**) promoted by ETFDO deserves special attention. With this substrate, in addition to the alcohol and ketone products deriving from oxygenation at the most activated C-H bonds at C-2 (**P3-OH2** + **P3-O2**) and C-5 (**P3-OH5** + **P3-O5**) in 33.4% and 32.6% combined yield, respectively, *cis*- and *trans*-3-methyl-8-oxabicyclo[5.1.0]octan-3-ol (**P3-1**) were also observed among the reaction products in 13% combined yield (**Scheme 8.3**). The formation of products **P3-1** can be rationalized on the basis of the mechanism proposed by Groves and coworkers in the oxygenation on bicyclo[4.1.0]heptane (**S2**) promoted by cytochrome P450 enzymes.<sup>15a</sup> The carbon radical formed following HAT from C-2 can undergo, in addition to the canonical OH rebound and radical rearrangement pathways, one-electron oxidation to give a cationic intermediate that, after rearrangement, is converted into the hydroxylated product by OH-transfer or nucleophilic capture by water (**Scheme 8.7**).



**Scheme 8.7** Proposed mechanism for the oxygenation of **S2** promoted by cytochrome P450 enzymes.<sup>15a</sup>



An analogous mechanism can be proposed for the oxidation of **S3**, where formation of 1-methylcyclohept-3-en-1-ol is initiated by HAT from the C<sub>5</sub>-H bond, and this product is then rapidly converted into **P3-1** as a diastereomeric mixture via epoxidation promoted by ETFDO.<sup>27</sup> This hypothesis is well supported by the results of the computational studies. The oxidation site-selectivity (Figure 4) follows the order: *cis* C<sub>5</sub>-H ( $\Delta\Delta G^\ddagger = 0$  kcal mol<sup>-1</sup>), *cis* C<sub>2</sub>-H ( $\Delta\Delta G^\ddagger = 0.3$  kcal mol<sup>-1</sup>), *trans* C<sub>2</sub>-H ( $\Delta\Delta G^\ddagger = 1.1$  kcal mol<sup>-1</sup>), and *trans* C<sub>5</sub>-H ( $\Delta\Delta G^\ddagger = 2.7$  kcal mol<sup>-1</sup>), confirming the stronger hyperconjugative activation of the *cis*  $\alpha$ -C-H bonds over the corresponding *trans* ones. The computed free energy profiles displayed in **Figure 8.5** predict concerted oxidation through asynchronous HAT from the *cis* and *trans* C<sub>2</sub>-H bonds via **S3-TS1<sub>C2cis</sub>** and **S3-TS1<sub>C2trans</sub>** = 21.3 and 22.1 kcal mol<sup>-1</sup>, respectively, coupled to OH-rebound to give products **P3-OH2**. Homoallylic tertiary carbocation intermediate (**S3-Int1**, -44.0 kcal mol<sup>-1</sup>) is formed through asynchronous HAT from *cis* and *trans* C<sub>5</sub>-H bonds (**S3-TS1<sub>C5cis</sub>** and **S3-TS1<sub>C5trans</sub>** = 21.0 and 23.7 kcal mol<sup>-1</sup>, respectively), coupled to electron transfer (ET), and can then undergo hydroxylation at C-5 through **S3-TS2<sub>C5cis</sub>** (-39.5 kcal mol<sup>-1</sup>) and **S3-TS2<sub>C5trans</sub>** (-37.6 kcal mol<sup>-1</sup>) to give products **P3-OH5**. 3D figures of the intermediate **S3-Int1** and hydroxylation transition state structures **S3-TS2<sub>C5cis</sub>** and **S3-TS2<sub>C5trans</sub>** are shown in **8.7 Supplementary Information** as **Figure 8.15**. **Figure 8.5** shows moreover that **S3-Int1** can undergo competitive hydroxylation at C-2 through **S3-TS3** (-41.1 kcal mol<sup>-1</sup>) to form 1-methylcyclohept-3-en-1-ol, **S3-Int2** (-73.8 kcal mol<sup>-1</sup>), that is then converted into 3-methyl-8-oxabicyclo[5.1.0]octan-3-ols **P3-1** by oxygen atom transfer from ETFDO. The proposed mechanistic pathways for oxidation of **S3** promoted by EFTDO are summarized in **Scheme 8.8**.



**Scheme 8.8** Proposed mechanistic pathways for the oxygenation of **S3** promoted by ETFDO.

The reaction is initiated by HAT from the C<sub>2</sub>-H and C<sub>5</sub>-H bonds of **S3** to ETFDO to give the hydroxylation products **P3-OH2** (and **P3-OH5**) and homoallylic tertiary carbocation **S3-Int1** and dioxirane derived oxyanion ion-pair, via coupled OH-rebound and ET, respectively. Within the ion-pair, different hydroxylation pathways are accessible, all characterized by very similar free energy barriers (**Figure 8.5**): OH transfer at C-5 and C-2 of **S3-Int1** to deliver products **P3-OH5** and 1-methylcyclohept-3-en-1-ol, respectively. The rearranged alcohol product is finally converted into diastereomeric products **P3-1** through epoxidation promoted by ETFDO. The lack of products deriving from ring-opening in the first formed carbon radical reflects the magnitude of the unimolecular rate constant for ring-opening of this  $\alpha$ -cyclopropyl carbon radical ( $k_r = 2 \times 10^8 \text{ s}^{-1}$  for norcarane)<sup>15a</sup> that, because of the extremely short lifetime of the incipient radical couple ( $\leq 200 \text{ fs}$ ),<sup>16,18b</sup> cannot compete with radical recombination. This result indicates moreover that also ET within this couple must be significantly faster than  $k_r$ .

Interestingly, the analysis of the reaction shows the exclusive formation of rearranged products deriving from initial HAT at the C<sub>5</sub>-H bond, with no formation of the analogous isomeric products deriving from the C<sub>2</sub>-H bond. Although ET within the two incipient radical couples should occur with similar rates, this observation reasonably reflects the different stabilization of

the intermediate tertiary and secondary homoallylic cations deriving from the two pathways, where hyperconjugation imparted by the C–H bonds of the C-1 methyl group can assist the nascent cationic intermediate.<sup>28</sup>

Supportive evidence in favor of an ET pathway was also gained from the results obtained in the study of solvent effects on the oxygenation of **S3** promoted by ETFDO. By analyzing the products deriving from initial HAT at C-5, a decrease in the ratio between rearranged (**P3-1**) and unrearranged (**P3-OH5** and **P3-O5**) products with decreasing solvent HBD ability was observed, i.e. going from HFIP to TFE and MeCN ( $(\mathbf{P3-1}/(\mathbf{P3-OH5} + \mathbf{P3-O5})) = 0.40, 0.16$  and  $<0.01$ , respectively). This behavior can be associated to the strong HBD ability of fluorinated alcohols that, compared to non-HBD or weaker HBD solvents, have been shown to promote ET reactions via an increase in the oxidizing power of ET reagents and the ability to stabilize cationic intermediates.<sup>29</sup>

**Oxygenation of spirocyclic substrates (S7, S8, P8a-OH and P8c-OH).** The results obtained in the oxidation of spiro[2.5]octane (**S7**) and 6-*tert*-butylspiro[2.5]octane (**S8**) promoted by ETFDO were compared with those obtained for the corresponding reaction of 1,1-dimethylcyclohexane (**S6**) taken as a reference substrate, and are displayed in **Scheme 8.4**. With **S6**, the reaction carried out for 48 hours, followed by treatment with chromic acid, afforded the ketone products deriving from oxidation at C-2 (**P6-O**), C-3 (**P6-O3**) and C-4 (**P6-O4**), in 14%, 21% and 11% yield, respectively (substrate conversion 49%, overall product yield 46%). Under the same conditions, the reaction of **S7** led to the ketone products deriving from oxidation at C-4 (**P7-O**), C-5 (**P7-O5**) and C-6 (**P7-O6**), in 66%, 9.2% and 7% yield, respectively, accompanied by the rearranged product bicyclo[4.2.0]octan-1-ol (**P7b-OH**) in 4.8% yield (substrate conversion 95%,

overall product yield 87%). With **S8**, the reaction mixture was not subjected to follow-up treatment with chromic acid, and the reaction carried out for 3 hours showed the exclusive formation of the axial alcohol at C-4 (**P8a-OH**) in 8.8% yield (substrate conversion 9.4%). By increasing reaction time to 48 hours, **P8a-OH** was formed in 54% yield, accompanied by the corresponding ketone (**P8-O**) and the rearranged alcohol *cis*-4-(*tert*-butyl)-bicyclo[4.2.0]octan-1-ol (**P8b-OH**) in 20% and 5.5% yield, respectively (substrate conversion 84%, overall product yield 79.5%). With this substrate, oxygenation products at C-5 and C-6 as well as the equatorial alcohol at C-4, **P8c-OH**, were never observed among the reaction products.

As discussed in the introduction, formation of the rearranged alcohols **P7b-OH** and **P8b-OH** in the oxygenation of **S7** and **S8** promoted by ETFDO (**Scheme 8.4**) provides conclusive evidence on the involvement of a cationic intermediate, uncovering the contribution of ET pathways to the overall reactivity.<sup>15a,17</sup> This hypothesis is again well supported by the results of the computational studies. The  $\Delta\Delta G^\ddagger$  values for HAT from the C–H bonds of **S7** and **S8** to ETFDO are displayed in **Figure 8.6** with comparison to the experimental results. Based on the computations, with **S7** HAT from the C<sub>4</sub>–H bonds is characterized by the lowest energy barrier ( $\Delta\Delta G^\ddagger = 0 \text{ kcal mol}^{-1}$ ) compared to the C<sub>5</sub>–H and C<sub>6</sub>–H bonds ( $\Delta\Delta G^\ddagger = 0.6$  and  $1.6 \text{ kcal mol}^{-1}$ , respectively). Furthermore, we find that the activation barriers of axial C–H bonds are lower than those of the equatorial ones. The transition state structures are shown in **8.7 Supplementary Information** as **Figure 8.16**.

Hyperconjugation results in **S7-TS1**<sub>C4ax</sub> showing a slightly longer C<sub>1</sub>–C<sub>2</sub> distance (1.52 Å) and a shorter C<sub>1</sub>–C<sub>4</sub> distance (1.49 Å) in contrast to the other transition states without hyperconjugative interactions. Moreover, efficient hyperconjugation between axial C<sub>4</sub>–H bond and Walsh orbital in the transition state **S7-TS1**<sub>C4ax</sub> is evidenced.

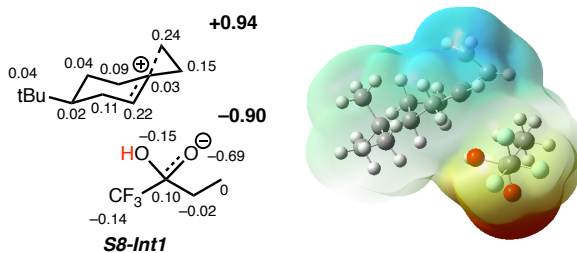
With **S8**, oxygenation of the axial C<sub>2</sub>–H bond is favored over the equatorial one by 1.9 kcal mol<sup>-1</sup> in good agreement with the experimental studies. Based on the analysis of the transition state structures (**Figure 8.17** in **8.7 Supplementary Information**), a hyperconjugative interaction by Walsh orbitals of the cyclopropane ring helps lower the barrier of the axial C<sub>4</sub>–H bond. Compared to **S8-TS1<sub>eq</sub>**, **S8-TS1<sub>ax</sub>** exhibits a slightly longer C<sub>1</sub>–C<sub>2</sub> distance (1.52 Å) and a shorter C<sub>1</sub>–C<sub>4</sub> distance (1.49 Å) due to hyperconjugation.

The observation of a stronger hyperconjugative activation of the axial C<sub>4</sub>–H bond over the equatorial one is also corroborated by the results obtained, under the same experimental conditions, in the oxidation of *trans*- and *cis*-6-*tert*-butylspiro[2.5]octan-4-ol (**P8a-OH** and **P8c-OH**, respectively) promoted by ETFDO (**Scheme 8.6a**). With both substrates, exclusive formation of the ketone product (**P8-O**) in 5% and 22% yield, respectively, was observed, indicating that the latter alcohol is 4.4 times more reactive than the former one. **P8c-OH** displays an axial C<sub>4</sub>–H bond that benefits from hyperconjugative activation, whereas with **P8a-OH** the equatorial C<sub>4</sub>–H bond C-4 cannot benefit from a similar activation. Additional support comes again from the results obtained in the substrate competitive oxidation of a 1:1 *trans-cis* mixture of 6-*tert*-butylspiro[2.5]octan-4-ols (**P8a-OH** and **P8c-OH**) promoted by ETFDO (**Scheme 8.6b**): 94% recovery of **P8a-OH** and 74% recovery of **P8c-OH**, together with an overall 31% yield of **P8-O** were obtained, indicating that the latter alcohol is 4.3 times more reactive than the former one, showing an excellent agreement between the two experiments.

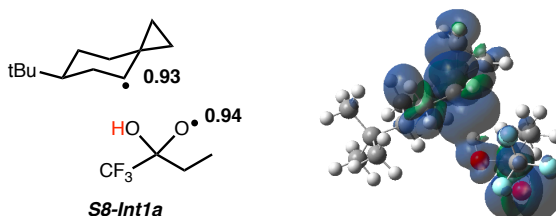
The energy profile of the hydroxylation of **S8** is presented in **Figure 8.7**. The axial C<sub>2</sub>–H bond undergoes asynchronous HAT to ETFDO through **TS1<sub>ax</sub>** (21.6 kcal mol<sup>-1</sup>) coupled to ET to directly form ion-pair **S8-Int1** (–39.1 kcal mol<sup>-1</sup>), and the subsequent OH rebound (**S8-TS2**, –37.3 kcal mol<sup>-1</sup>) gives the hydroxylation product **P8a-OH**. Hydroxylation of the equatorial C<sub>2</sub>–H

bond (**S8-TS1<sub>eq</sub>**, 23.5 kcal mol<sup>-1</sup>) occurs concertedly without generating charged intermediates. In order to confirm that **S8-Int1** is the intermediate ion-pair, CM5 calculation is employed to check the distribution of charges in **S8-Int1** (**Figure 8.9**). Charge is evenly distributed in the 6-*tert*-butylspiro[2.5]octanylium cation (+0.94) and trifluoro-2-hydroxybutan-2-olate anion (-0.90). Moreover, a hypothetical triplet radical pair **S8-Int1a** is noticeably unstable compared to ion-pair **S8-Int1** by 47.6 kcal mol<sup>-1</sup>.

a) CM5 charge calculation and ESP map of **S8-Int1**



b) Spin density calculation of hypothetical triplet radical pair **S8-Int1a**



$$\Delta G \text{ of } \mathbf{S8-Int1} \text{ and } \mathbf{S8-Int1a} = 48.9 \text{ kcal/mol}$$

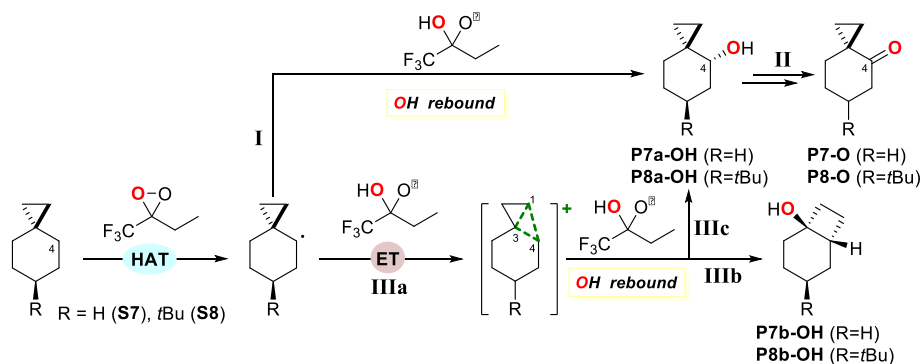
**Figure 8.9** a) Charge distribution of **S8-Int1** by CM5 calculations and electrostatic potential on a constant electron density surface. b) Spin density of hypothetical triplet radical pair **S8-Int1a**.

As presented in **Figure 8.7**, in order to account for the formation of **P8b-OH** observed in the product studies (**Scheme 8.4**) transition state **S8-TS2'** (-34.2 kcal mol<sup>-1</sup>) is found, which undertakes cyclopropylcarbinyl-type rearrangement and hydroxylation in a concerted fashion from ion-pair **S8-Int1**.<sup>30</sup> The activation energy of **S8-TS2'** is slightly higher in comparison with hydroxylation **S8-TS2** ( $\Delta\Delta G^\ddagger = 3.1$  kcal mol<sup>-1</sup>). This energy difference qualitatively matches with the experiment, explaining the low yield observed for **P8b-OH** formation. The 3D figures of the charge-separated intermediates and transition states are shown in **8.7 Supplementary**

**Information as Figure 8.17.** Also with **S8**, supportive experimental evidence in favor of an ET pathway was gained from the results obtained in the study of solvent effects on the oxidation reaction. Oxygenation of this substrate promoted by ETFDO was studied in MeCN, TFE and HFIP, and the ratio between rearranged (**P8b-OH**) and unrearranged (**P8a-OH + P8-O**) products was observed to decrease with decreasing solvent HBD ability, leading to the following **P8b-OH/(P8a-OH + P8-O)** ratios: 0.065, 0.028, <0.01, for HFIP, TFE and MeCN, respectively.

The energy profile of the oxygenation of **S7** is displayed in **8.7 Supplementary Information as Figure 8.18.** Ion-pair **S7-Int1<sub>C4</sub>** ( $-38.8 \text{ kcal mol}^{-1}$ ) is found on the potential energy surface after HAT from the C<sub>4</sub>-H bond via **S7-TS1<sub>C4ax</sub>** ( $\Delta G^\ddagger = 21.4 \text{ kcal mol}^{-1}$ ). **S7-Int1<sub>C4</sub>** undergoes either hydroxylation at C-4 through **S7-TS2<sub>C4</sub>** ( $\Delta G^\ddagger = -37.2 \text{ kcal mol}^{-1}$ ) or cyclopropylcarbinyl-type rearrangement/hydroxylation via **S7-TS2'<sub>C4</sub>** ( $\Delta G^\ddagger = -33.9 \text{ kcal mol}^{-1}$ ). In line with the experiment yielding **P7b-OH (Scheme 8.4)**, the prediction supports that the formation of the cationic intermediate is possible in the oxygenation process.

According to the experimental and computational results, and in keeping with the mechanism that has been recently proposed for the oxidation of **S7** and **S8** promoted by manganese-oxo species,<sup>17</sup> and with the one presented above in **Scheme 8.8** for the corresponding oxidation of **S3**, the proposed mechanism for oxidation of **S7** and **S8** by ETFDO is displayed in **Scheme 8.9**. For the sake of simplicity, with **S7** the competitive oxygenation pathways initiated by HAT from C<sub>5</sub>-H and C<sub>6</sub>-H bonds have been omitted, and the following discussion has been limited to the mechanistic description of the reaction of **S8**.



**Scheme 8.9** Proposed mechanism for the oxygenation of **S7** and **S8** promoted by ETFDO.

The reaction is initiated by HAT from the axial C<sub>4</sub>-H bond of **S8** to ETFDO to give directly, via coupled ET, ion-pair **S8-Int1**. Within **S8-Int1**, OH transfer at C-4 via **S8-TS2** delivers axial alcohol **P8a-OH**, while OH transfer at C-1 of the delocalized cationic intermediate<sup>30</sup> via **S8-TS2'** gives rearranged alcohol **P8b-OH**. The lack of the equatorial alcohol **P8c-OH** among the reaction products reflects the higher activation free energy associated to HAT from the equatorial C<sub>4</sub>-H bond compared to the corresponding axial one ( $\Delta\Delta G^\ddagger = 1.9 \text{ kcal mol}^{-1}$ , compare **S8-TS1eq** with **S8-TS1ax** in **Figure 8.7**). Most importantly, the observation that HAT from the axial C<sub>2</sub>-H bond can be coupled to ET whereas the competitive reaction from the equatorial C<sub>2</sub>-H bond (not observed in the experiments) occurs concertedly without generating charged intermediates, indicates that formation of the cationic intermediate must be associated to a specific stabilizing hyperconjugative interaction between the incipient carbon radical and the cyclopropane C-C bonding orbitals able to assist ET to the incipient 1,1,1-trifluoro-2-hydroxy-2-butoxyl radical, and only accessible through the former pathway.<sup>28</sup>

For what concerns the site-selectivities observed in the reactions of ETFDO with substrates **S6-S8**, the normalized product distributions are displayed in **Figure 8.10**. With **S6** comparable selectivities were observed for the three methylenic sites (C-2:C-3:C-4 = 1.0:1.5:1.5). The slightly lower selectivity for oxygenation at C-2 over C-3 and C-4 can be reasonably explained



on the basis of steric effects, where the presence of the two methyl groups limits accessibility of the adjacent C<sub>2</sub>–H bonds to ETFDO.

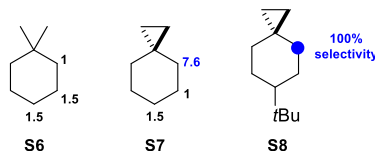


**Figure 8.10** Normalized site-selectivities observed in the oxygenation of 1,1-dimethylcyclohexane (**S6**), spiro[2.5]octane (**S7**) and 6-*tert*-butylspiro[2.5]octane (**S8**) promoted by ETFDO.

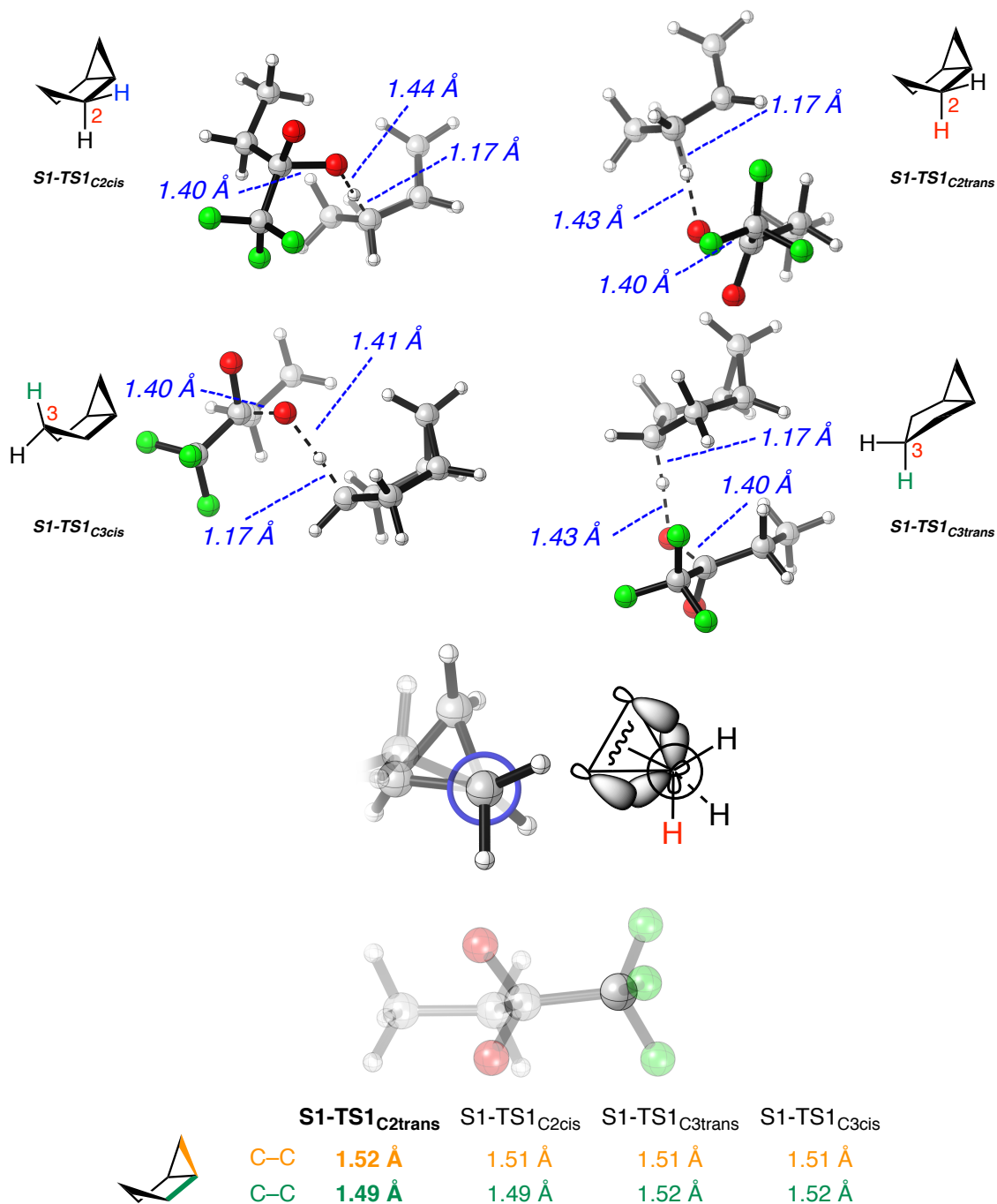
With **S7**, taking into account that the rearranged alcohol product **P7b-OH** derives from initial HAT from the C<sub>4</sub>–H bond (**Scheme 8.9**), the normalized product distributions (C-4:C-5:C-6 = 7.6:1.0:1.5) point toward a significant activation of the C<sub>4</sub>–H bonds compared to the other methylenic sites. These results are in good agreement with those obtained previously by White and Curci in the oxidation of **S7** promoted by the H<sub>2</sub>O<sub>2</sub>/(*S,S*)-Fe(pdp) system and by TFDO.<sup>11e,11f</sup> As mentioned above, this behavior reflects hyperconjugative activation of the C<sub>4</sub>–H bonds via overlap with the cyclopropane C–C bonding orbitals. The site-selectivity observed in the oxygenation of **S8**, for which exclusive formation of products deriving from initial HAT at the axial C<sub>4</sub>–H bond, reflects the synergistic cooperation of two effects: hyperconjugative C<sub>4</sub>–H bond activation together with C<sub>5</sub>–H and C<sub>6</sub>–H bond deactivation by torsional and steric effects determined by the presence of the bulky *tert*-butyl group at C-6.<sup>17,19</sup>

## 8.6 Conclusion

The results of product and computational studies on the C(*sp*<sup>3</sup>)–H bond oxygenation of bicyclic and spirocyclic hydrocarbons bearing cyclopropyl moieties promoted by ETFDO have led to a deeper understanding of the role of hyperconjugative effects in these processes. From good to outstanding site-selectivity for oxygenation at the α-C–H bonds is observed, highlighting the

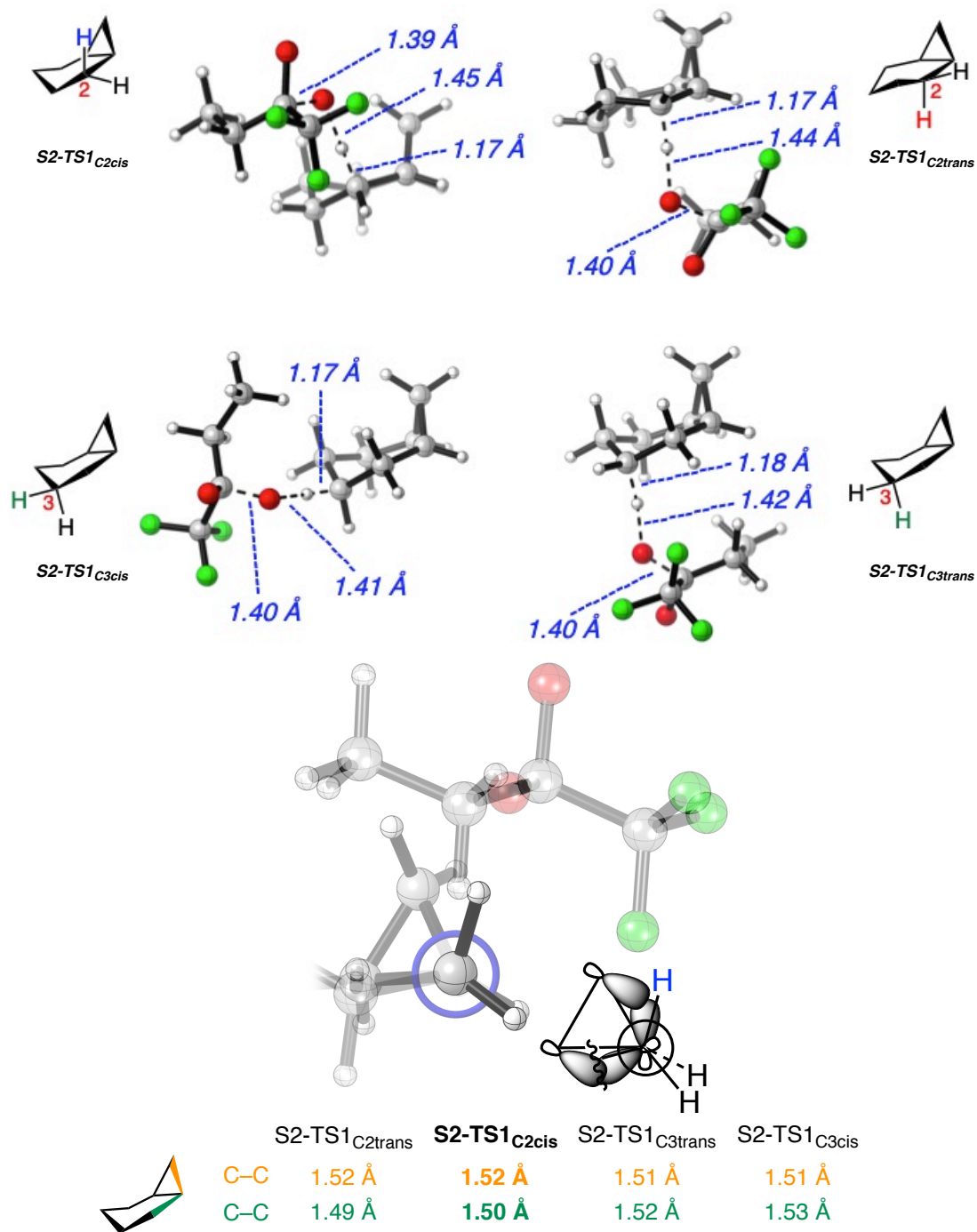
important contribution of hyperconjugative activation to the overall reactivity. Along a similar line, hydroxylation at this site typically occurs with good to outstanding diastereoselectivity with the exclusive detection of a single diastereoisomer in the reactions of bicyclo[6.1.0]nonane (**S5**) and 6-*tert*-butylspiro[2.5]octane (**S8**). This behavior reflects preferential hyperconjugative activation of one  $\alpha$ -C–H bond determined by substrate structure and by conformational effects, with the experimental findings that are in all cases well supported by the computational results. Last but not least, strong support in favor of the contribution of electron transfer pathways has been provided in the oxygenation of 1-methylbicyclo[4.1.0]heptane (**S3**), spiro[2.5]octane (**S7**) and 6-*tert*-butylspiro[2.5]octane (**S8**) promoted by ETFDO, where the detection of rearranged oxygenation products provides unambiguous evidence for the involvement of cationic intermediates in these reactions, providing the first examples on the operation of ET pathways in dioxirane-mediated aliphatic C–H bond oxygenations. Computational studies highlight the role of specific stabilizing hyperconjugative interactions able assist the electron transfer required for cation formation and to divert the reaction from the canonical HAT/rebound pathway.

## 8.7 Supplementary Information



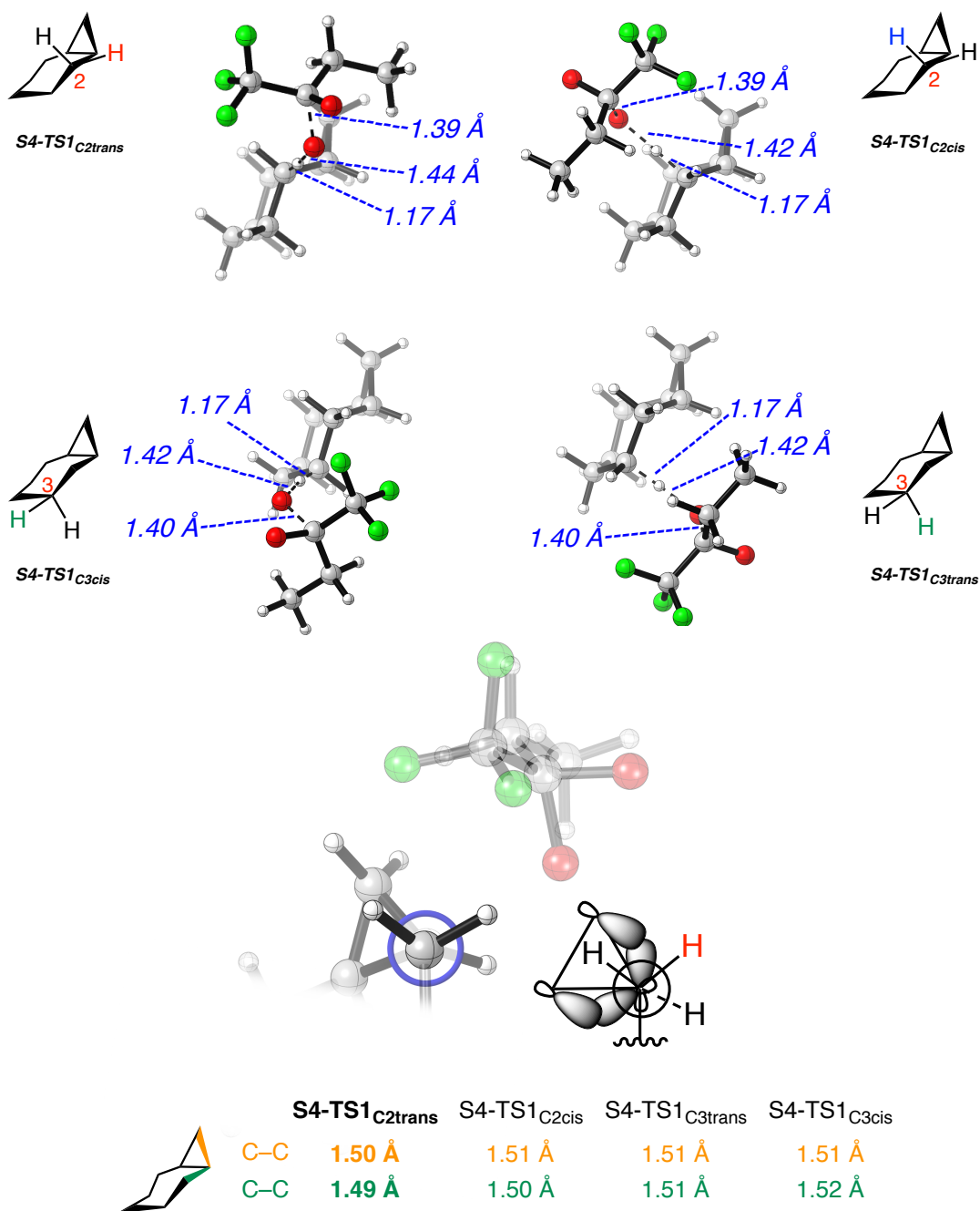
*Hyperconjugation effect on the C<sub>2</sub>-H bond activation*

**Figure 8.11** Transition state structures and structural analysis in C-H bond activation of bicyclo[3.1.0]hexane S1.



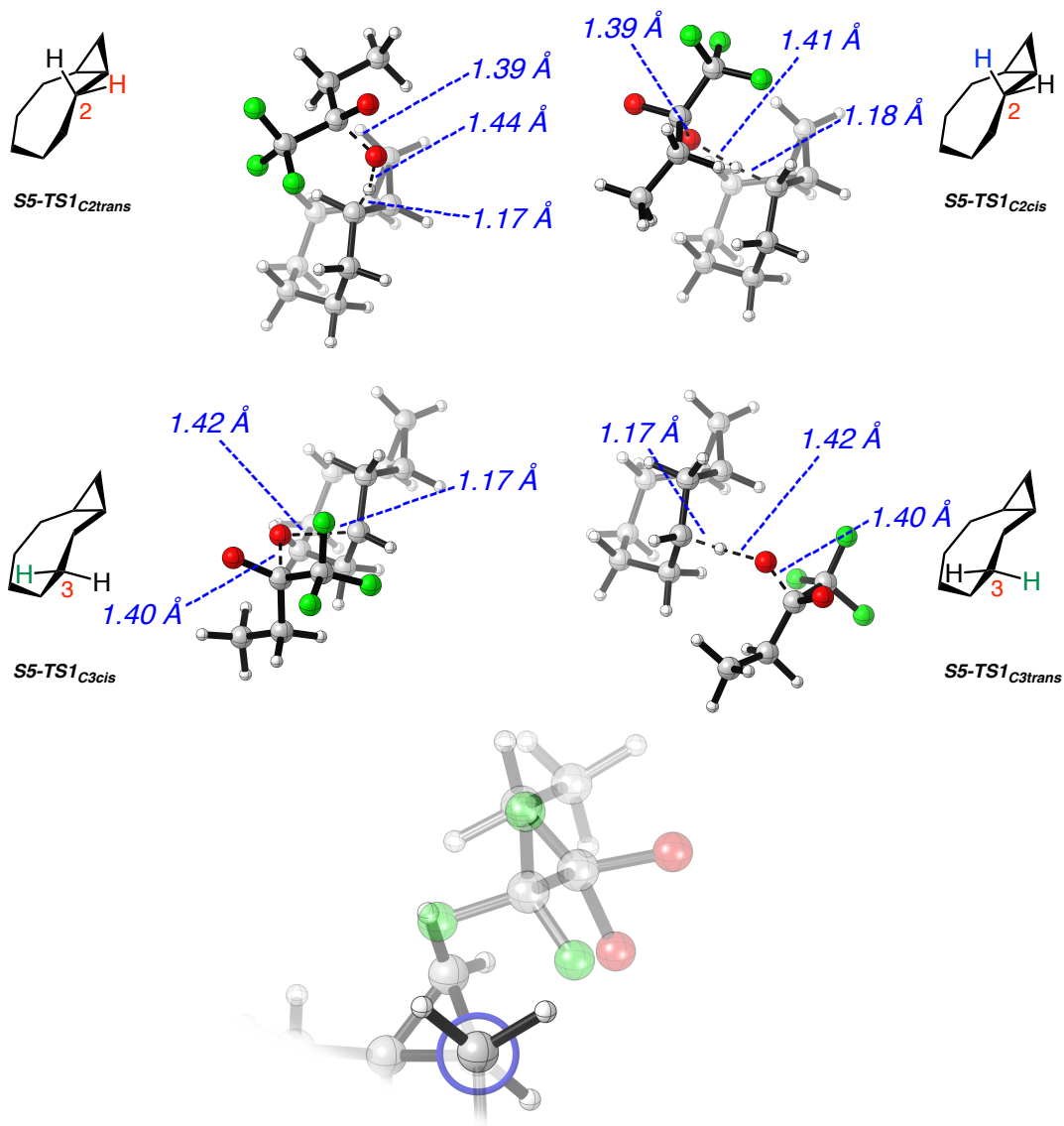
*Hyperconjugation effect on the C<sub>2</sub>-H bond activation*

**Figure 8.12** Transition state structures and structural analysis in C-H bond activation of bicyclo[4.1.0]heptane S2.



*Hyperconjugation effect on the trans C<sub>2</sub>-H bond*

**Figure 8.13** Transition state structures and structural analysis in C-H bond activation of bicyclo[5.1.0]octane S4.



	S5-TS1 <sub>C2trans</sub>	S5-TS1 <sub>C2cis</sub>	S5-TS1 <sub>C3trans</sub>	S5-TS1 <sub>C3cis</sub>
C-C	1.51 Å	1.50 Å	1.51 Å	1.51 Å
C-C	1.49 Å	1.50 Å	1.51 Å	1.51 Å

*Hyperconjugation effect on the trans C<sub>2</sub>-H bond*

**Figure 8.14** Transition state structures and structural analysis in C-H bond activation of bicyclo[6.1.0]nonane S5.

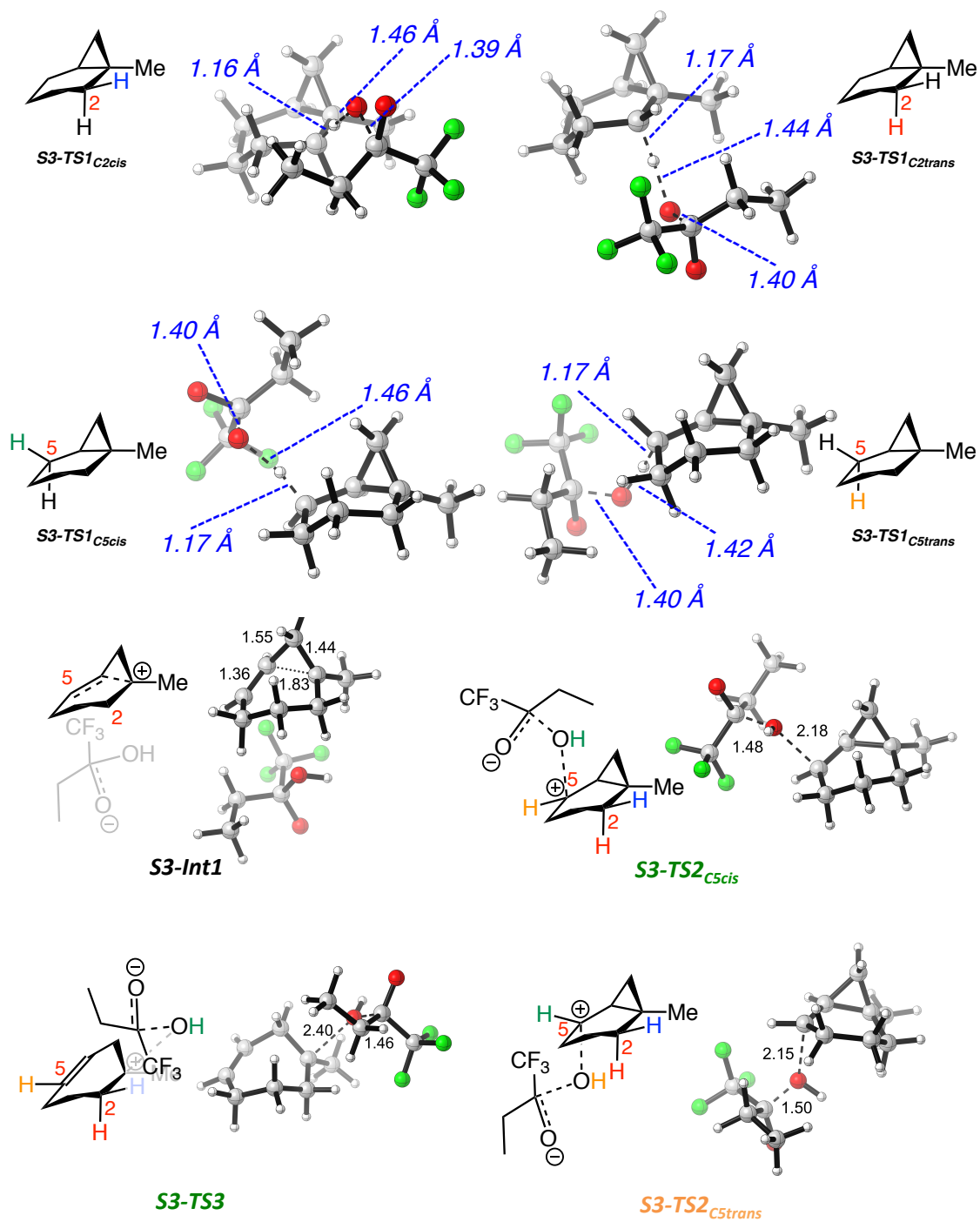
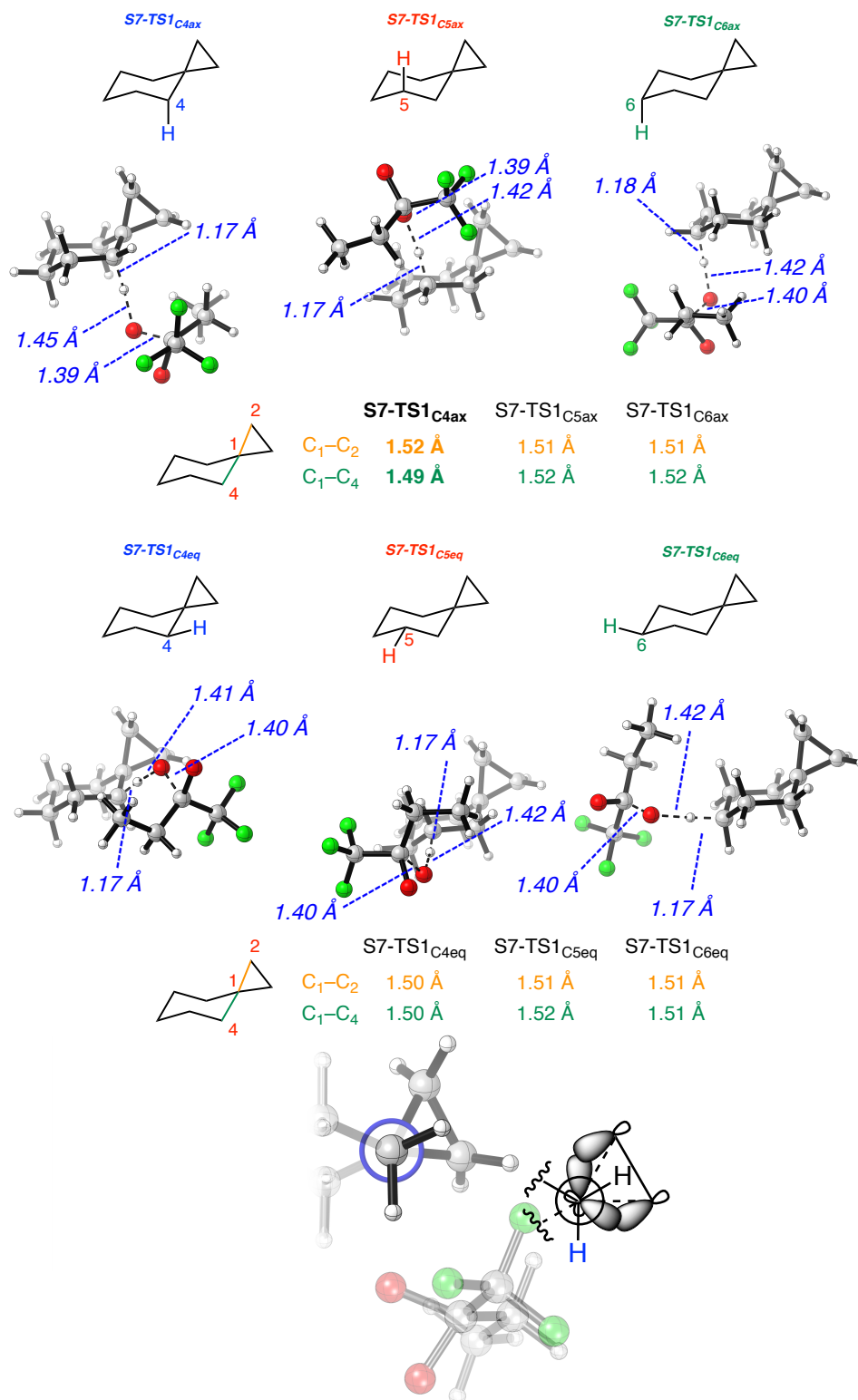


**Figure 8.15** Transition state and intermediate structures in the oxygenation with 1-methylbicyclo[4.1.0]heptane S3.



*Hyperconjugation effect on the axial C–H bond activation*

**Figure 8.16** Transition state and intermediate structures in the oxygenation with spiro[2.5]octanes S7.



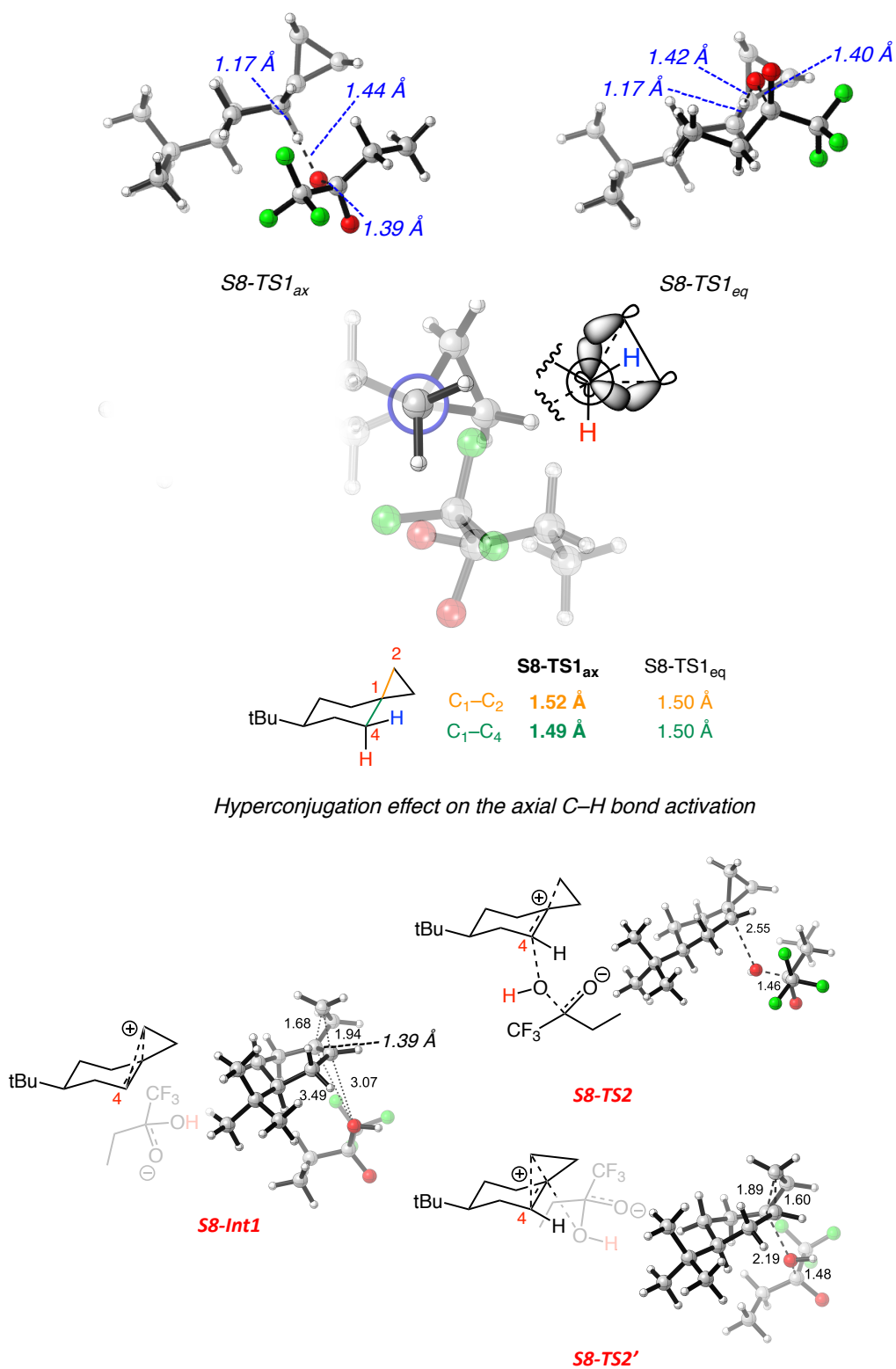


**Figure 8.17** Transition state and intermediate structures in the oxygenation with 6-(tert-butyl)spiro[2.5]octanes **S8**.

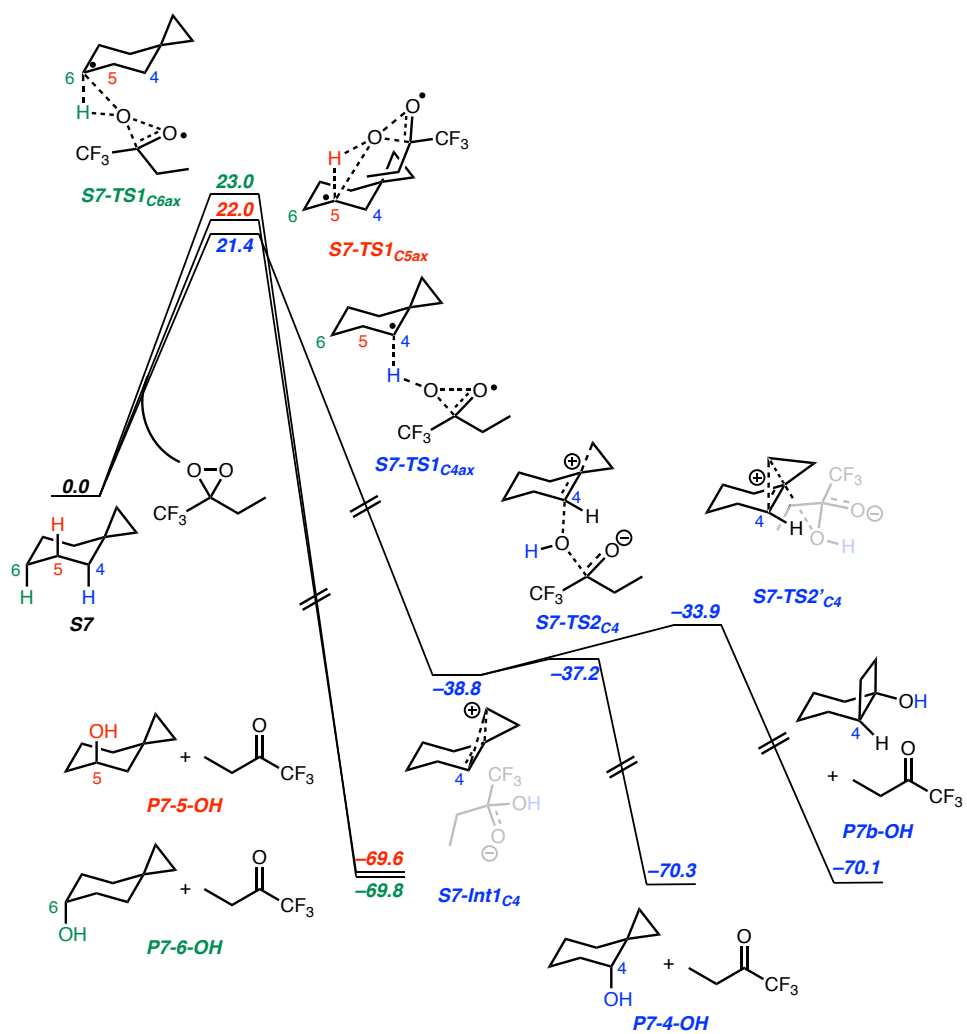


**Figure 8.18** Energy profile in the oxygenation with spiro[2.5]octanes S7.

## 8.8 References

- (1) De Meijere, A. Bonding Properties of Cyclopropane and Their Chemical Consequences. *Angew. Chem. Int. Ed. Engl.* **1979**, *18*, 809-826.
- (2) (a) Schneider, T. F.; Kaschel, J.; Werz, D. B. A New Golden Age for Donor–Acceptor Cyclopropanes. *Angew. Chem. Int. Ed.* **2014**, *53*, 5504-5523. (b) Cohen, Y.; Cohen, A.; Marek, I. Creating Stereocenters within Acyclic Systems by C–C Bond Cleavage of Cyclopropanes. *Chem Rev.* **2021**, *121*, 140-161. (c) Pirenne, V.; Muriel, B.; Waser, J. Catalytic Enantioselective Ring-Opening Reactions of Cyclopropanes. *Chem. Rev.* **2021**, *121*, 227-263.
- (3) Talele, T. T. The “Cyclopropyl Fragment” is a Versatile Player that Frequently Appears in Preclinical/Clinical Drug Molecules. *J. Med. Chem.* **2016**, *59*, 8712-8756.
- (4) (a) de Meijere, A.; Kozhuskkov, S. I.; Schill, H. Three-Membered-Ring-Based Molecular Architectures. *Chem. Rev.* **2006**, *106*, 4926-4996. (b) Mizuno, A.; Matsui, K.; Shuto, S. From Peptides to Peptidomimetics: A Strategy Based on the Structural Features of Cyclopropane. *Chem. Eur. J.* **2017**, *23*, 14394-14409.
- (5) (a) Wessjohann, L. A.; Brandt, W. Biosynthesis and Metabolism of Cyclopropane Rings in Natural Compounds. *Chem. Rev.* **2003**, *103*, 1625-1647. (b) Chen, D. Y.-K.; Pouwer, R. H.; Richard, J.-A. Recent advances in the total synthesis of cyclopropane-containing natural products. *Chem. Soc. Rev.* **2012**, *41*, 4631-4642. (c) Fan, Y.-Y.; Gao, X.-H.; Yue, J.-M. Attractive natural products with strained cyclopropane and/or cyclobutane ring systems. *Sci. China Chem.* **2016**, *59*, 1126-1141. (d) Brill, Z. G.; Condakes, M. L.; Ting, C. P.; Maimone, T. J. Navigating the Chiral Pool in the Total Synthesis of Complex Terpene Natural Products. *Chem. Rev.* **2017**, *117*, 11753-11795. (e) Li, X.; Shimaya, R.; Dairi, T.; Chang, W.-C.; Ogasawara, Y. Identification of Cyclopropane Formation in the Biosyntheses of Hormaomycins and

Belactosins: Sequential Nitration and Cyclopropanation by Metalloenzymes. *Angew. Chem. Int. Ed.* **2022**, *61*, e202113189.

(6) (a) Newhouse, T.; Baran, P. S. If C–H Bonds Could Talk: Selective C–H Bond Oxidation. *Angew. Chem. Int. Ed.* **2011**, *50*, 3362-3374. (b) Yamaguchi, J.; Yamaguchi, A. D.; Itami, K. C–H Bond Functionalization: Emerging Synthetic Tools for Natural Products and Pharmaceuticals. *Angew. Chem. Int. Ed.* **2012**, *51*, 8960-9009. (c) Hartwig, J. F. Evolution of C–H Bond Functionalization from Methane to Methodology. *J. Am. Chem. Soc.* **2016**, *138*, 2-24. (d) White, M. C.; Zhao, J. *J. Am. Chem. Soc.* **2018**, *140*, 13988-14009. (e) Li, J.; Zhang, Z.; Wu, L.; Zhang, W.; Chen, P.; Lin, Z.; Liu, G. Site-specific allylic C–H bond functionalization with a copper-bound N-centred radical. *Nature* **2019**, *574*, 516-521. (f) Davies, H. M. L.; Liao, K. Dirhodium tetracarboxylates as catalysts for selective intermolecular C–H functionalization. *Nature Rev. Chem.* **2019**, *3*, 347-360. (g) Galeotti, M.; Salamone, M.; Bietti, M. Electronic control over site-selectivity in hydrogen atom transfer (HAT) based C(sp<sup>3</sup>)–H functionalization promoted by electrophilic reagents. *Chem. Soc. Rev.* **2022**, *51*, 2171-2223. (h) Capaldo, L.; Ravelli, D.; Fagnoni, M. Direct Photocatalyzed Hydrogen Atom Transfer (HAT) for Aliphatic C–H Bonds Elaboration. *Chem. Rev.* **2022**, *122*, 1875-1924.

(7) Nonhebel, D. C. The chemistry of cyclopropylmethyl and related radicals. *Chem. Soc. Rev.* **1993**, *22*, 347-359.

(8) (a) Huang, X.; Groves, J. T. Oxygen Activation and Radical Transformations in Heme Proteins and Metalloporphyrins. *Chem. Rev.* **2018**, *118*, 2491-2553. (b) Vicens, L.; Olivo, G.; Costas, M. Rational Design of Bioinspired Catalysts for Selective Oxidations. *ACS Catal.* **2020**, *10*, 8611-8631.

(9) (a) Curci, R.; D'Accolti, L.; Fusco, C. A Novel Approach to the Efficient Oxygenation of Hydrocarbons under Mild Conditions. Superior Oxo Transfer Selectivity Using Dioxiranes. *Acc. Chem. Res.* **2006**, *39*, 1-9. (b) D'Accolti, L.; Annese C.; Fusco, C. Continued Progress towards Efficient Functionalization of Natural and Non-natural Targets under Mild Conditions: Oxygenation by C–H Bond Activation with Dioxirane. *Chem. Eur. J.* **2019**, *25*, 12003-12017.

(10) (a) Adams, A. M.; Du Bois, J. Organocatalytic C–H hydroxylation with Oxone enabled by an aqueous fluoroalcohol solvent system. *Chem. Sci.* **2014**, *5*, 656-659. (b) Rotella, M. E.; Dyer, R. M. B.; Hilinski, M. K.; Gutierrez, O. Mechanism of Iminium Salt-Catalyzed C(sp<sup>3</sup>)–H Amination: Factors Controlling Hydride Transfer versus H-Atom Abstraction. *ACS Catal.* **2020**, *10*, 897-906. (c) Hahn, P. L.; Lowe, J. M.; Xu, Y.; Burns, K. L.; Hilinski, M. K. Amine Organocatalysis of Remote, Chemoselective C(sp<sup>3</sup>)–H Hydroxylation. *ACS Catal.* **2022**, *12*, 4302-4309.

(11) (a) Proksch, E.; de Meijere, A. Oxidation of Cyclopropyl Hydrocarbons with Ozone. *Angew. Chem. Int. Ed. Engl.* **1976**, *88*, 761-762. (b) Banwell, M. G.; Haddad, N.; Huglin, J. A.; MacKay, M. F.; Reum, M. E.; Ryan, J. H.; Turner, K. A. The Chromium Trioxide-3,5-Dimethylpyrazole Complex: a Mild and Selective Reagent for the Oxidation of Cyclopropyl Hydrocarbons. *J. Chem. Soc., Chem. Commun.* **1993**, 954-957. (c) Coudret, J. L.; Zollner, S.; Ravoo, B. J.; Malara, L.; Hanisch, C.; Dorre, K.; de Meijere, A.; Waegell, B. Role of Cyclopropanes as Activating Groups during Oxidation Reactions with RuO<sub>4</sub> Generated *in situ*. *Tetrahedron Lett.* **1996**, *37*, 2425-2428. (d) Dehmlow, E. V.; Heiligenstädt, N. Dimethyldioxirane Oxidations of Some Cyclopropanes. *Tetrahedron Lett.* **1996**, 5363-5364. (e) D'Accolti, L.; Dinoi, A.; Fusco, C.; Russo, A.; Curci, R. Oxyfunctionalization of Non-Natural Targets by Dioxiranes. 5. Selective Oxidation of Hydrocarbons Bearing Cyclopropyl Moieties. *J.*

*Org. Chem.* **2003**, *68*, 7806-7810. (f) Chen, M. S.; White, M. C. Combined Effects on Selectivity in Fe-Catalyzed Methylene Oxidation. *Science* **2010**, *327*, 566-571. (g) Sedenkova, K. N.; Andriasov, K. S.; Stepanova, S. A.; Gloriozov, I. P.; Grishin, Y. K.; Kuznetsova, T. S.; Averina, E. B. Direct Oxidation of Cyclopropanated Cyclooctanes as a Synthetic Approach to Polycyclic Cyclopropyl Ketones. *Eur. J. Org. Chem.* **2018**, 879-884.

(12) Brinker, U. H.; Lin, G.; Xu, L.; Smith, W. B.; Miesusset, J.-L. Dihalocarbene Insertion Reactions into C-H Bonds of Compounds Containing Small Rings: Mechanisms and Regio- and Stereoselectivities. *J. Org. Chem.* **2007**, *72*, 8434-8451.

(13) Kawamura, S.; Chu, H.; Baran, P. S. Nineteen-step total synthesis of (+)-phorbol. *Nature* **2016**, *532*, 90-93.

(14) (a) Liu, W.; Groves, J. T. Manganese Porphyrins Catalyze Selective C-H Bond Halogenations. *J. Am. Chem. Soc.* **2010**, *132*, 12847-12849. (b) Aguila, M. J. B.; Badiei, Y. M.; Warren, T. H. Mechanistic Insights into C-H Amination via Dicopper Nitrenes. *J. Am. Chem. Soc.* **2013**, *135*, 9399-9406. (c) Pitts, C. R.; Ling, B.; Snyder, J. A.; Bragg, A. E.; Lectka, T. Direct, Catalytic Monofluorination of  $sp^3$  C-H Bonds: A Radical-Based Mechanism with Ionic Selectivity. *J. Am. Chem. Soc.* **2014**, *136*, 9780-9791. (d) Guo, S.; Zhang, X.; Tang, P. Silver-Mediated Oxidative Aliphatic C-H Trifluoromethylthiolation. *Angew. Chem. Int. Ed.* **2015**, *54*, 4065-4069. (e) Huang, X.; Bergsten, T. M.; Groves, J. T. Manganese-Catalyzed Late-Stage Aliphatic C-H Azidation. *J. Am. Chem. Soc.* **2015**, *137*, 5300-5303. (f) Liu, W.; Cheng, M.-J.; Nielsen, R. J.; Goddard III, W. A.; Groves, J. T. Probing the C-O Bond-Formation Step in Metalloporphyrin-Catalyzed C-H Oxygenation Reactions. *ACS Catal.* **2017**, *7*, 4182-4188. (g) Kariofillis, S. K.; Jiang, S.; Żurański, A. M.; Gandhi, S. S.; Alvarado, J. I. M.; Doyle, A. G. Using Data Science to Guide Aryl Bromide Substrate Scope Analysis in a Ni/Photoredox-

Catalyzed Cross-Coupling with Acetals as Alcohol-Derived Radical Sources. *J. Am. Chem. Soc.* **2022**, *144*, 1045-1055.

(15) (a) Auclair, K.; Hu, Z.; Little, D. M.; Ortiz de Montellano, P. R.; Groves, J. T. Revisiting the Mechanism of P450 Enzymes with the Radical Clocks Norcarane and Spiro[2,5]octane. *J. Am. Chem. Soc.* **2002**, *124*, 6020-6027. (b) Baik, M.-H.; Newcomb, M.; Friesner, R. A.; Lippard, S. J. Mechanistic Studies on the Hydroxylation of Methane by Methane Monooxygenase. *Chem. Rev.* **2003**, *103*, 2385-2419.

(16) Simakov, P. A.; Choi, S.-Y.; Newcomb, M. Dimethyldioxirane hydroxylation of a hypersensitive radical probe: Supporting evidence for an oxene insertion pathway. *Tetrahedron Lett.* **1998**, *39*, 8187-8190.

(17) Galeotti, M.; Vicens, L.; Salamone, M.; Costas, M.; Bietti, M. Resolving Oxygenation Pathways in Manganese-Catalyzed C(sp<sup>3</sup>)-H Functionalization via Radical and Cationic Intermediates. *J. Am. Chem. Soc.* **2022**, *144*, 7391-7401.

(18) (a) Zou, L.; Paton, R. S.; Eschenmoser, A.; Newhouse, T.; Baran, P. S.; Houk, K. N. Enhanced Reactivity in Dioxirane C-H Oxidations via Strain Release: A Computational and Experimental Study. *J. Org. Chem.* **2013**, *78*, 4037-4048. (b) Yang, Z.; Yu, P.; Houk, K. N. Molecular Dynamics of Dimethyldioxirane C-H Oxidation. *J. Am. Chem. Soc.* **2016**, *138*, 4237-4242.

(19) Martin, T.; Galeotti, M.; Salamone, M.; Liu, F.; Yu, Y.; Duan, M.; Houk, K. N.; Bietti, M., Deciphering Reactivity and Selectivity Patterns in Aliphatic C-H Bond Oxygenation of Cyclopentane and Cyclohexane Derivatives. *J. Org. Chem.* **2021**, *86*, 9925-9937.

(20) Frisch, M. J.; Trucks, G. W.; Schlegel, H. B.; Scuseria, G. E.; Robb, M. A.; Cheeseman, J. R.; Scalmani, G.; Barone, V.; Petersson, G. A.; Nakatsuji, H.; Li, X.; Caricato, M.; Marenich, A.

V.; Bloino, J.; Janesko, B. G.; Gomperts, R.; Mennucci, B.; Hratchian, H. P.; Ortiz, J. V.; Izmaylov, A. F.; Sonnenberg, J. L.; Williams-Young, D.; Ding, F.; Lipparini, F.; Egidi, F.; Goings, J.; Peng, B.; Petrone, A.; Henderson, T.; Ranasinghe, D.; Zakrzewski, V. G.; Gao, J.; Rega, N.; Zheng, G.; Liang, W.; Hada, M.; Ehara, M.; Toyota, K.; Fukuda, R.; Hasegawa, J.; Ishida, M.; Nakajima, T.; Honda, Y.; Kitao, O.; Nakai, H.; Vreven, T.; Throssell, K.; Montgomery, J. A., Jr.; Peralta, J. E.; Ogliaro, F.; Bearpark, M. J.; Heyd, J. J.; Brothers, E. N.; Kudin, K. N.; Staroverov, V. N.; Keith, T. A.; Kobayashi, R.; Normand, J.; Raghavachari, K.; Rendell, A. P.; Burant, J. C.; Iyengar, S. S.; Tomasi, J.; Cossi, M.; Millam, J. M.; Klene, M.; Adamo, C.; Cammi, R.; Ochterski, J. W.; Martin, R. L.; Morokuma, K.; Farkas, O.; Foresman, J. B.; and Fox, D. J. *Gaussian 16*; Gaussian, Inc.: Wallingford, CT, **2016**.

(21) Chai, J.-D.; Head-Gordon, M. Long-range corrected hybrid density functionals with damped atom–atom dispersion corrections. *Phys. Chem. Chem. Phys.* **2008**, *10*, 6615-6620.

(22) Marenich, A. V.; Cramer, C. J.; Truhlar, D. G. Universal Solvation Model Based on Solute Electron Density and on a Continuum Model of the Solvent Defined by the Bulk Dielectric Constant and Atomic Surface Tensions. *J. Phys. Chem. B* **2009**, *113*, 6378-6396.

(23) (a) Grimme, S. Supramolecular binding thermodynamics by dispersion-corrected density functional theory. *Chem. Eur. J.* **2012**, *18*, 9955-9964; (b) Luchini, G.; Alegre-Requena J. V.; Guan, Y.; Funes-Ardoiz, I.; Paton, R. S. (2019). GoodVibes: *GoodVibes 3.0.1* DOI: 10.5281/zenodo.595246.

(24) Legault, C. Y. *CYLview*, 1.0b; Université de Sherbrooke, **2009**; <http://www.cylview.org>.

(25) (a) Dantignana, V.; Milan, M.; Cussó, O.; Company, A.; Bietti, M.; Costas, M. Chemoselective Aliphatic C–HBond Oxidation Enabled by Polarity Reversal. *ACS Cent. Sci.* **2017**, *3*, 1350-1358. (b) Bietti, M. Activation and Deactivation Strategies Promoted by Medium



Effects for Selective Aliphatic C–H Bond Functionalization. *Angew. Chem. Int. Ed.* **2018**, *57*, 16618-16637. (c) Borrell, M.; Gil-Caballero, S.; Bietti, M.; Costas, M. Site-Selective and Product Chemoselective Aliphatic C–H Bond Hydroxylation of Polyhydroxylated Substrates. *ACS Catal.* **2020**, *10*, 4702-4709.

(26) Luo, Y.-R. *Comprehensive Handbook of Chemical Bond Energies*, CRC Press, Boca Raton, Florida, **2007**.

(27) In oxidations promoted by dioxiranes, epoxidations have been shown to be strongly favored over C(*sp*<sup>3</sup>)–H hydroxylations. See for example: (a) Cicala, G.; Curci, R.; Fiorentino, M.; Laricchiuta, O. Stereo- and Regioselectivities in the Epoxidation of Some Allylic Alcohols by the Dioxirane Intermediate Generated in the Reaction of Potassium Caroate with Acetone. *J. Org. Chem.* **1982**, *47*, 2670-2673. (b) Legros, J.; Crousse, B.; Bourdon, J.; Bonnet-Delpon, D.; Bégué, J.-P. An efficient and robust fluoroketone catalyst epoxidation. *Tetrahedron Lett.* **2001**, *42*, 4463-4466.

(28) Soler, J.; Gergel, S.; Klaus, C.; Hammer, S. C.; Garcia-Borràs, M. Enzymatic Control over Reactive Intermediates Enables Direct Oxidation of Alkenes to Carbonyls by a P450 Iron-Oxo Species. *J. Am. Chem. Soc.* **2022**, *144*, 15954-15968.

(29) (a) Colomer, I.; Batchelor-McAuley, C.; Odell, B.; Donohoe, T. J.; Compton, R. G. Hydrogen Bonding to Hexafluoroisopropanol Controls the Oxidative Strength of Hypervalent Iodine Reagents. *J. Am. Chem. Soc.* **2016**, *138*, 8855-8861. (b) Colomer, I.; Chamberlain, A. E. R.; Haughey, M. B.; Donohoe, T. J. Hexafluoroisopropanol as a highly versatile solvent. *Nat. Rev. Chem.* **2017**, *1*, 0088.

(30) (a) Olah, G. A.; Fung, A. P.; Rawdah, T. N.; Prakash, G. K. S. The Spiro[2.5]oct-4-yl Cation, a Long-Lived Secondary Cyclohexyl Cation. *J. Am. Chem. Soc.* **1981**, *103*, 4647-4648.

(b) Olah, G. A.; Reddy, V. P.; Prakash, G. K. S. Long-Lived Cyclopropylcarbinyl Cations.

*Chem. Rev.* **1992**, *92*, 69-95.